Borehole stability in unconsolidated sands

Determining minimum distance to ensure stability for nearby foundations

A.J. Timmermans Arribas

Delft University of Technology

TU Delft

Borehole stability in unconsolidated sands

Determining minimum distance to ensure stability for nearby foundations

by

A.J. Timmermans Arribas

to obtain the degree of Master of Science in Civil Engineering
at the Delft University of Technology,
to be defended publicly on **Thursday July 23, 2026 at 14:00**.

Project duration:	January 28, 2026 – July 23, 2026	
Thesis committee:	Prof. dr. P. J. Vardon,	TU Delft, chair
	Dr. J. M. Bloemendal,	TU Delft, supervisor
	Ir. T. M. Grubben,	TU Delft, supervisor

Cover: Rotary Drilling Rig SWDM60 (Modified)
Style: TU Delft Report Style, with modifications by Daan Zwaneveld

An electronic version of this thesis is available at http://repository.tudelft.nl/
The code repository is available at https://github.com/AJGoest/CPT_Analysis.git

TU Delft

Abstract

To transition towards climate-neutral heating and cooling, the need for sustainable underground heat storage systems such as Aquifer Thermal Energy Storage (ATES) is increasing. In dense urban areas, ATES boreholes may need to be installed close to existing foundation piles. Currently, a Dutch rule-of-thumb is used based on ten times the borehole diameter (Stichting Infrastructuur Kwaliteitsborging Bodembeheer (SIKB), 2021). The rule is simple, but does not consider the influence zone of nearby objects or soil behaviour around the borehole. As a result, the required distance may be overly conservative for larger borehole diameters, creating an inefficient use of space in already crowded urban areas.

This research investigates the minimum centre-to-centre distance between an ATES borehole and nearby foundation piles in unconsolidated sand. The objective is to determine whether the existing rule-of-thumb can be refined by combining field-based CPT interpretation with numerical modelling of stress redistribution around a borehole. The study focuses on a Delft case study, supported by additional qualitative comparisons from the Wezep and Zwolle case studies.

The field analysis consisted of cone penetration test interpretation before and after borehole installation. Cone resistance, sleeve friction, Robertson soil behaviour type, horizontal stress, relative density and cone trajectory were analysed to assess whether measurable soil changes occurred after drilling. Additional CPT data from Wezep and Zwolle were used to evaluate whether similar soil behaviour trends could be observed at other locations. The numerical analysis was performed in PLAXIS using Linear Elastic, Mohr-Coulomb and SANISAND constitutive models on calibrated Ottawa sand parameters. The borehole was simulated by stepwise unloading of the borehole wall, and the resulting radial, hoop and vertical stress redistribution was evaluated. The final numerical distance was based on the SANISAND model, because this is the most advanced model and predicted the largest stress redistribution zone.

The Delft CPT results showed no clear systematic change in cone resistance, sleeve friction or Robertson soil behaviour type induced by drilling. Local differences between CPTs were mainly interpreted as spatial variability rather than borehole-induced. The CPT-based interpretation resulted in a borehole influence distance of $3.33D_b$. When the Koppejan pile influence zone is included, the proposed distance becomes $4.7D_{eq} + 3.33D_b$.

The numerical model showed that the borehole-induced stress redistribution decreases rapidly with distance and scales with the borehole diameter. Based on recovery of vertical stress to 95% of the far-field value, the proposed numerical borehole influence distance is D_nD_b, where $D_n = 2.5$ for initial void ratios below 0.8 and $D_n = 3.0$ for initial void ratios equal to or greater than 0.8. Including the Koppejan pile influence zone gives a proposed distance of $4.7D_{eq} + D_nD_b$. The void ratio boundary at 0.8 should be interpreted as a behavioural transition within the Ottawa sand used for SANISAND, not as a critical-state boundary.

The results indicate that the SIKB rule-of-thumb can be conservative for larger borehole diameters, because it scales only with borehole diameter and does not consider the foundation pile influence zone. However, the rule is not conservative for small borehole diameters. A practical minimum centre-to-centre distance of 1.5 m is therefore recommended before applying the proposed expressions, unless project-specific conditions justify adjustment by the responsible engineer.

This research provides a more rational framework for assessing borehole placement near existing pile foundations. By separating the borehole influence zone from the pile influence zone, the proposed method can be adapted to different pile dimensions and potentially to other underground objects. Further research should focus on field validation at closer CPT distances, site-specific SANISAND calibration and a more accurate definition of the foundation pile influence zone.

Acknowledgements

Fortunately and unfortunately, this thesis marks the end of my journey at the Technical University of Delft. The journey has simply been incredible, with some downs and an infinite number of ups. The university and the Civil Engineering track have given me everything I could have wished for. The level of the courses, the passion of the professors and the way of thinking have truly challenged me and changed the way I approach problems and challenges. As my grandfather used to say: "You have passed university, but has university passed through you?" This is the most accurate description of how I have developed over the years and how I have changed compared with when I first came to university.

First of all, I would like to thank my committee. Phil and Martin, you may not know this, but since the day I followed the Energy Storage course during my Bachelor's, I knew I wanted to do my thesis on a topic related to underground heat storage systems. This decision changed my entire plan for the direction of my Master's, as I was planning to specialise in offshore hydraulic structures. Fortunately, I did not. The passion and knowledge you have on this topic truly captured my interest, and the positive effect this field can have on society is incredible. I would like to thank you both for your guidance, advice and passion for this topic. Last, and certainly not least, I would like to thank Tessel. No matter the time or day of the week, you were always available to give advice. Outside the scientific chatter, I also had great fun talking about similar problems we faced in research and about our experiences studying in Delft. Without your guidance and experience, I think this journey would have been much harder. I wish you all the best finishing your PhD, and I am convinced that the world will be at your feet.

Now, the moment to thank everyone who has been there every step of the journey, giving a listening ear to my complaints and frustrations, and giving me unconditional support along the way. Bob, Núria and Carlota, thank you for everything. The distance makes it difficult, and my terrible explanations of the problems I was facing during the research probably did not make it any easier for you to help either. Still, when I was feeling less motivated, or on the contrary very motivated, you were there to tell me to keep pushing and finish the work that I had started. This not only applies to the thesis, but to everything I have done in my life. I cannot wait to be back with the three of you again.

Agnès, I cannot thank you enough for all the support and patience you have had. The distance makes it incredibly difficult, yet you have always found a way to be there. These last couple of months were probably the most difficult, with my rollercoaster of moods depending on whether my model crashed again or gave me another error. This marks the end of the thesis, and I cannot wait move to Spain and to be with you.

I would like to thank everyone from my Master's cohort. I did not expect that such a small group with so many different backgrounds would form such a family. All the trips, activities and fun that we had during the Master's have caused it to fly by. It gives a bittersweet feeling to finish my Master's. I still hope to see everyone in the near future and, of course, I wish everyone the best of luck. If I forgot to mention it: you all looked amazing during the gala!

One particular person from the Master's I would like to thank is Tijmen. We shared a friend group, although I did not know you that well. But oh boy, I did not know it was going to be such a match. Both of us had a completely different track in mind for the Master's and collectively decided only a few days in advance to go for geo. In my eyes, this was the best choice we could have made. With all the fun during the activities, trips, group projects and lectures, the years have flown by. I did not know there was someone who shared equally, or even more, the importance of everything around studying. To this day, I am still astonished by everything you have accomplished over the years. Our time at university is over, however, the good friendship will not be lost.

I would like to thank all the roommates I have had over the years, the new ones and the old ones. The old ones for showing gratitude for my dreadful cooking and joining me during all the cowboy years at

the university. The new ones for making sure that, if my mind was not overloaded enough after a day of grinding on my thesis, it certainly would be after geopolitical or history discussions that could last for days and were not for the faint-hearted.

I would also like to thank my group of friends at the faculty. Even though the group may have been created in what some would call an unorthodox manner, it still has become an incredible group with great people. The trips and other activities organised by enthusiastic people can always count on my presence. Hoog!

Ahora vamos al castellano para dar las gracias a dos amigos muy importantes de la península ibérica. Carles, verdaderamente eres mi mejor amigo y siempre has estado a mi lado. Siempre has podido y querido ayudar cuando ha sido necesario, y aprecio muchísimo tu amistad. Es curioso y, a la vez, muy lógico que hayamos escogido las mismas carreras y tomado decisiones tan parecidas en nuestras vidas. El mundo se va a tener que preparar.

Nunu, aunque no tengamos mucho contacto online, no cabe duda en que eres infalible. Creo que no hay bar en Begues en el que no haya probado el café durante todas nuestras quedadas. Tengo muchas ganas de volver a tomar esos cafés caundo esté por Begues.

Avi, iaia y opa que os echo mucho de menos y, aunque no estéis, estoy seguro de que estaríais orgullosos. No hay un día que pase en el que no pienso en vosotros. Siempre me acompañaréis. Os quiero mucho.

Oma, Mariëtte en Wilbert, bedankt voor alle superleuke momenten. Ik zal zeker nooit vergeten hoe vaak jullie mij geholpen hebben op de momenten dat ik het nodig had.

I will certainly have forgotten some people, and please forgive me for that, but thank you all for the good times and support over the years.

A.J. Timmermans Arribas
Delft, July 2026

Contents

Abstract i

Preface ii

Nomenclature vii

1 Introduction 1
- 1.1 Background . . . 1
- 1.2 Problem statement . . . 1
- 1.3 Objective and research questions . . . 2
- 1.4 Thesis outline . . . 2

2 State of the art 4
- 2.1 Drilling in unconsolidated soil . . . 4
  - 2.1.1 Subsurface characteristics and processes . . . 4
  - 2.1.2 Prior research . . . 6
- 2.2 Pile foundation bearing capacity . . . 7
  - 2.2.1 Subsurface characteristics and processes . . . 7
  - 2.2.2 Prior research . . . 9
- 2.3 Case studies . . . 12
  - 2.3.1 Delft . . . 12
  - 2.3.2 Wezep . . . 13
  - 2.3.3 Zwolle . . . 13
- 2.4 CPT . . . 14
  - 2.4.1 Principle and development of CPT . . . 14
  - 2.4.2 CPT-based soil interpretation . . . 14
  - 2.4.3 Reliability and limitations . . . 15
  - 2.4.4 Relevance for research . . . 15
- 2.5 Horizontal stress . . . 16
- 2.6 Robertson-Lengkeek classification . . . 16
- 2.7 Constitutive soil models . . . 19
  - 2.7.1 Linear Elastic model . . . 19
  - 2.7.2 Mohr-Coulomb . . . 20
  - 2.7.3 SANISAND . . . 22

3 Methods and Materials 26
- 3.1 Field data and CPT processing . . . 26
  - 3.1.1 Cone trajectory . . . 26
  - 3.1.2 GEF data processing . . . 27
  - 3.1.3 Soil classification . . . 28
  - 3.1.4 Material characteristics . . . 29
  - 3.1.5 Robertson chart . . . 29
  - 3.1.6 Relative density . . . 30
  - 3.1.7 Horizontal stress . . . 31
  - 3.1.8 Additional case studies . . . 31
- 3.2 Numerical modelling approach . . . 32
  - 3.2.1 Modelling limitations and assumptions . . . 32
  - 3.2.2 Geometry, mesh and boundary conditions . . . 32
  - 3.2.3 Soil layering and material assignment . . . 33
  - 3.2.4 Borehole modelling and unloading phases . . . 34
  - 3.2.5 Constitutive models . . . 35

3.2.6 Extraction of results . . . 35
3.2.7 Comparison and evaluation procedure . . . 37
3.3 Determination of pile-to-borehole distance . . . 37
3.3.1 Pile influence according to Koppejan . . . 37
3.3.2 Framework for comparison . . . 38

4 Results Delft **39**
4.1 In-situ data interpretation . . . 39
4.1.1 Cone Trajectory . . . 39
4.1.2 Soil profile and parameters . . . 41
4.1.3 CPT measurements . . . 43
4.1.4 Relative density . . . 50
4.1.5 Derived horizontal stress . . . 51
4.2 Numerical model stress distribution . . . 54
4.2.1 Linear-Elastic . . . 54
4.2.2 Mohr-Coulomb . . . 56
4.2.3 SANISAND . . . 58
4.2.4 Comparison between models . . . 61
4.2.5 Borehole radius influence . . . 68
4.2.6 Vertical stress . . . 70
4.2.7 Alternating void ratios . . . 73
4.2.8 Critical void ratio Ottawa sand . . . 75
4.3 Pile to borehole distance interpretation . . . 76
4.3.1 CPT-based . . . 76
4.3.2 Numerical model based . . . 77
4.4 Comparing minimum distances . . . 80
4.4.1 CPT-based without pile zone . . . 80
4.4.2 CPT-based with pile zone . . . 81
4.4.3 Numerical model based without pile zone . . . 81
4.4.4 Numerical model based with pile zone . . . 82

5 Results Wezep & Zwolle **83**
5.1 Soil profile . . . 83
5.1.1 Wezep . . . 83
5.1.2 Zwolle . . . 85
5.2 Soil behaviour type . . . 88
5.2.1 Wezep . . . 89
5.2.2 Zwolle . . . 92

6 Discussion and limitations **97**
6.1 Interpretation of results . . . 97
6.1.1 Delft CPT soil classification . . . 97
6.1.2 CPT-based distance . . . 98
6.1.3 Numerical model based distance . . . 98
6.1.4 Additional case studies . . . 100
6.2 Limitations . . . 100
6.2.1 Soil classification . . . 100
6.2.2 CPT-based distance . . . 101
6.2.3 Numerical model-based distance . . . 101
6.2.4 Additional case studies . . . 102
6.3 Practical implications . . . 102
6.3.1 CPT classification . . . 102
6.3.2 Borehole to foundation pile distance . . . 102

7 Conclusion and recommendations **104**
7.1 Summary of findings . . . 104
7.2 Contribution to knowledge . . . 105
7.3 Practical implications . . . 105

7.4 Limitations . . . 105
7.5 Recommendations for further research . . . 106
7.6 Closing statement . . . 106

A Soil classification **111**

B Soil distribution Delft **112**
B.1 Soil profile . . . 112
B.2 Cone resistance delta . . . 114
B.3 Sleeve friction delta . . . 115
B.4 Boxplots friction ratio in foundation pile sand layer . . . 118
B.5 Robertson charts foundation pile sand layer around -18.5 m NAP . . . 120
B.6 Confidence ellipse Robertson charts for other layers . . . 122
B.7 Soil parameters per layer . . . 125
B.8 SANISAND parameters Ottawa sand . . . 126

C Numerical model results **127**
C.1 Linear results . . . 128
C.2 Mohr-Coulomb . . . 130
C.3 SANISAND . . . 132
C.4 Comparing models . . . 134
C.5 Vertical stress . . . 136
C.6 Vertical stress under different initial void ratio . . . 140
C.7 Hoop and radial stress and strain under different initial void ratio . . . 143

D Github repository **149**

E Soil distribution Wezep & Zwolle **150**
E.1 Soil profile . . . 150
E.1.1 Wezep . . . 150
E.1.2 Zwolle . . . 152

Nomenclature

Abbreviations

Abbreviation	Definition
NAP	Nieuw Amsterdam Peil
OCR	Over Consolidation Ratio
EU	European Union
PUSH-IT	Piloting Underground Seasonal Heat Storage in Geothermal Reservoirs)
HT-ATES	High Temperature Aquifer Thermal Energy Storage
CPT	Cone Penetration Test
DMT	Marchetti Dilatometer Test
SBT	Soil Behaviour Type
CPT1-2	Cone penetration test before drilling 2 m from borehole centre
CPT1-4	Cone penetration test before drilling 4 m from borehole centre
CPT2-2	Cone penetration test after drilling 2 m from borehole centre
CPT2-4	Cone penetration test after drilling 4 m from borehole centre
SIKB	Stichting Infrastructuur Kwaliteitsborging Bodembeheer
ATES	Aquifer Thermal Energy Storage
TBM	Tunnel Boring Machine
SPT	Standard Penetration Test
GEF	Geotechnical Exchange Format
PLAXIS	Finite element software used for geotechnical analysis
SANISAND	Simple Anisotropic Sand model
CSL	Critical State Line
MC	Mohr-Coulomb
LE	Linear Elastic

Symbols

Symbol	Definition	Unit
q_c	Cone resistance	[MPa]
f_s	Sleeve friction	[MPa]
R_f	Friction ratio	[%]
u_2	Pore pressure	[MPa]
u_0	hydrostatic pore pressure	[kPa]
q_t	Corrected cone resistance	[MPa]
Q_t	Normalised cone resistance	[-]

Symbol	Definition	Unit
D_{50}	Median particle diameter	[mm]
q_b	Foundation pile base resistance	[MPa]
q_s	Foundation pile shaft resistance	[MPa]
A_s	Surface area of pile shaft	[m^2]
τ_f	Average shaft friction	[MPa]
α_s	Pile shaft factor	[-]
α_p	Pile tip bearing capacity factor	[-]
N_q	Foundation pile bearing capacity factor	[-]
σ'_v	Effective vertical stress	[kPa]
σ'_h	Effective horizontal stress	[kPa]
p_a	Atmospheric pressure	[MPa]
D_{eq}	Equivalent pile base diameter	[m]
B_{qt}	Normalised pore pressure ratio	[-]
I_{SBT}	Soil behaviour type index	[-]
E	Young's modulus	[MPa]
ϵ	Extension of the material	[-]
ν	Poisson ratio	[-]
ϕ	Friction angle	[°]
c	Cohesion	[kPa]
ψ	Dilatancy angle	[°]
G	Elastic shear modulus	[kPa]
K	Elastic bulk modulus	[kPa]
e	Void ratio	[-]
e_c	Critical void ratio	[-]
D_r	Relative density	[%]
$e_{\min}$	Minimum void ratio	[-]
$e_{\max}$	Maximum void ratio	[-]
K_0	Coefficient of earth pressure at rest	[-]

1 Introduction

1.1. Background

The European commission aims for Europe to become climate neutral by 2050 (European Commission, 2026). To achieve reductions in greenhouse gas emissions the European Union funds research and projects that investigate this reduction. One of these funds has been dedicated to the PUSH-IT project, focused on developing a sustainable solution to overcome the seasonal mismatch in heat demand and heat generation (TU Delft, 2026). In Europe, 50% of the total energy demand is used for the heating and cooling of buildings. PUSH-IT aims to reduce the greenhouse gas production for heating through underground heat storage, such as Aquifer Thermal Energy Storage (ATES). However, implementing ATES in dense urban areas requires boreholes to be placed within already crowded subsurface environments.

In densely built-up environments in western Netherlands, where soft deltaic deposits are often underlain by sand layers, the installation of a borehole with almost zero overpressure may lead to stresses and strains in the soil that can have a negative impact on nearby foundations. Due to limited knowledge, a conservative rule of thumb has been adopted to avoid possible damages during drilling. This rule states that the minimum distance between the foundation and the centre of a borehole must be ten times the diameter of the borehole in question and in the case of a monumental building fifteen times (Stichting Infrastructuur Kwaliteitsborging Bodembeheer (SIKB), 2021). The exact explanation for this rule of thumb is not known, however, may have been chosen because the Mohr-Coulomb criterion suggests borehole failure due to a reduction in radial effective stress whilst drilling (Fjær et al., 2008). In practice however, boreholes tend to be stable, as recent results show that the sand matrix dilates, resulting in an increase in shear strength. This raises the question whether the currently applied rule of thumb is too conservative, and whether wells can therefore be placed closer to buildings.

As urban spatial availability remains scarce, there is an increasing interest in quantifying the minimum distance between ATES boreholes and foundations. An evidence-based distance maximises the spatial applicability of ATES systems in both existing and future urban areas.

1.2. Problem statement

Borehole stability in consolidated materials, such as rock, has been widely studied, these studies have focused on the conditions at or immediately around the borehole wall and at stress and strain developments away from the borehole. Research regarding unconsolidated sand is limited, however, recently more research has been conducted focused on failure initiations, filter cake development, well-bore strengthening additives and local stress changes (Grubben et al., 2025; Koulidis et al., 2025; Risnes et al., 1982). Risnes et al. (1982) developed an analytic method to determine radial and tangential stresses around a borehole using a Mohr-Coulomb elastoplastic framework. While this method provides valuable insight into well-bore stress distribution, it is one of three theoretical frameworks that lack in-situ data validation. As a result, the unverified theories have an unknown accuracy, limiting our ability to predict interactions between boreholes and nearby structural foundations. Previous work by

Hashemi et al. (2015) further indicates that the extent of the plastic zone strongly depends on borehole radius, suggesting that increasing borehole radius may increase stress and strain effects away from the borehole.

Different approaches exist to address this gap: one involves numerical modelling of stress and strain development, and the second to interpret direct pre and post CPT data surrounding the borehole. The SANISANDS model provides a possibility for predicting stress and strains around boreholes, but it has yet to be validated. On the other hand, the available field measurements, which still must be analysed and checked for errors, give real results of soil behaviour that can be exploited to perform predictive modelling. Nonetheless, for CPT, the measurements must be converted into vertical and horizontal stress components to asses its area of influence.

The missing part is an evidence based minimum distance from boreholes to foundations. To achieve such value a combined analysis should be performed which both quantifies the borehole induced stresses and strains surrounding the borehole and validates the predictions of the numerical models. This is not only interesting to determine a minimum distance to foundations in urban environments, but also to understand the effects of borehole induced stresses on the bearing capacity of a pile. Enabling more efficient minimum distance guidelines for ATES or other boreholes in urban areas

1.3. Objective and research questions

This research project aims to create a tool to determine, using field data and numerical model results, the minimum safe distance between varying borehole radii and piled foundations in different soil conditions.

The following research questions has been adopted:
What is the minimum safe distance between an ATES borehole and nearby piled foundations in unconsolidated sands?

To answer the research questions the following sub-questions are formulated:

1. How do unconsolidated sands behave under no overpressure drilling conditions according to different material models?
2. To what extent do CPT measurements provide reliable evidence to determine the development of stress in the subsurface?
3. To what extent can vertical stress be accurately derived to horizontal components?
4. How accurately do the elastic, Mohr-Coulomb and SANISAND predict stress changes in unconsolidated sands?
5. Is the current rule of thumb an over-conservative assumption that can be rectified by measured evidence?
6. How do different soil conditions change stress development?
7. How sensitive is the development of stress to alternations in borehole radius?

1.4. Thesis outline

The thesis is structured as follows. Chapter 2 presents the state of the art. It provides background information and previous research on drilling in unconsolidated soils, pile foundation bearing capacity, case studies, CPTs, horizontal stress, Robertson-Lengkeek soil classification and constitutive models.

Chapter 3 presents the methods and materials used in this research. Divided into three main sections: field data and CPT processing, numerical modelling approach and determination of the pile to borehole safe distance.

Chapter 4 and Chapter 5 present the results. Chapter 4 presents the results for the Delft case study, including the CPT data interpretation, numerical model results and determination of the pile to borehole safe distance. Chapter 5 presents the results for the Wezep and Zwolle case studies, including the

soil and the Robertson soil behaviour type classification. The latter chapter presents less extensively analysed results than the Delft case study.

Chapter 6 discusses the interpretation, limitation and practical implications of the results. Chapter 7 presents the final conclusion and final recommendations for further research. The appendices contain the additional soil classification, soil distribution, numerical model results, python code and Wezep and Zwolle results.

2

State of the art

This chapter provides the theoretical background required for this research. It reviews the relevant literature on drilling in unconsolidated soil, pile foundation bearing capacity, CPT interpretation, horizontal stress estimation, Robertson-Lengkeek soil classification and constitutive soil models. The case studies used in this research are also introduced. Together, these topics provide the basis for interpreting the field measurements, setting up the numerical model and determining the pile-to-borehole safe distance.

Section 2.1 discusses drilling in unconsolidated soil. Section 2.2 presents background on pile foundation bearing capacity mechanisms. Section 2.3 introduces the three case studies. Section 2.4 explains CPT interpretation, its limitations and relevance for this research. Section 2.5 discusses horizontal stress estimation. Section 2.6 presents the Robertson-Lengkeek classification. Finally, Section 2.7 describes the constitutive soil models used in the numerical analysis.

2.1. Drilling in unconsolidated soil

2.1.1. Subsurface characteristics and processes

Unconsolidated soils are a mixture of non-cemented mineral and/or organic particles, such as gravel, sand, silt, clay and peat (UNITRACC, n.d.). Sand and gravel are characterised by a loose granular structure in which particles are not strongly bonded, negatively affecting their shear strength. The shear resistance arises from friction and interlocking between particles, and in some cases minor cohesion in fine-grained soils (Terzaghi et al., 1996). In contrast, fine-grained and organic soils like clay and peat are characterised by stacked sheets or films carrying electrical charges responsible for inter particle bonding mechanisms (Terzaghi et al., 1996). These soils have a high moisture content, are highly compressible and have a very low shear strength (Firoozi et al., 2016; Zainorabidin & Wijeyesekera, 2008). As a result, unconsolidated soil formations typically exhibit relatively low shear strength compared with consolidated rock formations.

According to Terzaghi et al. (1996), mechanical behaviour of unconsolidated soils are influenced by density, grain size distribution, texture, structure, consistency, porosity, water content and unit weight. Unconsolidated sands are categorised as high porosity. This results from large pore spaces in its structure. There is a positive relationship between organic content of soil and its porosity. This relationship is reversed in the case of density. Greater organic content soil like peat start at a density of $10kN/m^3$ whilst sands have a density of $22kN/m^3$ (NEN, 2016). Unconsolidated sands are considered soft soils and by fluctuating changes in its mechanical characteristics instability can occur during drilling.

For geothermal wells in unconsolidated soils, rotary drilling is the most commonly employed technique (PatSnap, 2025). Rotary drilling was developed in the nineteenth and early twentieth century to address the temporary casing challenges in unstable formations when using percussion drilling techniques (Misstear et al., 2017).

Reverse circulation rotary drilling consists of a drill bit connected to a drill pipe, through which drilling

fluid is circulated to maintain the hydrostatic pressure during the drilling process. The fluid travels downward, purely by gravity, through the annulus and flows back through the drill pipe by air injection taking drilling debris up to the surface (Koulidis et al., 2025). At the surface, the solids are separated from the fluid in mud pits and the fluid is recirculated to the borehole. This cycle can also be reversed.

Two main rotary drilling configurations are used: the kelly-drive rig and the top-drive rig (Misstear et al., 2017). At present, the top-drive configuration is the most frequently used. In this system, the drill string is directly connected to a motorised rotary head that moves vertically as the borehole deepens, allowing additional drill pipe sections to be added sequentially during drilling. Figure 2.1 illustrates an example of a top-drive drilling system used in unconsolidated soils.

Figure 2.1: Top driven drilling in soft soils with drilling fluid (Conrad Stanen B.V., 2024)

During the drilling process soil is removed and the surrounding soil is unloaded. The pressure delivered by the drilling fluid can be applied to counter in the imbalance created by the unloading of the soil, preventing borehole collapse (Koulidis et al., 2025). When the pressure is too high there is a risk of removing soil around the borehole. This may result in borehole failure and also in a reduction in well performance.

In practice, however, boreholes in unconsolidated soils are often successfully drilled with drilling fluid overpressure close to zero (van der Schans et al., 2022). This observation appears inconsistent with predictions based on the Mohr–Coulomb failure criterion, which suggests that cohesion-less soils such as sands should fail when one of the principal stresses approaches zero (Jaeger et al., 2009). Consequently, field observations indicate that the assumptions underlying the Mohr–Coulomb model do not fully capture the mechanical behaviour of unconsolidated soils surrounding a borehole during drilling operations.

According to Xu (2012), the excavation of a borehole causes stress redistribution within the surrounding soil mass, leading to the development of stress concentrations around the borehole wall. When the interaction between soil particles is insufficient to sustain these stress changes, local instability may occur. Appropriate control of drilling fluid pressure is therefore essential to stabilise the borehole wall and limit the development of such instability mechanisms.

2.1.2. Prior research

Understanding the behaviour of soil surrounding a borehole is essential when assessing the potential interaction between drilling operations and nearby foundation piles. Previous research has investigated this behaviour from theoretical, experimental and practical perspectives.

The Mohr–Coulomb failure criterion predicts that the soil surrounding a borehole should fail when the shear stress increases during drilling. However, field observations show that boreholes in sandy soils often remain stable. Recent laboratory research by Grubben et al. (2025) suggests that this stability in sand may be explained by dilative behaviour during unloading. In compression and lateral extension triaxial tests performed by the authors, a greater inferred dilation angle was observed during lateral extension tests compared with compression tests. This indicates that dilation plays a more significant role under unloading conditions. The observed stability in sand may be explained by an increase in apparent shear strength and suggests that the shear strength assumed in conventional borehole stability theory may be underestimated. Although dilation may explain why boreholes remain stable in granular soils, this stability is not unlimited and practical constraints may arise when borehole diameters increase.

The dilative behaviour of sand may contribute to borehole stability, however, this stability does not apply for all large borehole diameters. van der Schans et al. (2022) investigated a novel drilling technique designed to expand borehole diameters in unconsolidated sands at depth. The method employs a pivoting arm equipped with a low-pressure water jet to enlarge the borehole perpendicular to the drilling direction. During field testing, a borehole drilled to a diameter of 600 mm at approximately 50 m depth was successfully expanded to 1570 mm without stability issues. However, a second borehole expanded from 600 mm to 2460 mm collapsed during the jetting process. These observations suggest that although boreholes in sand may remain stable due to dilative behaviour, there exists a practical limit to the achievable borehole diameter in which stresses become too great.

The potential influence of borehole dimensions and soil behaviour becomes particularly relevant when drilling is performed near existing foundations. Recent work by Bogaards (2025), commissioned for SIKB, reassessed the current rule of thumb used to determine safe distances between boreholes and existing pile foundations. The existing SIKB guideline prescribes a minimum distance of 10 times the borehole diameter (Stichting Infrastructuur Kwaliteitsborging Bodembeheer (SIKB), 2021). This rule is applied within SIKB protocol to ensure safety of foundation piles in the vicinity of boreholes. The study, however, concluded that this assumption may be overly conservative in certain situations. The research pointed out that the SIKB protocol did not take the sphere of influence of the existing pile into consideration. For example, a borehole with a diameter of 50 mm could be placed at a distance of 0.5 m from a large foundation pile, even though the estimated sphere of influence of that pile may extend between 1 and 1.5 m. In such cases it is therefore necessary to reassess the current guideline.

Using this formulation, the study compared the resulting safe distances with those prescribed by the SIKB protocol for a range of borehole diameters. For smaller boreholes (50–250 mm), the SIKB guidelines prescribe shorter separation distances than those obtained using the proposed formulation. For larger borehole diameters, however, the proposed method results in smaller recommended distances than those currently prescribed in the protocol.

Based on the analysis, the author proposed an alternative minimum distance criterion that accounts for the spheres of influence of both the borehole and the existing foundation pile. The recommended distance for drilling operations deeper than the existing foundation piles is expressed as:

$$S \geq 5D_{eq} + 1.5D_{borehole} \tag{2.1}$$

Where S represents the minimum safe distance between the centre of the borehole and the centre of the pile foundation, D_{eq} is the equivalent diameter of the existing pile and $D_{borehole}$ is the borehole diameter. The equivalent diameter of the pile is defined as:

$$D_{eq} = 1.13a\sqrt{\frac{b}{a}} \tag{2.2}$$

Where a and b denote the smallest and largest dimensions of the pile cross-section, respectively.

The newly determined distance criterion was formulated by analysing the spheres of influence of both the borehole and the existing foundation pile. Safe distances were determined by ensuring that these influence zones do not overlap. While this approach provides a conservative basis for determining reduced separation distances compared with the existing SIKB guideline, it does not directly address whether limited overlap between the influence zones of a borehole and an existing pile could still result in stable conditions.

While the studies discussed above provide theoretical and analytical insight into borehole stability and safe drilling distances, relatively little field research has been conducted on the direct effects of drilling near existing foundation piles. Although no in-situ research or measurements have been conducted on the effects of borehole drilling on nearby foundation piles, soil deformation caused by excavation near existing structures has been extensively studied. Field measurements performed by Ter Linde (1999) during diaphragm wall installation for the tram infrastructure in The Hague showed a maximum settlement of approximately 0.15% of wall depth adjacent to the wall and 0.04% of wall depth at a horizontal distance equal to the wall depth. The project involved the installation of diaphragm walls with a depth of approximately 30 m, a thickness of 1.5 m and panel widths of 4–5 m. Measurements indicated vertical surface settlements of approximately 5–6 mm at distances of 2–3 m from the wall.

Further analysis of soil settlements next to diaphragm walls by Gaba, Simpson, et al. (2003) in stiff clays also showed a similar settlement profile. The maximum measured vertical settlement, located next to the diaphragm wall, corresponds to approximately 0.05% of the excavation depth and decreases rapidly with increasing distance from the wall. At a horizontal distance of half the wall depth the settlement is 0.02%, while at a distance equal to the wall depth the vertical displacement approaches zero. The general shape of this settlement distribution and the settlement horizontal and vertical values are illustrated in Figure 2.2.

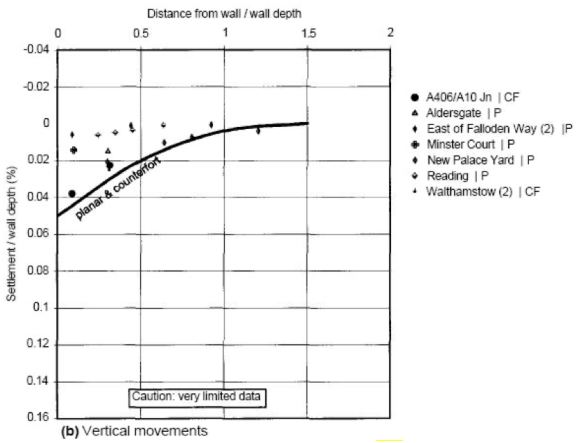

(a) Vertical deformations due to diaphragm wall installation

Wall type	Horizontal movements		Vertical movements	
	Max % depth wall	Extent influence (m)	Max % depth wall	Extent influence (m)
Contiguous bored pile	0.04	1.5	0.04	2
Secant bored pile	0.08	1.5	0.05	2
Diaphragm walls	0.05	1.5	0.05	1.5

(b) Movements due to wall installation

Figure 2.2: Measured ground movements adjacent to diaphragm wall installation (Gaba, Simpson, et al., 2003)

Although excavation differs from drilling in both geometry and scale, both processes involve the removal of soil and the resulting redistribution of stresses in the surrounding ground. Excavation typically represents a larger disturbance of the soil mass than drilling.

2.2. Pile foundation bearing capacity

2.2.1. Subsurface characteristics and processes

Pile foundations transfer structural loads through two primary mechanisms: shaft resistance (q_s) over the pile length and base resistance (q_b) at the pile tip. These resistances depend on the mechanical behaviour of the surrounding soil, the installation process and the interaction between the pile surface and the soil mass. Research on foundation piles has provided insight into the total bearing capacity (Q_t) through improved understanding of these mechanisms.

$$Q_t = q_s + q_b \tag{2.3}$$

Shaft resistance

Shaft resistance develops along the interface between the pile and the surrounding soil over the entire embedded length of the pile. Its determination therefore depends on both the pile surface area and the shear resistance mobilised along that surface. Field experiments conducted by Lehane et al. (1993) on driven piles showed that the shear resistance along the pile shaft is governed by the effective radial stresses acting on the pile, which are generated by frictional interaction between the pile and the soil. This research, conducted in loose to medium-dense quartz sand, demonstrated that the effective radial stress decreases with increasing relative depth of the pile tip (h/R). Consequently, shaft resistance is typically highest near the pile tip and gradually reduces to zero towards the ground surface.

This behaviour has been attributed to the progressive cycling of the soil during pile installation, which alters both the stress state and the fabric of the surrounding soil mass (Lehane & Bittar, 2022). The same study also concluded that open-ended piles, which induce less soil displacement during installation, result in lower radial stresses and reduced shaft friction. Further investigations on non-displacement piles by Gavin et al. (2021) identified a consistent correlation factor between the measured cone resistance (q_c) and the average shaft resistance. According to the Dutch standard NEN (2016), the shaft bearing capacity is determined as follows:

$$q_s = \tau_f A_s \tag{2.4}$$

where A_s is the surface area of the pile shaft and τ_f is the average shaft friction. The average shaft friction is determined by:

$$\tau_f = \alpha_s q_c \tag{2.5}$$

where α_s is a factor dependent on pile characteristics and installation method. Values for α_s are provided in Table 7.c of NEN (2016).

Base resistance

Base resistance develops at the pile tip, where the soil beneath the pile is compressed and sheared during installation and subsequent loading. The magnitude of base resistance is strongly influenced by soil type, displacement piles installed in clay generally mobilise lower base resistance than those installed in sand (Lehane & Bittar, 2022).

A simplified approach for estimating base resistance in coarse-grained soils is provided by the United States Navy method. In this method, the base resistance is determined by multiplying a bearing capacity factor N_q with the vertical effective stress σ'_v. The factor N_q is assigned based on soil density, with typical values of 20 (medium), 40 (dense), and 50 (very dense). Corresponding maximum bearing capacity limits of 5 MPa, 10 MPa, and 12 MPa are applied. Soil classification is based on SPT values and relative density, as presented in Figure A.1 in Appendix A.

$$q_b = N_q \sigma'_v \tag{2.6}$$

In Dutch practice, base resistance is commonly determined using the Koppejan method, which includes both a simplified and a refined formulation (NEN, 2016). Both formulations utilise an averaging procedure for the cone resistance (q_c), which is discussed in detail in subsection CPT.

The simplified formulation expresses the base resistance as:

$$q_b = \alpha_p q_c \tag{2.7}$$

where α_p is a factor dependent on pile type and installation method, with values provided in Table 7.c of NEN (2016).

The refined formulation is given by:

$$q_{b,\text{max}} = 0.5\,\alpha_p\,\beta\,s\left(\frac{q_{c;I;\text{mean}} + q_{c;II;\text{mean}}}{2} + q_{c;III;\text{mean}}\right) \leq 15 \text{ MPa} \tag{2.8}$$

where $q_{c;I;\text{mean}}$ is the average cone resistance over a depth ranging from the pile base to between 0.7 and 4 times the equivalent pile base diameter (D_{eq}) below the base. $q_{c;II;\text{mean}}$ represents the average of the lowest cone resistance values over the depth extending upward from the critical depth to the pile base. $q_{c;III;\text{mean}}$ is the average cone resistance over a depth extending up to 8 times the pile base diameter above the base (or up to $8a$ when $b > 1.5a$). The factors α_p, β, and s account for pile type, installation effects, and pile base geometry, respectively. This formulation reflects the influence of soil conditions over a larger zone surrounding the pile tip, shown in Figure 2.3 below, highlighting the importance of CPT measurements in determining pile bearing capacity.

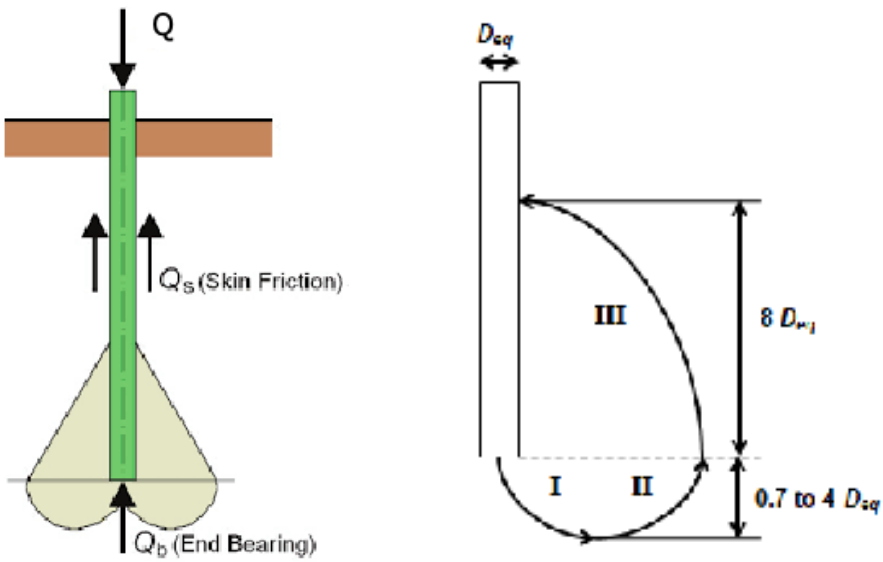

(a) Load distribution (Q_s and Q_b)

(b) Koppejan averaging zones

Figure 2.3: Illustration of the Koppejan method for determining pile bearing capacity (Adapted from Gavin (2025)).

2.2.2. Prior research

Extensive research has been conducted on monitoring and predicting the effects of excavating and tunnelling near existing foundation piles. However, comparatively little research conducted on the interaction of foundation piles with nearby vertical boreholes. In order to evaluate the potential response of piles to drilling operations, it is therefore useful to consider previous studies on pile behaviour during excavation and tunnelling activities. These construction processes generally induce significantly larger ground disturbances than vertical boreholes, as larger quantities of soil are removed or displaced. Consequently, findings from these studies can provide valuable insight into the potential behaviour of pile foundations subjected to nearby drilling.

Ground movements and changes in stress caused by excavation or tunnelling may lead to settlements and rotation of nearby structures. To assess the damage to structures a criteria based on settlement

and angular distortion is used. One of the earliest approaches was proposed by Skempton and MacDonald (1956), who introduced the concept of relative rotation defined as $\delta S/l$, in which δS represents the relative settlement between two points and l the distance between them. According to the developed criterion a relative rotation of $1/500$ is considered safe to cracking, whereas rotations approaching a value of $1/150$ lead to structural damage in beams or columns. Figure 2.4 below depicts the different damage criteria for angular distortion. An alternative approach was developed by Polshin and Tokar (1957) regarding unreinforced load bearing walls. Polshin and Tokar (1957) introduced the deflection ratio Δ/L, where L is the distance between two separate joints and Δ the maximum deflection. For sagging deformation patterns, values between approximately $1/3300$ and $1/2500$ have been suggested as limiting values, while hogging deformation patterns require stricter limits of approximately $1/5000$ (Burland & Wroth, 1974). Buildings are generally more vulnerable to hogging, as they possess limited tensile strength to resist the extension forces generated by differential settlement at the building's periphery. Similarly, Rankin (1988) suggested that settlements smaller than approximately 10 mm combined with slopes not exceeding 1:500 are unlikely to cause structural damage.

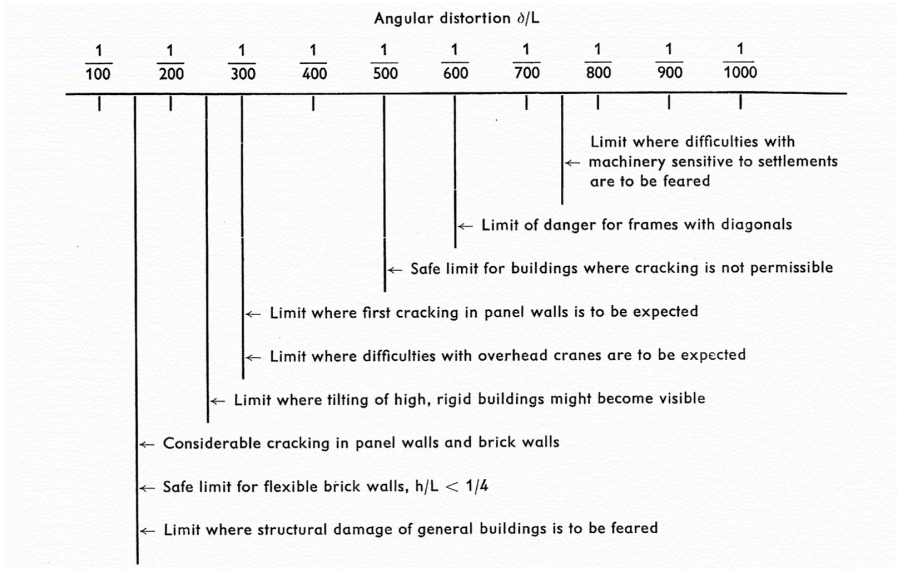

Figure 2.4: Damage criteria based on angular distortion (Bjerrum, 1963)

Excavation works are a major source for soil displacement and stress changes in urban environments. Excavations require the removal of soil and often involve temporary lowering of the groundwater level, which leads to stress redistribution and volume changes in the surrounding soil. Field observations indicate that horizontal soil displacements around excavations can exceed vertical settlements, particularly in sandy soils where the magnitude of horizontal movement is positively correlated with excavation depth (Korff, 2009). In clay soils both horizontal and vertical displacements may be larger due to the lower stiffness of the soil. Measurements reported by Korff (2009) further indicate that soil movements decrease with distance from the excavation and become negligible at distances greater than approximately two times the excavation depth ($2H$). Even for deep excavations, maximum horizontal displacements of approximately 20 cm have been reported, while settlements at distances comparable to the excavation depth may reach approximately 2% of the excavation depth.

Another process in urban environments that causes stress and volume changes in urban environments is tunnelling. In addition to excavations, tunnelling operations can also induce ground movements that affect nearby pile foundations. Analytical approaches have been used to investigate this interaction. One analytical approach was done by Chen et al. (1999), it analysed the response of foundation piles subjected to tunnelling-induced soil displacements using the analytical programmes PALLAS and PIES, which simulate lateral and vertical pile behaviour respectively. The results indicated that piles extending below the tunnel level experience lateral deflections comparable to the surrounding soil displacement, which may result in bending of the piles. Later numerical studies have attempted to model these in-

teractions using finite element methods. Early finite element models were often unable to capture the non-linear behaviour of soils accurately, leading to limited predictive capability (Addenbrooke et al., 2000). Subsequent studies improved the modelling approach by incorporating more advanced soil constitutive models. Mroueh and Shahrour (2002) simulated tunnelling in two stages, first by applying the existing axial loads in the piles and subsequently by modelling tunnel excavation through removal of soil elements and activation of lining elements. Revealing that the tunnelling induced internal forces in pile foundations strongly depends on the position of the pile tip with regard to the tunnel horizontal axis.

Field tests conducted by Peck (1963), further help understand pile behaviour during close proximity TBM drilling. Giving insight on both the soil conditions and the pile foundation behaviour before and after passage of the TBM. Tunnel excavation typically causes settlement due to volume loss around the tunnel. The measurements conducted in the field test indicate volume losses between approximately 1% and 3% shown in Figure 2.5 (Kaalberg et al., 2006). Centrifuge experiments performed at Deltares showed that a volume loss of approximately 3% in very soft clay deposits can lead to surface settlements exceeding 10 cm. Based on these observations, Bezuijen and Van der Schrier (1994) suggested maintaining a minimum distance between tunnel axes and pile toes equal to approximately two times the tunnel diameter in order to limit pile deformation.

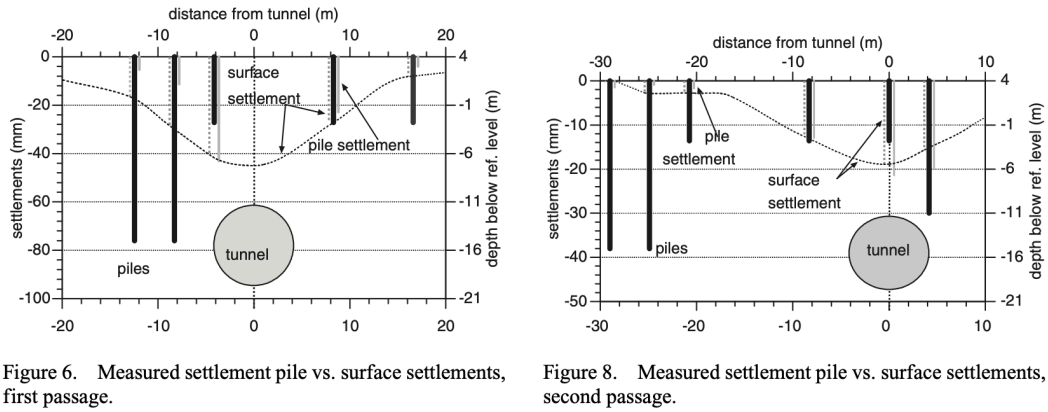

Figure 2.5: TBM passing settlements, the second passing (right) had improved grout injections, volume loss at surface 75% (Kaalberg et al., 2006)

Another finding by Kaalberg et al. (2006) was an influence zone for pile foundations due to tunnels. The research proposed three different zones at different angles from the tunnel horizontal axis that each had different effects on the foundation piles, seen in Figure 2.6. Piles found in Zone A undergo a pile toe deformation minimally equal or slightly larger to the surface-level subsidence on a corresponding location, Zone B generally about equal the surface-level subsidence and for Zone C the pile subsidence is significantly smaller than the corresponding deformation of the ground level.

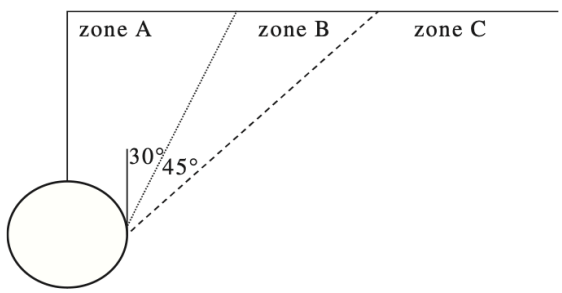

Figure 2.6: Pile toe influence zone (Kaalberg et al., 2006)

Detailed field investigations further indicate that the axial bearing capacity of piles is generally not significantly affected by nearby tunnelling activities. For example, Netzel and Kaalberg (2001) compared

cone penetration test results obtained before and after tunnelling near pile foundations and found no significant differences in the measured cone resistance. Assuming a direct relationship between cone resistance and pile capacity, these results suggest that the bearing capacity of the piles remained essentially unchanged. Nevertheless, settlement and rotation of the piles were observed due to the steep settlement trough generated around the tunnel axis. In these studies, end-bearing piles tended to follow the greenfield settlement profile, while friction piles followed the surface settlement pattern more closely. Settlements of approximately 7 mm were recorded when tunnels passed directly beneath end-bearing piles.

Overall, previous research indicates that activities such as excavation and tunnelling can induce settlement and rotation of pile foundations due to soil displacements. However, these studies show that the axial bearing capacity of the piles remains largely unchanged. The main concern therefore lies in the deformation of the piles and the rotation of supported structures from settlements. Since tunnelling and excavation typically cause larger soil disturbances than vertical borehole drilling, the findings from these studies provide a reference for evaluating the potential effects of borehole construction near existing pile foundations. However, the different orientation of tunnels compared to boreholes should also be considered.

2.3. Case studies

2.3.1. Delft

The EU aims to become climate neutral by 2050 and reduce its net greenhouse gas emissions by at least 55% by 2030 (European Commission, 2026). To achieve these goals, the EU provides grants to invest in research and development related to sustainable energy systems. One of the research sites is located at the Delft University of Technology campus, where ATES wells are being developed (TU Delft, 2026).

The project in Delft consists of ATES wells that will function as heat storage for the heat plant on campus. The system will be integrated into the existing heat network to provide heating and cooling for a majority of the university buildings. One of these well locations is located on the southern part of the campus, on an open field south of the nuclear reactor, shown in Figure 2.7. There are no buildings within a radius of approximately 100 m and the borehole radius is 0.45 m.

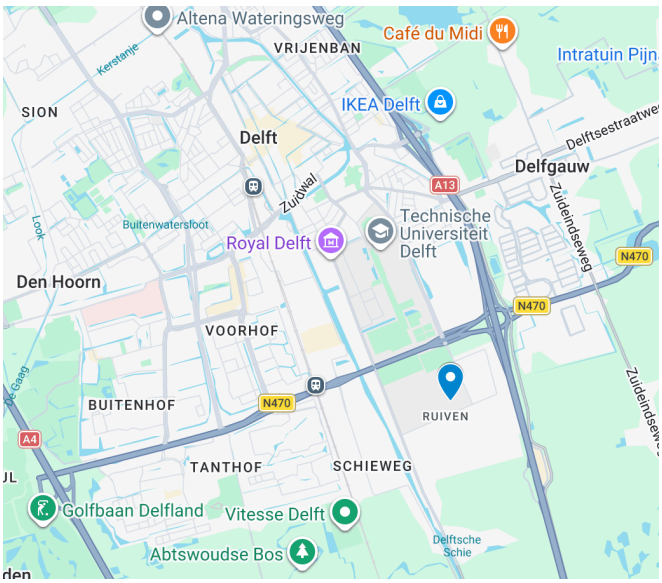

Figure 2.7: ATES and CPT location Delft (Timmermans Arribas, n.d.)

The subsurface conditions in Delft are typical for the deltaic region of the Netherlands. The soil profile generally consists of organic and fine-grained deposits near the surface, followed by alternating sand, clay and silt layers. At greater depth, a thicker sand layer is present. This deeper sand layer is relevant

for this research because it is the layer where a majority of the foundation piles are installed. The groundwater level in Delft is typically located only a few metres below ground level, resulting in largely saturated subsurface conditions.

Based on nearby DINOloket subsurface data, this deeper sand layer is classified as coarse sand and is expected to correspond to the first aquifer (Gemeente Delft, 2025; TNO – Geological Survey of the Netherlands, 2025). Therefore, the layer is assumed to be a permeable, uncemented sand layer. Its Holocene origin is not assumed as it is located on the border of Holocene and Pleistocene.

2.3.2. Wezep

The Wezep case study concerns a new construction project where boreholes were installed. A total of 12 boreholes were drilled, with diameters between 0.15 m and 0.20 m. Before and after drilling, 16 CPTs were performed around the boreholes. Figure 2.8 shows the site location.

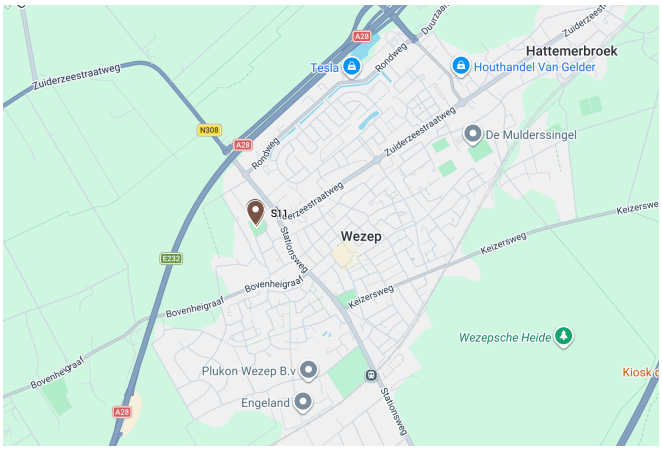

Figure 2.8: ATES and CPT location Wezep (Timmermans Arribas, n.d.)

Compared with the Delft case study, the Wezep soil profile is more sand-dominated. The soil profiles generally show a thin shallow clay layer, followed by predominantly sand and sand mixtures.

2.3.3. Zwolle

The Wezep case study concerns a new construction project where boreholes were installed. A total of 60 boreholes were drilled, with diameters between 0.15 m and 0.20 m. Before and after drilling, 29 CPTs were performed around the boreholes. Figure 2.9 shows the site location.

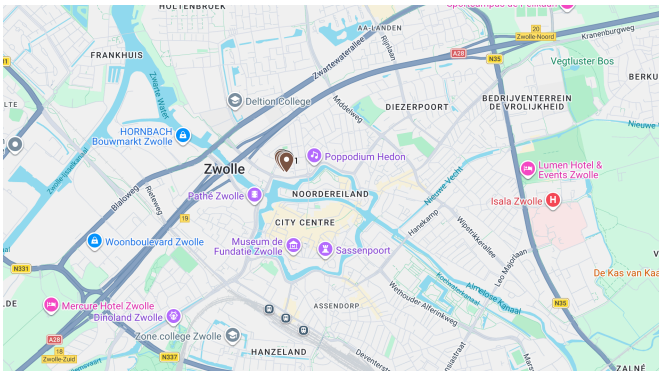

Figure 2.9: ATES and CPT location Zwolle (Timmermans Arribas, n.d.)

The Zwolle case study is similar to that of Wezep. A shallow thin clay layer is followed by predominantly sand and sand mixtures, however, an thin organic layer is found at a depth of -1 m NAP.

2.4. CPT

2.4.1. Principle and development of CPT

The CPT is a measurement done with a cone at the end of a series of rods connected to each other, pushed at a constant speed into the ground. During this process consistent measurements are taken to register the cone resistance q_c, the sleeve friction f_s and if possible the pore pressure u_2. The first system was used in 1932 and was manually operated (Robertson & Cabal, 2024). As the years passed the helpfulness of using CPT to map out stratigraphy was further recognised. The design kept improving and additional sensors were added. The test proved to be a very effective method to determine the stratigraphy in first softer soils and eventually stiff to very stiff and in some cases soft rock.

The CPT has three main measured parameters: cone resistance, sleeve friction and pore pressure. The cone resistance and the sleeve friction are calculated by dividing the force acting on the cone or friction sleeve by the surface area of that surface. The pore pressure is measured through a filter between the cone and the friction sleeve. A typical result of a CPT test is shown in Figure 2.10. The three main measured values of the cone can be converted to friction ratio R_f and normalised cone resistance Q_t.

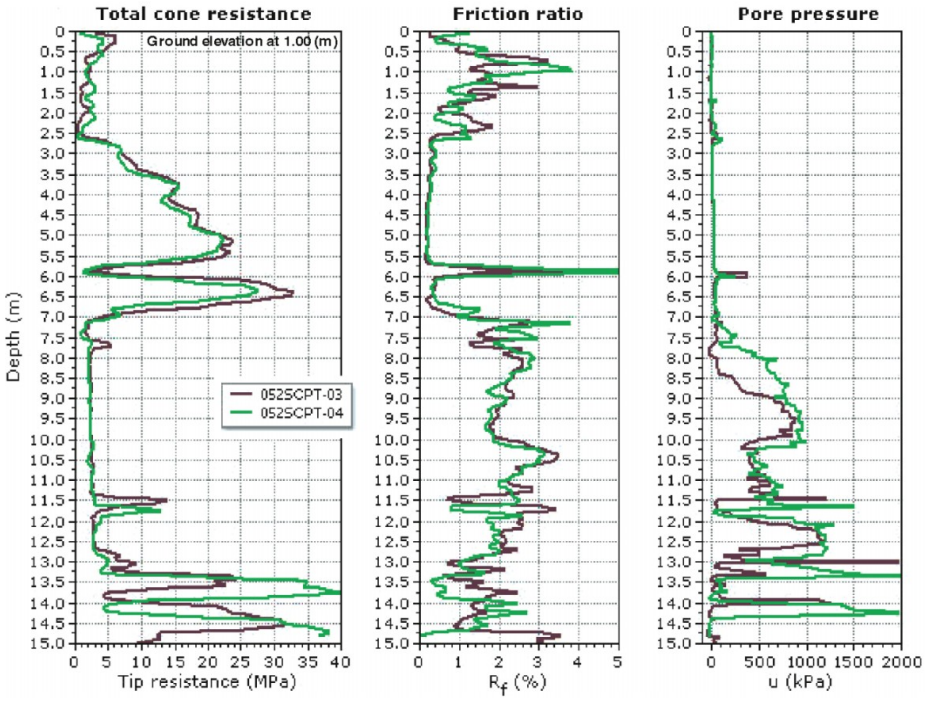

Figure 2.10: CPT measurement representation (Robertson, 2009).

Currently depending on the installed sensors the CPT is able to measure a selection of parameters such as: cone inclination, temperature, geophones/accelerometers, pressure meter, camera, etc. (Robertson & Cabal, 2024).

2.4.2. CPT-based soil interpretation

As shown in Figure 2.10, the CPT does not directly measure soil type. Instead, the test records the response of the soil to the penetration of the cone. Houlsby and Hitchman (1988) found that cone resistance is strongly influenced by horizontal stress and friction angle. Based on the measured cone resistance and sleeve friction, the soil at a given depth can be interpreted and classified. A common method used in The Netherlands is Table 2.B in the NEN (2016). Where soil is categorised by its cone resistance. Another common categorisation method is the Robertson soil behaviour chart, which classifies soil based on the normalised cone resistance Q_t and the friction ratio R_f and provides an indication of the OCR of the soil.

CPT interpretation is not only useful for identifying soil behaviour type, but also for determining soil parameters such as unit weight, relative density and stiffness. Parameters which are used to determine soil behaviour and capacity for construction.

2.4.3. Reliability and limitations

The CPT interpretation relies on empirical correlations and soil behaviour type charts. Soil classifications should be applied with care, because the reliability depends on the similarity between the investigated soil and the database from which the classification boundaries were developed. The situation may arise in which measured characteristics fall on the boundary of between two soil behaviour zones. This can introduce uncertainty, because neighbouring zones can have different soil parameters.

The cone resistance q_c is seen as the most robust CPT measurement and is commonly used for identifying soil layering and estimating relative density in sands (Robertson, 2009). However, q_c is still influenced by the in-situ stress state and drainage conditions around the cone. As a result, large changes in cone resistance can occur when the cone passes from one soil layer to another. These transitions can be difficult to classify. In addition, they may also influence average cone resistance values over a depth interval.

The sleeve friction f_s is generally more uncertain than the cone resistance. Mayne (2014) notes that sleeve friction is one of the less reliable piezocone measurements. This is important because sleeve friction is used to determine friction ratio, which is one of the two classification factors for soil in the Robertson chart. It also affects empirical correlations in which f_s is used to estimate unit weight or horizontal stress. The uncertainty in sleeve friction becomes especially relevant in soft soils and very loose sands, where small measured sleeve friction values can lead to relatively large interpretation errors (Lunne et al., 1986; Mayne, 2014).

The measurements from the CPT are also not constant. The line fluctuates constantly and therefore mean, max and min values are taken to represent a certain depth. This has both benefits and negative effects as sudden peaks that are very small should not influence all the data, while sometimes it is important to include stronger parts of soil.

CPT measurements also show local fluctuations with depth. These fluctuations may be caused by small changes in soil type, local variations in density or measurement noise. Consequently, mean, minimum and maximum values are frequently used to characterise a selected depth interval, such as in determining pile bearing capacity (Gavin, 2025). This approach reduces the influence of isolated local peaks, but it can also smooth out thin stronger or weaker soil layers that may still be relevant for interpretation.

Although CPTs are often interpreted as vertical profiles, the cone can deviate horizontally during penetration. This deviation may be caused by initial inclination or frictional interaction between cone and surrounding soil. The deviation may be small at shallow depth, but it can become more significant as penetration depth increases. This introduces uncertainty for determining the exact soil conditions under the CPT starting point.

2.4.4. Relevance for research

The CPT measurement form the base of this research. Results are used to determine the stratigraphy and to evaluate differences between CPTs performed before and after drilling. In addition, results are also used to determine the soil parameters of the different layers. These parameters are necessary for the simulations in the numerical model.

Although CPT results are important for determining soil characteristics, the measurements can also provide evidence for changes in soil conditions. If drilling alters relative density or horizontal stress, a CPT could measure differences in cone resistance and sleeve friction. However, changes in measurement cannot be interpreted independently. It must be assessed together with the CPT location, cone trajectory and soil layering. A difference in measurements is not direct evidence of borehole influence.

The cone trajectory is very important for this research. Cone deviations may lead to an increase in horizontal distance from the borehole. Resulting in the possibility for the cone to be located outside the affected zone.

2.5. Horizontal stress

The in-situ horizontal stress is an important parameter for geotechnical problems to determine soil stability, deformations and stress on underground structures. The vertical effective stress is governed by the weight of the overlying soil, determined by its unit weight. The horizontal effective stress, however, depends not only on the vertical effective stress, but also on in-situ stress state, soil density, stress and strain history, age, cementation and soil sensitivity (Robertson, 2016). These factors are unlikely to be unique for all soils, resulting in correlations. Therefore, a ratio has been developed between the horizontal and vertical effective under conditions of zero lateral strain expressed as the coefficient of earth pressure at rest K_0:

$$\sigma'_{h0} = K_0 \sigma'_{v0} \tag{2.9}$$

where $\sigma' h0$ is the initial effective horizontal stress, K_0 is the coefficient of earth pressure at rest and $\sigma' v0$ is the initial effective vertical stress. The corresponding total horizontal stress is obtained by adding the pore pressure:

$$\sigma_{h0} = \sigma'_{h0} + u_0 \tag{2.10}$$

where u_0 is the pore pressure.

Empirical determination of horizontal stress has proven to be difficult. Marchetti (2015) showed an in-situ approach combining CPT and DMT capable of estimating horizontal stress. However, Robertson (2016) challenges the efficiency and result of combining these two measurements as both tests are performed at different locations, creating the uncertainty of not measuring the same soil volume. In addition, combining both tests increases the cost and complexity of the soil investigation.

An alternative approach was proposed by Robertson (2016). This method uses cone resistance q_c and sleeve friction f_s to estimate K_0 from CPT data. This proposal is based on the observation by Hughes and Robertson (1985) that the horizontal stress around the friction sleeve can be related to the horizontal stress before the cone passed through the soil. During penetration, the cone generates stress relief and cavity expansion. As a result, the measured sleeve friction can be correlated to the horizontal effective stress around the sleeve (Robertson, 2016).

The Robertson approach plots the normalised cone resistance Q_t and the normalised friction ratio R_f in the Robertson soil chart. There suggested K_0 lines have been drawn shown in Figure 2.11. Normally consolidated soils, located between the two blue dotted lines, are generally associated with $K_0 = 0.5$ or lower, while more consolidated, aged or cemented soils are associated with higher K_0 values. The location of a soil in the chart can therefore be key to estimate the corresponding K_0 value.

A different approach developed by Ahmadi and Golestani Dariani (2017) estimates the horizontal stress in young, uncemented sands by correlating CPT cone resistance with the initial vertical stress and relative density. Within this framework, the relative density is derived from a calibrated empirical chart provided in their study.

Both approaches contain uncertainty. The Robertson method depends on the interpretation of soil data within the chart. A soil layer is generally represented by a range of points rather than a single point. As a result, the data may cross or fall between different contour lines, which introduces uncertainty in the selected value. The Ahmadi-Golestani method also introduces uncertainty because several required values are read or interpolated from published figures.

2.6. Robertson-Lengkeek classification

Lengkeek (2024) proposed a new CPT based method that is better suited for Holocene soils commonly found in The Netherlands. The method builds on the soil behaviour type classification developed by Robertson (2010b), but modifies the classification of organic soils. The Robertson soil behaviour chart is a widely used soil classification method that classifies soil using the friction ratio R_f and the corrected cone resistance q_t/p_a. The corrected cone resistance is calculated as:

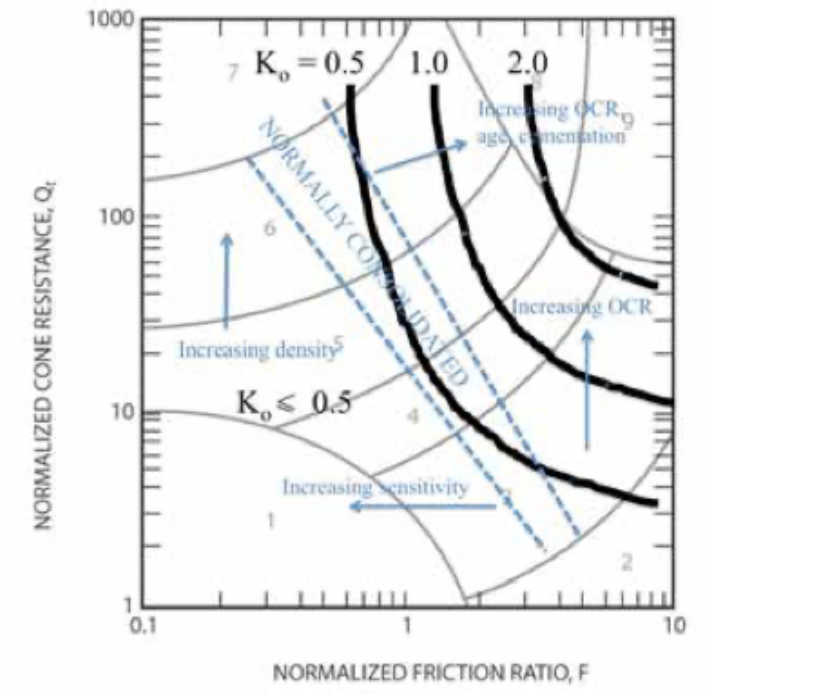

Figure 2.11: Suggested contours of K0 lines from CPT (Adapted from (Robertson, 2016)).

$$q_t/p_a = \frac{q_c + u_2(1-a)}{p_a} \tag{2.11}$$

where q_c is the cone resistance (MPa), u_2 is the pore pressure (MPa), a is the net area ratio of the cone (-) and p_a is the atmospheric pressure (MPa).

According to Lengkeek (2024), the SBT performs well in classifying mineral soils, but lacked classification of soft organic clays and peats, which are common in Dutch deltaic deposits. To improve the classification of these soils, two additional soil behaviour zones were introduced for peat and organic clay. These zones are located in the lower-right part of the chart shown in Figure 2.12. Except for modifications to zone 4, all other zones remained unchanged. This addition made it easier to separate organic from mineral soils.

Table 2.1 portrays the SBT zones used in the classification. Equations 2.12 to 2.15 define the boundary of the organic zone, the condition for peat, the condition for organic clay and the calculation for the normalised pore pressure ratio B_{qt}.

Equations 2.12 to 2.15 show the boundary of the zone, the condition for peat, the condition for organic clay and the equation to calculate B_{qt}.

$$I_{sbt} > 2.9 \tag{2.12}$$

$$I_{sbt} > 3.33 - 0.06R_f - 4.1B_{qt} \tag{2.13}$$

$$I_{sbt} < 3.66 + 0.25R_f - 4.1B_{qt} \tag{2.14}$$

$$B_{qt} = \frac{u_2 - u_0}{q_t} \tag{2.15}$$

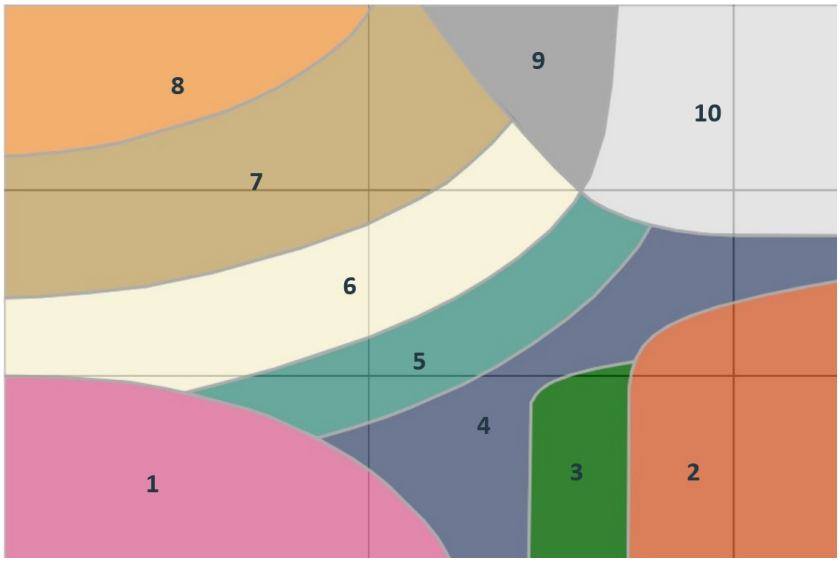

Figure 2.12: Suggested soil classification chart by Lengkeek (Witteveen+Bos, 2026)

Table 2.1: Soil Behavior Type (SBT) zones and corresponding soil behavior type index (I_{sbt}) (Robertson & Cabal, 2024).

Zone	Soil Behavior Type	I_{sbt}
1	Sensitive, fine grained	N/A
2	Peat	Eq. 2.13
3	Organic clay	Eq. 2.14
4	Clays – silty clay to clay	$2.9 - 3.6$
5	Silt mixtures – clayey silt to silty clay	$2.60 - 2.95$
6	Sand mixtures – silty sand to sandy silt	$2.05 - 2.6$
7	Sands – clean sand to silty sand	$1.31 - 2.05$
8	Gravelly sand to dense sand	< 1.31
9	Very stiff sand to clayey sand*	N/A
10	Very stiff, fine grained*	N/A

* Heavily overconsolidated or cemented

The Robertson SBT charts can provide qualitative information about the stress history of a soil. As Figure 2.11 shows, an approximately diagonal zone can be observed from upper-left to lower-right, where soils are generally considered normally consolidated. Soils to the right of this region are associated with higher degree of consolidation, whereas soils to the left are associated with lower degree of consolidation.

This is relevant as OCR describes the relationship between the maximum past effective vertical stress and the current. A high OCR suggests that the soil has experienced a higher effective stress in the past and a low OCR suggests that the soil has experienced a lower effective stress in the past. This correlation becomes relevant, as CPT measurements before and after drilling could give more insight into whether the soil state has been affected by the borehole. However, this interpretation should be treated with care, because changes in chart position can also result from natural spatial variability, measurement uncertainty or differences in cone trajectory.

2.7. Constitutive soil models

The response of soil to external loading is naturally non-linear and dependent on factors such as the current stress state, the history of the stress path and the magnitude of the strain. Different constitutive models have been developed to simulate soil behaviour ranging from simple to complex model. Each of these have their own advantages and limitations. For this research, the three models: Linear Elastic, Mohr-Coulomb and SANISAND, were selected to represent a progression in model complexity.

The Linear Elastic model provides a simple fundamental baseline derived from Hooke's law of isotropic elasticity. The Mohr-Coulomb model builds upon this by integrating isotropic elasticity with a perfect plasticity framework and a fixed failure criterion. Lastly, the SANISAND model is and advanced elasto-plastic model based on critical state soil mechanics and the concept of rotational hardening (Dafalias & Manzari, 2004). Together, these models provide the opportunity to compare soil response of different levels of model complexity.

2.7.1. Linear Elastic model

The linear elastic model represents the most fundamental constitutive relationship in continuum mechanics. It is governed by Hooke's law, which states that the extension of a material, in this case soil, is proportional to the stress (Geoengineer.org, n.d.-a). This relationship is characterised by its constant slope, as illustrated in Figure 2.13 below.

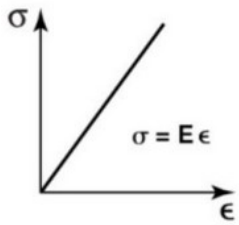

Figure 2.13: Linear elastic stress-strain relationship (Adapted from Geoengineer.org, n.d.-b).

The relationship can be expressed as:

$$\sigma = E\epsilon \tag{2.16}$$

where E represents the Young's Modulus and ϵ the extension of the material. The main assumption in this model is that all strains are purely elastic and therefore are completely recoverable. In the event of unloading and reloading, the material returns to its original state along the stress-strain path without undergoing permanent deformation. Furthermore, the basic linear elastic model does not incorporate a yield criterion or a failure limit. In the software PLAXIS, the linear-elastic model is defined by the elastic parameters: Young's modulus E and the Poisson ratio ν.

The linear elastic model is computationally efficient and provides an initial approximation of soil stiffness at very small strains, usually up to a strain of 0.2% (Xometry, 2023). The model is however not able

to capture non-linear soil behaviour. As it lacks a failure limit or a yield criterion, the model generates mathematically valid but physically impossible stress values. In reality soil non-linear stiffness and undergoes irreversible plastic deformations before reaching significant stress levels (Janbu, 1963). The linear elastic model is valuable as a computational baseline at low strains, however, its inability to simulate non-linear soil behaviour makes it unsuitable for detailed design or complex soil-structure interaction.

Table 2.2: Advantages and Limitations of the Linear Elastic Model.

Advantages	Limitations
Computationally Efficient: A linear system of equations is solved	**Lack of Failure Criteria:** Does not account for soil shear strength. Stresses can increase infinitely.
Parameter Simplicity: Requires only two independent constants (E and ν) for isotropic materials.	**Irreversibility:** Fails to model plastic (permanent) strains.
Small-Strain Accuracy: Provides a reliable estimate of behavior in the very small strain region (typically less than 0.2% strain).	**Constant Stiffness:** Does not account for the fact that soil stiffness increases with depth and confining pressure (Gao et al., 2024).
Structural Modelling: Highly accurate for modelling non-soil components like concrete piles or steel reinforcement.	**Dilatancy:** Cannot capture volume changes (contraction or dilation) during shear operations.

2.7.2. Mohr-Coulomb

The Mohr-Coulomb model is a linear elastic, perfectly plastic constitutive model used as an approximation for soil failure. The basic principle of elastoplasticity is that strain and strain rates are decomposed into an elastic part and a plastic component (Seequent, 2024):

$$\epsilon = \epsilon^e + \epsilon^p \tag{2.17}$$

$$\dot{\epsilon} = \dot{\epsilon^e} + \dot{\epsilon^p} \tag{2.18}$$

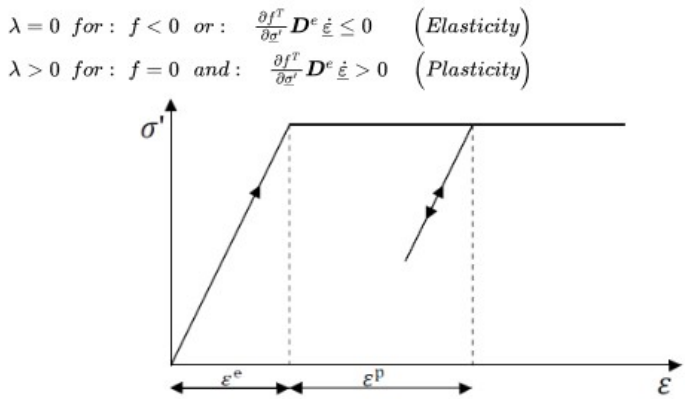

Figure 2.14: Basic idea of elastic perfectly plastic model in which D represents the young's modulus matrix (Seequent, 2024).

The linear elastic component of the model is governed by Hooke's law of isotropic elasticity, requiring the Young's Modulus (E) and Poisson's ratio (ν). The plastic component is introduced once the stress state reaches the yield surface, occurring when the yield function, f, is equal to zero. The yield surface is represented by a hexagonal cone in the principal stress space. Defined by principal stresses(σ_1' and σ_3'), friction angle (ϕ) and cohesion (c). The model makes use of six yield functions to account for all different principal stress combinations (Seequent, 2024).

$$
\begin{aligned}
f_{1a} &= \frac{1}{2}(\sigma_2' - \sigma_3') + \frac{1}{2}(\sigma_2' + \sigma_3')\sin(\phi) - c\cos(\phi) \leq 0 \\
f_{1b} &= \frac{1}{2}(\sigma_3' - \sigma_2') + \frac{1}{2}(\sigma_3' + \sigma_2')\sin(\phi) - c\cos(\phi) \leq 0 \\
f_{2a} &= \frac{1}{2}(\sigma_3' - \sigma_1') + \frac{1}{2}(\sigma_3' + \sigma_1')\sin(\phi) - c\cos(\phi) \leq 0 \\
f_{2b} &= \frac{1}{2}(\sigma_1' - \sigma_3') + \frac{1}{2}(\sigma_1' + \sigma_3')\sin(\phi) - c\cos(\phi) \leq 0 \\
f_{3a} &= \frac{1}{2}(\sigma_1' - \sigma_2') + \frac{1}{2}(\sigma_1' + \sigma_2')\sin(\phi) - c\cos(\phi) \leq 0 \\
f_{3b} &= \frac{1}{2}(\sigma_2' - \sigma_1') + \frac{1}{2}(\sigma_2' + \sigma_1')\sin(\phi) - c\cos(\phi) \leq 0
\end{aligned}
\tag{2.19}
$$

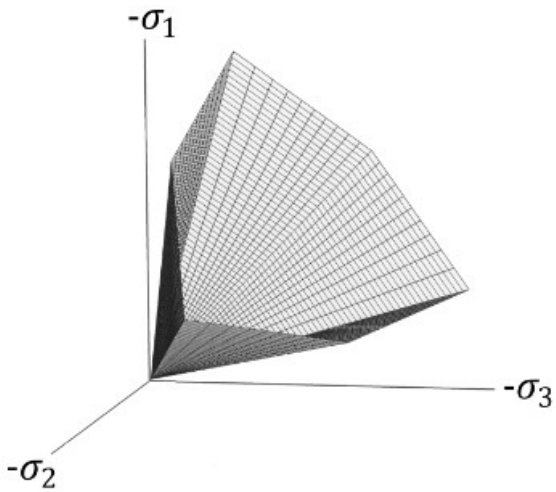

Figure 2.15: Mohr-Coulomb yield surface in principal stress space (c=0) (Seequent, 2024).

An important feature implemented in the Mohr-Coulomb model is the use of plastic potential functions (g). These functions define the direction of the plastic strain increment vector (Seequent, 2024). To model positive plastic volumetric strain increments in dense soils, a plasticity parameter, dilatancy angle (ψ), is added.

$$
\begin{aligned}
g_{1a} &= \frac{1}{2}(\sigma_2' - \sigma_3') + \frac{1}{2}(\sigma_2' + \sigma_3')\sin(\psi) \leq 0 \\
g_{1b} &= \frac{1}{2}(\sigma_3' - \sigma_2') + \frac{1}{2}(\sigma_3' + \sigma_2')\sin(\psi) \leq 0 \\
g_{2a} &= \frac{1}{2}(\sigma_3' - \sigma_1') + \frac{1}{2}(\sigma_3' + \sigma_1')\sin(\psi) \leq 0 \\
g_{2b} &= \frac{1}{2}(\sigma_1' - \sigma_3') + \frac{1}{2}(\sigma_1' + \sigma_3')\sin(\psi) \leq 0 \\
g_{3a} &= \frac{1}{2}(\sigma_1' - \sigma_2') + \frac{1}{2}(\sigma_1' + \sigma_2')\sin(\psi) \leq 0 \\
g_{3b} &= \frac{1}{2}(\sigma_2' - \sigma_1') + \frac{1}{2}(\sigma_2' + \sigma_1')\sin(\psi) \leq 0
\end{aligned}
\tag{2.20}
$$

While the standard Mohr-Coulomb criterion allows for tensile strength as cohesion increases, soil is unable to sustain such tension. Therefore, a tension cut off is applied, introducing three additional yield functions, limiting the allowable tensile stress (often set to zero).

$$
\begin{aligned}
f_4 &= \sigma_1' - \sigma_t \leq 0 \\
f_5 &= \sigma_2' - \sigma_t \leq 0 \\
f_6 &= \sigma_3' - \sigma_t \leq 0
\end{aligned}
\tag{2.21}
$$

Table 2.3: Advantages and Limitations of the Mohr-Coulomb Model.

Advantages	**Limitations**
Incorporation of Failure: Stress state is limited via a fixed failure envelope defined by c and ϕ.	**Constant Stiffness:** Young's modulus (E) is considered constant and does not increase with depth or confining pressure.
Computational Robustness: Provides a stable and relatively fast numerical solution for slope stability and bearing capacity.	**Simplified Plasticity:** Uses "perfect plasticity," meaning it does not account for strain hardening or softening observed in real soils.
Standard Parameters: Requires only five parameters (E, ν, c, ϕ, ψ).	**Small Strain Overestimation:** It often overestimates soil stiffness at small strain levels because it lacks a non-linear decay curve.
Dilatancy Control: The inclusion of the dilatancy angle (ψ) allows for the modelling of volume changes during shear failure.	**Stress Path Independence:** The model is less accurate for complex loading/unloading cycles as it doesn't "remember" the stress history.

2.7.3. SANISAND

The term SANISAND stands for Simple ANIsotropic Sand and is used to represent the family of advanced constitutive models originating from the two-surface plasticity model developed by Manzari and Dafalias (1997). The researchers created a model able to realistically simulate stress-strain behaviours of sand under monotonic and cyclic, drained and undrained conditions. This has been achieved with relative computational efficiency and ease as an increase in stress under a constant stress ratio is assumed to create almost only elastic strain (Dafalias & Manzari, 2004). Since the model development in 1997, there have been numerous updates to improve on its limitations or on different stress situations, with the latest being done by Reyes et al. (2025). In the following research the SANISAND model used was developed by Liu et al. (2019) and is based on work done by Dafalias and Manzari (2004).

The SANISAND model was mainly designed to simulate cyclic loads, however, has been further developed for use in other fields where permanent strains due to cyclic loads also occur. Examples of such are high-speed traffic loads, machine vibrations, and other sources of cyclic loads. The model has been able to do so by formulating a triaxial stress space with elastic and plastic parts defined by deviatoric stress ($q = \sigma_1 - \sigma_3$), mean pressure ($p = (1/3)(\sigma_1 + \sigma_3)$), deviatoric strain ($\epsilon_q = (2/3)(\epsilon_1 - \epsilon_3)$), volumetric strain ($\epsilon_v = \epsilon_1 + 2\epsilon_3$) and stress ratio ($\eta = q/p$). Giving basic equations of plastic and elastic stress-strain:

$$
d\epsilon_q^e = \frac{dq}{3G}; \quad d\epsilon_v^e = \frac{dp}{K} \tag{2.22}
$$

$$
d\epsilon_q^p = \frac{d\eta}{H}; \quad d\epsilon_v^p = d|d\epsilon_q^p| \tag{2.23}
$$

$$
G = G_0 p_{at} \frac{(2.97 - e)^2}{1 + e} \left(\frac{p}{p_{at}} \right)^{1/2}; \quad K = \frac{2(1 + \nu)}{3(1 - 2\nu)} G \tag{2.24}
$$

where G and K are elastic shear and bulk moduli, G_0 is a constant, ν is Poisson ratio, p_{at} is atmospheric pressure, e and p are current void ratio and pressure, H is plastic hardening modulus and d, unless it is a derivative, represents dilatancy. From the basic equations and the elastic moduli G and K, a stress-ratio yield surface is formed following that deviatoric plasticity only occurs when $d\eta \neq 0$, giving the yield surface shown below:

$$f = |\eta - \alpha| - m = 0 \tag{2.25}$$

in which α tracks the kinematic hardening and m is the value for the yield opening. The yield surface defined represents a geometrical 'wedge' in the p-q space shown in Figure 2.16 as grey, through which the α sloped line runs through the middle and the wedge opening is $2mp$. Inside the grey zone the strains are elastic and when η satisfies $f = 0$ and the derivative is positive or negative, plasticity will occur following the plastic strain relation (Dafalias & Manzari, 2004).

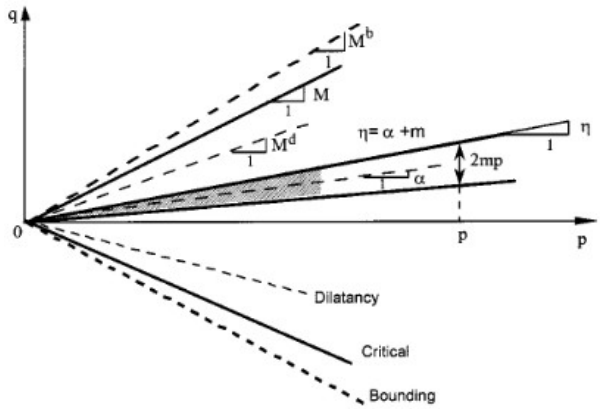

Figure 2.16: Schematisaion of yield, critical, dilatancy and bounding lines in q, p space (Dafalias & Manzari, 2004).

The model integrates the critical state of the soil in the form of a critical state line (CSL) in the e-p space and the critical state stress ratio, M, is shown as a solid straight line in Figure 2.16 (Dafalias & Manzari, 2004). The critical state of a soil is expressed as the combination of $q = q_c$, $p = p_c$ and critical void ratio $e = e_c$. M is related to the friction angle, whilst the e_c and p_c relation varies depending on soil and pressure. Usually a linear relationship between e_c and p_c was considered, however, Li and Wang (1998) suggests a different power relation

$$e_c = e_0 - \lambda_c (p_c/p_{at})^{\xi} \tag{2.26}$$

as it has a greater applicability for p_c. e_0 represents the void ratio at $p_c = 0$ and λ_c and ξ are constants(Dafalias & Manzari, 2004).

To determine how far the current state of the soil is compared to its critical state Been and Jefferies (1985) introduced $\Psi = e - e_c$, which simply measures the distance. Implementing this value in the determination of M^d and M^b values, bounding stress ratio and dilatancy stress ratio respectively, solves two main shortcomings the constitutive relations had in forward and reverse loading, under drained and undrained conditions. Firstly, is the impossible prediction of unlimited change in volume and secondly the inability to simulate softening response of dense samples under drained loading. Li and Dafalias (2000) proposed the following definitions

$$M^b = Mexp(-n^b \Psi) \tag{2.27}$$

$$M^d = Mexp(n^d \Psi) \tag{2.28}$$

with n^b and n^d as positive material constants. The stress ratios are now defined as functions of the material state rather than being fixed constants. In this configuration, for states denser than critical (Ψ<0), the relationship $M^d < M < M^b$ holds, allowing the stress ration η to exceed M and reach a peak at M^b before softening toward the critical value M as Ψ approaches zero (Dafalias & Manzari, 2004). This ensures that as the soil deforms, the surfaces converge at the critical state (Ψ=0), where

$M^d = M = M^b$. Satisfying the requirement for continuous shear deformation with no further change in volume.

Dafalias and Manzari (2004) added a critical feature to the SANISAND model to simulate the response of sand under cyclic loading, specifically the phenomenon of liquefaction. A large amount of models is unable to capture the pore pressure build-up during cyclic loads, leading to an early and unrealistic stabilisation of the stress path. For sands cyclic undrained loads lead to very low effective pressure levels, which eventually result in liquefaction and large permanent displacements in geo-structures (Dafalias & Manzari, 2004). To rectify, the fabric dilatancy variable z is introduced to characterise the microscopic changes in grain arrangement that occur during the dilation phase. In standard models, when the direction of shearing is reversed the model tends to ”forget” the arrangement of the particles. In reality dilation in the grain particles make the soil prone to much more contraction when load is reversed. By introducing the parameter, z, which only changes during dilation (dϵ_v^p<0). When the cycle is reversed, the model uses the accumulated value of z to artificially increase the dilatancy parameter A_d. Resulting in larger contractive tendency than it would have without the z parameter and creating a sharp drop in effective pressure known as the ”butterfly path”.

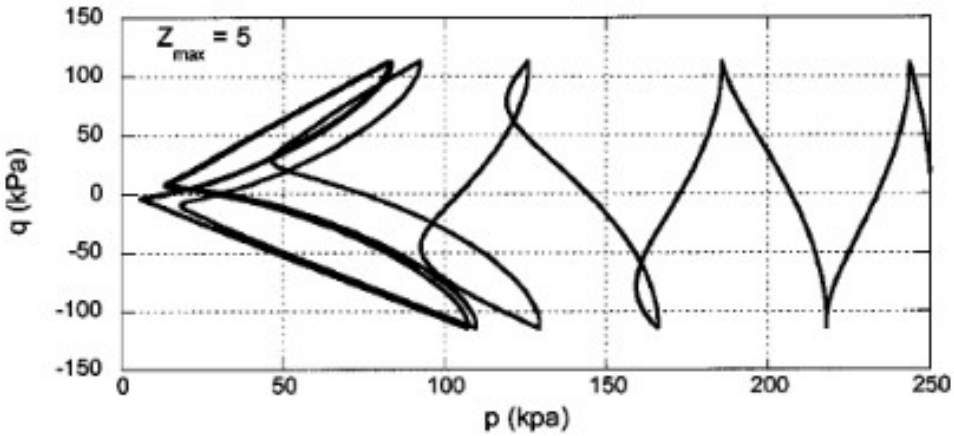

Figure 2.17: Illustration of cyclic undrained response with fabric-dilatancy tensor z (Dafalias & Manzari, 2004).

As illustrated in Figure 2.17, this mechanism allows the model to capture the characteristic ”butterfly” shape. Each cycle of dilation followed by reversal further reduces the effective mean principal stress, leading to the eventual approach of the stress path toward the origin representing liquefaction. This process is determined by two empirical constants: z_{max}, the maximum attainable fabric value, and c_z, which controls the pace of fabric evolution and are determined using trial-and-error processes. By incorporating these parameters SANISAND is able to simulate modulus degradation and permanent displacements under cyclic loading.

Table 2.4: Advantages and Limitations of the SANISAND Model.

Advantages	Limitations
State dependency: Material constants are used to simulate material response for different pressures and densities.	**Complexity:** Requires more parameters compared to a Mohr-Coulomb model.
Realistic cyclic response: The fabric-dilatancy variable permits accurate representation of pore pressure and effective pressure development.	**Calibration:** Determination of z_{max} and c_z values require trial-and-error procedure before being determined.
Critical state compatibility: Ensures soil deforms with zero volume change at the critical state.	**Constant stress ratio assumption:** Assume plastic strain occurs only when stress ratio changes ($d\eta \neq 0$). Does not account for plastic strains under constant stress ratio.
Softening and hardening: Capable of modelling the hardening of loose samples and softening of dense samples.	**Triaxial to multiaxial mapping:** Complex implementation from triaxial to multiaxial and dependence on the Lode angle.

3

Methods and Materials

This chapter presents the methodology used in this research. The chapter is divided into three sections. Section 3.1 explains the processing and interpretation of the CPT data. Section 3.2 describes the numerical modelling approach and the extraction of simulation results. Section 3.3 presents the method used to determine the final pile-to-borehole safe distance.

3.1. Field data and CPT processing

This section presents the methods used to process and interpret the CPT data. The analysis includes the cone trajectory, soil classification, material characteristics, Robertson soil behaviour type, relative density and horizontal stress. Relative density is determined with respect to the maximum and minimum void ratios of Ottawa sand, because no laboratory results were available for the sand at pile foundation depth. Ottawa sand with a similar D_{50} was therefore used as a reference material.

3.1.1. Cone trajectory

The cone trajectory was determined to evaluate the actual position of the CPT cone during penetration. The cone is prone to deviate during the measurement process, altering its position relative to the borehole compared with the starting point. Determining the cone distance from the borehole wall is therefore important for comparison with simulation results.

The trajectory was determined from the inclination data stored in the GEF files. The GEF parser reads the cone inclination in the x- and y-directions, together with the penetration depth and the CPT start coordinates. The CPT start coordinates were obtained from the GEF header, while the depth measurements were converted to elevation relative to NAP.

The horizontal displacement in the x- and y-directions was calculated using the point-wise inclination. The displacement components were then accumulated over depth to obtain the cone trajectory. The trajectory was expressed relative to the CPT start point, so that the horizontal displacement at the start of the measurement was taken as zero. The calculation was formulated as:

$$\Delta x_i = \Delta z_i \tan(\alpha_{x,i}) \tag{3.1}$$

$$\Delta y_i = \Delta z_i \tan(\alpha_{y,i}) \tag{3.2}$$

where Δx_i and Δy_i are the incremental horizontal displacements in the x- and y-directions, Δz_i is the vertical depth increment, and $\alpha_{x,i}$ and $\alpha_{y,i}$ are the measured cone inclinations in the x- and y-directions. The cumulative horizontal displacement was then obtained using:

$$x_i = \sum_{j=1}^{i} \Delta x_j \tag{3.3}$$

$$y_i = \sum_{j=1}^{i} \Delta y_j \tag{3.4}$$

where x_i and y_i are the cumulative horizontal displacements at depth increment i. The total horizontal offset from the CPT start point was calculated as:

$$r_i = \sqrt{x_i^2 + y_i^2} \tag{3.5}$$

where r_i is the horizontal distance from the CPT start point at depth increment i.

The sign convention of the inclination measurements was provided by the company Fugro. The resulting trajectory was plotted in the x-direction, the y-direction, top view and in 3D. These plots were used to evaluate the direction and magnitude of the cone deviation over depth.

3.1.2. GEF data processing

The CPT measurements were provided as GEF files. During each CPT, measurements are recorded at depth intervals of 2 cm. The relevant measured output parameters include the penetration depth, cone resistance q_c, sleeve friction f_s, friction ratio R_f, pore pressure u_2, cone inclination in the x- and y-directions, corrected penetration depth and time. These variables form the basis for the analyses performed in this research.

In addition to the measured CPT data, the GEF files contain header information required for processing the measurements. This includes the column definitions, the CPT start elevation relative to NAP, starting point coordinates, the net area ratio of the cone and groundwater level. This additional information is important for determining quantities such as cone trajectory and Robertson classification, which are used for comparison between CPT measurements.

The GEF files were processed using a Python parser. The parser first reads the header of the GEF file and assigns column definitions to the measured data. The parser also reads the CPT start elevation relative to NAP from the GEF header and stores the coordinates and net area ratio where these values are available.

The CPT start elevation is used to convert the measured penetration depth to an elevation relative to NAP. This was done using:

$$z_{NAP} = z_{start} - d \tag{3.6}$$

where z_{NAP} is the elevation of the measurement point relative to NAP, z_{start} is the CPT start elevation relative to NAP, and d is the measured penetration depth below the CPT start level. This conversion was applied because NAP provides a fixed vertical reference level, allowing different CPT measurements to be compared consistently.

The parser also performs several data-cleaning steps. GEF void values are replaced by missing values, rows with missing essential data are removed, and measurements with non-positive cone resistance are excluded. If the friction ratio is not directly available in the GEF file, it is calculated from the measured cone resistance and sleeve friction:

$$R_f = \frac{f_s}{q_c} \cdot 100 \tag{3.7}$$

The processed output consists of a dataframe containing the CPT measurements and associated metadata. This dataframe is then used as input for the soil classification, layer interpretation and parameter

assignment described in the following subsection. This Python parser has been adapted to analyse different GEF files from CPT measurements. The full Python implementation of the GEF parser is included in the code repository provided in Appendix D.

3.1.3. Soil classification

The Python parser processes the GEF file and generates an editable dataframe. The processed values are then used to automatically assign each CPT point to a soil type in accordance with Lengkeek (2024). Every point in the dataframe is assigned to a soil type and then converted to a continuous soil layer with a user-defined minimum thickness.

The first step in creating the soil distribution over depth is to calculate the derived parameters used in the Lengkeek-Robertson soil classification. The cone resistance is converted to the dimensionless corrected cone resistance over pressure q_t/p_a.

$$q_t = q_c + u_2(1 - a) \tag{3.8}$$

where q_c is the cone resistance, u_2 is the pore pressure measured behind the cone and a is the net area ratio of the cone. The corrected cone resistance is then normalised by the atmospheric pressure.

$$q_t/p_a = \frac{q_t \cdot 1000}{100} \tag{3.9}$$

In accordance with Robertson (2010b) and Lengkeek (2024), the normalised corrected cone resistance, pore pressure and friction ratio are used to determine the non-normalised Robertson soil behaviour type index I_{SBT} and the parameter B_{qt}.

$$I_{SBT} = [(3.47 - \log(q_t/p_a))^2 + (\log(R_f) + 1.22)^2]^{0.5} \tag{3.10}$$

$$B_{qt} = \frac{u_2 - u_0}{q_t} \tag{3.11}$$

where u_0 is the hydrostatic pore pressure. These derived quantities were used as inputs for the Lengkeek L2024-R2010 soil classification, which was selected because it is suitable for Dutch organic and Holocene soil conditions (Lengkeek, 2024). First, each CPT point was evaluated using the organic-soil criteria with the calculated B_{qt} and I_{SBT}. If the point is classified as organic soil, it is assigned either as ”Peat” or ”Organic clay”, depending on its value. If the point does not satisfy the organic soil criteria, it is classified by the 2010 Robertson classification with the following categorisations: unknown material, fine-grained soil, clay & silt, silty clay / clayey silt, sand mixtures, sand or dense sand / gravelly sand. The result is a soil classification per CPT measured point.

The point classification was then converted into interpreted soil layers. A new soil layer was created when the classified soil type changed with depth. Each layer was registered with top and bottom elevation relative to NAP and soil classification. To avoid an overly sensitive soil classification, caused by local variations in the measurements, a minimum layer thickness of 0.3 m was applied. Layers thinner than this threshold were merged with the layer above.

After the soil layers were defined, each interpreted layer was assigned a layer number and unique ID. This was registered in the dataframe, so that each point retained both its point-wise soil classification and the layer to which it belonged. This creates the possibility to analyse the dataframe as categorised soil layers or separate points.

This workflow produces two outputs: a dataframe of the points and an interpreted layer file. The dataframe contains the original parameters, calculated parameters and soil classifications per point. The layer output contains the interpreted soil layers, top and bottom elevation, thickness, soil type and soil-ID. These outputs form the basis for further processing.

3.1.4. Material characteristics

All points have been classified and converted into interpreted soil layers. The interpreted layers were then assigned soil characteristics in accordance with the Dutch NEN (2016). These characteristics will be used to run the numerical model simulations. The process was automated to ensure the same method was applied to different CPT measurements.

For each interpreted layer, the mean cone resistance q_c and sleeve friction f_s were calculated over the depth interval of that layer. These average values were used to assign representative soil parameters based on NEN-EN Table 2.B. The assigned parameters include the unsaturated unit weight γ_{unsat}, saturated unit weight γ_{sat}, Young's modulus E', cohesion c' and friction angle ϕ'. Where the table provided parameter ranges, the average of the range was used. For cone resistance values between tabulated values, linear interpolation was applied. If the average cone resistance was outside the range of the table, the parameter value was clipped to the closest available tabulated value. This prevented extrapolation beyond the range for which the table values are defined.

The dilatancy angle, ψ, was not taken directly from NEN-EN Table 2.B. Instead, it was derived from the friction angle. For granular soils, such as sand and sand mixtures, the commonly used relationship was:

$$\psi = \phi' - 30^\circ \tag{3.12}$$

where ϕ is the assigned friction angle (Seequent, 2024). For cohesive and organic soils, the dilatancy angle was set to zero. Negative dilatancy values were not applied.

Because the CPT classification classes do not correspond directly to the NEN-EN Table 2.B soil categories, a fixed mapping was applied. Dense sand/gravelly sand was assigned to weak silty gravel, sand to clean sand, sand mixtures to strongly silty sand, silty clay/clayey silt to weak sandy silt, clay and silt to weak sandy clay, organic clay to organic clay, and peat to the peat category.

After assigning parameters to the interpreted layers, neighbouring layers with identical soil classification and material parameters were merged. This reduces the number of layers used in the numerical model and reduces the computation time and resources. For the foundation pile sand layer, extending approximately from -18 m NAP to -30 m NAP, the sand layers were combined using a thickness based weighted average of the assigned material parameters.

According to CROW (2022) there are varying values for the Poisson's ratio. In the case of drained conditions the value for sand is from 0.2-0.3, whilst for clay and peat it is from 0.3-0.45. For undrained conditions the value for clay goes up to 0.45-0.5. Because the CPT results contain different soil types and the numerical model is considered drained, two Poisson's ratio categories were used. One category used a value of 0.25 for sand and sand mixtures, while the other used a value of 0.35 for clay, peat, silt and organic mixtures.

3.1.5. Robertson chart

After the Robertson parameters were calculated for each point in the dataframe, separate points can be plotted as a classified soil layer. This is useful for assessing differences in soil behaviour, including the position of the data with respect to the overconsolidation regions.

The script plots the selected soil layers in the q_t/p_a and R_f space. For analytical purposes, the mean value of the layer is also determined and marked in the plot, permitting comparison to before and after drilling measurements.

The mean value alone, however, is not sufficient to assess differences in measurements. Soils are non-homogeneous and variations in the horizontal direction are common. To address this, a confidence ellipse was added quantifying the spread of the points. The ellipses were calculated from the covariance matrix of the selected data points. The centre of each ellipse represents the mean value of the dataset, while the orientation and shape of the ellipse represent the correlation and spread of the data in the q_t/p_a and R_f space. The chosen confidence ellipses are 68.3% and 90%, corresponding to standard deviations of 1.52 and 2.14 respectively for a two-dimensional confidence ellipse (Sapkota, 2023).

The interpreted soil profiles and their top and bottom elevations are compared with software developed by the company Witteveen+Bos. The software analyses GEF files, detects soil layers and classifies them in the Robertson chart. The two systems may differ in methodology and internal settings, however, a point of comparison for the developed soil classification system is useful to determine its accuracy. This comparison was therefore used as a qualitative check rather than as an absolute validation, since differences may also arise from the assumptions and internal settings of the reference software.

3.1.6. Relative density

Three different methodologies to determine relative density have been selected for comparison. The methods by Baldi et al. (1986) and (Robertson & Cabal, 2023) were selected as older and more recent CPT-based approaches for determining relative density. The Ahmadi and Golestani Dariani (2017) method requires analysis of the CPT measurements and value determination from figures developed in the laboratory.

The relative density of the sand layers was estimated using three CPT based approaches. This was done because CPT measurements are not able to extract this value. In addition, no laboratory tests were available to determine the in-situ minimum and maximum void ratios of the Delft sand. To assess this uncertainty, the calibrated Ottawa sand used in the SANISAND model was adopted as a reference material, because it has a similar D_{50} to the sand in the Delft foundation pile sand layer.

First the CPT points for the selected sand layers were extracted from the dataframe. The total vertical stress σ_{v0} and effective vertical stress σ'_{v0} were calculated from the interpreted soil profile and assigned unit weights. Compression was taken as positive.

The first method used was the Robertson method, where the relative density is determined through the normalised cone resistance, Q_t (Robertson, 2010a). The corrected cone resistance was converted to kPa and the normalised cone resistance was calculated as:

$$Q_t = \frac{q_t - \sigma_{v0}}{\sigma'_{v0}} \tag{3.13}$$

where q_t is the corrected cone resistance, σ_{v0} is the total vertical stress and σ'_{v0} is the effective vertical stress. This was followed by the calculation of the relative density:

$$D_r^2 = \frac{Q_t}{350} \tag{3.14}$$

where Q_t is the normalised cone resistance. The denominator represents a variable value that depends on the sand type. The range is from 300 for young fine sands to 400 for old coarse sands (International Organization for Standardization, 2017). Because the soil in this study is classified as a medium sand, a value of 350 was selected.

The second method used was developed by Baldi et al. (1986), relating cone resistance, effective vertical stress and relative density using empirical correlations for sand. The relative density was calculated as:

$$D_r = \frac{1}{C_2} \ln\left(\frac{q_c}{C_0(\sigma'_{v0})^{C_1}}\right) \tag{3.15}$$

where q_c is the measured cone resistance in kPa, σ'_{v0} is the effective vertical stress in kPa, and C_0, C_1 and C_2 are empirical constants. The values used in the calculation were $C_0 = 157$, $C_1 = 0.55$ and $C_2 = 2.41$.

The third method was based on the Ahmadi-Golestani approach. This method consists of laboratory calibrated figures, from which the relative density could be read depending on the cone resistance and sleeve friction values. Because values must be read from figures, the method contains interpretation uncertainty.

After calculating the relative density for the different methods, it was converted to the void ratio using:

$$D_r = \frac{e_{max} - e}{e_{max} - e_{min}} \tag{3.16}$$

where e_{max} is the maximum void ratio, e_{min} the minimum void ratio and e the void ratio. If the D_r is expressed as a percentage, $D_r/100$ is used in the equation. Since no laboratory test has been performed on the sand to determine void ratio, the similar D_{50} calibrated Ottawa sand maximum and minimum void ratios were adopted. This does however add a level of uncertainty to the void ratio. A benefit of using this sand was that it is also calibrated to be used in the SANISAND constitutive model.

3.1.7. Horizontal stress

Two methods were used to estimate the horizontal stress in the sand layer: the Robertson K_0 estimation method and the Ahmadi-Golestani method. The purpose of using two methods was to compare their results with the numerical model and each other.

The first method is based on the K_0 estimation proposed by Robertson (2016). As shown in Figure 2.11, the coefficient of earth pressure at rest depends on the stress history of the soil. The K_0 value was therefore selected based on the position of the soil layer in the Robertson chart. The effective horizontal stress was then calculated using:

$$\sigma'_{h0} = K_0 \sigma'_{v0} \tag{3.17}$$

where σ'_{h0} is the initial effective horizontal stress and σ'_{v0} is the initial effective vertical stress. The total horizontal stress was obtained by adding the hydrostatic pore pressure:

$$\sigma_{h0} = \sigma'_{h0} + u_0 \tag{3.18}$$

where u_0 is the hydrostatic pore pressure. This method provides an estimate of the initial horizontal stress state.

The second method is the Ahmadi-Golestani method. This method uses CPT measurements to estimate the initial effective horizontal stress in sandy soil. The method is based on sleeve friction, cone resistance and the initial effective vertical stress. First, the relative density is estimated from the sleeve friction and initial effective vertical stress using the calibrated relationship. The estimated relative density is then used together with the cone resistance to determine the initial effective horizontal stress.

This method was applied at selected depths in the foundation pile sand layer to coincide with the extraction points in the numerical model.

An important limitation of this method is the required reading of values from plots. This may result in interpretation uncertainty.

3.1.8. Additional case studies

Additional CPT measurements from the Wezep and Zwolle case studies were analysed as a qualitative comparison to the Delft soil classification and soil behaviour.

For both locations, CPT measurements before and after drilling were selected based on their horizontal distance to the borehole. For the Wezep case study, CPTs within a radius of 4 m from the borehole were considered, while for the Zwolle case study a radius of 2 m was implemented. The different selected radii were used because fewer close proximity CPT measurements were available for Wezep.

The selected CPTs before and after drilling were processed using the same GEF parser, soil classification procedure and Robertson soil behaviour type plotting as applied to the Delft case study. For both additional locations, only the sand layers were plotted in the Robertson chart. Sand mixtures were not included in these plots. This choice was made as the Delft interpretation was based on the behaviour of sand.

The additional case studies were analysed less extensively than the Delft case study. The cone trajectory, relative density, horizontal stress and soil characteristics were not derived, and no numerical

model was created for these locations. The purpose of the additional CPT analysis was to identify whether there are visual differences in before and after sand measurements. The results will be compared to the interpretations of the Delft sand behaviour.

3.2. Numerical modelling approach

This section presents the numerical modelling approach used to analyse stress and strain redistribution around the borehole using PLAXIS 3D version 2025.1.2.76. The model limitations, assumptions, geometry, mesh, boundary conditions, soil layering, material assignment and unloading phases are described. The section also presents the constitutive models used in the simulations and the procedure used to extract and transform the numerical results. Finally, the comparison and evaluation procedure is introduced, including the verification against the Kirsch solution, the comparison between constitutive models, and the assessment of borehole radius and initial void ratio effects.

3.2.1. Modelling limitations and assumptions

Several assumptions were made to reduce the complexity and computational cost of the numerical model. These assumptions are important for the analysis and comparison with other models, however, should be taken into consideration.

The models were run under drained conditions. This means that excess pore pressures generated during unloading were not considered. The focus is on the redistribution of effective stress around the borehole. This assumption was made because the research is mainly focused on the pile foundation sand layer, where drained behaviour is assumed.

The groundwater level was considered to be at ground level. This results in a fully saturated soil profile. The actual groundwater level may vary in practice, however, the assumption provides a consistent pore pressure condition for all simulations. The pore-water pressure was included as a steady-state pore pressure, while excess pore-pressure generation was not considered because of the drained modelling approach.

The initial horizontal stress state was determined with the constant value of $K_0 = 0.5$. In addition, the horizontal stresses were considered to be equal in the two directions. As a result, the stress around the borehole was simplified and represented a horizontally isotropic initial stress condition.

The soil was assumed to be horizontally homogeneous. Each layer was assigned one representative set of material parameters based on the CPT interpretations. Layer thickness and material properties were assumed to not vary in the horizontal direction.

The numerical analysis focuses on the foundation pile sand layer. This layer is important because it contributes significantly to the bearing capacity of foundation piles. Therefore, it is the most relevant for assessment with different computationally intensive models. Modelling all layers with advanced models would be computationally too intensive and would significantly increase the run time. For this reason, all soil layers above the foundation pile sand layer were modelled with the linear-elastic model. The foundation pile sand layer was then analysed using different constitutive models.

The soil parameters used as inputs for the numerical model were derived from CPT interpretations. Laboratory tests of the studied soil were unavailable. For the SANISAND model, calibrated parameters from Ottawa sand were adapted due to its similar D_{50}. The SANISAND results should therefore be interpreted as an estimate of stress and strain developments.

The borehole was simulated through stepwise removal of the back pressure acting on the wall, representing the pressure originally provided by the removed soil. This approach simplifies the drilling process and permits the regulation of the steps taken for reduction of pressure. Stepwise unloading is required because large pressure reductions in a single phase can result in instability or undetected developments.

3.2.2. Geometry, mesh and boundary conditions

The numerical model was constructed around the borehole. Instead of modelling the full three-dimensional soil domain around the borehole, only a quarter of the borehole and the surrounding soil were modelled. This was done to reduce the computational cost of the simulations. Since the borehole is circular and

the soil has equal horizontal stress, the quarter model was considered sufficient to determine the stress and strain development surrounding the borehole. Figure 3.1 shows the geometry and boundaries used in PLAXIS.

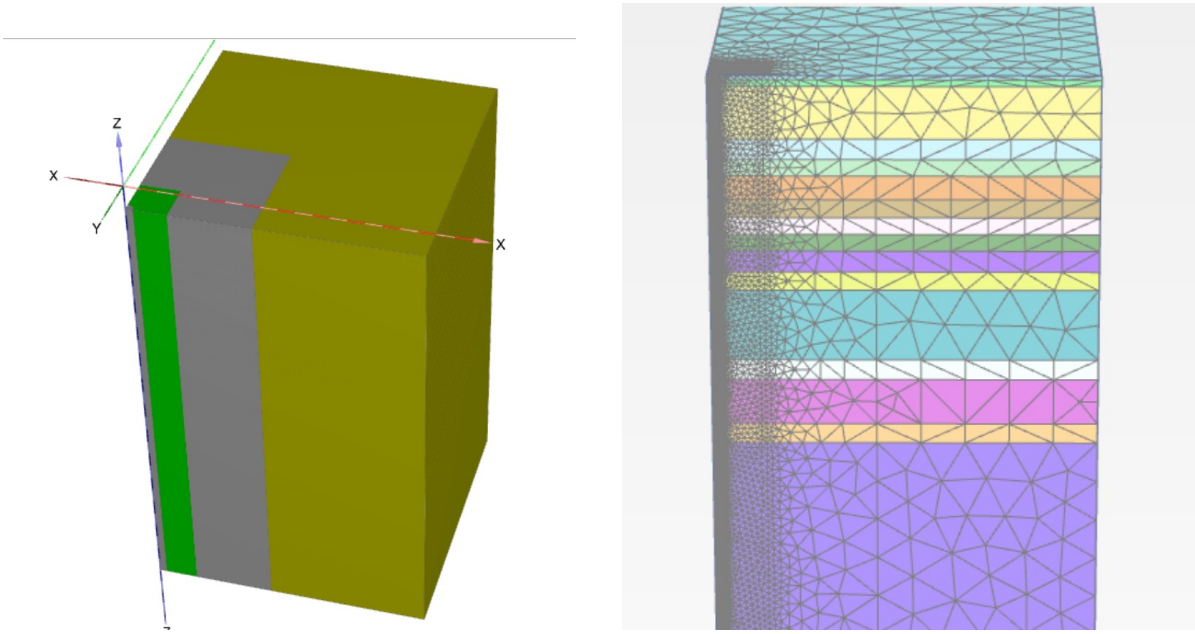

(a) PLAXIS structures overview. **(b)** PLAXIS mesh overview.

Figure 3.1: PLAXIS structures and mesh overview for the constitutive models.

The horizontal model boundary was defined by the borehole radius and three radial zones. The boundaries were calculated as:

$$L = R + D_1 + D_2 + D_3 \tag{3.19}$$

where R is the radius, $D_1 = 2$, $D_2 = 5$, $D_3 = 10$. This distance was selected, as it would represent a distance larger than twenty times the radius of the drill. This would create the possibility to evaluate the existing rule-of-thumb. Placing the boundary at this distance also minimises the influence on the calculated stress and strain distribution. Horizontal displacement was restricted at the boundaries, while vertical displacement was permitted. The bottom boundary was fixed in vertical displacement, while the upper boundary was not.

The mesh was refined around the borehole because the largest stress and strain changes were expected to occur close to the borehole wall. Further away from the borehole, a coarser mesh was used because changes in stress and strain were expected to be smaller. A structured mesh refinement concentrates finer meshes in areas where larger changes are expected, while using larger elements in areas where small stress changes are expected. For this purpose, radial zones were created with their assigned mesh coarseness factor. The borders between the refinement zones were straight lines, as it was not possible to make them circular like the borehole. This reduces the calculation time while maintaining sufficient accuracy near the borehole.

The numerical results were extracted along a $45°$ line from the borehole centre. This line was chosen to avoid the symmetry boundaries. Along this line, the results were extracted at different distances from the borehole and expressed as a normalised radius from the borehole centre.

3.2.3. Soil layering and material assignment

The soil layering and material assignment were performed in PLAXIS using an automated workflow. The minimum 0.3 m thick interpreted soil layers and assigned material parameters from the CPT processing were exported to an Excel file, which was read by a Python script that loads the soil distribution

in PLAXIS. Automating this process made it possible to generate the numerical model in a consistent way for different constitutive models and borehole radii simulations. The result of the automation is shown in Figure 3.2.

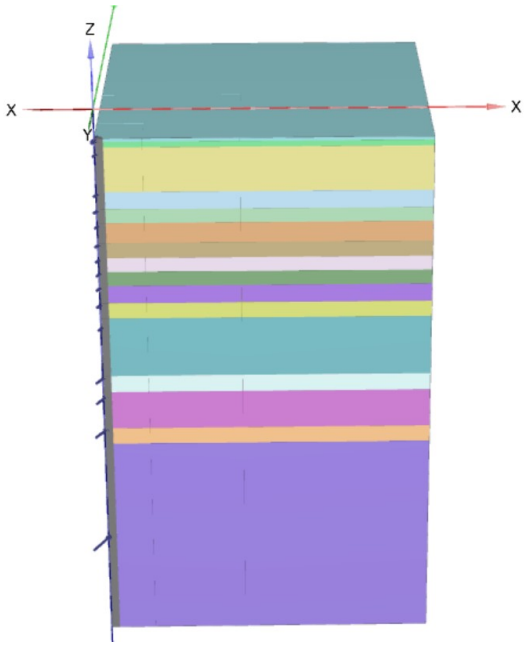

Figure 3.2: PLAXIS soil distribution.

The Excel file consists of two main parts. The first defines the soil profile, including the layer names and elevations. The second part defines the material properties of the defined soils. During model generation, the script generates the ground profile volumes and then creates soil materials that are assigned to each volume. The material property sheet also contains the constitutive model assigned to the layer, creating the possibility to run different constitutive models depending on the Excel input.

3.2.4. Borehole modelling and unloading phases

A quarter of the cylindrical borehole was modelled spanning over the entire depth. During the initial phase, the soil volume inside the borehole was still active. In the following phases, the soil inside the borehole was deactivated and the back pressure was activated. This represents the pressure generated by the removed soil.

The back pressure was based on the same principle the software was using to determine the horizontal effective stress. A point-wise horizontal effective stress was calculated using the vertical effective stress and the assumed value of $K_0 = 0.5$.

The drilling of the borehole was simulated by a stepwise reduction of the back pressure. A load factor was used, starting at 1 and decreasing to 0 in user-defined steps of 0.1. This simplification was used because the main objective of the numerical model was to study the stress and strain redistribution around the borehole, rather than to reproduce the full drilling process.

Different borehole radii can be analysed by changing the radius input in the Python script. The script then automatically rebuilds the borehole geometry, radial refinement zones and extraction locations for the selected radius.

The use of multiple unloading phases also made it possible to extract results at different stages of the pressure reduction. This was important because the stress and strain changes do not occur only in the final unloaded state, but develop progressively as the borehole pressure is reduced.

3.2.5. Constitutive models

Three constitutive models were used in the numerical analysis: Linear Elastic, Mohr-Coulomb and SANISAND. These models were selected to compare different levels of model complexity. The theoretical background of these models has been discussed in the state of the art. This subsection only describes how the models were implemented in the numerical analysis.

For numerical simplicity, the foundation pile sand layer was represented by one sand layer. This was done, as explained before, by combining the sand layers at a depth below -18.5 m NAP. When present, the sand mixtures layers were also combined in the sand layer.

Linear-Elastic model
The linear-elastic model was the simplest model used in the software. The required input parameters for this model are the Young's modulus and the Poisson's ratio. This model was assigned to all layers above the pile foundation layer and to the pile foundation layer if necessary. The model does not include yield, plastic strain or dilatancy and serves as a baseline to evaluate elastic stress distribution.

Mohr-Coulomb model
The Mohr-Coulomb model was used as a simple elasto-plastic model. Compared with the linear-elastic model, it includes a failure criterion and allows plastic strain to develop once the yield surface has been reached. The required input parameters for this model are the Young's modulus, Poisson's ratio, cohesion, friction angle and dilatancy angle.

SANISAND
The SANISAND model was used as the most advanced model to calculate the behaviour of sand. In PLAXIS, the model is a user-defined material model based on the model by Liu et al. (2019), which is based on the work of Dafalias and Manzari (2004).

The SANISAND model requires calibrated laboratory tests to generate its inputs. There were however no calibrated laboratory tests performed on the foundation pile soil in Delft. Therefore, the parameters were adopted from a calibrated Ottawa sand with similar D_{50} by Chong and Santamarina (2016). Because the SANISAND input parameters are adopted from a different sand, the SANISAND results should be interpreted as an estimate of possible sand behaviour.

The corresponding material parameters used for this model are presented in Table B.5 in Appendix B.8.

The initial void ratio e_{ini} was a varied input parameter for the SANISAND model. Additional simulations were performed with different values, ranging from e_{min} to e_{max}, to evaluate the sensitivity of the predicted stress distribution with respect to the initial density.

The critical void ratio e_{cs} was determined to understand the sand state relative to the critical state. This is relevant because sands with higher void ratio than the critical state tend to contract during shearing, while sands with lower void ratio than the critical state tend to dilate. In this research the unloading process generates the relevant shear. The critical void ratio was calculated using the formula from Seequent (2024).

$$e_{cs} = e_0 - \lambda(\frac{P}{P_{atm}})^{\xi} \tag{3.20}$$

3.2.6. Extraction of results

The Cartesian stresses were transformed into polar stresses using the stress transformation equations provided by Roylance (2001).

Similar to the automation of soil structure and the mesh, the extraction of numerical results was also automated. The purpose was to extract stress and strain values around the borehole at different depths and phases. These results were later used to compare different constitutive models and development of stress and strain within each model.

The extracted stress components were the Cartesian effective stresses σ'_{xx}, σ'_{yy} and σ'_{zz}, the shear stresses σ_{xy}, σ_{yz} and σ_{zx}, and the principal effective stresses σ'_1, σ'_2 and σ'_3. The extracted strain

components were ε_{xx}, ε_{yy}, ε_{zz}, γ_{xy}, γ_{yz} and γ_{zx}. These values were stored for each selected phase, layer, depth and radial distance from the borehole.

The three extraction points were on a $45°$ line from the borehole centre in the horizontal plane at depths -21.78 m NAP, -24.78 m NAP and -27.78 m NAP. Along the line results were extracted in relation to the distance from the borehole wall. The extraction distances were small close to the borehole wall, where the largest stress and strain gradients were expected, and became larger further away from the borehole.

The horizontal extraction distance was defined relative to the borehole wall. For each extraction point, the radial distance from the borehole centre was calculated as:

$$r = R + d \tag{3.21}$$

where r is the radial distance from the borehole centre, R is the borehole radius and d is the distance from the borehole wall. The coordinates of each extraction point were then calculated using:

$$x = x_{BH} + r\cos(\theta) \tag{3.22}$$

$$y = y_{BH} + r\sin(\theta) \tag{3.23}$$

where x_{BH} and y_{BH} are the borehole centre coordinates and $\theta = 45°$ is the extraction angle.

The vertical extraction locations depended on the constitutive model simulation. For the linear-elastic model, results were extracted at the middle of each interpreted soil layer and at multiple depths in the final sand layer. For the Mohr-Coulomb and SANISAND simulations, results were extracted only in the pile foundation sand layer. This was done because the soil above was run with a linear-elastic model, which would give the same values as the linear-elastic model simulation. This resulted in a reduction in time and storage required for extracting those values. In the pile foundation sand layer, three extraction points were defined at regular intervals to evaluate whether the numerical response varied with depth. This was done because the bearing capacity of piles in sand beneath soft soil can depend on the relative thickness of the overlying soft layers and the embedded length of the pile within the sand layer (Lehane, 2020). Therefore, evaluating only one depth in the sand layer would provide a limited representation of the response. By extracting results at multiple depths, the variation within the sand layer could be assessed and the findings could be interpreted more broadly for different subsurface conditions.

The PLAXIS output provides stress and strain in Cartesian components. Since the borehole response is evaluated in radial direction, the horizontal Cartesian components were transformed to polar. The radial and hoop components were derived from the extracted Cartesian ones using the transformation equations given by Roylance (2001):

$$\sigma_r = \sigma_x \cos^2\theta + \sigma_y \sin^2\theta + 2\sigma_{xy}\sin\theta\cos\theta \tag{3.24}$$

$$\sigma_\theta = \sigma_x \sin^2\theta + \sigma_y \cos^2\theta - 2\sigma_{xy}\sin\theta\cos\theta \tag{3.25}$$

where σ_r is the radial stress, σ_θ is the hoop stress, σ_x and σ_y are the Cartesian horizontal stress components, σ_{xy} is the shear stress component and θ is the angle of the extraction point relative to the global x-axis. The same transformation principle was used to obtain radial and hoop strain components substituting σ with ε.

After transformation, the results were expressed as a function of normalised radius:

$$\frac{r}{R} \tag{3.26}$$

where R is the borehole radius. This normalisation allows results from different borehole radii to be compared using the same dimensionless distance measure. The results were then used to plot radial stress, hoop stress, vertical stress, radial strain and hoop strain profiles for the selected depths and unloading phases.

3.2.7. Comparison and evaluation procedure

The numerical results were compared with different methodologies and different goals. These methodologies were important to assess whether the model response was physically reasonable, to compare constitutive models and to relate predictions to CPT results.

First, the linear-elastic model was compared with the Kirsch solution. The Kirsch solution determines the elastic stress redistribution around a circular opening and is governed by linear-elastic behaviour. This comparison was used as a verification for the linear-elastic model results, vertical stress and the step-wise reduction of the borehole back pressure. If the results coincide, the model geometry, boundary conditions and extraction method can be considered consistent.

Second, the results of the different constitutive models were compared with each other. The Linear Elastic, Mohr-Coulomb and SANISAND models were evaluated using the same borehole geometry, phase and extraction locations. This made it possible to assess the differences between constitutive model predicted soil behaviour.

Third, the vertical stress development was extracted from the numerical model. The purpose of this comparison was to assess whether borehole unloading caused vertical stress changes in the surrounding soil and whether these changes extended to the CPT locations. This was especially relevant for interpreting whether the CPT measurements could be used to validate the numerical model response.

Fourth, the numerical trends were compared with the CPT-based observations. This comparison focused on whether the predicted affected zone reached the CPT locations and whether the CPT measurements showed corresponding changes in cone resistance, soil classification, relative density or interpreted soil state.

Finally, the influence of borehole radius and initial void ratio was evaluated. The radius comparison was used to assess whether the affected distance scales with the borehole radius when expressed as a normalised radius. The void-ratio comparison was used to evaluate the sensitivity of the SANISAND results to the assumed initial density of the sand. Together, these comparisons were used to assess which modelling assumptions have the strongest influence on the predicted stress and strain redistribution around the borehole.

3.3. Determination of pile-to-borehole distance

The minimum pile-to-borehole distance is determined by considering both the influence zone around the existing foundation pile and the influence zone around the borehole. The pile influence zone represents the soil volume that contributes to the bearing capacity of the pile, while the borehole influence zone represents the soil volume in which stress redistribution may occur as a result of drilling. The total minimum distance is therefore interpreted as a combination of these two zones.

The distance is evaluated as a centre-to-centre distance between the foundation pile and the borehole. This definition is used consistently in the comparison with the existing rule-of-thumb. The determination of the final distance is based on the following components: the pile influence zone according to Koppejan, the borehole influence zone derived from the CPT and numerical model results, and the comparison with the existing SIKB rule-of-thumb.

3.3.1. Pile influence according to Koppejan

The Koppejan method considers a zone around the pile tip that contributes to the bearing capacity of the foundation pile. This zone is schematically shown in Figure 2.3. The influence zone consists of two parts with different heights, which both extend from the pile and meet at the same horizontal distance from the pile tip.

For the present interpretation, the lower influence zone is used to define the horizontal extent of the pile zone. This lower zone is represented by a semicircular shape. The height of this zone is defined in relation to the equivalent pile diameter, the corresponding radius can be determined directly from the Koppejan geometry. The radius extent varies between $0.7D_{eq}$ and $4.0D_{eq}$. In this research, the midpoint of this range, $2.35D_{eq}$, is selected as representative value. The corresponding diameter becomes $4.7D_{eq}$. This value is used to describe the pile generated zone of influence. The equivalent pile diameter is determined as:

$$D_{eq} = 1.13a\sqrt{\frac{b}{a}} \tag{3.27}$$

where a and b denote the smallest and largest dimensions of the pile cross-section, respectively.

The use of the corresponding diameter $4.7D_{eq}$ should be interpreted as an approximation, Bogaards (2025) used a larger corresponding diameter of $5D_{eq}$. Because the resulting range for the influence zone is substantial for D_{eq}, the parameter requires further investigation to determine how it depends on soil conditions, such as void ratio, density and stress state.

3.3.2. Framework for comparison

The comparison between the proposed distances and the SIKB rule-of-thumb is made for a range of borehole diameters and foundation pile diameters. The borehole diameter controls the borehole influence zone, while the foundation pile diameter controls the Koppejan pile influence zone. This allows the comparison of the proposed distance to the SIKB protocol at equal borehole diameters.

An additional comparison is included in which the Koppejan zone is not considered. In this comparison the limit of the borehole influence zone reaches the centre of the foundation pile. This comparison is not realistic because of the level of interaction between the zones, however, it does provide an overview of the possibilities in distance reduction with greater zone interaction.

Four interpretations of the borehole influence zone are compared. These interpretations are divided into two categories: CPT-based and numerical model-based. The CPT-based interpretations use the absence of clear measurable changes at the cone location to define the borehole influence distance. Two CPT-based cases are considered: one without the Koppejan pile influence zone and one with the Koppejan pile influence zone included.

The second category is based on the SANISAND numerical model results. In this approach, the borehole influence distance is determined from the normalised radius at which the vertical stress has recovered to 95% of the far-field value. This choice was made because the pile base resistance is directly related to the vertical effective stress at the pile tip, and because the SANISAND model uses state dependent sand behaviour and predicts the largest stress redistribution zone. A reduction in vertical effective stress in the pile foundation sand layer may result in a reduction in the stress level contributing to the pile base resistance. For the numerical model-based interpretation, a distinction is made between initial void ratios below 0.8 and initial void ratios equal to or greater than 0.8. Similar to the CPT-based category, two numerical model-based cases are considered: one without the Koppejan pile influence zone and one with the Koppejan pile influence zone included.

4

Results Delft

This chapter presents and discusses the results obtained from the soil analysis and the numerical model simulations. The soil analysis is based on four CPT measurements performed close to a borehole. CPT1-2 and CPT1-4 were conducted 2 m and 4 m west of the borehole before drilling, while CPT2-2 and CPT2-4 were conducted 2 m and 4 m east of the borehole after drilling. The numerical model simulations were performed in PLAXIS using Linear Elastic, Mohr-Coulomb and SANISAND constitutive models. The soil parameters for the Linear Elastic and Mohr-Coulomb models were determined using Table 2.b from NEN (2016). For the SANISAND model, calibrated Ottawa sand parameters with a similar D_{50} were used due to the lack of calibrated sand parameters for the site.

The chapter is divided into four sections. Section 4.1 presents the interpretation of the CPT results. Section 4.2 presents the stress redistribution obtained from the numerical models. Section 4.3 derives expressions for the minimum distance between an ATES borehole and a foundation pile. Finally, Section 4.4 compares the proposed distances with the existing rule-of-thumb.

4.1. In-situ data interpretation

This section presents the results for the CPT analysis using the methodology described in Section 3.1. The interpretation includes the cone trajectory, soil profile, CPT measurements, relative density and derived horizontal stress.

4.1.1. Cone Trajectory

Figure 4.1 shows the measured cone trajectories of CPT2-2 and CPT2-4 after drilling. The figures present the horizontal displacement in the x- and y-directions, the top-view trajectory and the three-dimensional trajectory. For the CPT measurements performed before drilling, trajectory information was available, but the orientation of the measurements was not established. These trajectories could therefore not be used for the spatial interpretation.

Monitoring the cone trajectory is important to ensure no collision with the borehole. This situation did not arise during the measurements, however, cone trajectories show that the cone travels away from the borehole. This has consequences for the validation of the constitutive model vertical stress results. The deviation may result in a positioning of the cone too far away from the borehole to measure any changes in soil conditions.

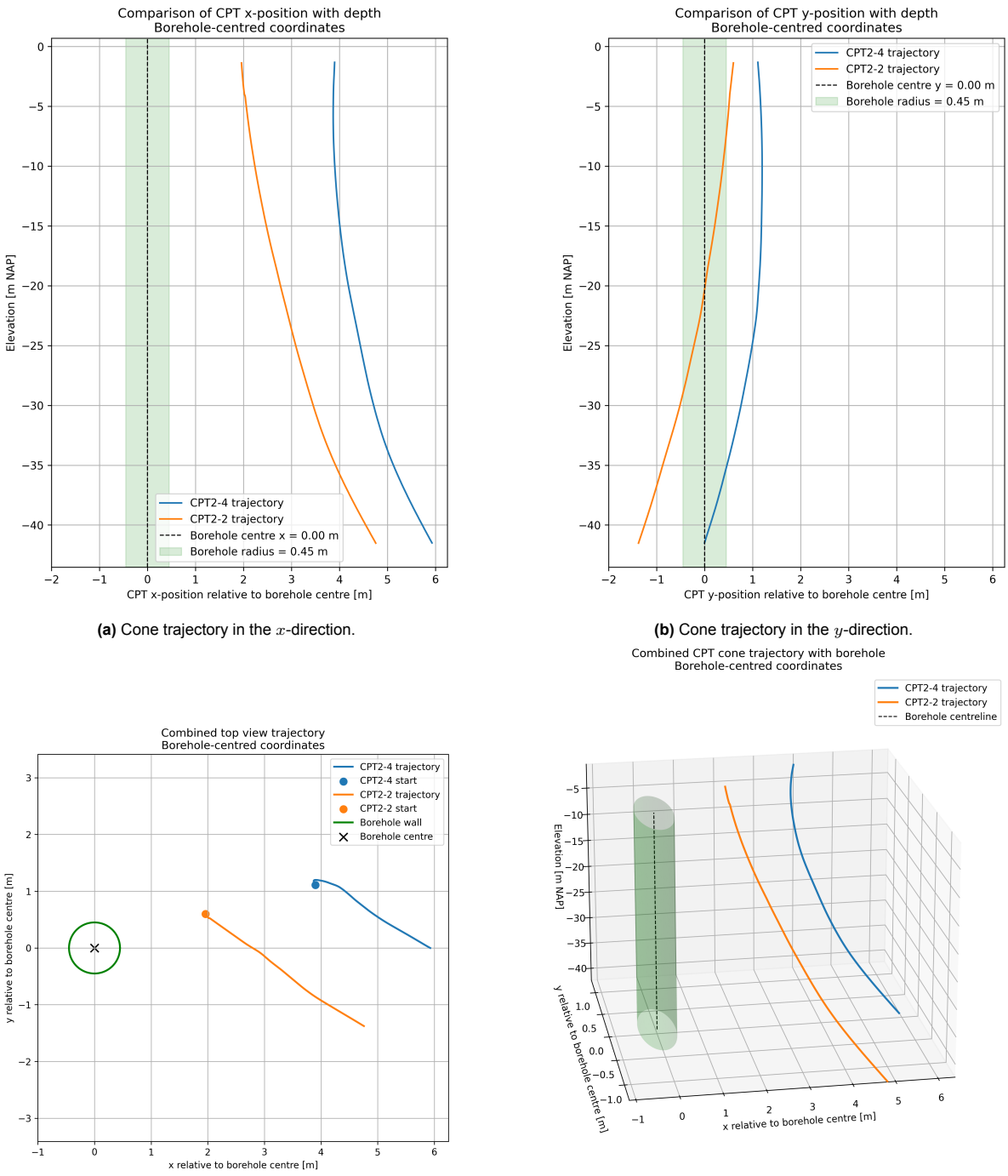

(a) Cone trajectory in the x-direction.

(b) Cone trajectory in the y-direction.

(c) Top view of the cone trajectory.

(d) Three-dimensional cone trajectory.

Figure 4.1: Cone trajectory of CPT2-2 and CPT2-4, showing the horizontal displacement components in the x- and y-directions, the top-view trajectory and the three-dimensional trajectory.

Figure 4.1 shows that CPT2-2 deviates in both the x- and y-directions. The deviation increases with depth, resulting in approximately 1 m displacement in the x-direction at around -24 m NAP and approximately 1 m displacement in the y-direction at around -27 m NAP. This deviation is relevant because the SANISAND model predicts, shown in the following chapter, that the stress changes caused by borehole unloading are highly localised around the borehole. With an expected convergence back to the steady state within five times the normalised radius. Therefore, even a lateral deviation of approximately 1

m can place the CPT outside the predicted influence zone. This complicates direct validation of the constitutive model, as the CPT did not measure the soil volumes where the largest stress changes were expected.

Figure 4.1 shows a similar overall behaviour for CPT2-4. The cone initially moves in one direction in the y-plane and then changes direction at approximately -5 m NAP. At maximum depth, the total deviation remains smaller than that of CPT2-2, but the cone still moves away from the borehole. This reduces the possibility of detecting borehole induced stress changes and therefore also the validation of the constitutive model.

The cone trajectories therefore provide an important explanation for the limited validation possibilities of the numerical model. The absence of clear changes in cone resistance or Robertson classification cannot be interpreted as direct proof that no stress changes occurred close to the borehole. Instead, it indicates that no clear changes were detected at the actual CPT locations. Since the CPTs moved away from the borehole, the measurements were taken outside the predicted influence zone.

The cone deviation limits validation of the stress response near boreholes predicted by the constitutive model. A CPT positioned closer to the borehole wall would have been more suitable for validation, provided that the test could be safely monitored to avoid collision with the borehole.

4.1.2. Soil profile and parameters

Figure 4.2 presents the interpreted soil profiles derived from the four analysed CPT measurements up to a depth of -30 m NAP.

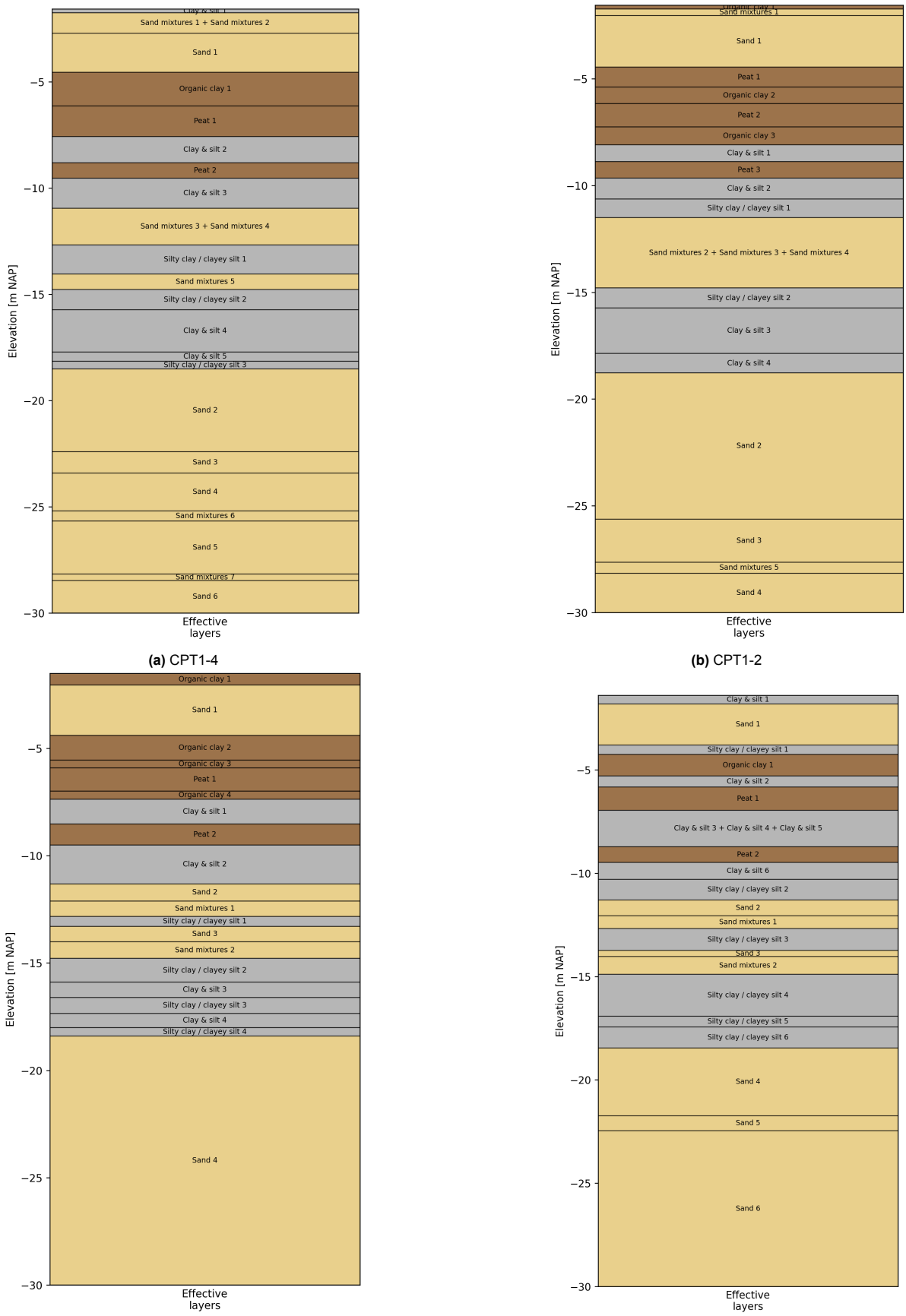

(a) CPT1-4

(b) CPT1-2

(c) CPT2-2

(d) CPT2-4

Figure 4.2: Interpreted soil profiles for the four CPT locations after applying a minimum layer thickness of 0.3 m. Adjacent layers were merged where their assigned material parameters were identical.

In Appendix B.1 figures are presented with the soil layer distribution to the maximum CPT depth, with the corresponding cone resistance and friction ratio. The classified soil profiles shown in Figure 4.2 were processed using a minimum layer thickness of 0.3 m. In addition, adjacent layers with identical assigned material parameters were merged into a single layer. This procedure reduces the number of classified layers, resulting in a clearer visual and a more efficient computational model.

Overall, the four interpreted profiles show a high degree of similarity. All profiles start with a thin clay or organic layer at the surface, followed by a shallow sand layer, also known as the first sand layer. Underneath this sand layer, most CPTs show a relatively thick organic deposit consisting of organic clay and peat, followed by an alternating clay, silt and peat layers.

Some local differences are observed between the CPTs. CPT2-4 differs from the other profiles because the thick organic layer below the first sand layer is less clearly present. The organic layer is reduced in thickness as a result of the presence of silty clay layers above and within the organic layers.

At approximately -12 m NAP, all profiles show the start of a sand or sand-mixture layer, although a silty clay/clayey silt layer occurs within this interval in most profiles. This is followed by a thick clay and silt layer extending to approximately -18.5 m NAP.

Below approximately -18.5 m NAP, all CPTs indicate a continuous sand layer. This layer is identified as the foundation pile sand layer, as it provides the primary bearing function for the foundation piles. The interpreted profiles were limited at -30 m NAP. This depth provides a sufficient margin below the expected pile toe level for evaluating the stress and strain development around the borehole.

The material parameters assigned to the foundation pile sand layer are summarised in Table 4.1. The parameters for this layer have been presented separately because it is the most important soil layer for the research. A parameter overview with all classified layers is provided in Appendix B.7.

Table 4.1: Parameters of the deepest sand layer based on Table 2.b from NEN (2016).

CPT	Layer	Top [m NAP]	Bottom [m NAP]	γ_{sat} [kN/m^3]	E' [kPa]	ν' [-]	c' [kPa]	ϕ' [°]	ψ [°]
CPT1-2	Sand 2	-18.78	-30	20.49	57921	0.250	0	33.77	3.88
CPT1-4	Sand 2	-18.51	-30	20.38	54904	0.250	0	33.38	3.55
CPT2-2	Sand 4	-18.41	-30	20.5	59950	0.250	0	34.1	4.1
CPT2-4	Sand 4	-18.46	-30	20.72	67744	0.250	0	34.88	4.88

Table 4.1 presents the assigned parameters for the foundation pile sand layer, obtained by averaging the cone resistance and sleeve friction values over the depth of this layer. Similar to the interpreted soil classification, the derived parameters show a degree of similarity between CPT locations. The unit weight, Young's modulus, friction angle and dilatancy angle are generally comparable for three CPTs. CPT2-4 is a slight exception, as it shows higher values for these parameters, suggesting a locally stronger sand layer. This consistency between the CPT-derived parameters is important for evaluating the potential influence of the vertical borehole installation on the surrounding soil.

4.1.3. CPT measurements

This subsection compares the CPT measurements before and after borehole installation. The analysis focuses on cone resistance q_c, sleeve friction f_s, corrected cone resistance q_t and Robertson soil behaviour classification. The purpose of this comparison is to assess whether measurable differences can be observed between the CPTs at different distances before and after drilling.

First, the measured cone resistance and sleeve friction are compared in Figures 4.3. The figure shows the CPT measurements before and after drilling plotted on the same axes. Before drilling, the cone resistance profiles follow a similar trend with depth. Larger local differences mainly occur near layer transitions, where small spatial variations in the position or thickness of soil layers can result in differences between the CPTs. The sleeve friction profiles show more scatter than the cone resistance profiles, which is in line with the more sporadic character of sleeve friction measurements reported by (Robertson, 2010a). The measurements after drilling show a similar overall pattern. The most notable

difference is observed in the sand layer below approximately -20 m NAP, where the cone resistance is higher, suggesting a locally stronger sand layer.

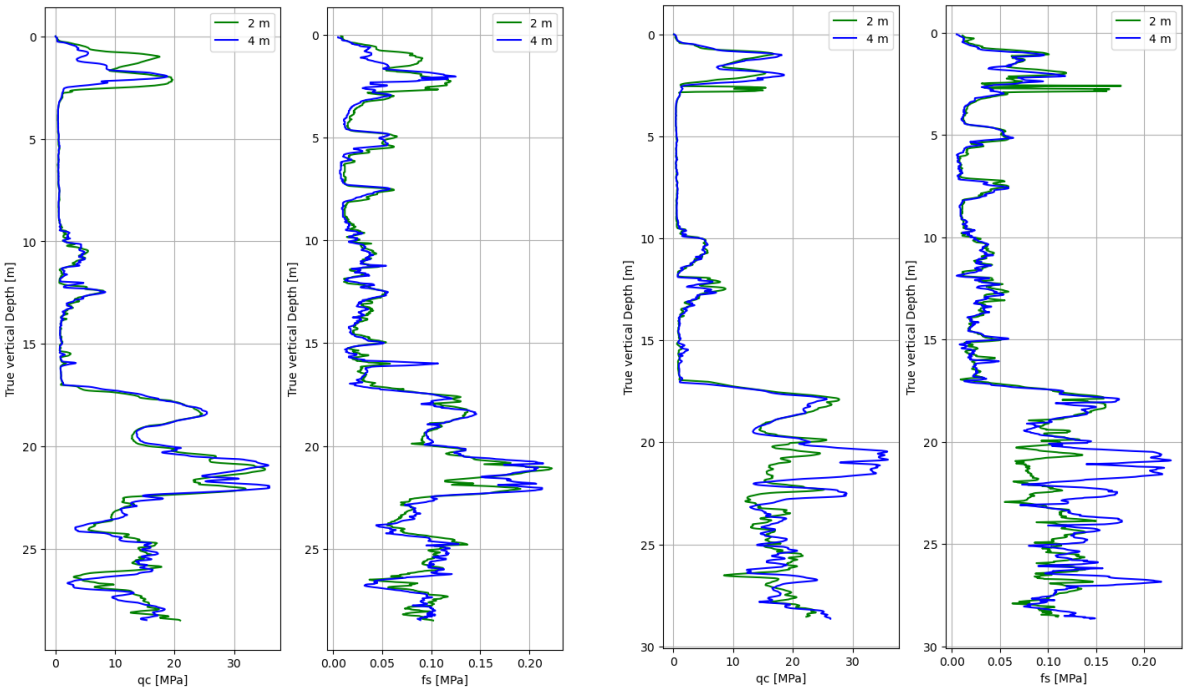

(a) Before drilling **(b)** After drilling

Figure 4.3: Cone resistance q_c and sleeve friction f_s profiles before and after drilling at distances of 2 m and 4 m from the borehole centre.

Figure 4.4 presents the differences in cone resistance between selected CPT measurements before and after drilling. The upper row compares the CPTs at 2 m and 4 m distance from the borehole centre before and after drilling, while the lower row compares selected before and after combinations. In general, the differences in cone resistance are not large enough to alter the soil classification. Larger local differences mainly occur near transitions between organic, clayey and sandy layers, where small differences in layer boundary depths can lead to relatively large cone resistance differences.

Figure 4.4d shows a local reduction in cone resistance in the foundation pile sand layer of CPT2-2 around a relative depth of 20 m. At approximately the same depth, CPT2-4 shows relatively high cone resistance. This could initially suggest a borehole-induced change, since CPT2-2 is located closer to the borehole. However, a similar local difference is also observed comparing CPT2-4 to the two measurements CPT1-2 and CPT1-4 before drilling, indicating that the contrast is mainly related to the locally higher cone resistance in CPT2-4.

Figure 4.4d also shows a large difference between CPT1-2 and CPT2-2 around a depth of 20 m. Table 4.2 presents the relative densities for different depth intervals within the foundation pile sand layer, calculated using the Robertson method described in Subsection 3.1.6 with respect to the Ottawa sand. The results show a clear relation between relative density and cone resistance. In the interval depth of 20 to 22.5 m, CPT2-2 has a lower relative density than the other measurements, corresponding to its lower cone resistance. Above a 20 m depth, the after-drilling measurements show slightly higher relative density, while below 22.5 m depth the relative densities are nearly identical.

The locally lower cone resistance in CPT2-2 could therefore initially suggest an effect of nearby drilling. However, when the full depth interval is considered, the difference is better explained by local variation in relative density within the sand layer. The local difference from 20 to 22.5 m depth is therefore interpreted as spatial variability rather than clear evidence of borehole-induced disturbance. Appendix B.2 presents the cone resistance differences between CPT1-4 and the measurements after drilling.

Considering their distance and variability in soil they were not deemed important for the comparison in this section.

The corresponding sleeve friction differences are provided in Appendix B.3. These results show similar general trends to the cone resistance, but with larger relative fluctuations because sleeve friction is more sensitive to local measurement variability.

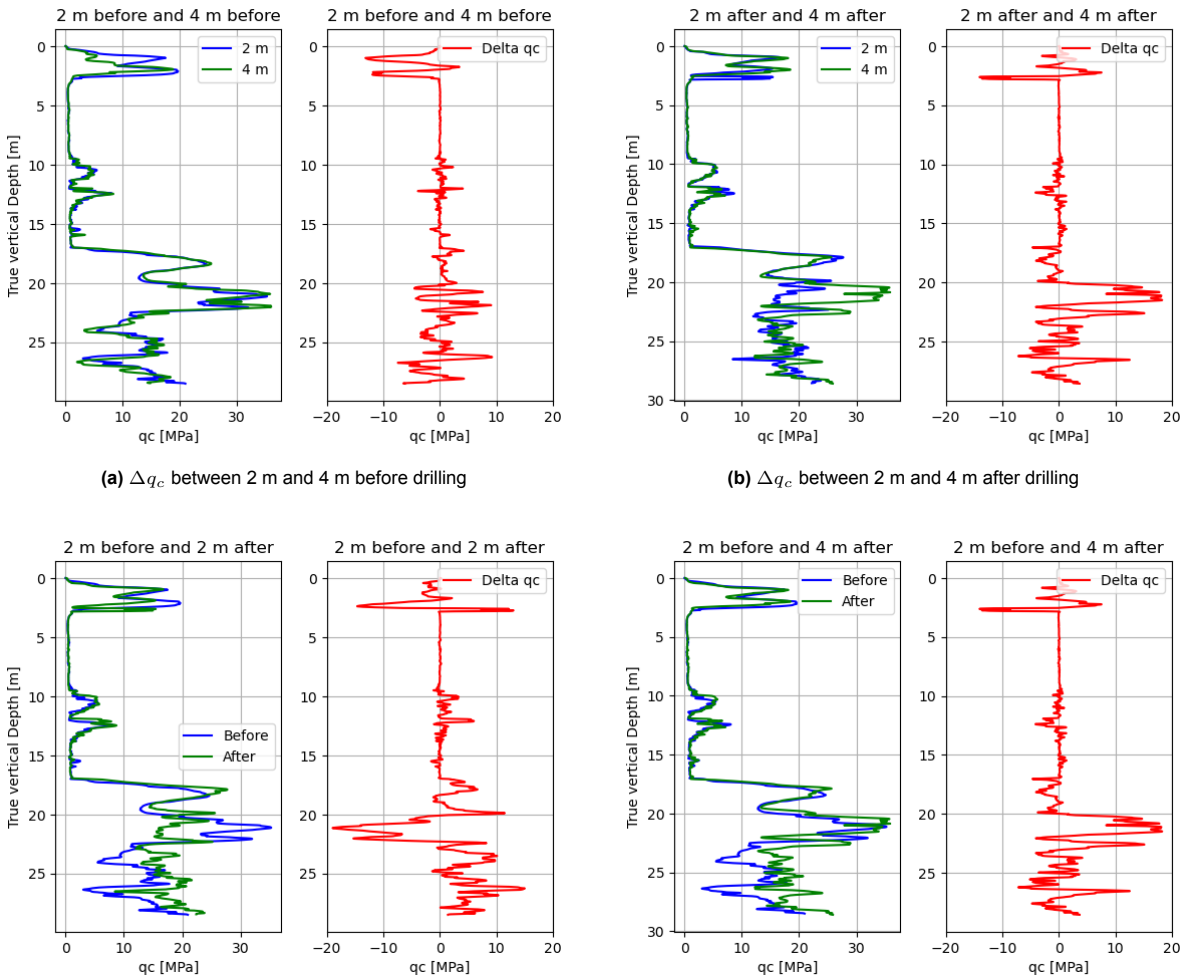

(a) Δq_c between 2 m and 4 m before drilling

(b) Δq_c between 2 m and 4 m after drilling

(c) Δq_c between 2 m before and 2 m after drilling

(d) Δq_c between 2 m before and 4 m after drilling

Figure 4.4: Comparison of cone resistance differences before and after drilling. The upper row shows the difference between CPT measurements at 2 m and 4 m from the borehole centre before and after drilling. The lower row shows before–after differences for selected measurement locations.

Table 4.2: Relative density, with respect to Ottawa sand, over different true vertical depth intervals in the foundation sand layer using the Robertson method.

Measurement	< 20 m [%]	20 to 22.5 m [%]	> 22.5 [%]
CPT1-2	47	66	63
CPT1-4	47	67	63
CPT2-2	51	57	60
CPT2-4	53	67	62

The analysis is then narrowed to the foundation pile sand layer. Whereas the previous figures evaluate variations in cone resistance over depth, the following boxplots summarise the distribution of corrected

cone resistance normalised by atmospheric pressure, q_t/p_a, within the sand layers identified in this interval. The average soil parameters over the full depth of this layer are presented in Table 4.1. This parameter is important because it is used in the Robertson soil behaviour type classification and indicates the consolidation state and soil type.

Figure 4.5 shows that the combined sand layers of CPT1-2 and CPT1-4 have similar median and mean values. The combined values of CPT2-2 and CPT2-4 are slightly higher, although they remain within a comparable range to the measurements before. For CPTs with multiple identified sand layers, the variation is mainly caused by one or two layers with slightly higher or lower normalised cone resistance, while the remaining layers show comparable values.

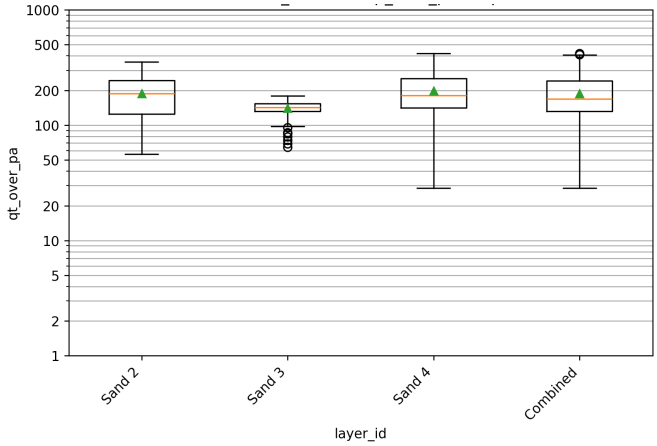

(a) Boxplot of q_t/p_a for the pile-carrying sand layer at CPT1-2.

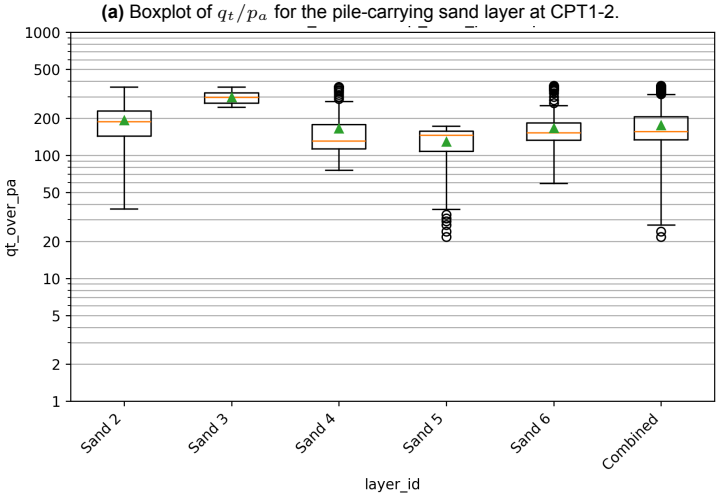

(b) Boxplot of q_t/p_a for the pile-carrying sand layer at CPT1-4.

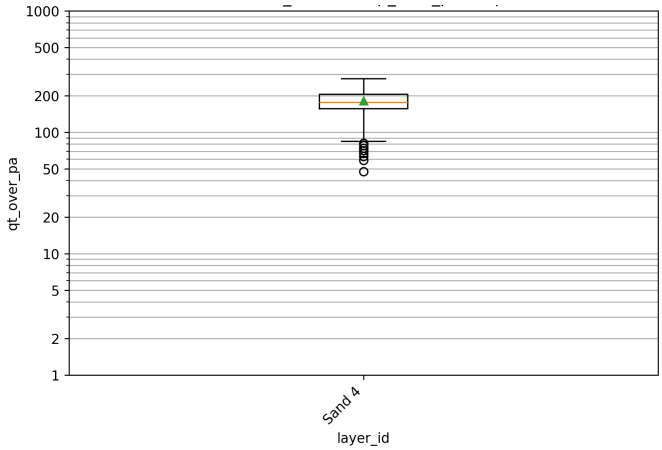

(c) Boxplot of q_t/p_a for the pile-carrying sand layer at CPT2-2.

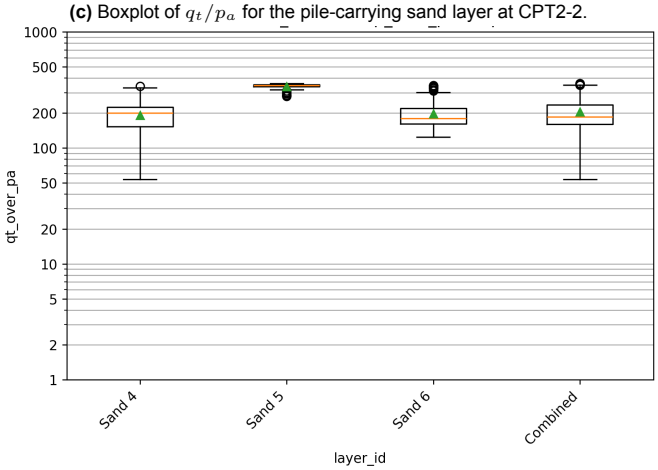

(d) Boxplot of q_t/p_a for the pile-carrying sand layer at CPT2-4.

Figure 4.5: Boxplots of normalised cone resistance q_t/p_a for the pile-carrying sand layer at the four CPT locations.

Finally, the Robertson classification is used to compare the soil behaviour type of the selected sand layer. In Figure 4.6, all measured points within the pile foundation sand layer have been plotted. Each CPT measurement is shown with a different colour. The cross represents the mean value, while the ellipse marks the 68.3% confidence interval. The mean values of the four measurements are close to each other, making it difficult to distinguish between the points. All the mean values and a majority of the measured points fall within the normally consolidated region of the Robertson chart.

The orientation of the confidence ellipses differs slightly between the measurements before and after drilling. The ellipses for the measurements after drilling are slightly more tilted and smaller, indicating that the friction ratio varies more for small changes in normalised cone resistance and that the measured points are more concentrated around the mean. A slight reduction in R_f is also observed for CPT2-2, which is likely influenced by the lower relative density over the depth interval from -20 m to -22.5 m NAP. Because the mean values are close to each other and the points remain within the same soil behaviour region, this difference is not considered sufficient evidence of a systematic change in soil behaviour.

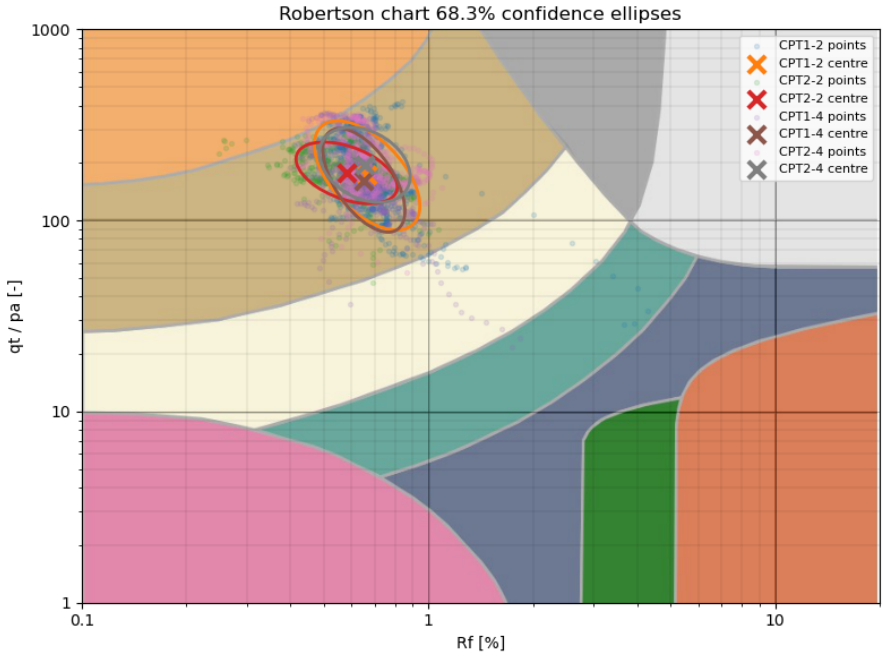

(a) Robertson chart with 68.3% confidence ellipses.

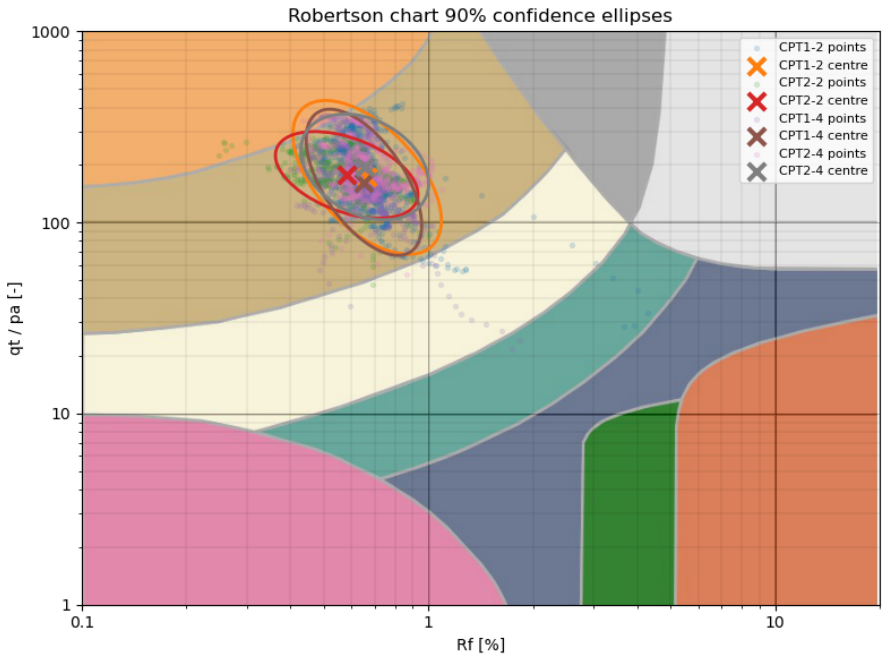

(b) Robertson chart with 90% confidence ellipses.

Figure 4.6: Robertson classification for the selected foundation pile sand layer using 68.3% and 90% confidence ellipses.

CPT2-2 and CPT2-4 deviate slightly from the measurements before drilling in both the orientation of the confidence ellipses and the location of the mean values. The mean points are positioned slightly differently, indicating small differences in the soil behaviour of the foundation pile sand layer after drilling. However, the observed shift does not indicate a weaker sand response. Instead, the measurements after drilling show a slightly stronger sand layer, which is also consistent with the derived soil parameter values.

Although this difference could initially be interpreted as a possible effect of borehole installation, due to the different direction of strengthening of the two measurements, no strong conclusion can be drawn

from this observation. If the deviation were caused directly by the borehole installation, a clearer difference would be expected in the same direction between the CPT at 2 m distance and the CPT at 4 m distance. Since both CPT2-2 and CPT2-4 show a slightly stronger response, the observed difference is more likely related to natural spatial variability within the sand layer than to a local disturbance caused by the borehole.

This highlights an important limitation of comparing CPT measurements at different locations. Although the CPTs were performed at comparable distances from the borehole, they do not measure the exact same soil volume. Local differences in soil composition, cone resistance and layer boundaries can therefore influence the Robertson classification. For this reason, small local deviations in the mean points should not be interpreted as direct evidence of borehole-induced soil disturbance. The use of a confidence ellipse is therefore highly recommended to observe similarities in area.

Overall, the Robertson charts show that the mean values of the CPT measurements are close to each other and that the measured points fall within the same normally consolidated region. Together with the limited variation in cone resistance, sleeve friction and normalised cone resistance, this indicates that no major adverse changes in soil stratification or material properties are observed in the foundation pile sand layer at a distance of 2 and 4 m from the borehole. Therefore, based on the available CPT data, the borehole installation does not appear to have caused a clearly measurable weakening or disturbance of the surrounding sand layer at this distance.

Additional Robertson charts for all measured soil layers before and after drilling are provided in Appendix B.5 and B.6. These figures show that differences between individual layers can occur due to natural variability, as the soil profile is not homogeneous.

4.1.4. Relative density

The relative density and corresponding void ratio, with respect to Ottawa sand e_{min} and e_{max}, were derived for both the first sand layer and the foundation-bearing sand layer using the Robertson and Cabal (2023) and Baldi et al. (1986) methods described in Chapter 3. The results are presented in Tables 4.3 and 4.4. The comparison shows that the derived sand state depends strongly on the selected processing methodology, especially for the first sand layer.

Table 4.3 shows that the Robertson method gives void ratios of approximately 0.69 to 0.71 for the foundation-bearing sand layer. These values are close to the reference void ratio of the Ottawa sand used in the SANISAND simulations. This indicates that, for the sand layer at pile foundation depth, the Robertson method gives a soil state that is comparable to the sand state adopted in the numerical model.

For the first sand layer, however, the Robertson method gives very high relative density values and correspondingly low void ratios. The calculated relative densities exceed 100% for all CPTs, with void ratios ranging from approximately 0.32 to 0.54. Although a dense state may be expected in the shallow sand layer, these values are remarkably low and should therefore be interpreted with caution. A very low void ratio implies a very dense sand state, which would generally be expected to correspond with high cone resistance values. Since the cone resistance response of the first sand layer does surpass the values of deeper soil layers, the Robertson-derived void ratios for this layer are considered uncertain.

Table 4.3: Comparison of relative density and void ratio for the first sand layer and foundation-bearing sand layer at the different CPT locations using Robertson method.

Measurement	Sand layer	Relative density, D_r [%]	Void ratio, e [-]
CPT1-2	First	155	0.38
CPT1-2	Foundation	50	0.71
CPT1-4	First	101	0.54
CPT1-4	Foundation	50	0.71
CPT2-2	First	156	0.38
CPT2-2	Foundation	54	0.69
CPT2-4	First	175	0.32
CPT2-4	Foundation	55	0.69
SANISAND input	Foundation	56.3	0.686

The Baldi method gives different results. As shown in Table 4.4, the first sand layer obtains lower relative densities and higher void ratios than with the Robertson method. These values appear more realistic for the shallow sand layer. However, for the foundation-bearing sand layer, the Baldi method gives void ratios of approximately 0.61 to 0.65, which are lower than the reference void ratio used for the Ottawa sand in the SANISAND model.

Table 4.4: Comparison of relative density and void ratio for the first sand layer and foundation-bearing sand layer at the different CPT locations using Baldi method.

Measurement	Sand layer	Relative density, D_r [%]	Void ratio, e [-]
CPT1-2	First	109	0.52
CPT1-2	Foundation	70	0.64
CPT1-4	First	74	0.63
CPT1-4	Foundation	69	0.65
CPT2-2	First	105	0.53
CPT2-2	Foundation	78	0.62
CPT2-4	First	121	0.49
CPT2-4	Foundation	80	0.61
SANISAND input	Foundation	56.3	0.686

The comparison therefore shows a clear methodological uncertainty. The Baldi method gives more plausible results for the first sand layer, whereas the Robertson method gives results that are closer to the Ottawa sand state for the foundation-bearing sand layer. Since the numerical analysis mainly focuses on the behaviour of the foundation-bearing sand layer around the borehole, the Robertson method is selected for the final interpretation of the sand state.

This choice does not imply that the Robertson method is more accurate for all sand layers. Rather, it provides the most consistent basis for the numerical model at the depth range that is most relevant to this research. The uncertainty in the exact in-situ relative density remains important, but is partly addressed by performing the SANISAND simulations for different relative densities.

4.1.5. Derived horizontal stress

The horizontal stress in the soil is an important parameter for pile foundations, as the generated skin friction along a pile depends on the normal stress acting on the interface. A higher horizontal stress results in a higher interface shear resistance, whereas a reduction in horizontal stress may reduce the mobilised skin friction. Therefore, estimating the horizontal stress in the foundation pile sand layer is important for evaluating the possible effects of borehole installations on nearby foundation piles.

Two empirical approaches were used to estimate the horizontal stress over depth: the K_0 method and the Ahmadi-Golestani method. The K_0 method estimates the horizontal stress from the vertical effective stress and an assumed coefficient of earth pressure at rest. The Ahmadi-Golestani method

uses CPT-based input parameters and calibrated figures to determine effective horizontal stress. Both methods were evaluated to assess whether they provide a suitable estimate of the horizontal stress in the foundation pile sand layer.

Figure 4.7 shows the horizontal stress profile in the foundation pile sand layer according to the K_0 method. The calculated stress profile increases linearly with depth. This is expected, as according to this methodology horizontal stress is directly related to the vertical stress. Since the unit weight and the assumed K_0 value are constant within the selected sand layer, the resulting horizontal stress profile follows a linear trend.

Although the K_0 method gives an estimate of the initial stress state, it is not able to represent the actual stress distribution caused by borehole installation. The method assumes soil at rest and does not account for stress changes around a cylindrical opening. However, the installation of a vertical borehole disturbs the stress field locally, which means that the horizontal stress σ_h at a certain distance from the borehole is expected to converge to undisturbed conditions. The K_0 method should therefore be interpreted as a reference initial stress condition, rather than a direct estimate of the post-installation horizontal stress around the borehole.

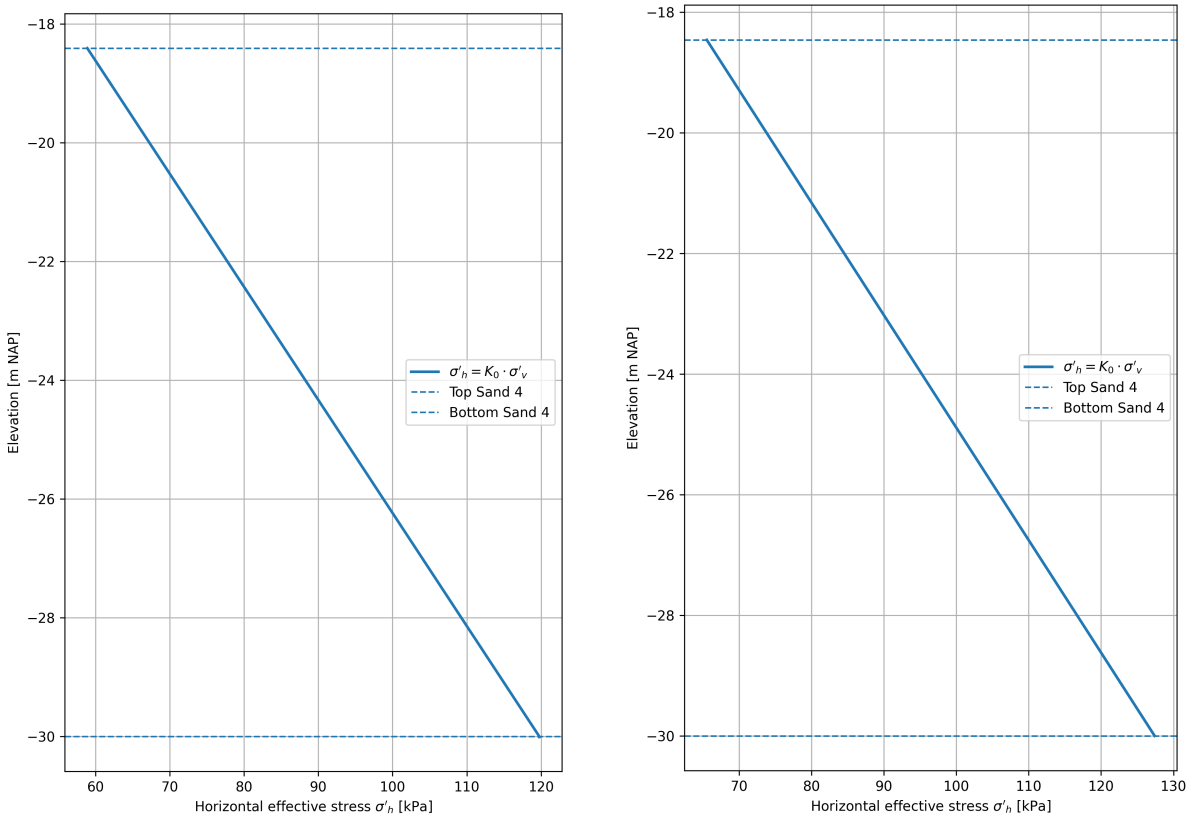

(a) CPT2-2 horizontal stress in the foundation pile sand layer according to the $K0$ method.

(b) CPT2-4 horizontal stress in the foundation pile sand layer according to the $K0$ method.

Figure 4.7: Horizontal stress development for CPT2-2 and CPT2-4 according to $K0$ method.

The Ahmadi-Golestani method was applied at the same depths as the numerical model extraction points. This allows the calculated stresses to be compared directly with the stress levels extracted from the numerical simulations. Table 4.5 presents the results for CPT2-2.

At the first selected depth of -21.77 m, the ratio between the vertical effective stress and the effective horizontal stress is close to the value obtained from the K_0 estimate. At -24.7 m NAP, the calculated horizontal effective stress reaches its lowest value. This result is likely caused by the sensitivity of the method to sleeve friction and relative density. At the next depth of -27.77 m, the effective horizontal stress increases, but remains lower than at the first depth. This is physically not realistic for a soil.

In general, the effective horizontal stress is expected to increase with depth, following the increase in vertical effective stress. The calculated reduction in horizontal effective stress with depth therefore indicates that the Ahmadi-Golestani method is not robust for the selected CPT2-2 input points.

From figures in the report the relative density can also be determined. The average calculated relative density values for CPT2-2 are 6% above the relative densities obtained using the Baldi method, as shown in Table 4.4. This indicates that the relative density estimate itself is not the main source of the problem. Instead, the unrealistic horizontal effective stress is mainly caused by the sensitivity of the method to cone resistance and sleeve friction values. This sensitivity is important because sleeve friction measurements are generally more scattered than cone resistance measurements. This was also observed by Ahmadi and Golestani Dariani (2017), who found that the agreement for sleeve friction was less strong than for cone tip resistance.

Table 4.5: Calculated horizontal stress values for CPT2-2 using the analytical Ahmadi Golestani method

Depth NAP (m)	q_c (MPa)	f_s (kPa)	σ'_{v0} (kPa)	D_r (%)	σ'_{h0} (kPa)
-21.77	19.94	84	153.10	78	84
-24.77	18.63	120	184.60	85	36
-27.77	17.19	124	216.10	80	56

Table 4.6 presents the corresponding results for CPT2-4. The first selected depth, the calculated horizontal effective stress is lower than the value obtained from the K_0 estimate, despite the relatively high cone resistance and sleeve friction measured at this depth. At the second selected depth, the calculated horizontal effective stress is approximately half of the value obtained at the first depth, even though the measurement point is located 3 m deeper. At the final selected depth, the calculated value increases again and becomes slightly higher than the first value, but remains well below the value obtained from the K_0 estimate.

This trend in effective horizontal stresses is physically not possible. Horizontal effective stress is expected to increase with depth. These values are a result of the sensitivity in the method linked to cone resistance and sleeve friction. Variations in cone resistance and sleeve friction can occur within soil bodies, even if it is the same soil type. This makes it difficult to predict induced horizontal stress conditions in soils. Another limitation of the method is that it was developed for sandy soils under controlled calibration chamber and numerical modelling conditions. Although the method is applicable for sand, the sands detected at depths of -20 m NAP are not homogeneous and may have local variations in void ratio, relative density and stress history. These parameter changes have a significant effect on the resulting horizontal stress.

The calculated relative density for CPT2-4 has an average of 84%. This value is 10% higher than the average obtained from the Baldi method and considerably higher than that of the Robertson method. Since the Baldi and Robertson methods are more commonly used for relative density estimation, the Ahmadi-Golestani relative density values for CPT2-4 appear unrealistically high. Compared with CPT2-2, the CPT2-4 values deviate more strongly from the other methods. This further questions the suitability of the Ahmadi-Golestani method for the selected CPT measurements.

Table 4.6: Calculated horizontal stress values for CPT2-4 using the analytical Ahmadi Golestani method

Depth NAP (m)	q_c (MPa)	f_s (kPa)	σ'_{v0} (kPa)	D_r (%)	σ'_{h0} (kPa)
-21.78	35.76	188	166.67	98	60
-24.78	15.37	121	198.92	83	28
-27.78	14.13	98	231.00	73	64

Furthermore, the Ahmadi-Golestani method estimates the initial horizontal stress state of the sand from CPT measurements. It does not account for the radial and hoop stress redistribution caused by the installation of a vertical borehole. This distinction is important for this research, because the horizontal stress is required to evaluate the possible mobilised skin friction along the pile or borehole interface. Since borehole installation locally changes the stress field, a CPT based estimate of the initial in-situ horizontal stress cannot directly represent the post-installation horizontal stress around the borehole. A CPT based methodology to determine such effects has still to be developed.

The comparison of the two methods shows that neither approach provides a fully reliable determination of the horizontal stress state around the borehole after drilling. The K_0 method gives a stable reference stress state, but only represents undisturbed at rest conditions. The Ahmadi-Golestani method is more directly linked to the CPT measurements, but the results are sensitive to local CPT variability and can become unrealistic, as observed for CPT2-2 and CPT2-4. Therefore, the calculated horizontal stresses should be interpreted as indicative values rather than direct measurements of the post-installation horizontal stress state.

For the numerical model, the K_0-based horizontal stress is considered the more suitable reference initial condition. This does not mean that the K_0 method captures the actual stress redistribution around the borehole, but it provides a stable and physically consistent initial stress state. The uncertainty in the horizontal stress remains important, especially because the mobilised skin friction depends on the normal stress acting on the interface.

4.2. Numerical model stress distribution

This section presents the results for the numerical model analysis using the methodology described in Section 3.2. The results include the Linear-elastic model, Mohr-Coulomb model, SANISAND model, comparison between models, borehole radius influence, vertical stress, alternating void ratios and the critical void ratio of Ottawa sand.

4.2.1. Linear-Elastic

Figure 4.8 shows the hoop and radial stress at -24.78 m NAP for the linear-elastic model. The results show that reducing the borehole pressure leads to a reduction in the radial stress and an increase in the hoop stress close to the wall. The greatest differences in stress from the far-field are situated closest to the wall and gradually converge back with distance. The convergence to the far-field is found at a distance of five times the normalised radius.

The radial stress does not reach exactly zero in the final unloading phase. This is because the closest extraction point is located 0.02 m away from the borehole wall rather than on the boundary in order to avoid numerical errors. At the extraction point the Kirsch solution predicts a radial stress of 7 kPa, which explains why the numerical result does not reduce fully to zero.

The numerical results closely follow the Kirsch solution for both hoop and radial stress. This shows that the linear-elastic calculation gives the expected elastic stress redistribution around the borehole. It also supports the correct stepwise reduction of the borehole back pressure in each phase. The same can be observed from the results at other depths presented in Appendix C.1.

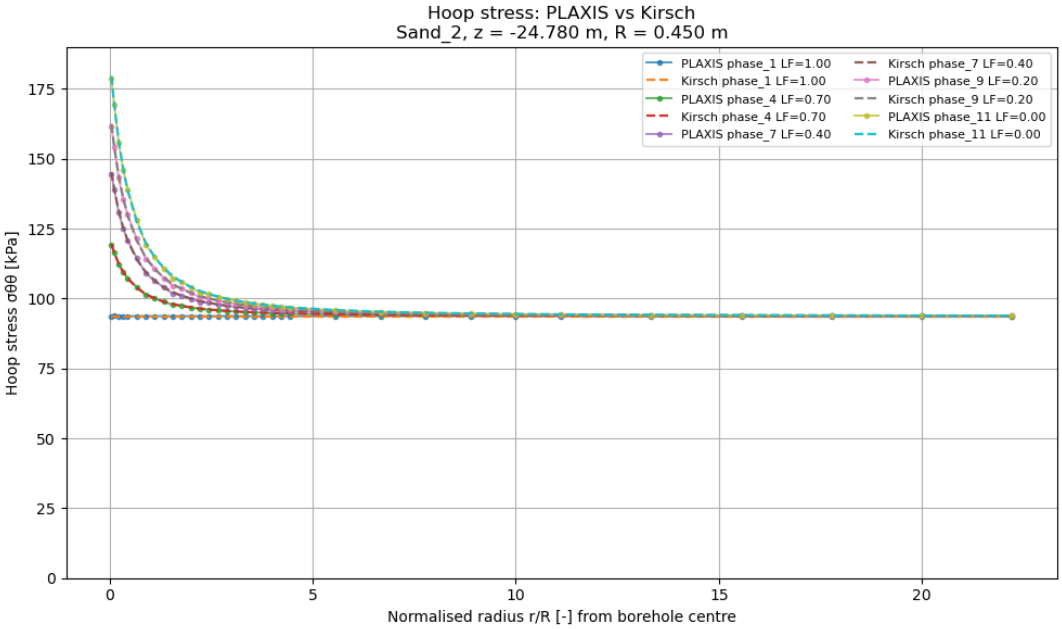

(a) Hoop stress at -24.78 m NAP compared to the Kirsch solution.

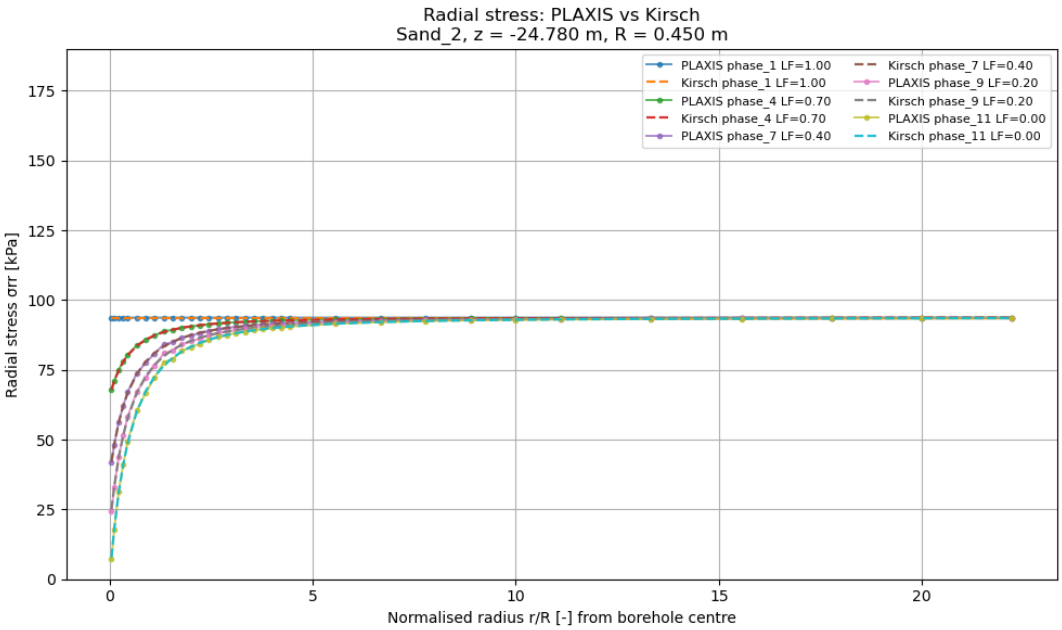

(b) Radial stress at -24.78 m NAP compared to the Kirsch solution.

Figure 4.8: Hoop and radial stress at -24.78 m NAP for Linear-Elastic model compared to the Kirsch solution.

Figure 4.9 portrays the hoop and radial strains at -24.78 m NAP for the linear-elastic model. The strain response follows the same pattern as the stress distribution. The reduction in radial stress and increase in hoop stress are accompanied by positive strain in the form of expansion and negative strain for compaction respectively. The largest strain occurs close to the wall and rapidly converges to zero, which it reaches before ten times the normalised radius.

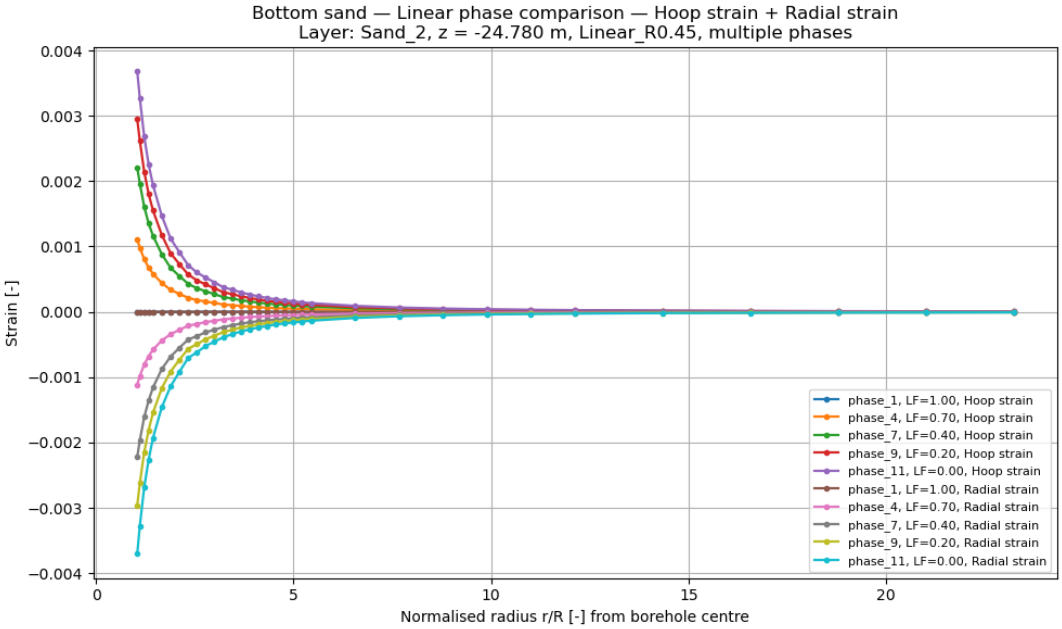

Figure 4.9: Hoop and radial strain at -24.78 m NAP for Linear-Elastic model.

No shear stress results are presented for the linear-elastic model. The finite element output showed only very small shear stress values, which fluctuated between positive and negative values. These values were therefore interpreted as numerical noise. Since the soil in the finite element method does not contain horizontal variation in properties or initial stress state, no meaningful shear stress development is generated or expected in the linear-elastic calculation.

The main limitation of the linear-elastic model is that it cannot represent yielding or plastic deformation of the soil. The stress and strain response is proportional regardless of the magnitude of loading or unloading. As a result, stresses and strains will continue to increase or decrease, without accounting for failure or dilatancy. Therefore the linear-elastic model is useful for a fast calculation of stresses and strains, but it is not sufficient to represent realistic behaviour of sand around a borehole during drilling.

4.2.2. Mohr-Coulomb

Figure 4.10 shows the hoop and radial stress at -24.78 m NAP for the Mohr-Coulomb model. The results should be interpreted phase by phase, as the model first responds elastically and eventually in a plastic manner once the stress state reaches the Mohr-Coulomb yield criterion. In the early unloading phases, phase 4 and 7, the stress developed is similar to that of the linear-elastic model. Hoop stress increases close to the wall, while radial stress decreases.

This elastic response changes once the plasticity develops near the borehole wall. In later unloading phases, the hoop stress close to the borehole wall reduces compared with the linear-elastic result. Instead of reaching its maximum directly at the borehole wall, the hoop stress starts at a lower point and increases with distance from the borehole, reaching a maximum further away from the wall, and then gradually converging back to the far-field stress field at ten times the normalised radius. This indicates that yielding near the borehole reduces the stresses near the borehole wall and shifts the maximum hoop stress away.

The size of the affected zone also increases as the borehole pressure is reduced. This is expected, as a larger reduction in radial support causes a larger part of the soil around the borehole to reach the yield criterion. Furthermore, Appendix C.2 shows that the distance at which the stresses converge to the far-field value appears to remain constant across the three selected depth points. The radial stress development remains more similar to the linear-elastic result. However, the hoop stress response clearly shows the influence of plasticity.

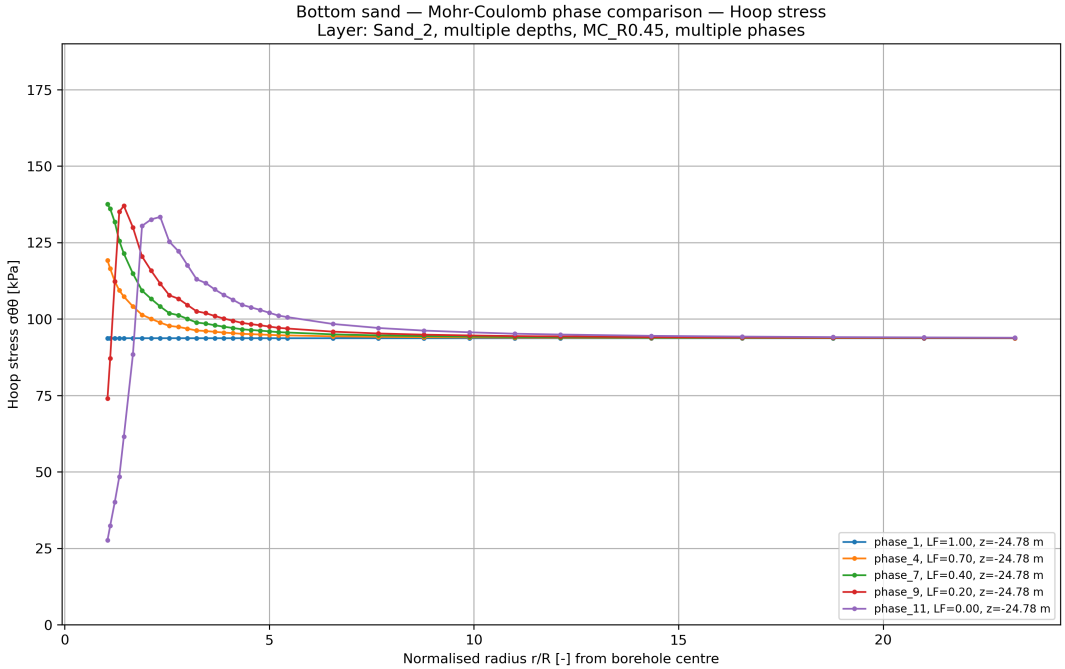

(a) Hoop stress at -24.78 m.

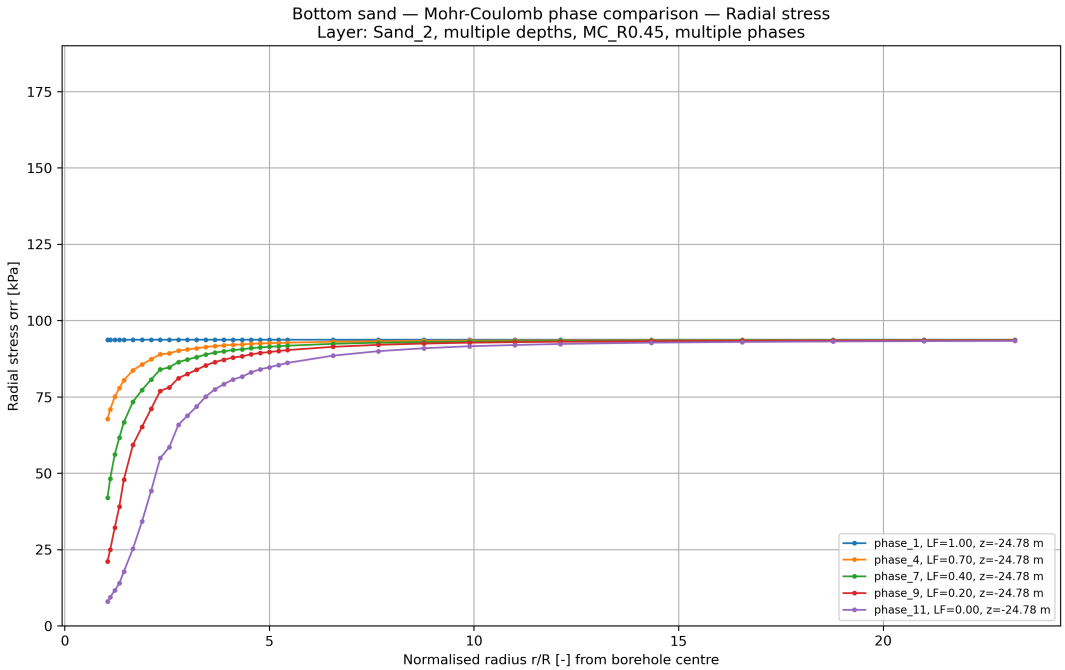

(b) Radial stress at -24.78 m NAP.

Figure 4.10: Hoop and radial stress at -24.78 m NAP for Mohr-Coulomb model.

Figure 4.11 shows the radial and hoop strain development at -24.78 m NAP for the Mohr-Coulomb model. The strain results show the same transition from elastic to plastic behaviour as observed in the stress development. In the early unloading phases, phases 4 and 7, the strain response is elastic. The radial and hoop strains develop in opposite directions and are of comparable magnitude.

This behaviour changes in phases 9 and 11, where larger strains develop close to the borehole. At this stage, the stress state has reached the Mohr-Coulomb yield criterion and plastic deformation occurs. Once yielding starts, additional unloading no longer results only in recoverable elastic strain, but also

in irreversible plastic strain. This explains why the strain magnitudes increase more strongly than in the linear-elastic model. For example, in phase 7 the maximum positive strain reaches approximately 0.006, compared with approximately 0.003 in the linear-elastic model. In contrast to the linear-elastic model, there is a difference in size between radial and hoop strain. As depicted, the radial strain is greater than the hoop strain. Similar to the stress development, the strain levels converge to zero at a distance of ten times the normalised radius.

The larger strain response is consistent with the elastic-perfectly plastic formulation of the Mohr-Coulomb model. Before yield, stress and strain are linked through the elastic stiffness parameters. After yield, the soil strength is limited by the friction angle, cohesion and dilation angle. Further loading or unloading results in plastic strain development. As a result, the model can show larger local deformations around the borehole than the linear-elastic model, even when the radial stress development appears similar.

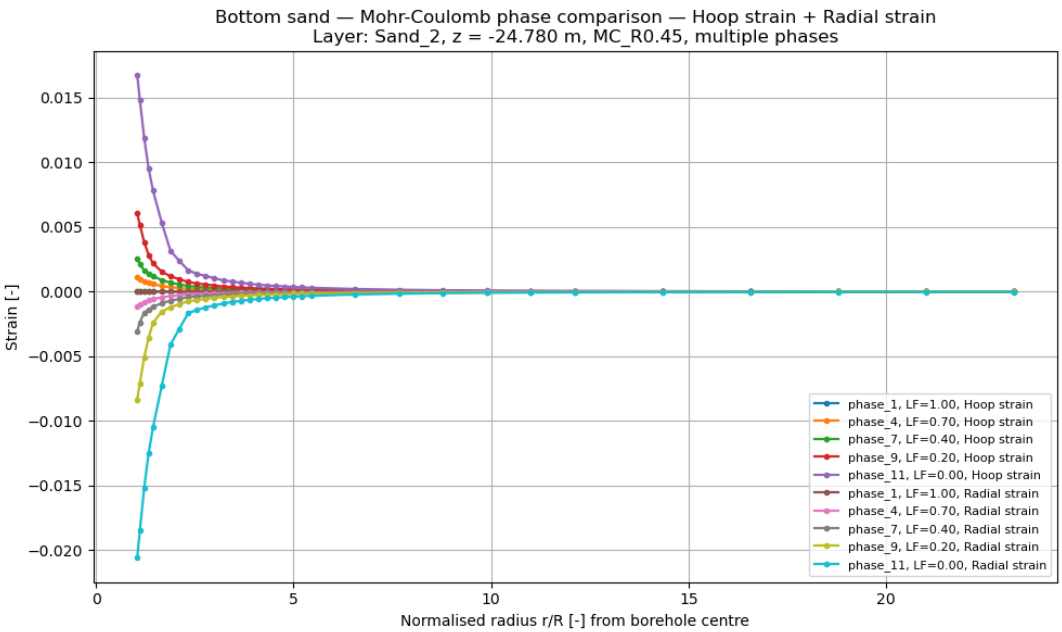

Figure 4.11: Hoop and radial strain at -24.78 m NAP for Mohr-Coulomb model.

Compared with the linear-elastic model, the Mohr-Coulomb model gives a more realistic response simulating yielding and plastic strain development. Nevertheless, it remains an idealised constitutive model. After yielding, the response is governed by an elastic-perfectly plastic failure criterion and does not include more advanced sand behaviour such as stress-dependent stiffness, state-dependent dilatancy or hardening. Therefore, the Mohr-Coulomb model is useful for identifying the development of a plastic zone around the borehole, but it should not be interpreted as a complete representation of the sand response.

Stress and strain development at different depths can be found in Appendix C.2.

4.2.3. SANISAND

Figure 4.12 shows the radial and hoop stress development at -24.78 m NAP for the SANISAND model. The stress response differs from both the linear-elastic and Mohr-Coulomb models. The maximum hoop stress remains lower than in the other models and does not exceed 125 kPa. This indicates that the stress concentration near the borehole is limited by the non-linear sand response in the SANISAND model.

For the radial stress, phase 4 follows a response that is similar to the linear-elastic model. Phase 7 appears to have reached plasticity, resulting in a higher hoop stress away from the borehole wall. In phase 9, the hoop stress shows a lower starting point as the borehole pressure is reduced, shifting the

peak stress further away from the borehole wall. In phase 11, where the borehole back pressure is fully removed, the radial stress at the borehole wall reduces to zero. Following the trend, the distance to the peak stress from the borehole wall increases and so does the distance to far-field convergence. This convergence occurs at approximately ten borehole radii from the borehole centre. Although a small stress difference remains at this distance, it is considered limited.

The hoop stress response shows a clear transition between the unloading phases. Phase 4 still has a shape that is close to the linear-elastic response, with the largest hoop stress occurring at the borehole wall. In phase 7, the hoop stress no longer starts with the highest value at the borehole wall. Instead, the hoop stress starts slightly higher than in phase 4, increases slightly with distance, reaches a maximum further away from the borehole, and then decreases towards the far-field value. This behaviour becomes more pronounced in phases 9 and 11. In phase 9, the hoop stress starts from a lower value near the borehole wall than in phase 7, while in phase 11 the starting point is close to zero. Both phases then increase to approximately the same maximum value as in phase 7, although this maximum occurs at greater distances from the borehole in accordance with their lower initial stress levels. Eventually, after reaching the peak, the stress returns to the far-field value within ten times the normalised radius.

For the radial stress, the SANISAND model follows a similar trend to the Mohr-Coulomb model. The main difference is observed in phase 11, where the slope towards the far-field is less steep.

This behaviour is consistent with the SANISAND formulation. The response depends on the sand state, stress ratio, dilatancy and hardening behaviour. As unloading progresses, plastic strains develop around the borehole and the soil can no longer sustain local hoop stress concentration. The stress is therefore redistributed over a larger zone around the borehole.

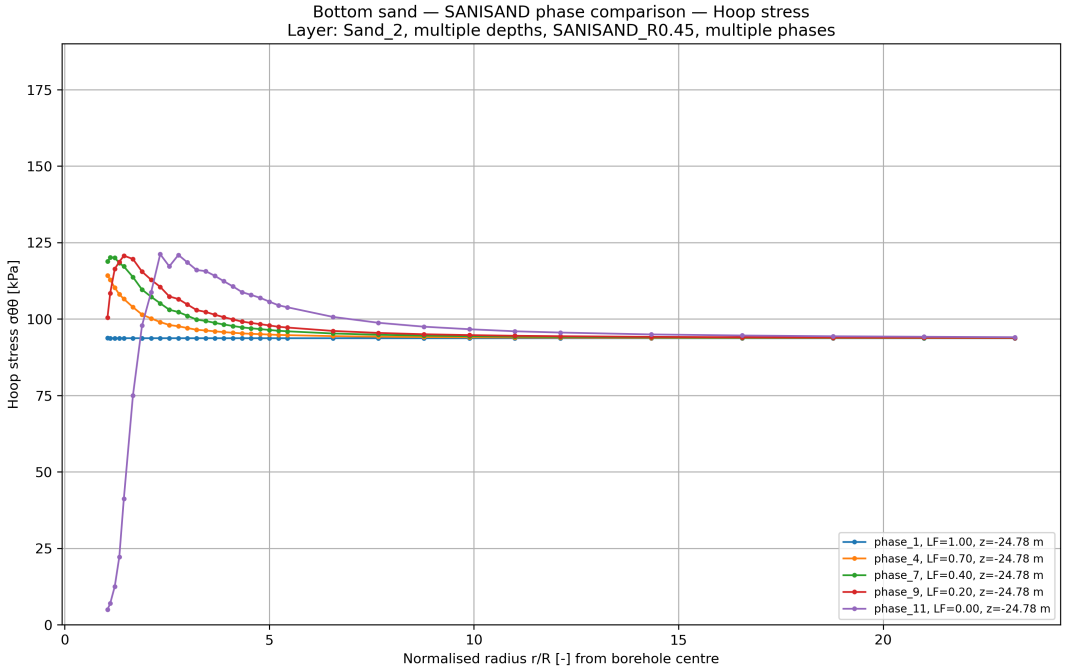

(a) Hoop stress at -24.78 m.

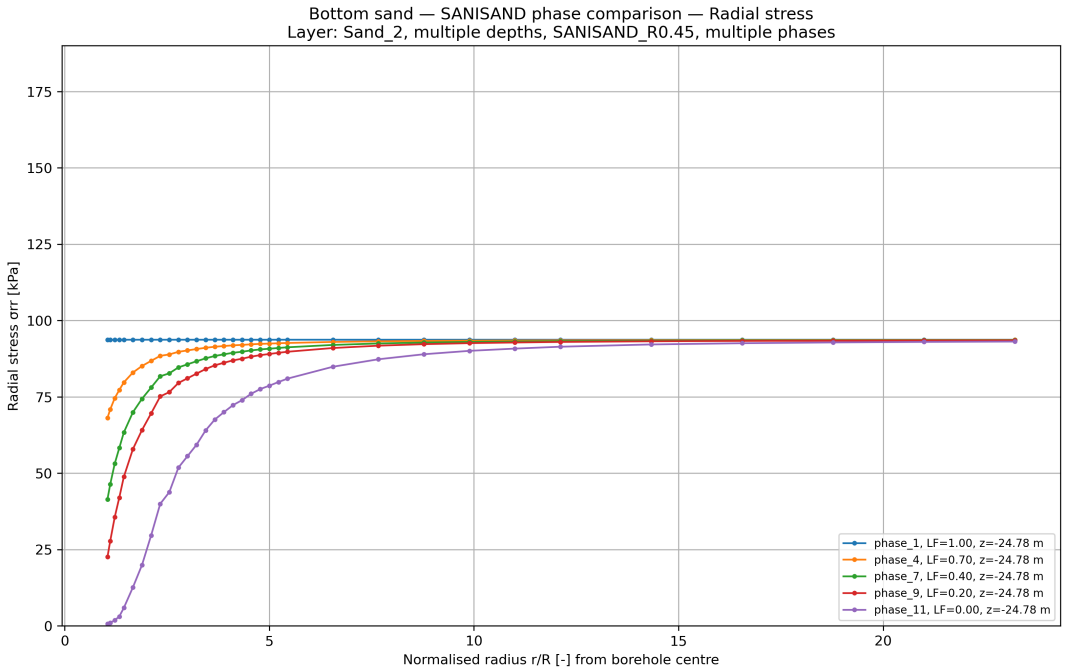

(b) Radial stress at -24.78 m NAP.

Figure 4.12: Hoop and radial stress at -24.78 m NAP for SANISAND model.

Figure 4.13 shows the hoop and radial strain development at a depth of -24.78 m NAP. Two important observations can be made from the figure. First, the strain increases rapidly between phases 9 and 11. From phase 4 to phase 9, the strain magnitude increases gradually, after which a clear increase occurs in phase 11. This indicates that the removal of the remaining borehole pressure causes a substantial additional deformation around the borehole.

The second observation is the difference in strain magnitude between the positive and negative directions. The SANISAND model predicts larger extensional strains than compressive strains. This

indicates that the deformation response is not symmetric during unloading. This extension is consistent with the dilative response of dense sand, where particle rearrangement during shearing can result in volume expansion and increased shear resistance. This is in line with the behaviour discussed by Grubben et al. (2025) in relation to sand dilation and the corresponding increase in shear stress.

The strain converges back to zero within five normalised radii from the borehole centre.

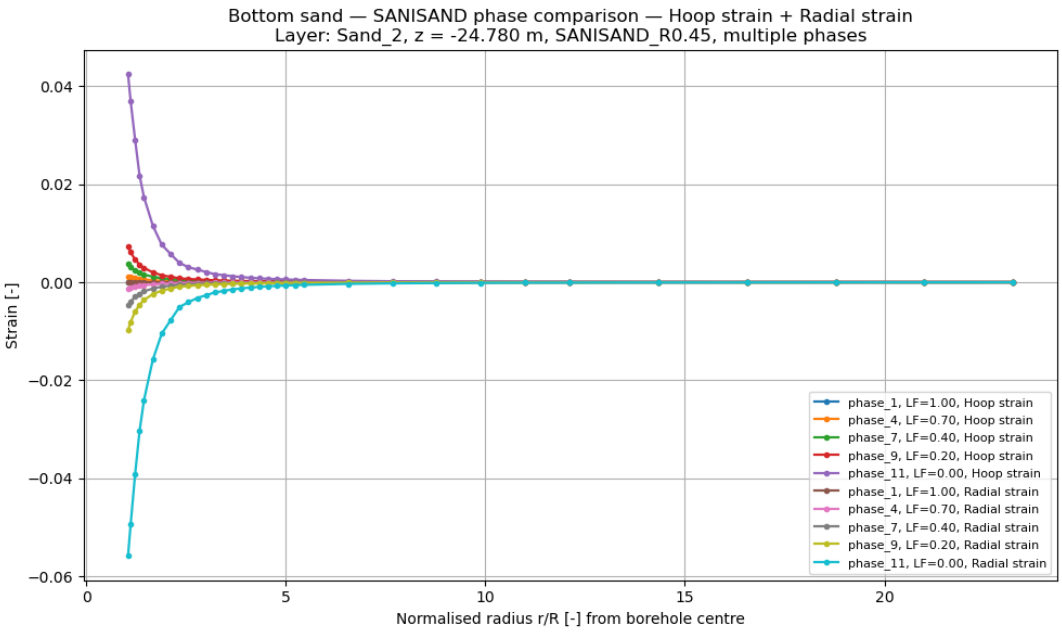

Figure 4.13: Hoop and radial strain at -24.78 m NAP for SANISAND model.

The SANISAND model includes a larger number of state-dependent parameters that influence the predicted sand behaviour during loading and unloading. Compared with the linear-elastic and Mohr-Coulomb models, SANISAND predicts larger strains around the borehole, while the maximum hoop stress remains lower. This indicates that the model redistributes the stresses over a wider zone instead of producing a high local stress concentration near the borehole.

The model may provide a more representative prediction of stress and strain development in sand, as it can account for non-linear sand behaviour. However, this also introduces practical limitations. The required parameters are more difficult to determine and generally require laboratory testing or careful calibration. In addition, the numerical calculations are more computationally demanding and require longer calculation times. Therefore, the SANISAND results are valuable for interpreting the possible stress redistribution around the borehole, but their reliability depends strongly on the quality of the input parameters.

4.2.4. Comparison between models

Figure 4.14 compares the hoop stress development for three constitutive models in back pressure reduction phases 7, 9 and 11. The phases were selected because the differences between the models become more pronounced during the later unloading stages. In the earlier phases, the Mohr-Coulomb and SANISAND models mainly respond elastically, resulting in smaller differences between the three.

In phase 7, the SANISAND model reaches a lower hoop stress than the linear-elastic and Mohr-Coulomb models. This suggests that stress redistribution has already started to develop around the borehole in the SANISAND model. The Mohr-Coulomb response remains closer to the linear-elastic result, although the maximum hoop stress is slightly lower. This indicates that the Mohr-Coulomb model may be approaching plastic behaviour. At larger distances from the borehole, the three models converge towards the same far-field stress.

In phase 9, differences between models become clearer. The linear-elastic model continues to show an

increasing hoop stress as borehole back pressure reduces. This response is consistent with the linear-elastic formulation, in which hoop stress increases proportionally to the decrease in radial stress and peaks at the borehole wall. The SANISAND model starts from a lower initial hoop stress, increases to a maximum further away from the borehole wall, and then gradually returns to the far-field value. Compared with phase 7, the location of the maximum hoop stress has shifted further away from the borehole wall. This indicates an expansion in the stress redistribution zone.

The Mohr-Coulomb model shows the largest change in hoop stress in phase 9. The hoop stress starts from a lower initial value near the borehole wall and increases to a higher maximum than in the SANISAND model. This results in a larger difference between the initial stress and the peak hoop stress. This difference in stress is accompanied by a shift of the stress peak away from the borehole wall. This follows from the development of plasticity in the model, where yielding causes stress redistribution close to the borehole wall. In contrast, the SANISAND has a lower maximum hoop stress and a smaller difference between initial stress and peak stress. The lower and wider stress peak predicted by SANISAND shows a more gradual redistribution. Both the Mohr-Coulomb and SANISAND peaks are located away from the borehole wall and therefore no longer coincide with the linear-elastic response. After the peak, both models gradually converge towards the far-field stress.

In phase 11, the borehole pressure has been reduced to zero. The linear-elastic model continues to predict, as expected, an increased hoop stress concentration near the borehole wall compared to the previous phase. The Mohr-Coulomb and SANISAND models show a different response, with low hoop stress near the borehole wall and a stress peak further away from the borehole. The SANISAND model starts close to zero hoop stress, while the Mohr-Coulomb model starts at approximately 25 kPa. This suggests that the SANISAND model predicts more stress redistribution close to the borehole wall.

The Mohr-Coulomb model reaches a higher maximum hoop stress than the SANISAND model, while the SANISAND peak occurs further away from the borehole. This indicates that SANISAND predicts a wider but lower stress redistribution zone. After reaching their respective peaks, the Mohr-Coulomb and SANISAND results only converge close to the point where the overall stress field returns to the far-field value.

Overall, the comparison shows that the selected constitutive model has a strong influence on both the maximum hoop stress and the distance over which borehole unloading affects the surrounding soil. The linear-elastic model predicts the highest local stress concentration near the borehole wall, while the Mohr-Coulomb and SANISAND models redistribute the stresses over a wider zone.

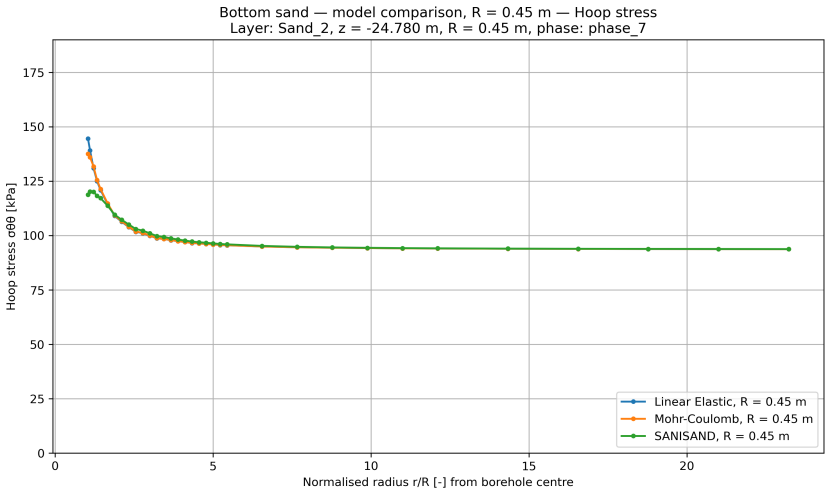

(a) Phase 7

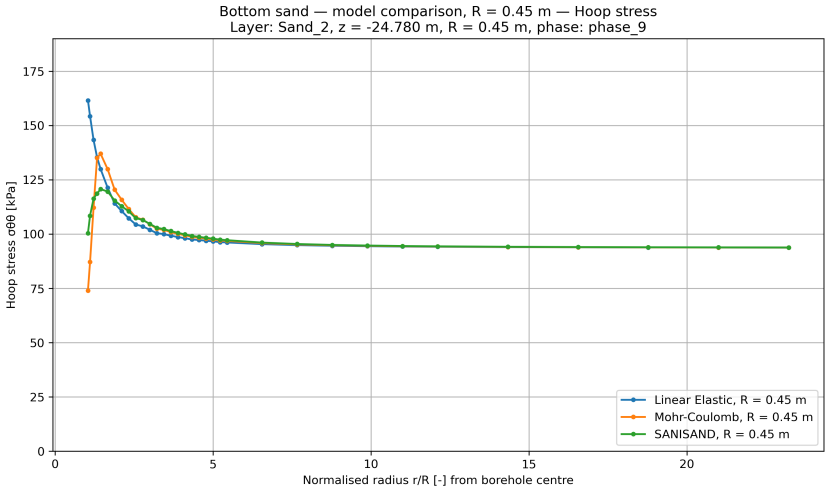

(b) Phase 9

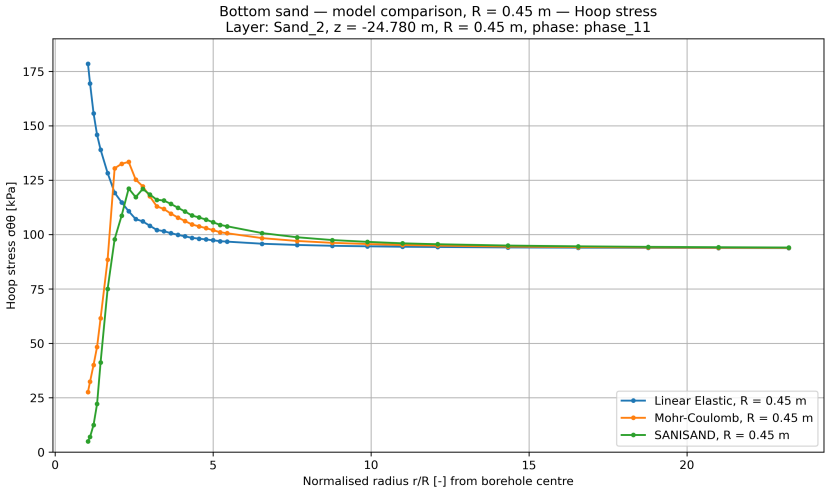

(c) Phase 11

Figure 4.14: Comparison of hoop stress at -24.78 m NAP for phases 7, 9 and 11 for all constitutive models.

Figure 4.15 compares the radial stress development for the three constitutive models in unloading phases 7, 9 and 11. Unlike the hoop stress response, the radial stress development shows a more

gradual change between the phases, eventually reaching zero. This is because the radial stress is strongly influenced by the borehole pressure.

As discussed in the linear-elastic Subsection 4.2.1, the extracted radial stress does not reduce fully to zero in the final unloading phase. This is caused by the location of the closest stress extraction point, which is positioned 0.02 m away from the borehole wall rather than directly on the boundary. This small distance is sufficient to produce a measurable radial stress. For the linear-elastic model, this was confirmed using the Kirsch solution. This assumption has not been made for the Mohr-Coulomb model as it cannot be confirmed.

In phase 7, the radial stress profiles of the three constitutive models follow a similar trend. In phase 9, differences between the models become more visible. The Mohr-Coulomb and SANISAND models show less steep gradients than the linear-elastic model, indicating that the radial stress redistribution extends over a larger distance from the borehole. In phase 11, the Mohr-Coulomb and SANISAND responses also separate from each other. The SANISAND model shows the least steep gradient and therefore requires a larger distance to converge towards the far-field stress.

In the last phase, the radial stress converges at a distance of approximately ten times the normalised radius. The less steep gradient predicted by the SANISAND model indicates a larger affected area compared with the Mohr-Coulomb and linear-elastic models. Similar to the hoop stress, the choice in constitutive model influences the predicted distance over which drilling affects the surrounding soil.

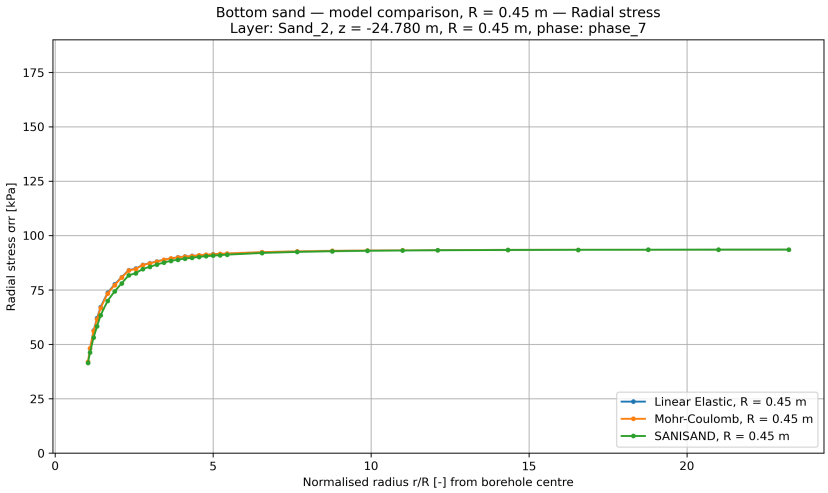

(a) Phase 7

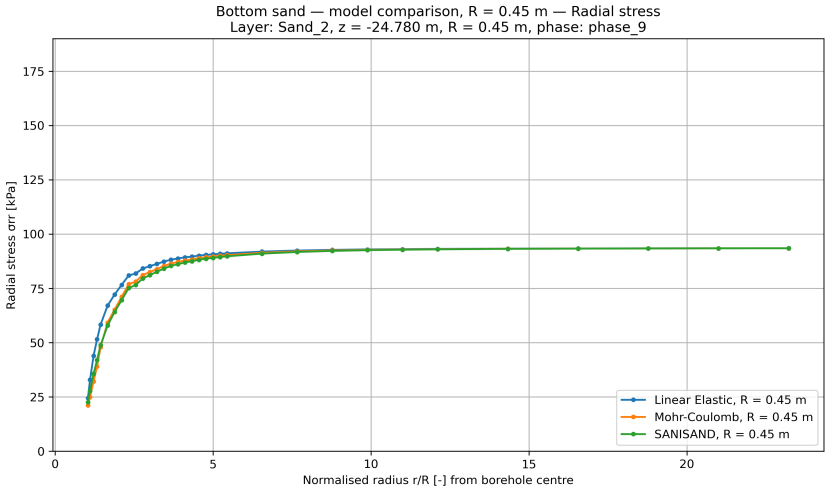

(b) Phase 9

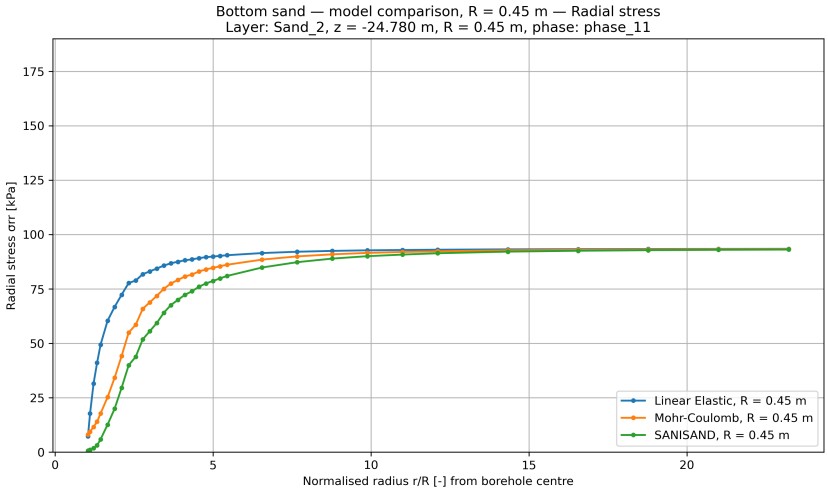

(c) Phase 11

Figure 4.15: Comparison of radial stress at -24.78 m NAP for phases 7, 9 and 11 for all constitutive models.

Figure 4.16 compares the hoop and radial strain development for three constitutive models in back pressure reduction phases 7, 9 and 11. The results show that the SANISAND model predicts the largest

strain magnitudes in all three phases. The Mohr-Coulomb model gives the second largest magnitude strains and the linear-elastic model gives the lowest strain values.

In phase 7, the differences between the constitutive models are slightly visible. The SANISAND model shows the largest strain response close to the borehole, indicating that non-linear sand behaviour is occurring. The Mohr-Coulomb model follows with lower strain magnitudes and the linear-elastic model remains the smallest.

In phase 9, strain magnitude increases for all models, however, the difference between radial and hoop strain is not visible yet for Mohr-Coulomb and SANISAND models. Both models predict larger strains than the linear-elastic model. In phase 11, the difference between hoop and radial strain becomes more distinct. The SANISAND model shows the largest strain response, followed by the Mohr-Coulomb model and then the linear-elastic model.

All models converge back towards negligible strain values within approximately five normalised radii from the borehole centre. Similar to the stress results, the SANISAND model requires the largest distance to converge, followed by the Mohr-Coulomb model and then the linear-elastic model. This indicates that the predicted deformation zone is largest for SANISAND and smallest for the linear-elastic model. The comparison therefore shows that the selected constitutive model influences not only the stress redistribution, but also the magnitude and extent of deformation around the borehole.

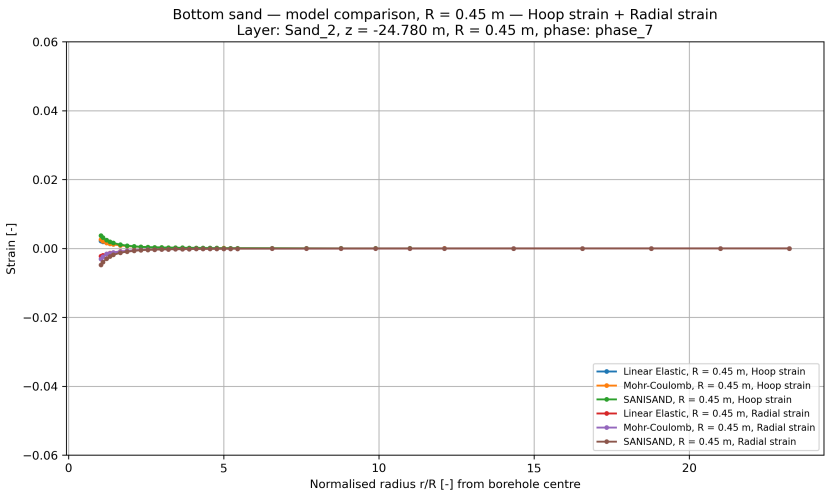

(a) Phase 7

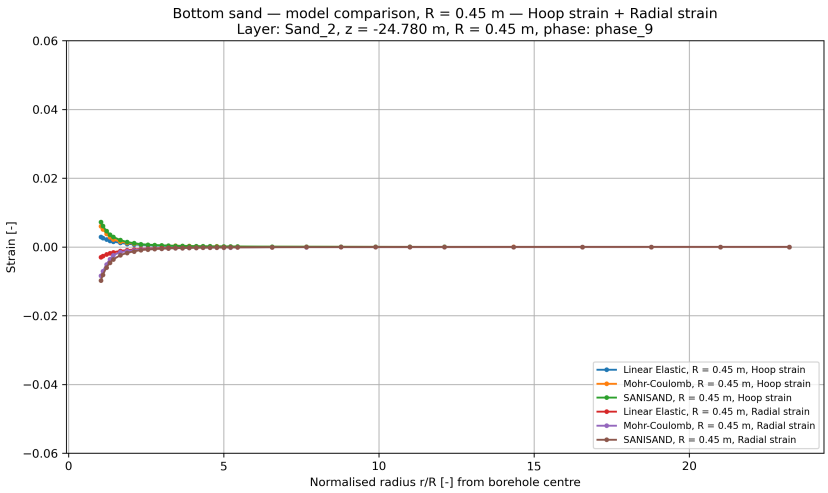

(b) Phase 9

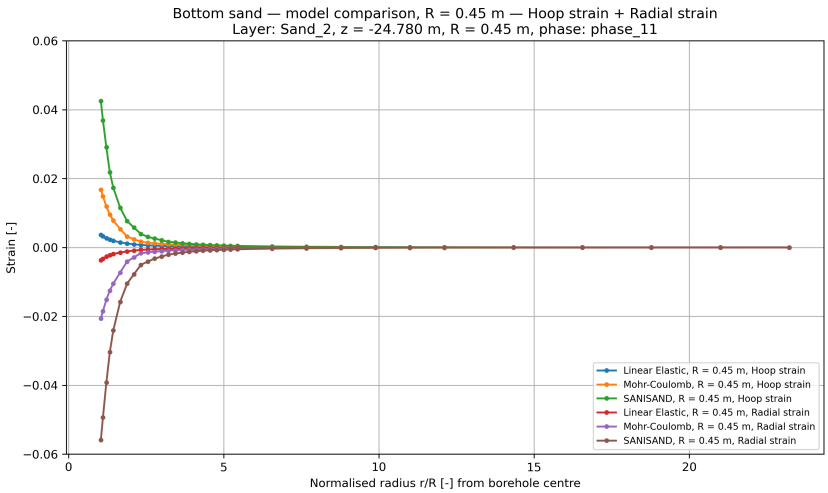

(c) Phase 11

Figure 4.16: Comparison of hoop and radial strain at -24.78 m NAP for phases 7, 9 and 11 for all constitutive models.

In Appendix C.4 phase 4 strains are shown.

4.2.5. Borehole radius influence

Figures 4.17 and 4.18 show the radial and hoop stress and strains development for different borehole radii using the linear-elastic and Mohr-Coulomb constitutive models. The results show that increasing the borehole radius increases the absolute distance over which stress and strain changes occur around the borehole. This indicates that the borehole radius is an important parameter controlling the size of the affected zone.

However, when the distance is expressed in normalised radii, the stress and strain profiles show a similar pattern for the different borehole radii. This indicates that the affected distance scales with the borehole radius. The use of a normalised radius is therefore useful for comparing boreholes of different sizes and for interpreting minimum separation distances relative to the borehole geometry.

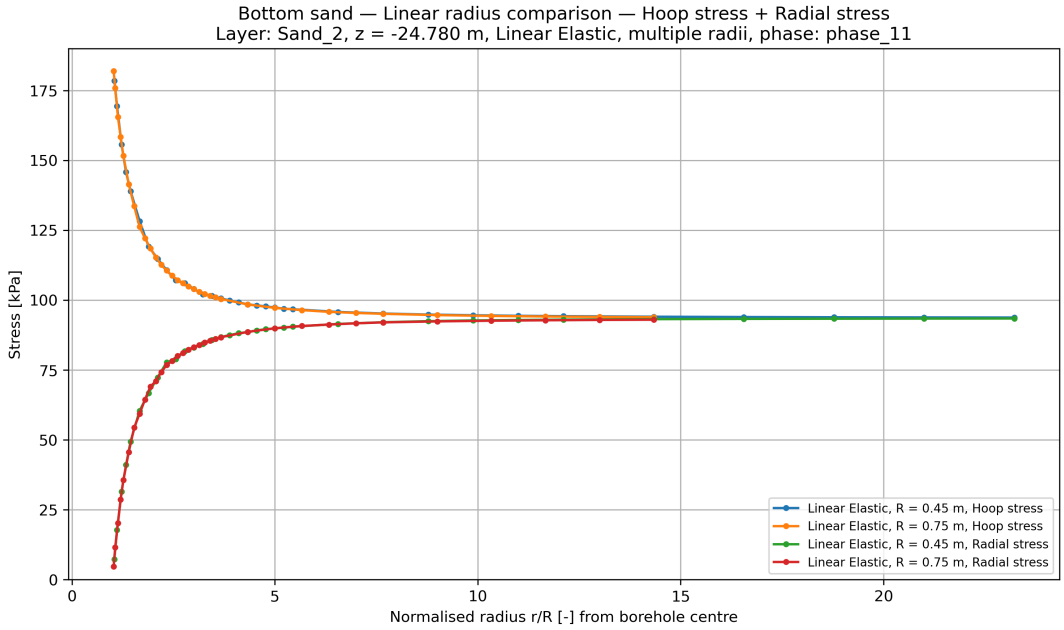

(a) Linear-Elastic hoop and radial stress at -24.78 m.

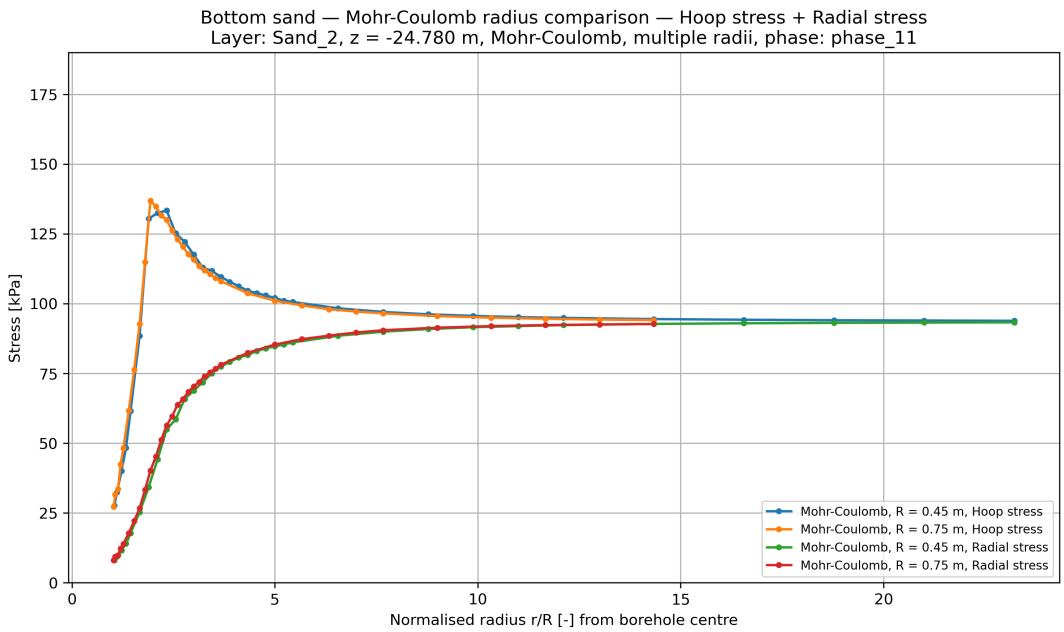

(b) Mohr-coulomb hoop and radial stress at -24.78 m NAP.

Figure 4.17: Hoop and radial stress at -24.78 m NAP for Linear-Elastic and Mohr-Coulomb constitutive models.

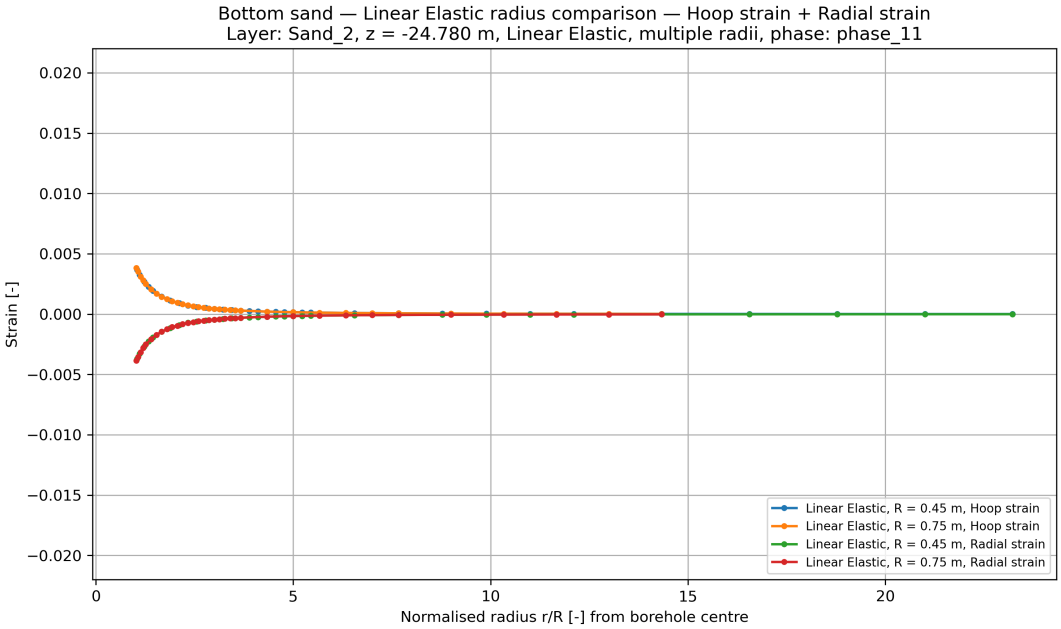

(a) Linear-Elastic hoop and radial strain at -24.78 m.

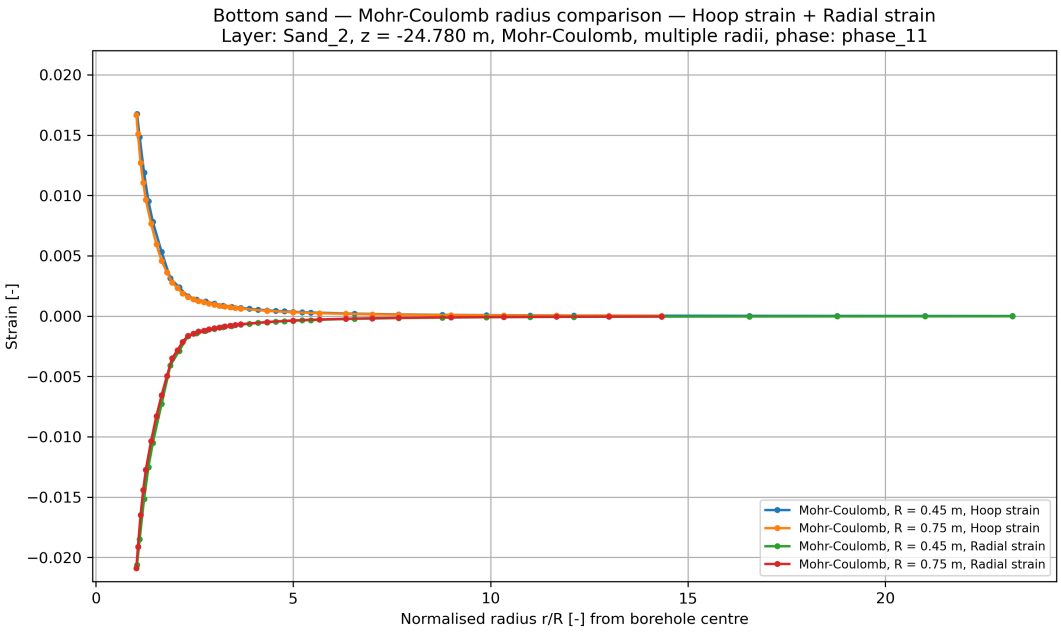

(b) Mohr-coulomb hoop and radial strain at -24.78 m NAP.

Figure 4.18: Hoop and radial strain at -24.78 m NAP for Linear-Elastic and Mohr-Coulomb constitutive models.

No linear SANISAND simulation was run for different radii, because the stress and strain profiles of the linear-elastic and Mohr-Coulomb models show that the affected distances scale with borehole radius when expressed in normalised borehole radius. Since the SANISAND simulation requires more time to run it was not deemed necessary for this part of the analysis.

These results support the use of the borehole radius as a reference parameter when defining a minimum separation distance. The observed scaling behaviour suggests that a rule-of-thumb based on normalised distance is physically meaningful, as the affected zone increases proportionally with the borehole radius.

4.2.6. Vertical stress

Figure 4.19 presents the calculated vertical stress development at a depth of -24.78 m NAP for the linear-elastic and SANISAND constitutive models. The Mohr-Coulomb results could not be obtained, as the calculation did not converge. As a result, this model could not be used for this specific comparison. As expected, the linear-elastic model does not predict noticeable changes in vertical stress. This is because the model is simplified as a two-dimensional plane-strain problem and is therefore unable to capture vertical stress redistribution in the longitudinal direction.

The SANISAND model, however, does predict changes in vertical stress during unloading. At the borehole wall, the vertical stress decreases as the borehole pressure is reduced in successive phases. In the final unloading phase, the vertical stress at the borehole wall reaches zero and then rapidly returns to the far-field value with increasing distance from the borehole. The stress change is localised, and the vertical stress returns to steady state within approximately five normalised radial distances from the borehole centre.

The purple vertical line in Figure 4.19, located at a normalised radial distance of 6.66, represents the CPT cone location at this depth. The CPT is therefore located outside the zone where the SANISAND model predicts vertical stress changes. More specifically, the cone is approximately 1.66 normalised radial distances beyond the point where the vertical stress has returned to steady state. This has two implications. Firstly, the SANISAND constitutive model cannot be validated directly using the CPT results at this depth, because the cone is located outside the predicted influence zone. Secondly, the Robertson charts for the foundation layer sand do not show an unusual change in soil state, which is consistent with the model prediction that no vertical stress change should be detectable at the CPT location. This does not validate the SANISAND model, but it does suggest that the vertical stress returns to steady state before reaching the horizontal distance of the CPT.

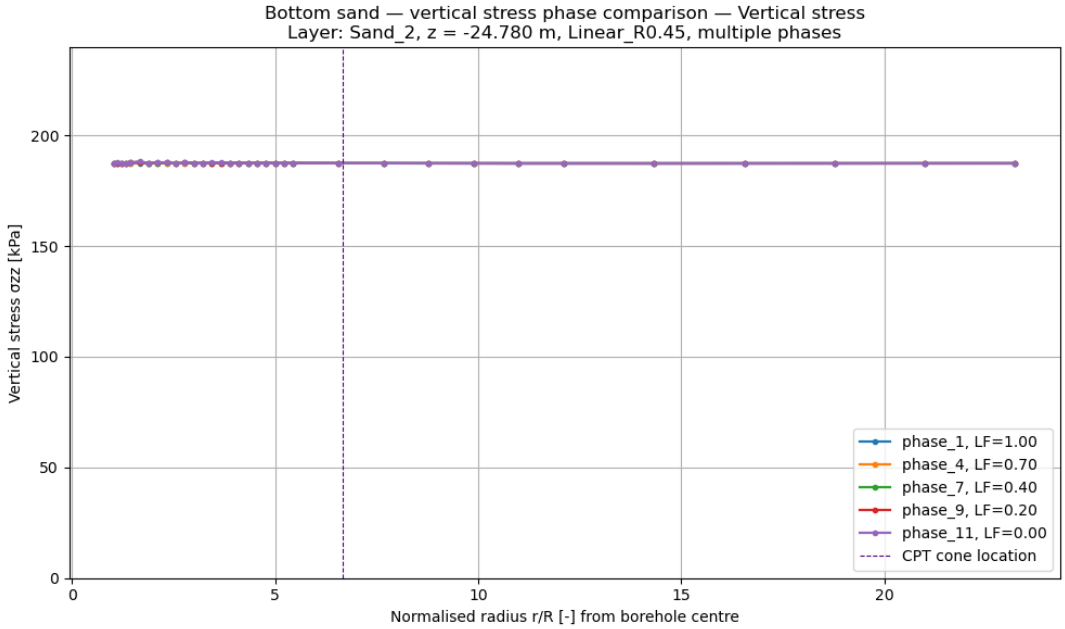

(a) Linear-elastic vertical stress development -24.78 m NAP for different phases.

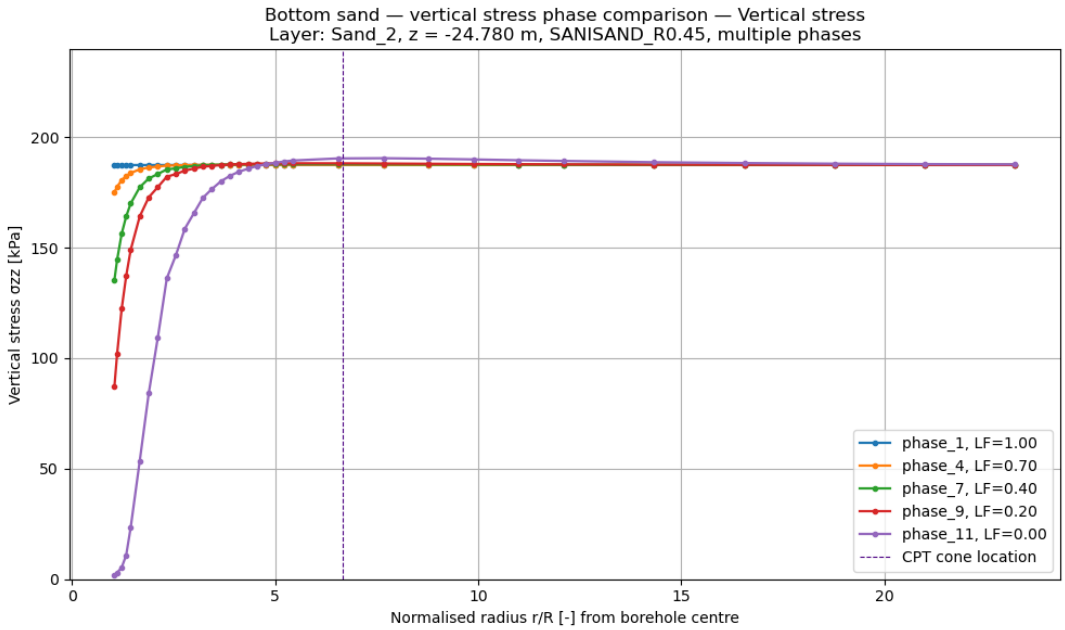

(b) SANISAND vertical stress development -24.78 m NAP for different phases.

Figure 4.19: Vertical stress development from different constitutive models at a depth of -24.78 m NAP. On the x-axis a vertical line is presented as a visualisation for the location of the CPT at that depth.

As shown by the results at a depth of -24.78 m NAP, the deflection of the CPT cone complicates the validation process of the SANISAND constitutive model. The cone deflection, which is discussed in the following subsection, increases with depth. To determine whether validation would be more feasible at shallower depth, the same calculations were performed for the first sand layer ranging from depth -2.04 m NAP to -4.46 m NAP. At this depth, the CPT cone is located closer to the borehole centre, increasing the possibility of detecting stress changes at the CPT location. The same calibrated SANISAND parameters as used for the foundation pile sand layer were applied in this calculation.

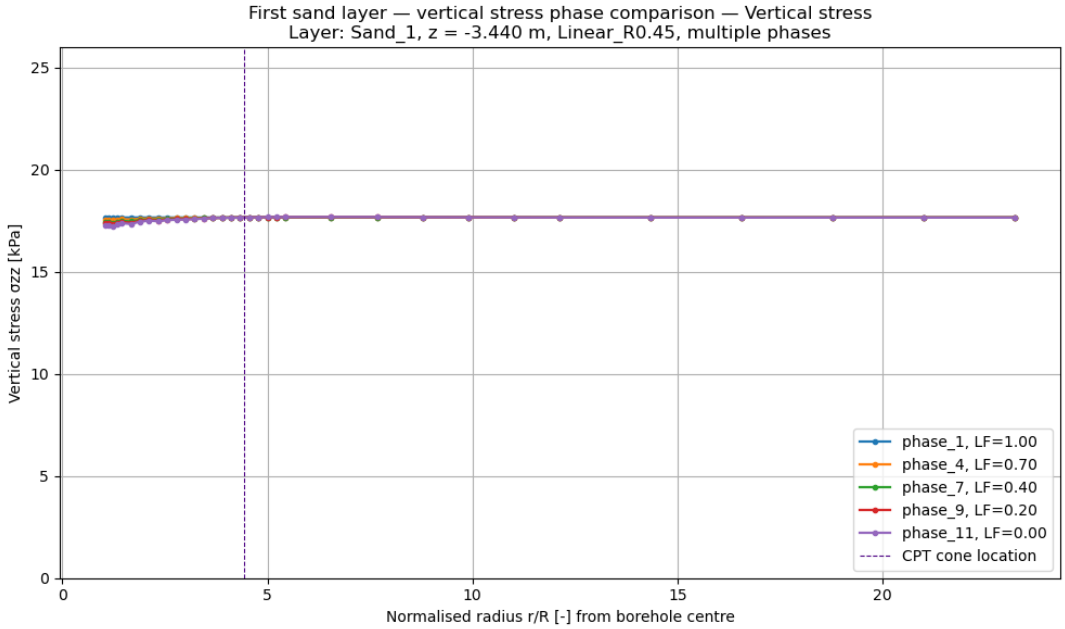

(a) Linear-elastic vertical stress development at -3.44 m NAP for different phases.

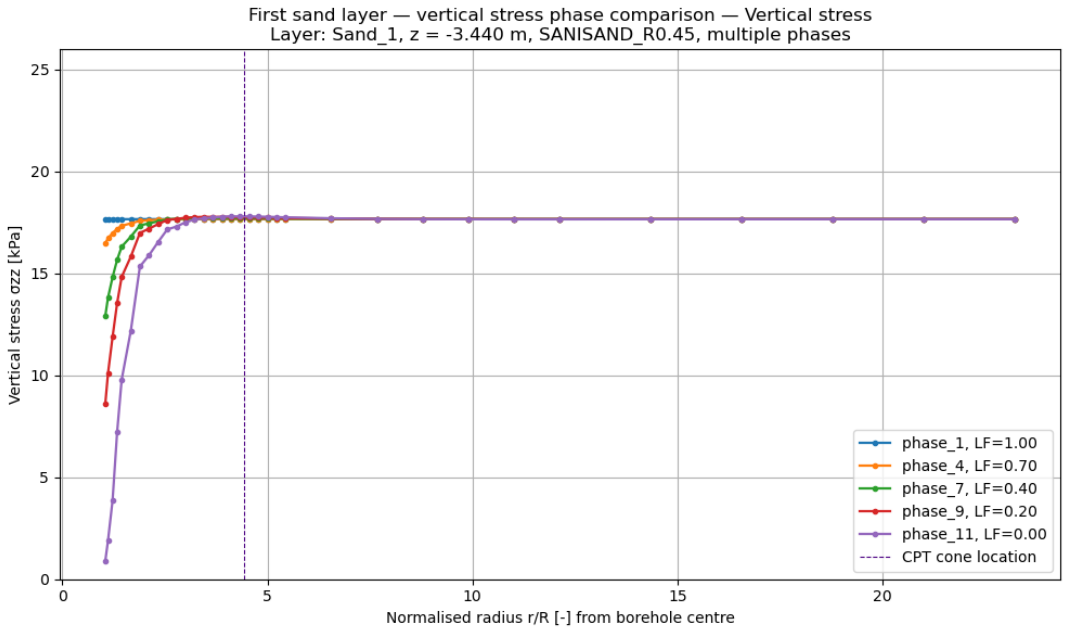

(b) SANISAND vertical stress development at -3.44 m NAP for different phases.

Figure 4.20: Vertical stress development from different constitutive models at a depth of -3.44 m NAP. The vertical line indicates the CPT location at that depth.

Figure 4.20 shows the calculated vertical stress development for both the linear-elastic model and the SANISAND model in the first sand layer. Similar to the results at a depth of -24.78 m NAP, the linear-elastic model does not show noticeable changes in vertical stress during unloading. The SANISAND model, however, does predict vertical stress changes during unloading. The stress development follows a similar trend to the results shown in Figure 4.19b, with the largest stress changes occurring close to the borehole wall. The vertical stress then rapidly returns to the far-field value with increasing distance from the borehole. Although the stress gradient is steeper in the first sand layer, the CPT location is again positioned beyond the point where the model predicts the vertical stress to have returned to steady state. Moreover, the Robertson chart results of the sand layer in Appendix B.6 do not show any noteworthy change in the soil state. Therefore, the same conclusion can be drawn as for the foundation

pile sand layer: the CPT measurements cannot be used to directly validate the SANISAND constitutive model, but they are consistent with the prediction that no vertical stress changes are detectable at the CPT location.

The first sand layer simulation was performed using the same SANISAND parameters as the foundation pile sand layer. This provides a consistent comparison with the main numerical analysis, but it also introduces uncertainty because the first sand layer may have different material properties. Both Baldi and Robertson derived results suggest that the first sand layer has a higher relative density and therefore lower void ratio than the foundation pile sand layer. However, the void ratio derived for the first sand layer falls outside the calibrated range of the SANISAND parameter set and could lead to unreliable model behaviour. For this reason, the calibrated parameters of the foundation pile sand layer were retained.

This modelling choice should therefore be interpreted as a simplified consistency check rather than a fully representative simulation of the first sand layer. The first sand layer has lower cone resistance values than the foundation pile sand layer, which suggests lower stiffness and dilatancy. At the same time, the derived relative density is higher, indicating a denser state. By using the foundation pile sand parameters, the calculation represents an approximation in which the shallow sand layer is not modelled with the extremely dense state or low stiffness and dilatancy suggested by the CPT interpretations. The purpose of this calculation is therefore to assess whether the predicted vertical stress influence zone could reach the CPT location at a shallower depth.

4.2.7. Alternating void ratios

The comparison was made for phase 92 of 101, with 9% of borehole back pressure remaining. This phase was selected because it was the last common phase for which all void-ratio simulations, ranging from $e_{ini} = 0.55$ to $e_{ini} = 0.85$, had converged. The interpretation of a model not converging after a phase vary from soil failure to software problems. This falls outside the scope of the research as the focus lays on the effects of changes in void ratio.

Figure 4.21 shows the hoop and radial stress development at a depth of -3.44 m NAP for the different initial void ratios. The hoop stress results show a clear relationship between void ratio, peak hoop stress and the location of the peak. Lower void ratios result in higher peak hoop stresses and a peak located closer to the borehole wall. The initial hoop stress near the borehole wall is also higher for the denser sand states. In contrast, higher void ratios result in a lower initial hoop stress and a lower peak hoop stress. The peak also shifts further away from the borehole wall, indicating a wider stress redistribution zone.

This behaviour is consistent with the expected response of sand with different densities. A lower void ratio represents a denser sand state, which can generally mobilise higher stiffness and shear resistance. As a result, the stress redistribution remains more concentrated near the borehole. A higher void ratio represents a looser sand state, which is less able to sustain a high local stress concentration. The stress is therefore redistributed over a larger distance from the borehole. For all analysed void ratios, the hoop stress converges towards the far-field stress within approximately ten normalised radii.

A similar trend is observed for the radial stress. The radial stress decreases near the borehole as the borehole pressure is reduced. For lower void ratios, the radial stress gradient is steeper, meaning that the stress field returns to the far-field value over a shorter distance. For higher void ratios, the gradient is less steep and the affected zone becomes larger. This indicates that looser sand states result in a more gradual redistribution of radial stress around the borehole.

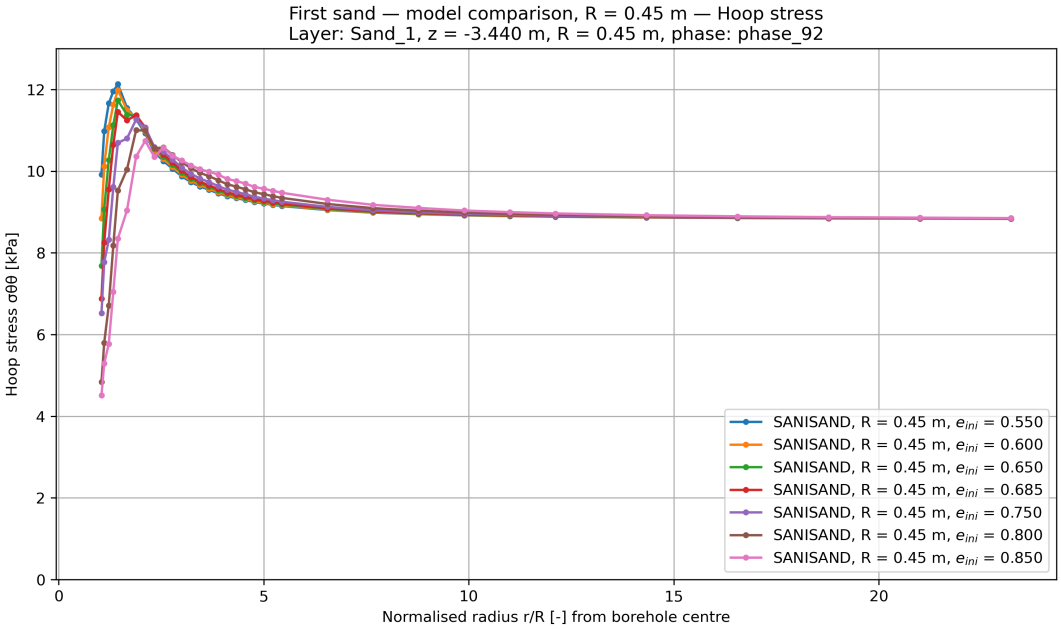

(a) Hoop stress at -3.44 m.

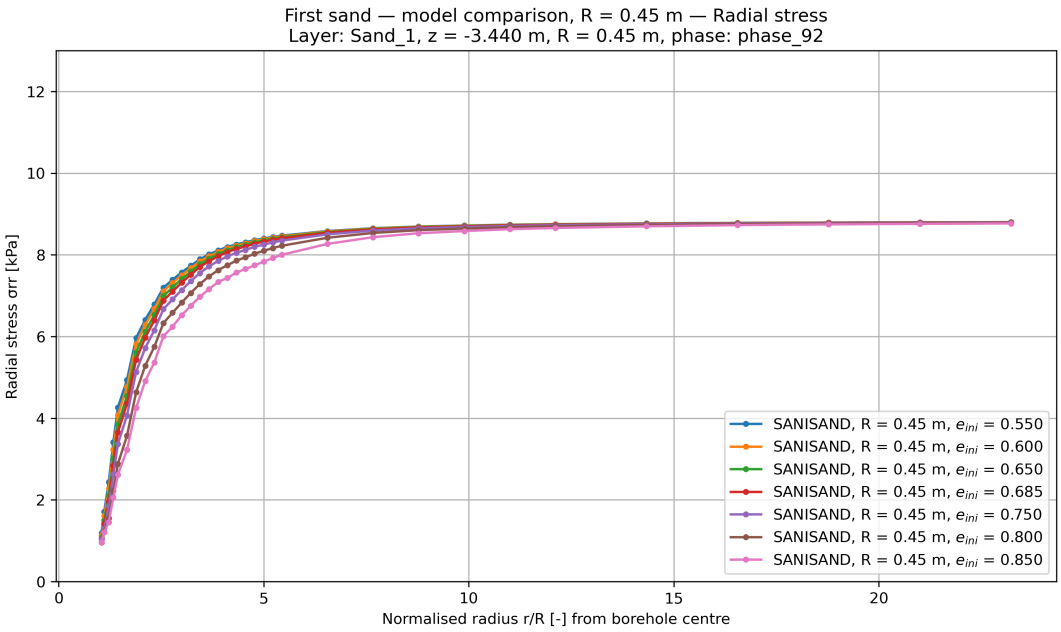

(b) Radial stress at -3.44 m NAP.

Figure 4.21: Hoop and radial stress at -3.44 m NAP for SANISAND model.

Figure 4.22 shows the hoop and radial strain developments at the same depth for different initial void ratios. The strain results show that the deformation is strongly affected by the initial void ratio. Higher void ratios generally result in larger strain. This is expected, as looser sand states have a lower resistance to deformation and therefore develop larger strains during unloading.

Nevertheless, it is important to mention that the low void ratio sand has not reached zero stress at the borehole wall. This would likely be achieved in the latest phase and would likely show an increase in magnitude of strain as a result of dilation.

In phase 92, the difference between hoop and radial strain remains relatively small up to an initial void ratio of approximately 0.685. For higher void ratios, the difference between the strain components

increases. The largest strain magnitudes are observed for the highest void ratios, which is consistent with the wider stress redistribution zone observed in the stress results.

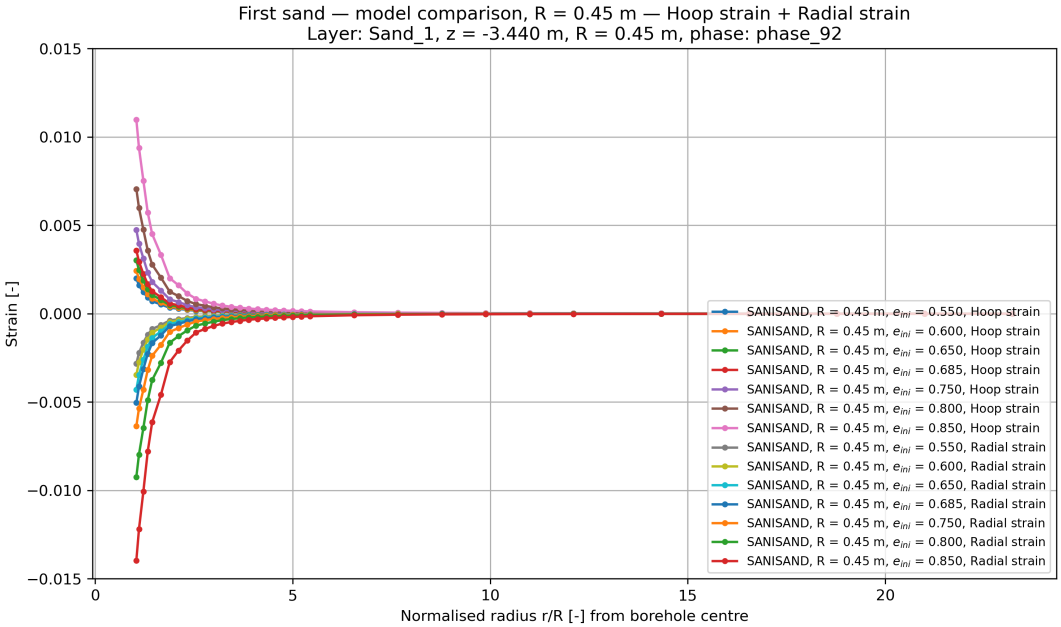

Figure 4.22: Hoop and radial strain at -3.44 m NAP for SANISAND model.

Overall, the void ratio comparison shows that the assumed initial density has a significant influence on the SANISAND predictions. Lower void ratios result in higher stress concentrations closer to the borehole and smaller deformation zones, while higher void ratios result in lower peak stresses, larger strains and a wider affected zone. This confirms that the initial void ratio is an important input parameter for the SANISAND model and should be selected carefully when interpreting stress redistribution around the borehole.

4.2.8. Critical void ratio Ottawa sand

Figure 4.23 shows the critical void ratio of the SANISAND calibrated Ottawa sand to a depth of -30 m NAP. The critical state line remains above the maximum initial void ratio used in the numerical simulations of the first sand layer. As a result of all simulated void ratios being lower than the critical void ratio, the sand is expected to show dilative behaviour in all simulations.

This has an important implication for the interpretation of the influence distance. The increase in influence distance observed at $e_{ini} = 0.8$ is not caused by the sand crossing the critical state line. The PLAXIS simulations were performed for initial void ratios between 0.55 and 0.85, corresponding to a relative density range of approximately 3% to 100% for the Ottawa sand. Over this range, the simulated void ratios remain below the calculated critical void ratio. The change in influence distance at $e_{ini} = 0.8$ therefore represents a behavioural change within the Ottawa sand, rather than a transition from dilative to contractive behaviour.

The adopted boundary at $e_{ini} = 0.8$ should therefore be interpreted as specific to the Ottawa sand parameter set used in this research. For sands with different characteristics, the transition in influence distance may occur at a different void ratio. Additional simulations with site calibrated SANISAND parameters would be required to determine whether the same boundary applies to the Delft sand. This falls outside the scope of the present research.

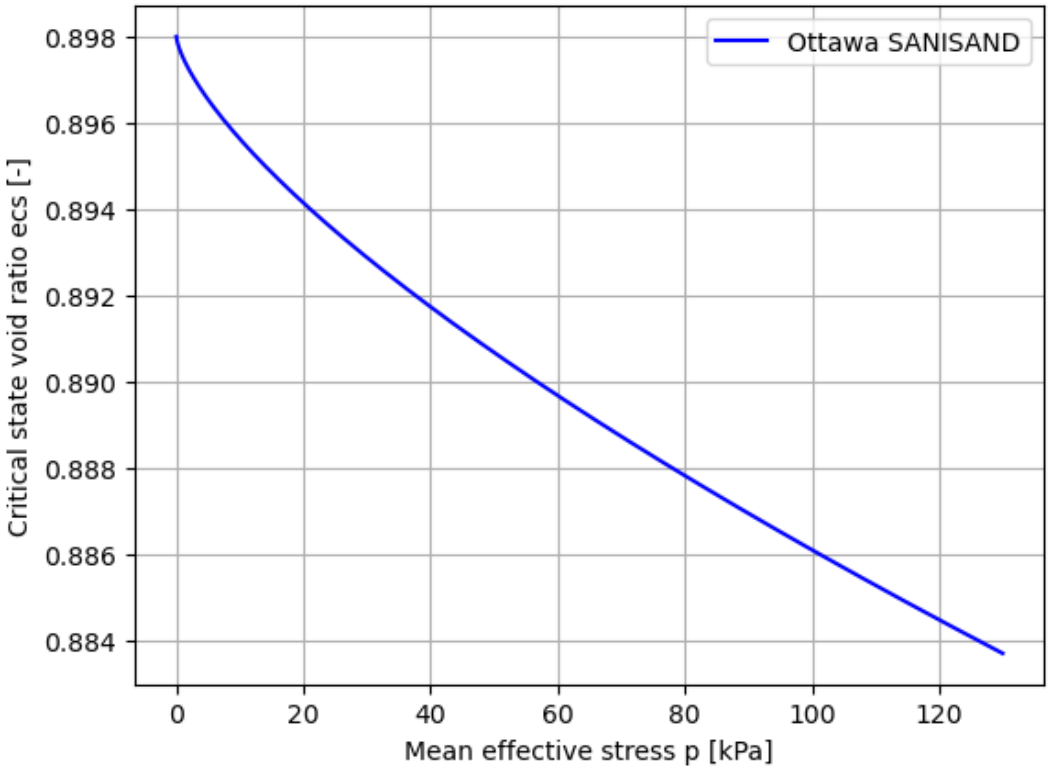

Figure 4.23: Critical state line for Ottawa SANISAND parameters to a depth of -30 m NAP.

4.3. Pile to borehole distance interpretation

This section presents the results of the pile-to-borehole interpretation 3.3. Consisting of CPT-based and numerical model-based.

4.3.1. CPT-based

The CPT-based interpretation of the minimum pile-to-borehole distance is mainly governed by the actual horizontal distance between the cone and the borehole at the studied depth. In contrast to the numerical model, the CPT measurement does not provide a continuous stress distribution around the borehole. Instead, it only provides information at the locations where the cone penetrates the soil. Therefore, the CPT-based interpretation should be regarded as an observational lower-bound assessment rather than a direct determination of the full borehole influence zone.

The numerical model results showed that the vertical stress response at different depths within the foundation pile sand layer converged towards the far-field stress at a comparable normalised radius. Based on this observation, the middle evaluation depth of -24.78 m NAP was selected as a representative depth for the CPT-based distance interpretation. At this depth, the cone location corresponded to a normalised radius of approximately 6.66. Expressed in terms of normalised borehole diameter, this corresponds to a normalised diameter of:

$$D_n = 3.33 \tag{4.1}$$

The CPT results discussed in the previous sections did not show clear measurable differences in cone resistance, sleeve friction or Robertson soil behaviour type classification. Therefore, the assumption is made that at a distance of $D_n = 3.33$, no clear borehole induced changes were detected in the surrounding soil. However, this does not prove that no stress redistribution occurred closer to the borehole. It only indicates that no significant changes were observed at the actual CPT measurement locations.

Based on this interpretation, the proposed CPT-based minimum distance without considering the pile influence zone is:

$$S \geq 3.33 D_b \tag{4.2}$$

where S is the minimum distance from the borehole centreline to the pile centreline and D_b is the borehole diameter.

When the pile influence zone according to Koppejan is included, the minimum distance is increased by the zone surrounding the foundation pile. The proposed expression then becomes:

$$S \geq 4.7 D_{eq} + 3.33 D_b \tag{4.3}$$

where D_{eq} is the equivalent diameter of the pile.

This expression results in a larger minimum distance than the distance proposed by Bogaards (2025). This is primarily caused by the horizontal distance of the CPT location.

4.3.2. Numerical model based

For the numerical model interpretation, the far-field condition is defined as the distance at which the vertical stress has recovered to at least 95% of the far-field value. At a depth of approximately -24.78 m NAP, this corresponds to a stress difference of approximately 9 kPa from the far-field stress. This difference is considered small, as it is lower than the vertical stress of approximately 0.5 m of sand. The 95% criterion is therefore used as a practical threshold for defining the end of the borehole influence zone.

The SANISAND model is used for the numerical interpretation because it is the most advanced model and it predicted the largest stress redistribution zone. Figure 4.24 shows the vertical stress development at different depths in the first sand layer and the foundation pile sand layer for an initial void ratio of 0.685. The results show that the vertical stress in the first sand layer reaches 95% of the far-field value at approximately 2.5 normalised radii from the borehole centre. In the foundation pile sand layer, the corresponding distance is approximately 5 normalised radii.

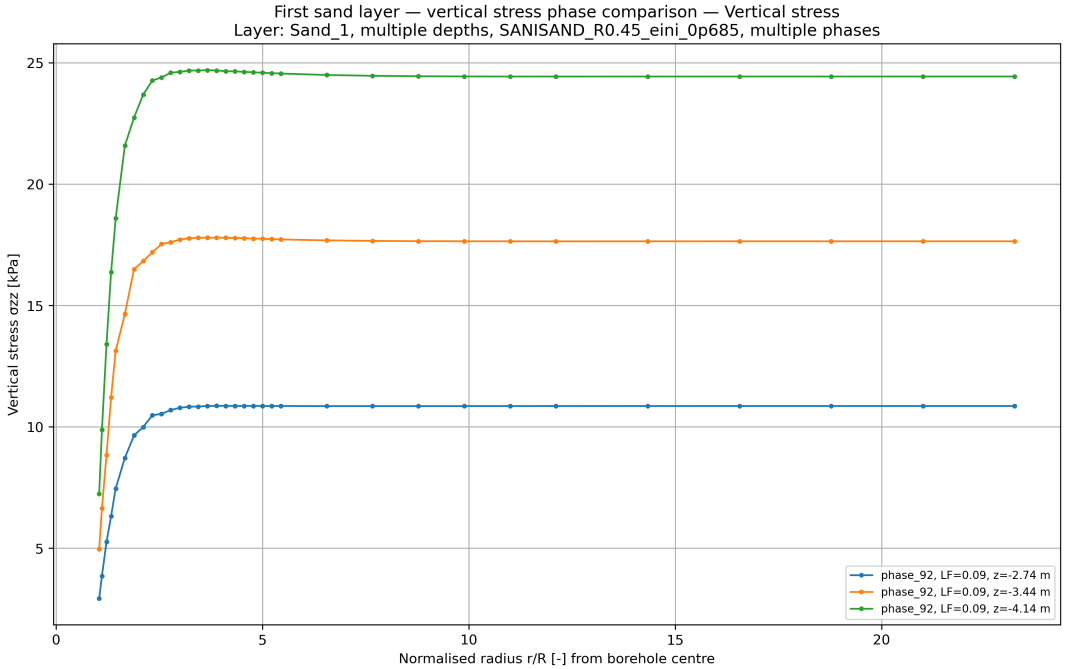

(a) Vertical stress in the first sand layer with void ratio 0.685 at different depths.

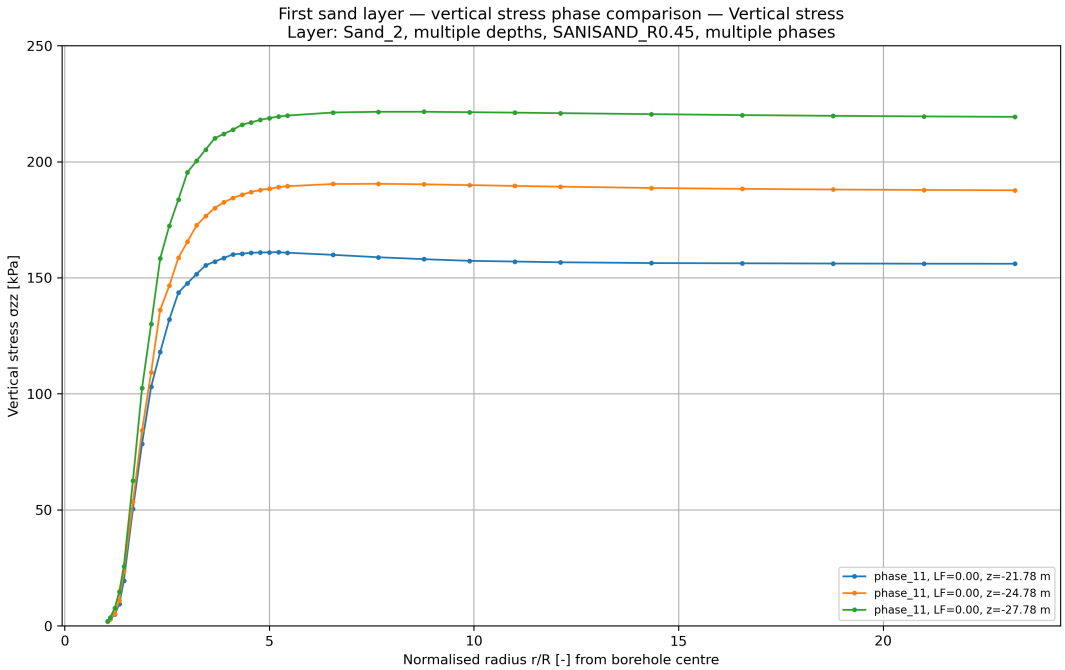

(b) Vertical stress in the foundation pile sand layer with void ratio 0.685 at different depths.

Figure 4.24: Vertical stress development in the first sand layer and foundation pile sand layer for an initial void ratio of 0.685.

The corresponding normalised radii at which 95% of the far-field stress is reached are summarised in Table 4.7. The results show a consistent difference between the shallow first sand layer and the deeper foundation pile sand layer. The deeper sand layer requires a larger normalised radius before the vertical stress has converged to the selected far-field criterion. This indicates that the depth level and associated stress state influence the radial extent of the borehole-induced stress redistribution.

The influence of the initial void ratio was evaluated using the first sand layer, because the numerical calculations for the foundation pile sand layer did not converge for all void ratios. The resulting vertical

Depth NAP [m]	Far-field stress (kPa)	Normalised radius to 95% of far-field
-2.74	11	2.5
-3.44	18	2.5
-4.14	25	2.5
-21.78	155	5
-24.78	190	5
-27.78	220	5

Table 4.7: Normalised radius reaching 95% of far-field at foundation pile depth.

stress development is shown in Figure 4.25. The results indicate that the initial void ratio has a limited influence on the convergence distance within the analysed range. However, the looser states, with initial void ratios of 0.800 and 0.850, show a slightly larger affected zone and converge at approximately 3 normalised radii, unlike 2.5 for the other void ratios.

These results should be interpreted with caution, because they were obtained before complete removal of the borehole back pressure. At the analysed phase, 9% of the back pressure was still present. It is therefore expected that the final unloading phase could shift the convergence distance slightly further away from the borehole. This effect may be more relevant for looser sand states, as they showed the largest convergence distance in the available results. However, because full convergence could not be evaluated for the foundation pile sand layer for all void ratios, no direct quantitative relation between initial void ratio and final influence distance can be derived. Therefore, a lightly larger convergence distance is proposed for void ratio higher than 0.8, although this should be interpreted with caution.

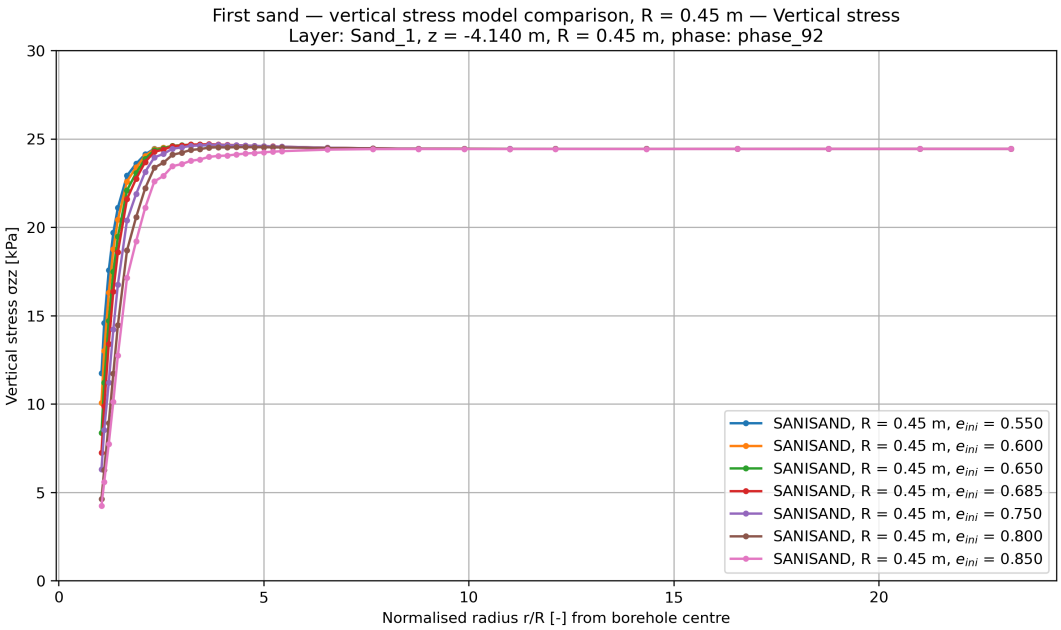

Figure 4.25: Vertical stress in first sand layer at depth -4.14 m NAP with varying initial void ratio

Additional figures are shown in Appendix C.6.

Based on the numerical results, a rule of thumb is proposed for the minimum distance at which the vertical stress has recovered to at least 95% of the far-field value. For initial void ratios below 0.8, a normalised radius of 5 is adopted. For initial void ratios equal to or greater than 0.8, a slightly larger normalised radius of 6 is proposed. This distinction is introduced to account for the slightly larger affected zone observed for looser sand states and for the uncertainty caused by incomplete convergence in the final unloading phase.

Initial void ratio	Normalised radius 95% to far-field	Normalised diameter [D_n]
< 0.8	5	2.5
$\geq$ 0.8	6	3

Table 4.8: Proposed numerical rule of thumb for reaching 95% of the far-field vertical stress.

The proposed numerical model-based minimum distance without considering the pile influence zone is:

$$S \geq D_n D_b \tag{4.4}$$

where D_b is the borehole diameter and D_n is the normalised diameter factor given in Table 4.8. For practical application, a conservative simplification would be to adopt $D_n = 3.0$ for all sand states. This corresponds to a distance of 6 borehole radii and avoids the need to distinguish between different initial void ratios when the in-situ sand state is uncertain.

When the pile influence zone is included, the proposed minimum distance becomes:

$$S \geq 4.7 D_{eq} + D_n D_b \tag{4.5}$$

where D_{eq} is the equivalent diameter of the foundation pile.

The resulting expression is comparable to the proposal by Bogaards (2025). In that proposal, a factor of 5 is used for the pile influence zone, while a factor of 2.5 is used for the borehole diameter contribution. The factor of 5 is slightly more conservative than the value of 4.7 used in this research. The borehole factor of 2.5 is consistent with the proposed value for denser sand states, while the value of 3.0 proposed provides an indication for looser soils. This result supports the recommendation by Bogaards (2025) that the minimum safe distance can be reduced compared with the current SIKB rule-of-thumb.

Overall, the CPT-based and numerical model-based interpretations lead to comparable minimum distance expressions. The CPT-based interpretation results in a borehole diameter factor of 3.33, while the numerical model gives a factor between 2.5 and 3.0 depending on the assumed sand state. Since the CPT-based factor is derived from the actual measurement location and no clear changes were observed at that distance, it may be regarded as the most conservative observational distance. The numerical model provides an interpretation of the stress redistribution, but remains an approximation as a result of the adopted Ottawa sand parameters. Therefore, the actual stress redistribution around the borehole remains uncertain.

4.4. Comparing minimum distances

This section compares the proposed minimum pile centre to borehole centre distances. The comparison includes CPT-based and numerical model-based interpretations, both with and without the additional pile influence zone according to Koppejan. The purpose of this comparison is to evaluate how the proposed expressions differ from the existing rule of thumb and to assess for which pile and borehole diameter combinations the differences become most relevant.

4.4.1. CPT-based without pile zone

Figure 4.26 shows the CPT-based proposed minimum distances without including the additional pile influence zone.

	Borehole Diameter [mm]																				
Distance	50	75	100	125	150	175	200	225	250	350	450	550	650	750	850	950	1050	1150	1250	1350	1450
SIKB rule-of-thumb	500	750	1000	1250	1500	1750	2000	2250	2500	3500	4500	5500	6500	7500	8500	9500	10500	11500	12500	13500	14500
Proposed distance	167	250	333	416	500	583	666	749	833	1166	1499	1832	2165	2498	2831	3164	3497	3830	4163	4496	4829

Figure 4.26: CPT-based proposed distance results

The results show that the CPT-based proposed distances are lower than the distances obtained from the SIKB rule-of-thumb for all analysed borehole diameters. This is expected, because the proposed expression is based only on the CPT-derived borehole influence distance and that factor is lower than that of the SIKB rule. The difference between the two proposed distances increases with increasing borehole diameter.

This table solely provides an overview of the borehole influence zone. For practical applications, the user may combine this borehole influence distance with a user-defined influence zone for another underground object. This allows the proposed approach to be adapted to determine safe distances between boreholes and varying objects.

Both methodologies recommend relatively small separation distances for small diameter boreholes. Although the recommend distance ensures the limits of the borehole influence area. A minimum distance is recommended for any drilling. This minimum distance could be account for visual, equipment positioning and general safety during drilling.

4.4.2. CPT-based with pile zone

Figure 4.27 shows the CPT-based proposed minimum distances when the Koppejan pile influence zone is included. Red indicates cases where the SIKB rule-of-thumb gives a smaller recommended distance, while green indicates cases where the newly proposed method gives a smaller recommended distance.

		Borehole Diameter [mm]																				
Distance		50	75	100	125	150	175	200	225	250	350	450	550	650	750	850	950	1050	1150	1250	1350	1450
SIKB rule-of-thumb		500	750	1000	1250	1500	1750	2000	2250	2500	3500	4500	5500	6500	7500	8500	9500	10500	11500	12500	13500	14500
Foundation pile diameter [mm]	200	1229	1312	1395	1478	1562	1645	1728	1811	1895	2228	2561	2894	3227	3560	3893	4226	4559	4892	5225	5558	5891
	300	1760	1843	1926	2010	2093	2176	2259	2343	2426	2759	3092	3425	3758	4091	4424	4757	5090	5423	5756	6089	6422
	400	2291	2374	2457	2541	2624	2707	2790	2874	2957	3290	3623	3956	4289	4622	4955	5288	5621	5954	6287	6620	6953
	500	2822	2905	2989	3072	3155	3238	3322	3405	3488	3821	4154	4487	4820	5153	5486	5819	6152	6485	6818	7151	7484
	600	3353	3436	3520	3603	3686	3769	3853	3936	4019	4352	4685	5018	5351	5684	6017	6350	6683	7016	7349	7682	8015

Figure 4.27: CPT-based proposed distance results with Koppejan zone

The comparison shows that the CPT-based expression with the Koppejan zone gives larger distances than the SIKB rule-of-thumb for small borehole diameters and larger pile diameters. This is mainly caused by the contribution of the pile influence zone, which becomes dominant when the borehole diameter is small.

A transition occurs as the borehole diameter increases. From borehole diameters of approximately 150 mm and larger, the proposed CPT-based distance becomes smaller than the SIKB rule-of-thumb for several pile diameter combinations. This difference becomes more pronounced for larger borehole diameters. Therefore, the proposed CPT-based expression is most relevant for larger borehole installations near existing pile foundations, where the SIKB rule-of-thumb can result in relatively large centre-to-centre distances.

The results indicate that including the pile zone gives a more conservative interpretation for small geometries, while still allowing reduced distances for larger borehole diameters.

4.4.3. Numerical model based without pile zone

Figure 4.28 and 4.29 show the numerical model-based proposed minimum distances for the two different void categories without including the pile influence zone.

Distance for void	Borehole Diameter [mm]																				
ratio under 0.8 [mm]	50	75	100	125	150	175	200	225	250	350	450	550	650	750	850	950	1050	1150	1250	1350	1450
SIKB rule-of-thumb	500	750	1000	1250	1500	1750	2000	2250	2500	3500	4500	5500	6500	7500	8500	9500	10500	11500	12500	13500	14500
Proposed distance	125	188	250	313	375	438	500	563	625	875	1125	1375	1625	1875	2125	2375	2625	2875	3125	3375	3625

Figure 4.28: Numerical based proposed distance results for void ratio below 0.8

Distance for void	Borehole Diameter [mm]																				
ratio above 0.8 [mm]	50	75	100	125	150	175	200	225	250	350	450	550	650	750	850	950	1050	1150	1250	1350	1450
SIKB rule-of-thumb	500	750	1000	1250	1500	1750	2000	2250	2500	3500	4500	5500	6500	7500	8500	9500	10500	11500	12500	13500	14500
Proposed distance	150	225	300	375	450	525	600	675	750	1050	1350	1650	1950	2250	2550	2850	3150	3450	3750	4050	4350

Figure 4.29: Numerical based proposed distance results for void ratio above 0.8

The numerical model-based proposed distances are lower for both void ratio categories than the SIKB rule-of-thumb for all analysed borehole diameters. This difference becomes increasingly large the greater the diameter of the borehole becomes.

Just like Figure 4.26, the table provides an overview of the borehole influence zone. For practical applications, the user may combine this borehole influence distance with a user-defined influence zone for another underground object. This allows the proposed approach to be adapted to determine safe distances between boreholes and varying objects.

4.4.4. Numerical model based with pile zone

Figures 4.30 and 4.31 show the numerical model-based proposed minimum distances including the Koppejan pile influence zone for different void ratio categories. Red indicates cases where the SIKB rule-of-thumb gives a smaller recommended distance, while green indicates cases where the newly proposed method gives a smaller recommended distance.

Distance for void ratio under 0.8 [mm]	Borehole Diameter [mm]																				
	50	75	100	125	150	175	200	225	250	350	450	550	650	750	850	950	1050	1150	1250	1350	1450
SIKB rule-of-thumb	500	750	1000	1250	1500	1750	2000	2250	2500	3500	4500	5500	6500	7500	8500	9500	10500	11500	12500	13500	14500
Foundation pile diameter [mm] 200	1187	1250	1312	1375	1437	1500	1562	1625	1687	1937	2187	2437	2687	2937	3187	3437	3687	3937	4187	4437	4687
300	1718	1781	1843	1906	1968	2031	2093	2156	2218	2468	2718	2968	3218	3468	3718	3968	4218	4468	4718	4968	5218
400	2249	2312	2374	2437	2499	2562	2624	2687	2749	2999	3249	3499	3749	3999	4249	4499	4749	4999	5249	5499	5749
500	2781	2843	2906	2968	3031	3093	3156	3218	3281	3531	3781	4031	4281	4531	4781	5031	5281	5531	5781	6031	6281
600	3312	3374	3437	3499	3562	3624	3687	3749	3812	4062	4312	4562	4812	5062	5312	5562	5812	6062	6312	6562	6812

Figure 4.30: Numerical proposed distance results with Koppejan zone for void ratio below 0.8

Distance for void ratio above 0.8 [mm]	Borehole Diameter [mm]																				
	50	75	100	125	150	175	200	225	250	350	450	550	650	750	850	950	1050	1150	1250	1350	1450
SIKB rule-of-thumb	500	750	1000	1250	1500	1750	2000	2250	2500	3500	4500	5500	6500	7500	8500	9500	10500	11500	12500	13500	14500
Foundation pile diameter [mm] 200	1212	1250	1312	1375	1437	1500	1562	1625	1687	1937	2187	2437	2687	2937	3187	3437	3687	3937	4187	4437	4687
300	1743	1818	1893	1968	2043	2118	2193	2268	2343	2643	2943	3243	3543	3843	4143	4443	4743	5043	5343	5643	5943
400	2274	2349	2424	2499	2574	2649	2724	2799	2874	3174	3474	3774	4074	4374	4674	4974	5274	5574	5874	6174	6474
500	2806	2881	2956	3031	3106	3181	3256	3331	3406	3706	4006	4306	4606	4906	5206	5506	5806	6106	6406	6706	7006
600	3337	3412	3487	3562	3637	3712	3787	3862	3937	4237	4537	4837	5137	5437	5737	6037	6337	6637	6937	7237	7537

Figure 4.31: Numerical proposed distance results with Koppejan zone for void ratio above 0.8

The results show that the numerical model-based expressions with pile zone give larger distances than the SIKB rule-of-thumb for small borehole diameters and larger pile diameters. This is again caused by the contribution of the Koppejan pile influence zone. This behaviour is reversed for larger diameter boreholes and foundation piles. Differences becoming increasingly bigger with larger diameters.

The proposed distances for void ratios equal to or greater than 0.8 are slightly larger because a larger borehole influence factor is used. This reflects the interpretation that looser sand states may require a larger distance before the vertical stress has recovered to the selected far-field criterion.

Overall, the comparison shows that the proposed expressions are most beneficial for larger borehole diameters, where the SIKB rule-of-thumb gives relatively large minimum distances. For smaller borehole diameters, the proposed expressions without pile zone result in very small distances and should therefore not be used as direct construction distances. When the Koppejan pile influence zone is included, the proposed expressions become more conservative for small geometries and more favourable for larger borehole diameters.

A practical minimum distance should be considered, to ensure visual, equipment positioning and general safety during drilling. A recommendation could be to have at least 1.5 m of distance between borehole centre and pile foundation centre. Then the methodology of shortest distance can be dominant. The distance of 1.5 m has been determined as it is the first point where the methodology with Koppejan zone is smaller than that of SIKB rule-of-thumb.

5

Results Wezep & Zwolle

This chapter presents the results of the Wezep and Zwolle case studies. These case studies were analysed less extensively than the Delft case study, only the soil classification and Robertson soil behaviour type were performed. The chapter is structured into two sections, Section 5.1 presents the analysis of CPT results, while Section 5.2 presents the soil behaviour type interpretation.

5.1. Soil profile

The Wezep and Zwolle case studies are located further east in the Netherlands than the Delft case study. As a result, the soil profile differs from the one in Delft. The Delft profile contains alternating organic, clayey, silty and sandy deposits, whereas the Wezep and Zwolle profiles are dominated by sand and sand mixtures below a relatively thin clay and silt layer at the surface

The CPT measurements at Wezep extend to approximately -15 m NAP. The CPT measurements at Zwolle extend deeper, locally reaching approximately -35 m NAP. The additional case studies therefore provide useful comparison data for sandy soil behaviour, but they do not represent the same soil profiles as in Delft.

5.1.1. Wezep

After applying the 4 m distance criterion, two boreholes were suitable for comparison: borehole 9 (B9) and borehole 10 (B10). Table 5.1 shows an overview of the corresponding CPT measurements, including whether the CPT was performed before or after drilling and the horizontal distance to the borehole. Figure 5.1 shows a map overview of the CPTs in blue and boreholes in brown.

Borehole	CPT before drilling	CPT after drilling
B9	CPT S6 (3.97 m)	CPT S13 (3.64 m)
B10	CPT S3 (3.50 m)	CPT S3A (3.37 m), CPT S11 (3.16 m)

Table 5.1: Selected boreholes and corresponding CPT measurements before and after drilling. Distances indicate the horizontal distance between CPT and the corresponding borehole.

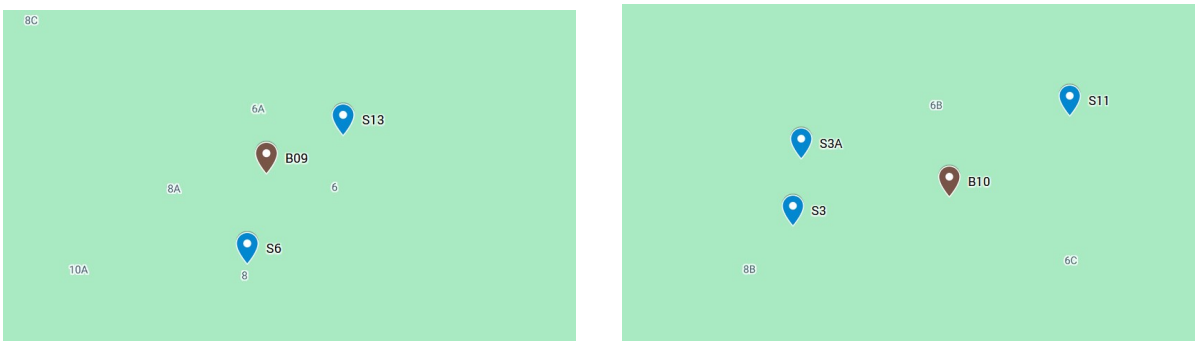

(a) Borehole 9 **(b)** Borehole 10

Figure 5.1: Map overview of boreholes B9 and B10 at the Wezep location.

As shown in Table 5.1, all selected CPT measurements are located more than 3 m from the corresponding borehole. Considering the relatively small borehole diameter of 0.15 m to 0.20 m and results obtained from the Delft case study, clear borehole-induced differences are not expected. Any observed differences between CPTs should therefore be interpreted with caution and are more likely related to natural horizontal variability in soil conditions than to the borehole installation.

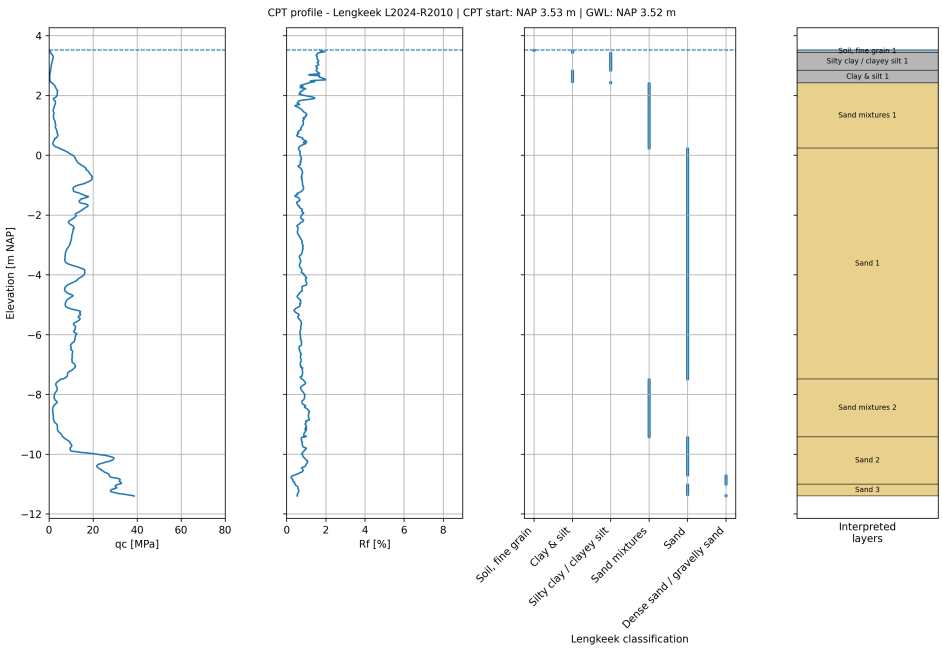

Figure 5.2: CPT measurement S3 before drilling B10.

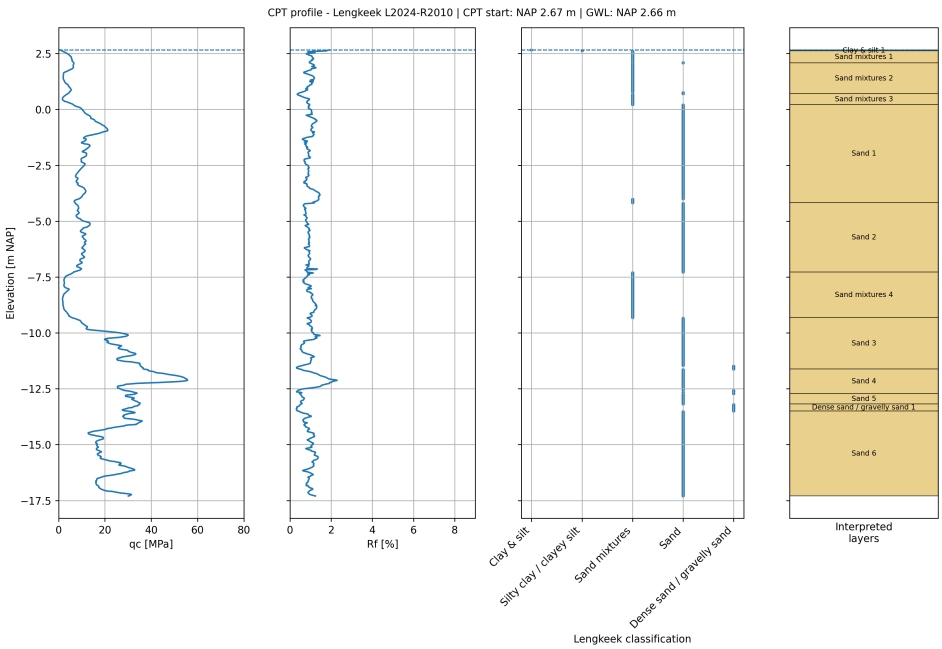

Figure 5.3: CPT measurement S3A after drilling B10.

Figures 5.2 and 5.3 show the interpreted CPT profiles near B10. The profiles indicate a predominantly sandy subsurface. CPT S3 contains a relatively thicker clay layer, whereas this clay layer is much thinner in CPT S3A. The lower measurement starting point after drilling could possibly be explained by excavation of clay for the construction of the building on the site. Despite this difference, both CPTs show comparable normalised cone resistance over the overlapping depth down to approximately -12 m NAP. The cone resistance is generally below 20 MPa down to approximately -10 m NAP and increases to values above 20 MPa below this depth. Similar CPT profiles are observed for the other Wezep measurements, which are included in Appendix E.1.1.

A direct before and after comparison is limited by the available penetration depth. Both CPT measurements before drilling extend only to approximately -13 m NAP, while the CPT measurements after drilling reach greater depths. As a result, the comparison between before and after drilling conditions is restricted to the overlapping depth. Deeper sand layers with normalised cone resistance values comparable to those of the Delft foundation pile sand layer cannot be directly compared.

5.1.2. Zwolle

After applying a 2 m distance criterion, four boreholes were suitable for comparison: borehole 25 (B25), borehole 26 (B26), borehole 52 (B52) and borehole 55 (B55). Table 5.2 shows an overview of the corresponding CPT measurements, including whether the CPT was performed before or after drilling and the horizontal distance to the borehole. Figure 5.4 shows a map overview of the CPT in blue and boreholes in brown.

Borehole	CPT before drilling	CPT after drilling
B25	CPT 1 (0.96 m)	CPT 6 (1.84 m)
B26	CPT 2 (1.11 m)	CPT 8 (0.24 m), CPT 16 (1.46 m), CPT 206 (1.83 m)
B52	CPT 3 (1.12 m)	CPT 10 (0.23 m), CPT 18 (1.45 m)
B55	CPT 4 (0.86 m)	CPT 12 (0.52 m), CPT 20 (1.76 m)

Table 5.2: Selected boreholes and corresponding CPT measurements before and after drilling. Distances indicate the horizontal distance between CPT and the corresponding borehole.

(a) Borehole 25 **(b)** Borehole 26

(c) Borehole 52 **(d)** Borehole 55

Figure 5.4: Map overview of selected boreholes at the Zwolle location.

As shown in Table 5.2, the selected CPT measurements in Zwolle are located closer to the boreholes than the ones selected in Wezep. According to the proposed numerical expression without the pile influence zone in Equation 4.4, and assuming a borehole diameter of 0.20 m with an initial void ratio below $e_{ini} = 0.8$, the calculated borehole influence distance is 0.5 m. Some CPT measurements are within this zone, nevertheless, no CPT before after combination is available within the borehole influence zone. This means that a direct comparison within the calculated borehole influence zone is not available. As a result, the Zwolle measurements can be used to assess whether large visual differences occur outside the expected influence zone, but they cannot directly confirm the boundary of the proposed borehole influence zone. Caution should therefore be taken as differences between CPTs may be caused by natural horizontal variability in soil conditions rather than by borehole installation.

Figures 5.5 and 5.6 show the interpreted CPT profiles near B25. An immediate observation is the difference in CPT measurement depth compared to the measurements done in Wezep. Instead of a maximum depth of approximately -17.5 m, the measurements reach a depth of at least -24 m NAP. Just like in Wezep the CPT measurements show a predominantly sandy soil. There are however clay and organic soil layers present close to the surface. A thin clay layer is found at surface followed by a thin sand layer and then by an organic layer. After the organic layer the soil remains sandy with some sand mixture layers. Similar CPT profiles are observed for the other Zwolle measurements, which are shown in Appendix E.1.2.

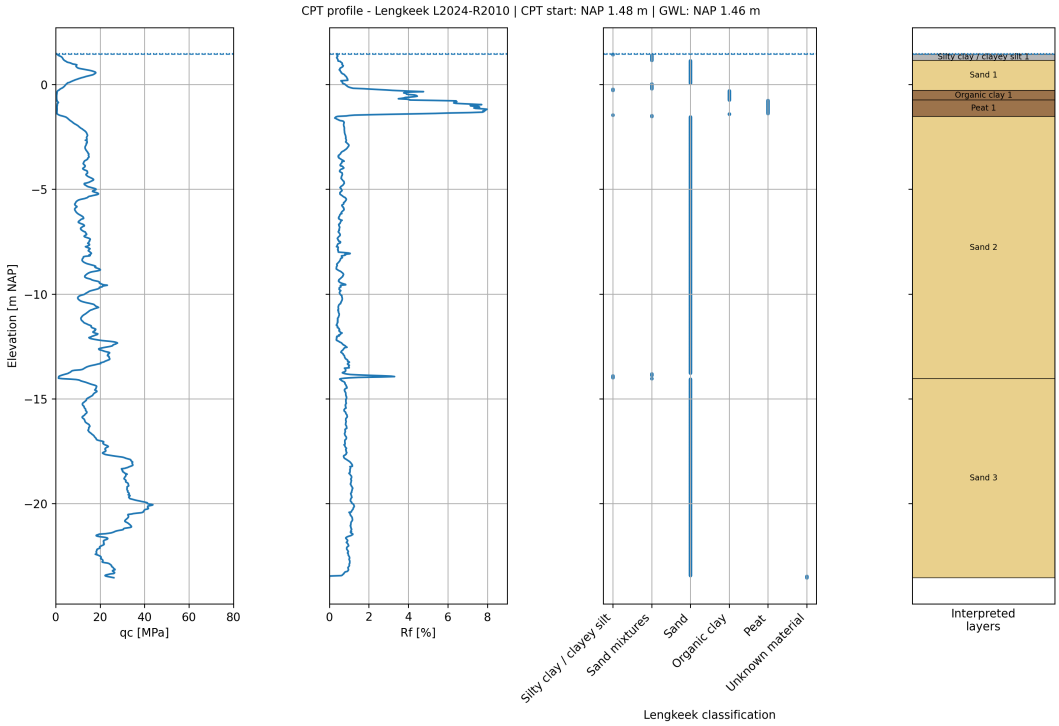

Figure 5.5: CPT measurement 1 before drilling B25.

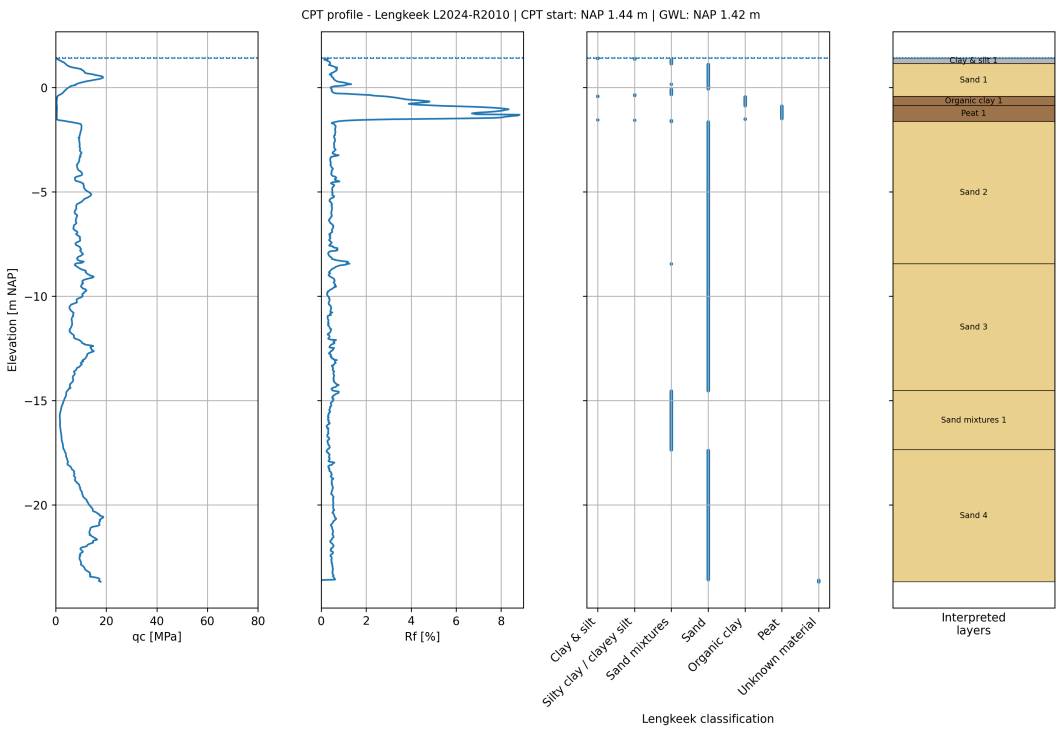

Figure 5.6: CPT measurement 6 after drilling B25.

Another observation from the figures is the difference in normalised cone resistance. CPT 6 contains a thicker sand mixture layer than the before drilling measurement. A sand mixture to silty clay interval can also be observed in CPT 1, although this interval is too thin to be classified as a separate layer

according to the minimum layer thickness criterion of 0.3 m. This shows that within small distances soil conditions can change.

5.2. Soil behaviour type

In the following section, the Robertson soil behaviour type charts are presented and discussed. Because the CPT measurements extend to different depths, the plots for each borehole were created using all sand layers down to the depth of the shallowest measurement. This allows the CPTs to be compared over the same depth interval, since deeper sand layers generally have higher normalised cone resistance.

The boreholes have been drilled with a diameter between 0.15 and 0.2 m. These boreholes are relatively small compared with the ATES borehole analysed in the Delft case study. According to the proposed numerical expression without the pile influence zone in Equation 4.4, and assuming a borehole diameter of 0.20 m with an initial void ratio below the critical value, the calculated borehole vertical stress influence distance is 0.5 m. Therefore large changes in the CPT soil behaviour are not expected at horizontal distances greater than 1 m.

5.2.1. Wezep

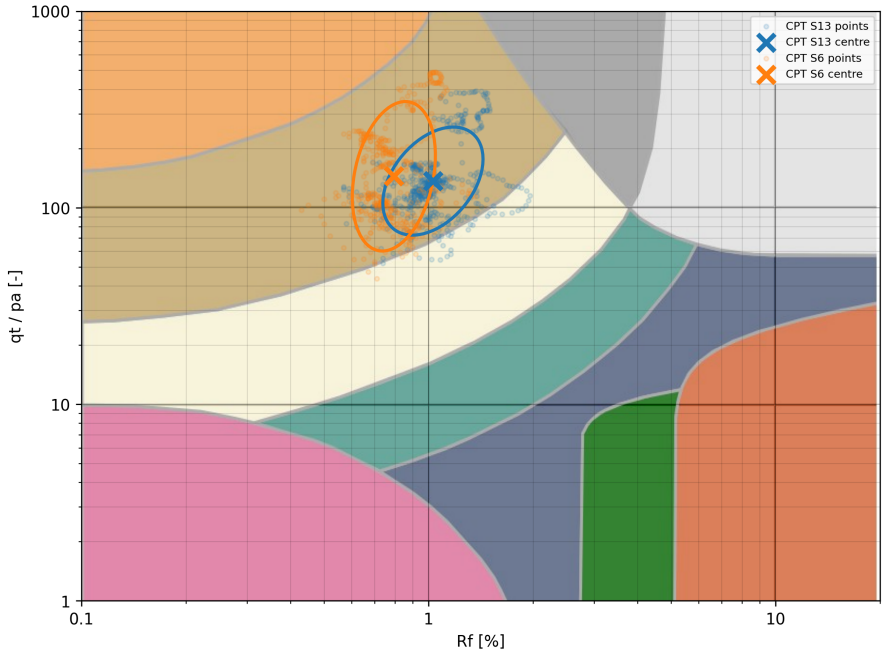

(a) Robertson chart with 68.3% confidence ellipses for B9.

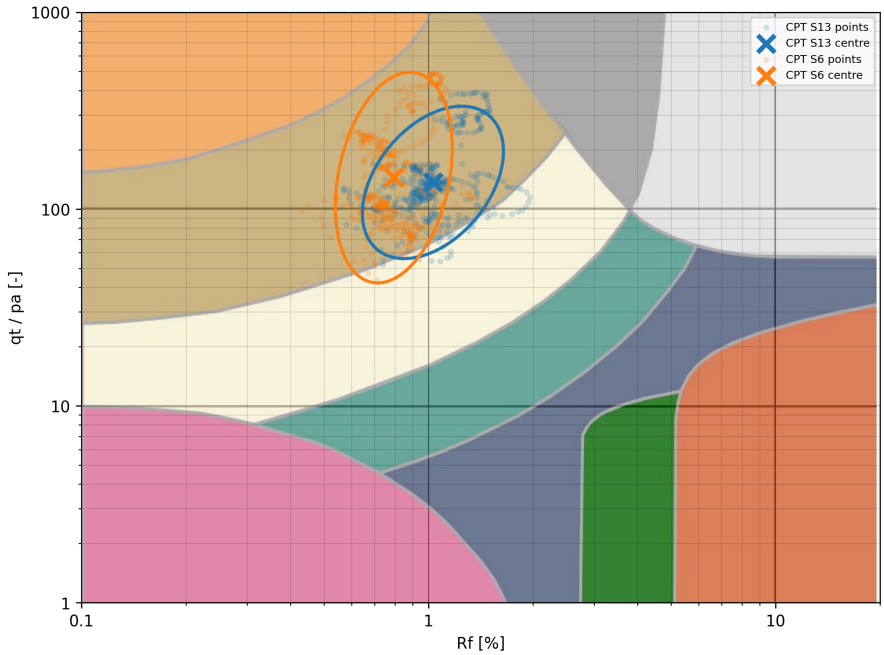

(b) Robertson chart with 90% confidence ellipses for B9.

Figure 5.7: Robertson classification for all sand layers in B9 using 68.3% and 90% confidence ellipses with S6 before and S13 after drilling.

Figure 5.7 shows the Robertson soil behaviour type plots for the CPTs around B9. Both CPT measurements are located almost 4 m from the borehole. The mean normalised cone resistance values are comparable, while the mean friction ratio values differ. The confidence ellipses also have a different orientation, indicating a different spread and correlation of the points in the Robertson chart. CPT S13 contains more points classified as sand mixtures, but these intervals are not thick enough to form a separate interpreted soil layer when the minimum layer thickness of 0.3 m is applied. Because both

CPTs are located outside the calculated borehole influence distance, the observed differences cannot be used to identify borehole-induced changes. They are more likely related to natural spatial variability and local differences in soil composition.

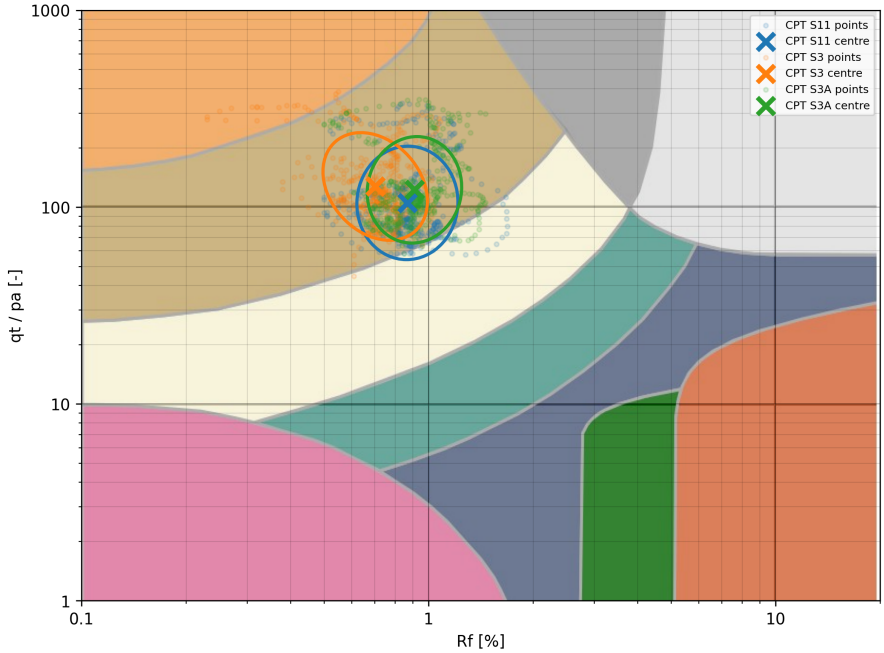

(a) Robertson chart with 68.3% confidence ellipses for B10.

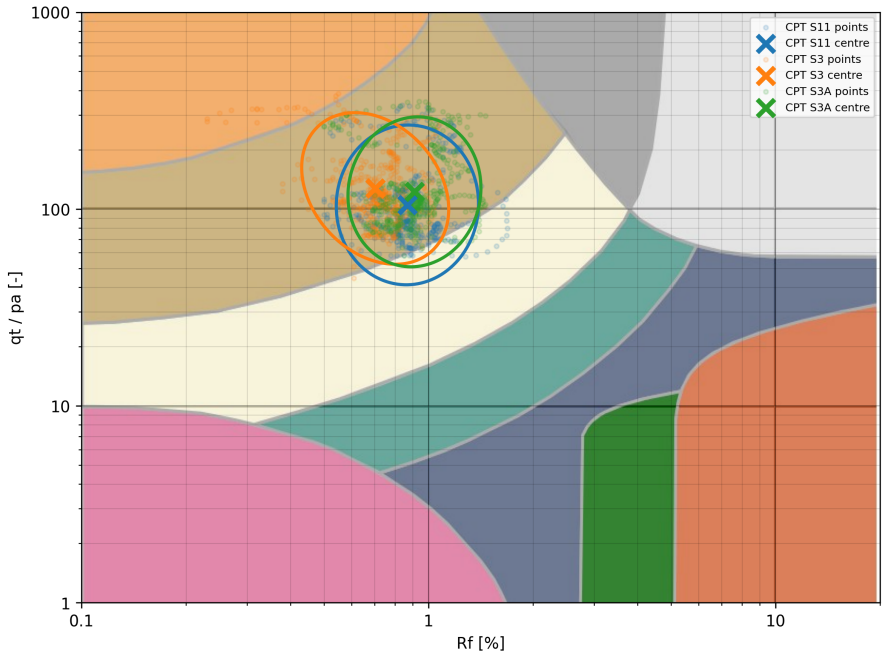

(b) Robertson chart with 90% confidence ellipses for B10.

Figure 5.8: Robertson classification for all sand layers in B10 using 68.3% and 90% confidence ellipses with CPT S3 and CPTs S3A and S11 after drilling.

Figure 5.8 shows the Robertson soil behaviour type plots for the CPTs around B10. CPTs S3 and S3A, which are 0.2 m apart, show similar mean normalised cone resistance values. However, they have very different friction ratio values. In the chart, CPT S3A is closer to S11 than S3 in terms of soil behaviour. This indicates significant spatial variation in the area when a minimum layer thickness of

0.3 m is applied. Nevertheless, identifying borehole-induced differences from these measurements is difficult, since all CPTs were performed more than 3.5 m from the borehole centre.

For both Wezep boreholes, the CPT measurements are located outside the calculated borehole influence distance. The distances are therefore too large to directly assess borehole-induced changes in soil behaviour. The observed differences should mainly be interpreted as part of the natural variability between CPT measurements and the sensitivity of the soil classification procedure. The Wezep results are not sufficiently close to the borehole to be used as comparison or validation.

5.2.2. Zwolle

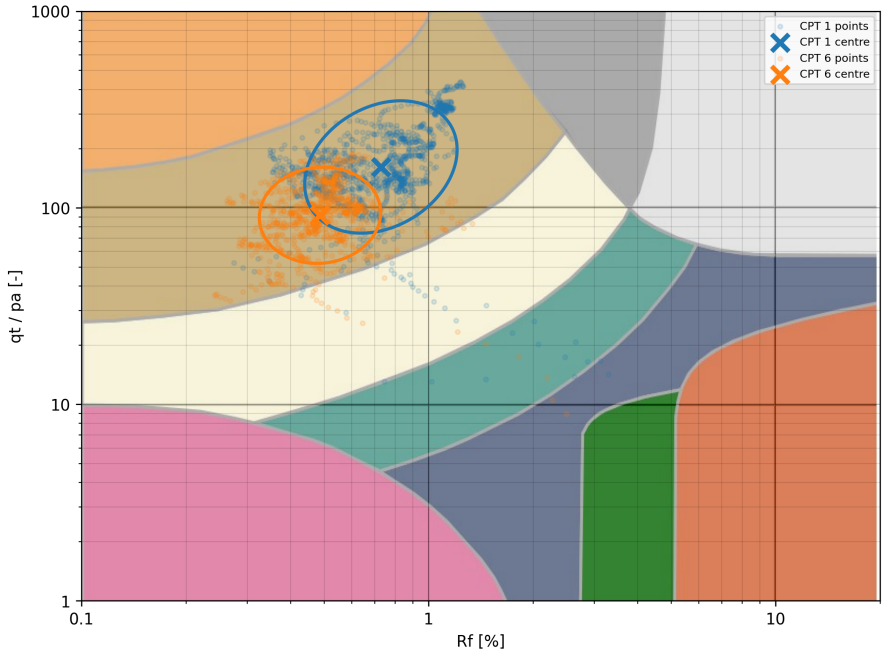

(a) Robertson chart with 68.3% confidence ellipses for B25.

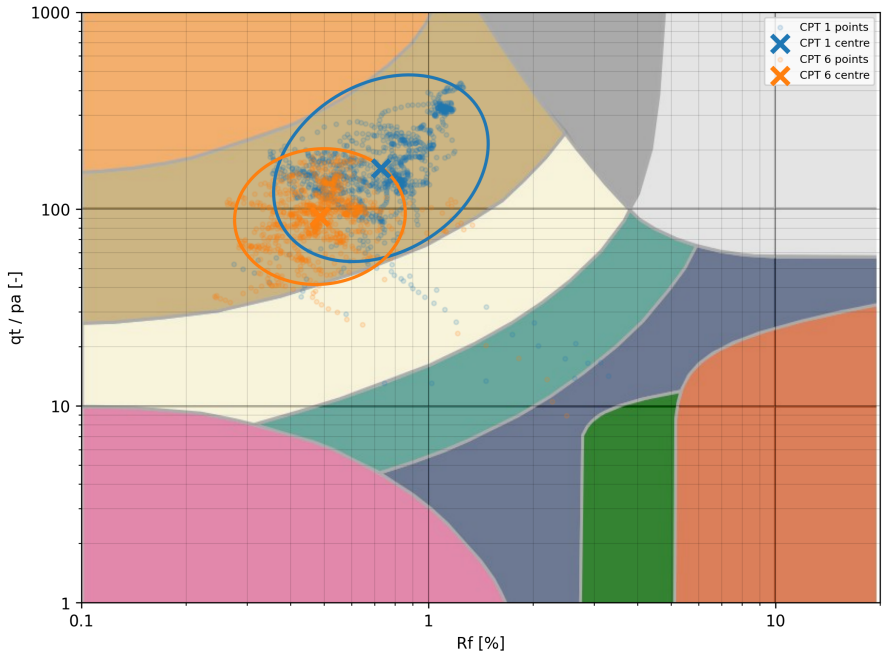

(b) Robertson chart with 90% confidence ellipses for B25.

Figure 5.9: Robertson classification for all sand layers in B25 using 68.3% and 90% confidence ellipses with CPT 1 before and CPT 6 after drilling.

Figure 5.9 shows the Robertson classification chart for B25. CPT 1 was performed before drilling at a distance of 0.96 m from the borehole, while CPT 6 was performed after drilling at a distance of 1.84 m. The Robertson plot shows a clear difference between the centre points of the two measurements. Since both CPTs are located outside the calculated borehole influence distance of 0.5 m, this difference cannot be directly attributed to borehole-induced stress changes. The difference is more likely related to spatial variability between the two CPT locations.

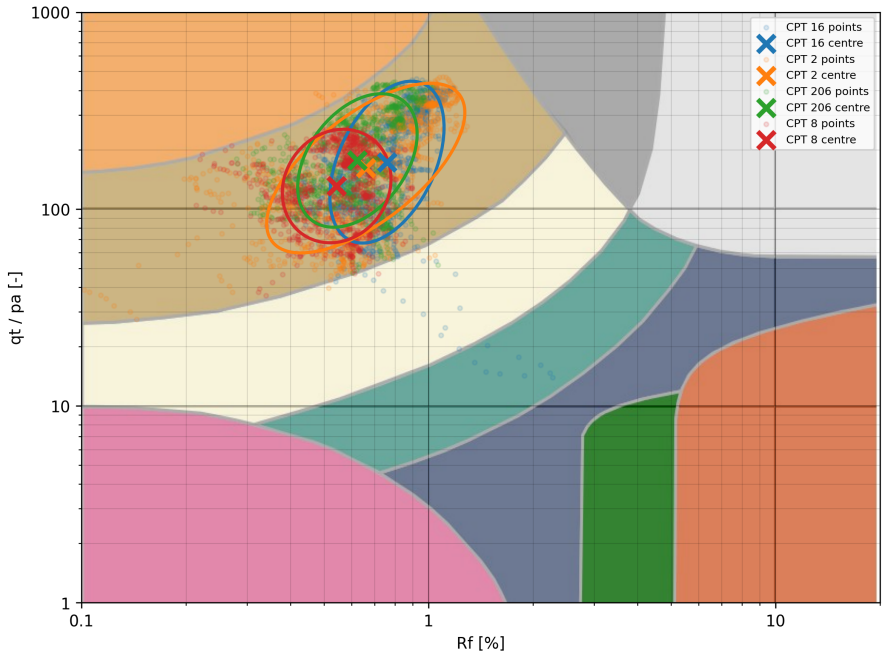

(a) Robertson chart with 68.3% confidence ellipses for B26.

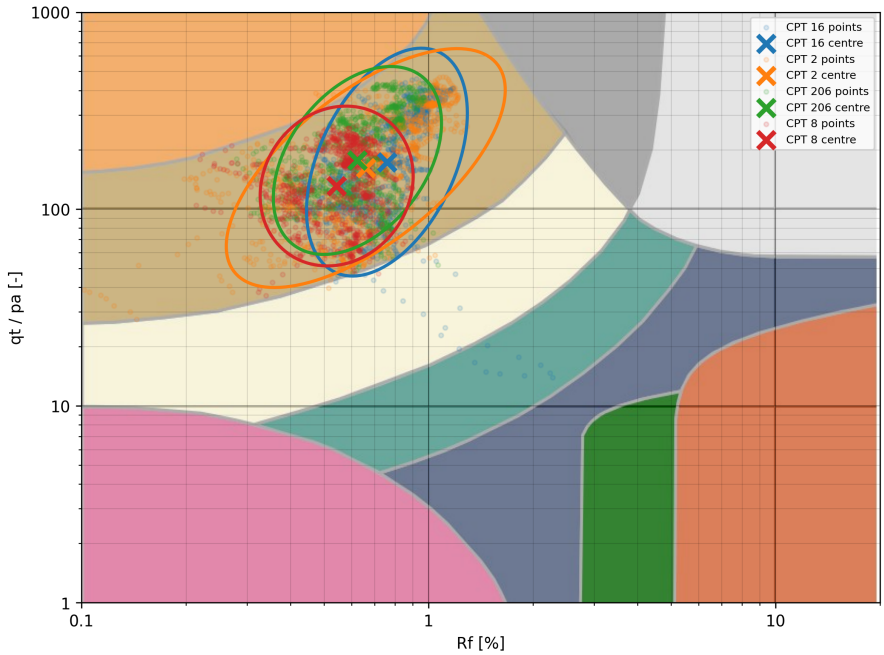

(b) Robertson chart with 90% confidence ellipses for B26.

Figure 5.10: Robertson classification for all sand layers in B26 using 68.3% and 90% confidence ellipses with CPT 2 before and CPTs 8,16 and 206 after drilling.

Figure 5.10 shows the Robertson classification chart for B26. CPT 2 was performed before drilling at a distance of 1.11 m, while CPTs 8, 16 and 206 were performed after drilling at distances of 0.24 m, 1.46 m and 1.83 m, respectively. CPT 2, CPT 16 and CPT 206 show broadly comparable centre points in the Robertson chart, despite being located on different sides of the borehole. CPT 8, located at 0.24 m from the borehole, shows lower normalised cone resistance and a lower friction ratio than the other CPTs. Since CPT 8 is located inside the calculated borehole influence distance, this result may indicate a borehole-induced effect. However, because only one CPT is located within this distance, the observed shift cannot be confirmed as borehole-induced.

The result of CPT 8 is relevant because Houlsby and Hitchman (1988) found that normalised cone resistance in sand is strongly influenced by horizontal stress and friction angle. The SANISAND simulations in Section 4.2.3 also showed that the horizontal stress influence zone, represented as radial stress, extends further than the vertical stress influence zone. The reduction in normalised cone resistance and friction ratio could therefore be explained by a reduction in radial stress around the borehole. This could be an indication of borehole-induced stress changes measured with CPT.

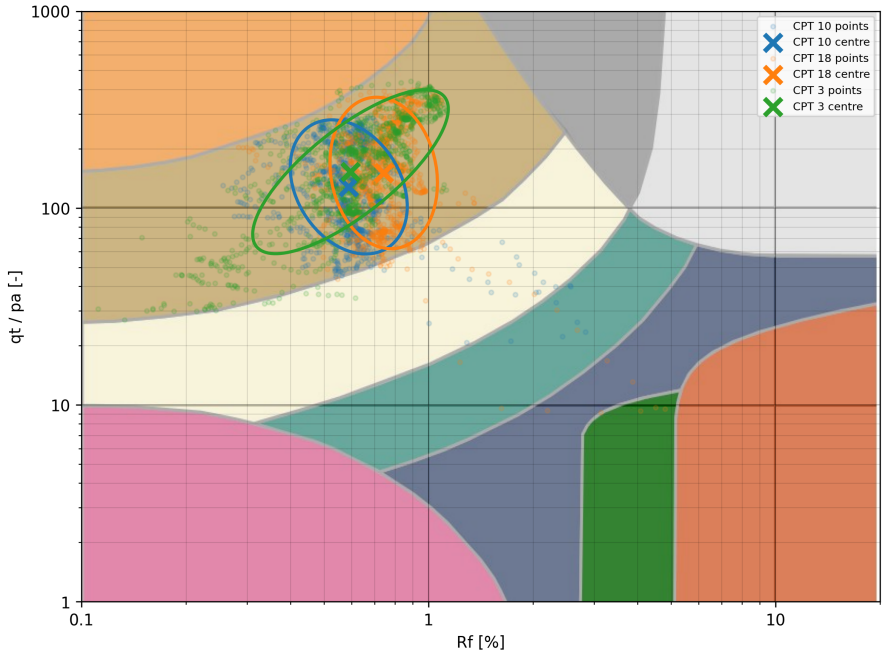

(a) Robertson chart with 68.3% confidence ellipses for B52.

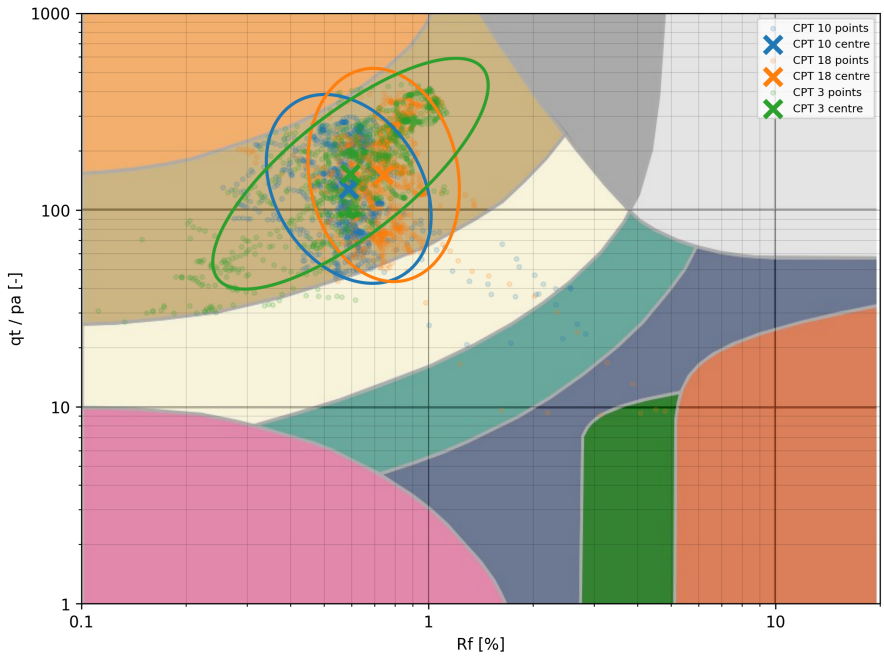

(b) Robertson chart with 90% confidence ellipses for B52.

Figure 5.11: Robertson classification for all sand layers in B52 using 68.3% and 90% confidence ellipses with CPT 3 before and CPTs 10 and 18 after drilling.

Figure 5.11 shows the Robertson classification chart for B52. CPT 3 was performed before drilling at

a distance of 1.12 m, while CPTs 10 and 18 were performed after drilling at distances of 0.23 m and 1.45 m, respectively. CPT 10 is located within the calculated borehole influence distance and shows a lower mean normalised cone resistance than the measurements further from B52. This is similar to the observation made for CPT 8 near B26. However, a clearly differently shaped confidence ellipse from the other measurements is not clear as it is similar to that of CPT 18. This is relevant because CPT 18 is located outside the predicted borehole-affected zone. The B52 result supports the observations made for B26, where normalised cone resistance and friction ratio reductions are observed close to the borehole. However, the role of spatial variability should not be overlooked.

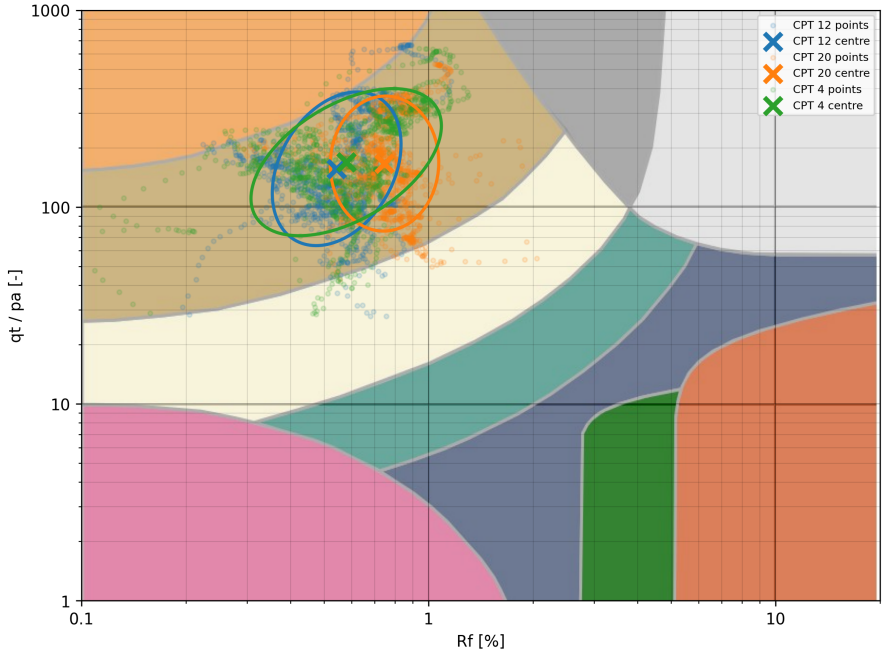

(a) Robertson chart with 68.3% confidence ellipses for B55.

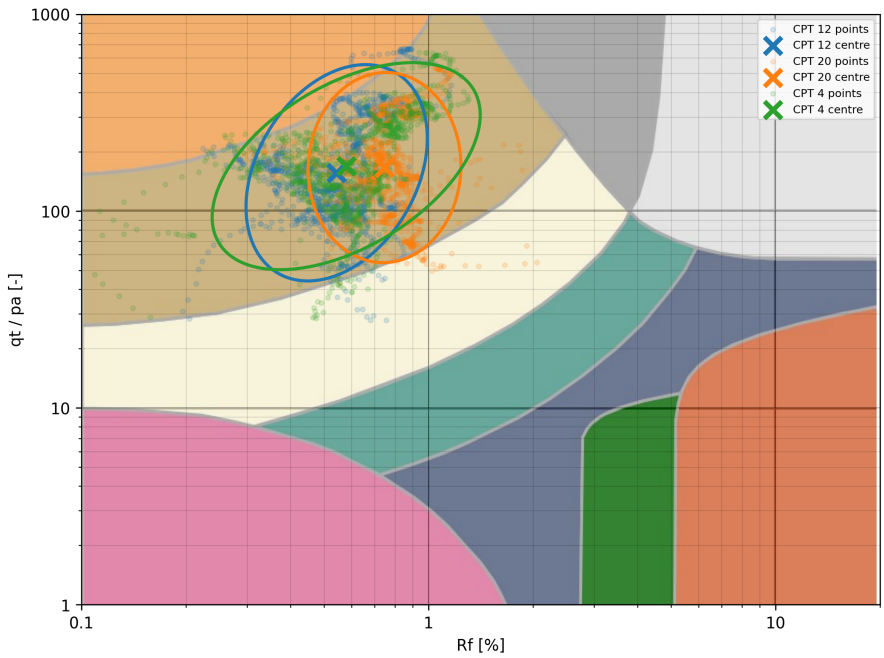

(b) Robertson chart with 90% confidence ellipses for B55.

Figure 5.12: Robertson classification for all sand layers in B55 using 68.3% and 90% confidence ellipses with CPT 4 before and CPTs 12 and 20 after drilling.

Figure 5.12 shows the Robertson classification chart for B55. CPT 4 was performed before drilling at a distance of 0.86 m, while CPTs 12 and 20 were performed after drilling at distances of 0.52 m and 1.76 m, respectively. CPT 12 is located just outside the vertical stress influence zone of the borehole, but shows a slightly lower normalised cone resistance than CPT 4 and 20. This observation is consistent with the trend observed for B26 and B52, where the closest CPTs showed lower normalised cone resistance. Considering that CPT 12 is located outside the calculated vertical stress influence distance, the reduction in normalised cone resistance may be related to the larger influence distance of the radial stress.

Overall, the Zwolle case study results indicate that near borehole CPT measurements may detect changes in soil behaviour, especially through reductions in normalised cone resistance and friction ratio. The observations are consistent with reduction of normalised cone resistance and friction ratio within the influence distance, and the possibility that the radial stress influence zone extends further than the vertical stress influence zone. This would explain why some CPTs just outside the vertical stress influence distance show lower normalised cone resistance and friction ratio.

However, the Zwolle results cannot be used as direct validation of the proposed minimum distance. As for none of the boreholes there is a pair of before and after CPT available within the calculated influence zone. In addition, natural spatial variability is clearly present between CPTs located outside the influence zone. The observed reductions should therefore be interpreted as possible indications of borehole-induced stress changes, not as confirmed effects. An increase in measurements within the borehole influence zone would reduce the uncertainty in spatial variability.

The practical relevance of these reductions depends on whether they affect the calculated pile bearing capacity. In the Koppejan method, the cone resistance used for pile base resistance is capped at 15 MPa. Therefore, a small reduction in cone resistance may not influence the calculated pile base resistance if the averaged cone resistance remains above this cap. Since the average cone resistance in the Delft foundation pile sand layer is above 15 MPa, it should be checked whether borehole-induced reductions would still remain above the capped value in the foundation pile sand layer. If this is the case, the reduction may be measurable in the CPT but not governing for the calculated pile base resistance. This is significant as measured reductions outside the newly proposed rule-of-thumb do not affect predicted pile bearing capacity.

6

Discussion and limitations

This chapter discusses the strengths and weaknesses of the CPT interpretation method and the numerical modelling approach, the interpretation of their results. The chapter is divided into three sections. Section 6.1 presents the interpretation of results. Section 6.2 discusses the limitations in the analysis, interpretation and output. Section 6.3 discusses the practical implications of the proposed approach.

6.1. Interpretation of results

6.1.1. Delft CPT soil classification

The CPT soil classification resulted in comparable soil profiles for the four CPT locations. All profiles show the same general stratigraphy: shallow organic and fine-grained deposits, followed by the first sand layer, alternating organic, clay and silt layers, and finally the foundation pile sand layer. This similarity is important because it indicates that the CPTs are located within the same general geological setting. The observed differences between the CPTs are mainly related to local layer thickness, thin intermediate layers and variation within the deeper sand layer.

The interpreted profile corresponds with the typical deltaic soil build-up in South Holland, where shallow organic and clayey deposits are commonly found above deeper sand layers. The soil classification also agrees reasonably well with the interpretation made by Witteveen+Bos. The main layer boundaries were similar, while the differences mainly occurred in thin layers and near layer transitions. This supports the conclusion that the classification method captured the main stratigraphy correctly in comparison to the company software.

Spatial variability is expected between CPT measurements because soil is not homogeneous. Small changes in layer thickness or soil composition can change cone resistance and shift a point from one soil behaviour class to another. This is especially relevant near soil layer transitions, therefore, the observed local differences are more likely related to natural variability and classification sensitivity than to nearby drilling.

The Robertson-Lengkeek classification provides an additional way to compare the CPTs. The measured points in the foundation pile sand layer remained within the same general soil behaviour region, and the mean values were close to each other. This is consistent with the interpreted soil profiles and suggests that the sand layer did not show a clear systematic change in behaviour after drilling. The small differences in the orientation and position of the confidence ellipses are therefore not sufficient to conclude that the borehole changed the soil behaviour. They are more likely caused by local variability in cone resistance and sleeve friction.

Overall, the CPT soil classification and soil behaviour type classification did not show clear systematic differences between the four CPTs. The main soil profile was consistent and the foundation pile sand layer remained within the same general region of the Robertson chart. This supports the interpretation that the observed local differences are mainly caused by spatial variability rather than by borehole installation.

6.1.2. CPT-based distance

The CPT-based interpretation resulted in a proposed borehole influence distance of $3.33D_b$. When the Koppejan pile influence zone is included, the corresponding proposed minimum centre-to-centre distance becomes:

$$S \geq 4.7D_{eq} + 3.33D_b \tag{6.1}$$

Without the Koppejan pile zone, the CPT-based distance is lower than the SIKB rule-of-thumb for all analysed borehole diameters. This is expected, because the CPT-derived borehole factor of 3.33 is smaller than the factor of 10 used in the SIKB rule. However, this comparison is incomplete from a foundation safety perspective, because it only considers the borehole influence zone and ignores the soil volume contributing to the bearing capacity of the pile.

When the Koppejan pile influence zone is included, the interpretation changes. For small borehole diameters and larger foundation piles, the CPT-based expression gives larger distances than the SIKB rule-of-thumb. This is caused by the pile influence zone, which becomes dominant when the borehole diameter is small. For larger borehole diameters, the borehole component becomes more important and the CPT-based expression gives smaller distances than the SIKB rule-of-thumb.

This result is consistent with the approach proposed by Bogaards (2025). That method also separates the pile influence zone from the borehole influence zone, instead of using only one distance factor based on borehole diameter. The difference is that the company proposal uses a pile contribution of $5D_{eq}$ and a borehole contribution of $2.5D_b$, whereas the CPT-based interpretation in this research uses $4.7D_{eq}$ and $3.33D_b$. The pile contribution is therefore comparable, but the borehole contribution derived from the CPT interpretation is larger. This makes the CPT-based proposal more conservative than the company proposal for the borehole component, but still less conservative than the SIKB rule-of-thumb for larger borehole diameters.

The CPT-based distance should be interpreted as an observational boundary. At the actual cone locations, no clear measurable change was observed in cone resistance, sleeve friction, normalised cone resistance or Robertson classification. This suggests that the borehole influence was no longer measurable at this distance. However, it does not prove that no stress redistribution occurred closer to the borehole. The cone trajectories show that the CPTs moved away from the borehole with depth, which means that the measurements were probably outside the main zone where the numerical model predicts stress changes. Therefore, the CPTs provide a useful outer boundary, but not a detailed validation of the stress distribution near the borehole wall.

The CPT-based proposal is therefore most useful for large borehole diameters, where the SIKB rule-of-thumb gives very large distances. For small borehole diameters, the CPT-based expression without pile zone gives very small centre-to-centre distances and should therefore be interpreted only as a borehole influence distance, not as a practical construction distance. With the Koppejan zone included, the method becomes more consistent because the foundation pile influence zone is included. A practical minimum centre-to-centre distance should still be considered for small boreholes to ensure a minimum level of safety with the surroundings.

The generality of the CPT-based distance remains limited. The factor $3.33D_b$ is based on the actual CPT measurement location and the absence of measurable changes at that location. It is therefore valid as a site-specific interpretation for the analysed soil profile, borehole geometry and cone trajectories. To apply this distance more generally, additional before-and-after CPT measurements at different sites and at smaller distances from the borehole are required.

6.1.3. Numerical model based distance

The numerical model-based interpretation resulted in a proposed borehole influence distance of $2.5D_b$ for initial void ratios below 0.8 and $3.0D_b$ for initial void ratios equal to or greater than 0.8. When the Koppejan pile influence zone is included, the proposed minimum distance becomes:

$$S \geq 4.7D_{eq} + D_n D_b \tag{6.2}$$

where D_n is the normalised diameter factor equal to 2.5 or 3.0, depending on the void ratio.

The numerical distance is smaller than the CPT-based distance. This is expected, because the numerical model defines the borehole influence zone from the recovery of vertical stress to 95% of the far-field value, whereas the CPT-based distance is derived from the actual measurement location. The CPT-based distance is therefore an observational outer boundary, while the numerical distance is a model-based estimate of where the stress redistribution difference becomes smaller than the selected criterion.

The numerical-based distance is also consistent with the stress redistribution observed in the model, where the affected zone is scaled with the borehole radius. This supports the use of a distance factor based on borehole diameter rather than one fixed absolute distance. It also explains why the proposed numerical distance becomes increasingly favourable compared with the SIKB rule-of-thumb for larger borehole diameters. The SIKB rule increases with $10D_b$, while the numerical interpretation suggests that the relevant borehole influence zone is closer to $2.5D_b$ to $3.0D_b$.

However, the numerical distance should not be interpreted as an exact physical boundary. The value depends on the selected stress criterion. In this research, the influence zone was defined as the distance where the vertical stress recovered to at least 95% of the far-field value. This is a practical engineering criterion, not a strict failure criterion. A different threshold would result in a different distance. The proposed factor should therefore be seen as a rule of thumb derived from the numerical response, rather than as an exact limit between affected and unaffected soil.

The choice of constitutive model is also important. The SANISAND model was used for the final interpretation because it is the most advanced constitutive model applied in this research and predicted the largest redistribution zone of the analysed material models. At the same time, the SANISAND parameters were not calibrated directly on the sand from the project location. The model parameters originate from a different sand in Ottawa, which means that the absolute stress and strain response may not fully represent the in-situ foundation pile sand layer. The model is therefore more reliable for interpreting the mechanism and relative influence distance than for predicting exact field values.

The distinction between void ratios below and above 0.8 should also be interpreted with caution. The larger distance for $e_{ini} \geq 0.8$ was introduced because the looser sand states showed a slightly larger affected zone. However, this conclusion was based on the first sand layer, because the foundation pile sand layer did not converge for all void ratios in the simulations. In addition, the comparison was made before complete removal of the borehole back pressure, with approximately 9% of the back pressure still present. The increase from $2.5D_b$ to $3.0D_b$ was therefore introduced as an additional safety margin. It accounts for the slightly larger affected zone observed in looser sand states and for the uncertainty caused by incomplete removal of the borehole back pressure. However, it should not be interpreted as the exact final convergence distance.

Without the pile zone, the numerical distance only describes the borehole-induced stress redistribution and gives very small distances for small boreholes. This is not sufficient for assessing the influence on a foundation pile. With the Koppejan zone included, the method becomes comparable in structure to the proposal by Bogaards (2025). The company proposal uses a borehole contribution of $2.5D_b$. This is equal to the numerical proposal for initial void ratios below 0.8, while the proposed value of $3.0D_b$ for initial void ratios equal to or greater than 0.8 is slightly more conservative. Compared with the original SIKB rule, both numerical variants remain less conservative for larger borehole diameters because the borehole contribution increases with $2.5D_b$ to $3.0D_b$ instead of $10D_b$.

Overall, the numerical model-based distance provides a mechanistic explanation for why the SIKB rule-of-thumb may be conservative for larger boreholes. The stress redistribution predicted by the model is localised and scales with borehole diameter. However, the result depends on model assumptions, non-site-specific SANISAND parameters, the selected void ratio range and the chosen stress recovery criterion. The numerical proposal should therefore be used as a practical engineering interpretation, not as a directly validated universal distance.

6.1.4. Additional case studies

The Wezep and Zwolle case studies were added to support the comparisons and observations made in the Delft case study. The stratigraphy of these case studies differs from that of Delft, because the interpreted soil profiles are more dominated by sand and contain only a relatively thin and shallow organic or fine-grained layer. Although the additional case studies do not have the same soil characteristics as the Delft case study, they provide useful comparison data for sand conditions.

The CPT interpretations for Wezep show the effect of spatial variability around a borehole. The selected CPTs were located within a radius of 4 m from the boreholes, but the closest measurement was still 3.16 m from the borehole centre. Because of these relatively large distances, the observed differences are unlikely to be caused by borehole installation and are more likely related to spatial variability. The Wezep measurements are therefore not suitable for determining whether the borehole influence zone can be detected using CPT measurements.

The Zwolle results provide a more relevant comparison because several CPTs were located close to the boreholes. Measurements showing lower corrected cone resistance were located within the radial stress influence zone, and all but one were also located within the vertical stress influence zone. This is consistent with the theoretical framework discussed earlier, where cone resistance and sleeve friction are sensitive to horizontal stress changes. Since radial stress represents the horizontal stress component and has a larger influence zone, it may explain the reduced corrected cone resistance measured at the point located outside the vertical stress influence zone. The Zwolle results may therefore indicate that CPT measurements can detect borehole-induced horizontal stress changes in the surrounding sand.

However, this interpretation cannot be confirmed with the available data. The measurements showing reductions in corrected cone resistance were performed after drilling and had no matching before drilling measurement within the influence zone. As a result, the observed reductions could reflect spatial variability rather than borehole-induced stress changes. The Zwolle results should therefore be interpreted as indications that are consistent with the expected stress response, not as direct validation of the proposed distance.

Overall, the additional case studies support the main interpretation that CPT differences must be evaluated carefully. Differences in cone resistance, sleeve friction or Robertson classification cannot automatically be attributed to drilling, because spatial variability can produce similar changes. The Wezep and Zwolle results therefore strengthen the need for close proximity CPT on the same location before and after drilling when attempting to validate borehole-induced effects in the field.

6.2. Limitations

6.2.1. Soil classification

A first limitation is the limited number of CPT measurements. The interpretation is based on four CPTs: two before drilling and two after drilling, placed at nominal distances of 2 m and 4 m from the borehole. This is sufficient to compare the general soil profile at the site, but it is limited for detecting small local changes caused by drilling.

The distance between the CPTs and the borehole is also important. The numerical model showed that the largest stress changes occur close to the borehole and decrease rapidly with distance. CPTs at 2 m and 4 m from the borehole were therefore too far away to measure the main stress redistribution zone.

Another limitation is that the CPTs were not repeated at the exact same location. Small differences in layer thickness, cone resistance or soil behaviour classification can therefore be caused by natural spatial variability. A more direct assessment of drilling-induced changes would require CPTs much closer to the borehole or repeated measurements as close as practically possible to the original cone trajectory.

The determination of relative density and void ratio also introduces uncertainty. The Robertson and Baldi methods gave different results for the analysed sand layers. This shows that the derived sand state depends strongly on the selected empirical method. Since no laboratory tests were available to

determine the minimum and maximum void ratios of the local sand, the calculated void ratios should be interpreted as CPT-based estimates rather than directly measured soil properties.

The assignment of soil parameters from the CPT interpretation is another limitation. The NEN-EN Table 2.B values were assigned using the average cone resistance over the interpreted layer. This means that lower cone resistance values near layer transitions are included in the layer average, which may reduce the assigned parameters for the stronger parts of the sand layer. In addition, the values were capped when the measured cone resistance exceeded the range given in the table. This avoids unsupported extrapolation, but it may underestimate the strength and stiffness of the foundation pile sand layer when the measured cone resistance is higher than the table range.

The layer interpretation itself also affects the parameter assignment. A minimum layer thickness of 0.3 m was used to avoid unnecessary subdivision of the soil profile. This gives a practical and stable soil profile for modelling, but thin weak or strong layers may be merged into thicker layers. The resulting soil parameters should therefore be interpreted as representative layer values rather than exact local values.

6.2.2. CPT-based distance

The main limitation of the CPT-based distance is that it depends on the actual cone trajectory. Although the CPTs were positioned at nominal distances of 2 m and 4 m, the cone moved laterally away from the borehole with depth. Therefore, the distance between the cone and the borehole changed over depth, and the evaluated distance had to be based on the actual cone position at the selected depth.

The CPT-based factor of $3.33D_b$ should therefore be interpreted as an observational boundary. It is based on the distance where no clear change was detected. The CPT data provide an outer limit for detectable changes, but not the exact radius of the borehole influence zone.

The CPT measurements only partly validate the numerical model. They support the interpretation that the borehole influence zone is localised, because no measurable changes were found at larger distances. However, they do not validate the magnitude or shape of the stress redistribution close to the borehole wall, where the numerical model predicts the largest changes.

6.2.3. Numerical model-based distance

The main limitation of the numerical model-based distance is that it depends on the selected constitutive model and material parameters. The SANISAND model was used because it includes state-dependent sand behaviour and gave the largest stress redistribution zone of the analysed models. However, the SANISAND parameters were not calibrated on the project sand, but were based on Ottawa sand. Differences in soil characteristics may therefore influence the actual stress redistribution around the borehole. The numerical distance should therefore be interpreted as a model-based estimate, not as a fully site-calibrated value. In addition, only the first sand layer and the foundation pile sand layer were analysed using multiple constitutive models. The other soil layers were modelled using the Linear Elastic model, which introduces uncertainty in the predicted response of the layers above the foundation pile sand layer.

The initial stress state and elastic parameters also introduce uncertainty. The numerical model uses assumed values for parameters such as Poisson's ratio and the horizontal stress ratio. These assumptions influence the initial stress distribution and the unloading response around the borehole. The same applies to the adopted minimum and maximum void ratios for the SANISAND model, which were based on Ottawa sand rather than laboratory tests on the project sand. These values affect the interpretation of the initial sand state and therefore the distinction between denser and looser sand behaviour.

The distinction between $2.5D_b$ and $3.0D_b$ also contains uncertainty. The larger distance for $e_{ini} \geq 0.8$ was based on the trend observed for looser sand states. However, this comparison was made in the first sand layer, because the foundation pile sand layer did not converge for all void ratios. In addition, the analysed phase was not the final unloading phase, since approximately 9% of the borehole back pressure was still present. The increase from $2.5D_b$ to $3.0D_b$ was therefore introduced as an additional safety margin and should not be interpreted as the exact final convergence distance.

All simulations were performed with initial void ratios below the calculated critical void ratio. Therefore,

the transition observed at $e_{ini} = 0.8$ should be interpreted as a behavioural change within the calibrated Ottawa sand, rather than a transition from dilative to contractive sand behaviour. To assess the transition to contractive behaviour, additional simulations would be required with initial void ratios above the critical void ratio.

Another limitation is the definition of the influence zone. In this research, the numerical distance was based on the point where the vertical stress recovered to at least 95% of the far-field value. This is a practical engineering criterion rather than a failure criterion. A different threshold would result in a different distance.

The model also simplifies the field situation. The borehole was modelled by staged unloading of the borehole wall pressure, while groundwater flow, drilling disturbance, time-dependent effects and volume loss were not explicitly modelled. The boundaries and mesh were idealised, and the pile itself was not included in the numerical model. As a result, the model describes the borehole-induced stress redistribution in the surrounding soil, but not the complete interaction between the borehole and an existing foundation pile.

6.2.4. Additional case studies

The Wezep and Zwolle case studies were analysed less extensively than the one in Delft. Only the soil classification and the Robertson soil behaviour type analysis were performed. The interpretation was based on the horizontal distance between CPT starting point and the borehole centre, rather than the actual position of the cone at depth.

Another limitation is that the CPTs did not always extend to the same depth. As a result, the comparison had to be limited to the overlapping depth interval. Comparing all sand layers over different depths would be misleading, because deeper sand layers may have higher cone resistance and different density. In addition, the measurements were compared by combining all sand layers from each CPT. This provides a general comparison, but may generalise layer specific behaviour. This simplification was made due to the limited time available for the additional case studies.

The additional case studies therefore provide qualitative support. They show that local variability can be significant and that CPTs close to boreholes can detect differences, but they cannot be used as direct validation of the proposed minimum distance.

6.3. Practical implications

6.3.1. CPT classification

The in-house CPT classification script provides a practical method for analysing CPT measurements in a consistent way. The script reads the CPT data, classifies the soil behaviour, generates interpreted soil profiles and plots the relevant CPT characteristics. This makes it possible to compare different CPTs objectively.

A practical advantage of this approach is that the classification is reproducible. The same classification rules, layer thickness criteria and plotting procedure are applied to each CPT. This reduces differences between individual interpretations and makes before-and-after comparisons easier to evaluate. The method is therefore useful as a first screening tool for any project in which soil behaviour and characteristics are important.

6.3.2. Borehole to foundation pile distance

The results show that the borehole influence zone and the pile influence zone should be considered in close proximity. This is important in practice, because the original SIKB rule does not account for the foundation pile diameter, while the proposed expressions include both D_b and D_{eq}.

For small borehole diameters, the expressions without the pile influence zone should not be used as direct pile distances. They only describe the borehole influence distance and can result in very small centre-to-centre distances. A minimum distance of 1.5 m is recommended as it is the first point where the proposed safe distance with Koppejan zone is smaller than that of SIKB rule-of-thumb. This distance can also account for visual, equipment positioning and general safety during drilling. Nevertheless, the direct effect of very small boreholes on pile bearing capacity of large piles is expected to be limited.

Borehole-induced stress redistribution scales with D_b and remains small, while large piles mobilise more resistance over its surface area.

Providing the borehole influence distance separately gives users flexibility in project specific assessments. The borehole contribution can be combined with a user defined influence zone for the nearby underground object. This allows the proposed approach to be applied beyond the specific pile-to-borehole case considered in this research.

When the Koppejan pile influence zone is included, the proposed expressions become more suitable for practical use. For small boreholes and larger piles, the pile influence zone can control the required distance. For larger borehole diameters, the proposed expressions can lead to smaller distances than the original SIKB rule, because the borehole contribution increases with a lower factor than $10D_b$. This makes the proposed approach especially relevant for larger ATES boreholes near existing pile foundations.

The proposed distances should therefore be used as engineering guidance rather than as absolute safety limits. They provide a more mechanically based interpretation of pile-to-borehole spacing, but they do not directly check pile settlement, rotation or bearing capacity loss.

7 Conclusion and recommendations

This chapter concludes the research. Section 7.1 summarises the findings. Section 7.2 presents the contribution to knowledge. Section 7.3 discusses the practical implications of the results. Section 7.4 outlines the limitations of this research. Section 7.5 presents recommendations for further research. Finally Section 7.6 presents the closing statement.

7.1. Summary of findings

This research investigated the minimum distance between an ATES borehole and nearby foundation piles in unconsolidated sand. The study combined CPT interpretation and numerical modelling to assess whether the existing rule-of-thumb can be reduced by assessing soil behaviour and stress redistribution around a borehole.

The Delft case study CPT interpretations showed no clear systematic change in cone resistance, sleeve friction, normalised cone resistance or Robertson classification after drilling. The soil profiles before and after drilling were comparable, the foundation pile sand layer displayed no difference in OCR. Local differences between the CPTs were more likely caused by spatial variability than by borehole installation.

The additional Wezep and Zwolle case studies supported the interpretation that CPT differences must be evaluated carefully. The Wezep measurements mainly showed the effect of spatial variability, because the CPTs were located too far from the boreholes to detect borehole-induced effects. The Zwolle measurements were closer to the boreholes and showed possible reductions in corrected cone resistance near the borehole. These observations are consistent with the expected stress response, but could not be validated because of lack of CPT measurements within the borehole influence sphere before drilling.

The CPT-based interpretation resulted in a borehole influence distance of:

$$S \geq 3.33 D_b \tag{7.1}$$

When the Koppejan pile influence zone is included, the corresponding proposed centre-to-centre distance becomes:

$$S \geq 4.7 D_{eq} + 3.33 D_b \tag{7.2}$$

The numerical model showed that the borehole-induced stress redistribution is localised and scales with borehole diameter. Based on the recovery of vertical stress to at least 95% of the far-field value, the proposed numerical borehole influence distance is:

$$S \geq D_n D_b \tag{7.3}$$

where $D_n = 2.5$ for initial void ratios below 0.8 and $D_n = 3.0$ for initial void ratios equal to or greater than 0.8. When the Koppejan pile influence zone is included, the proposed numerical distance becomes:

$$S \geq 4.7D_{eq} + D_n D_b \tag{7.4}$$

The results indicate that the original SIKB rule-of-thumb can be conservative for larger borehole diameters, because it scales only with borehole diameter and does not consider the foundation pile influence zone. The proposed expressions provide a more complete interpretation by considering the combined borehole and pile influence zones. This structure is consistent with the recommendation by Bogaards (2025), where the borehole influence zone and pile influence zone are also considered separately. The proposed expressions result in considerably lower recommended safe distances for larger borehole diameters, while for small borehole diameters the required distance may become larger because the foundation pile influence zone is included.

7.2. Contribution to knowledge

The main contribution of this research is that it provides a numerically based and field-supported interpretation of the pile-to-borehole distance. Instead of using only a single factor based on borehole diameter, the proposed approach considers the borehole-induced influence zone and the foundation pile influence zone.

The CPT-based interpretation provides an observational boundary where no measurable change in soil behaviour was detected. The numerical model provides a detailed explanation for the stress redistribution around the borehole. Together, these results support the conclusion that the SIKB rule-of-thumb can be conservative for larger borehole diameters when the foundation pile influence zone is not considered separately.

7.3. Practical implications

For practical application, the expressions including the Koppejan pile influence zone are preferred when assessing distances to foundation piles. The expressions without the pile influence zone describe only the borehole-induced influence distance. They should therefore not be used directly as construction distances to foundation piles, because they do not include the soil volume contributing to pile resistance.

A practical minimum centre-to-centre distance of 1.5 m is recommended before applying the proposed CPT-based or numerical model-based expressions. This distance should not be interpreted as a strict boundary, but as a practical lower limit for visual, equipment positioning and general safety. The responsible engineer may adjust this minimum distance when project specific circumstances justify, provided that the final distance still satisfies the proposed minimum safe distance expression. When the proposed expression gives a larger distance than 1.5 m, that larger distance should govern.

Providing the borehole influence distance separately also makes the methodology more versatile. This allows the approach to be adapted by the user to determine borehole interaction with other underground structures, provided that the influence zone of the nearby object is defined by the responsible engineer.

The proposed approach is especially relevant for larger ATES boreholes near existing pile foundations. In those cases, the original SIKB rule can lead to large required distances, while the proposed expressions provide a more specific assessment based on borehole diameter, pile diameter and soil behaviour.

7.4. Limitations

The conclusions should be interpreted within the limitations of this research. The CPT-based interpretation is based on four CPTs, located at nominal distances of 2 m and 4 m from the borehole. These distances were likely too large to measure the main stress redistribution zone close to the borehole. The CPT-based factor should therefore be interpreted as an observational boundary, not as the exact radius of the borehole influence zone.

The numerical model also contains uncertainty. The SANISAND parameters were not calibrated on

the project sand, but were based on Ottawa sand. In addition, the distinction between $2.5D_b$ and $3.0D_b$ depends on the selected void ratio range, the convergence of the numerical model and the chosen 95% vertical stress recovery criterion. The proposed numerical distance is therefore a practical engineering interpretation, not a universally validated boundary.

The interpretation of the void ratio boundary is also limited by the Ottawa sand. Because all the simulations were performed below the critical void ratio, the transition at $e_{ini} = 0.8$ should therefore be interpreted as a behavioural change within the Ottawa sand. To assess a transition from dilative to contractive behaviour, additional simulations with void ratios above the critical void ratio would be required.

The pile itself was not included in the numerical model. Therefore, the proposed expressions do not directly calculate pile settlement, rotation or bearing capacity loss. The Koppejan zone was added as an engineering interpretation of the pile influence zone, but the interaction between the borehole influence zone and the pile influence zone was not directly modelled.

The additional Wezep and Zwolle case studies were analysed less extensively than the Delft case study. Only the soil classification and Robertson soil behaviour type classification were performed. The results therefore provide qualitative support and cannot directly validate the proposed minimum distance.

7.5. Recommendations for further research

Further research should first focus on the proposed minimum distance in practice. A practical lower limit of approximately 1.5 m centre-to-centre distance is recommended before applying the proposed CPT-based or numerical model-based expressions.

The interaction between the borehole influence zone and the pile influence zone should be investigated in more detail. In this research, the two zones were treated as separate contributions. However, some overlap between both zones may be acceptable without directly causing loss of pile bearing capacity. The real required distance may therefore lie between the lower-bound case without pile influence zone and the conservative case where the full Koppejan zone is added.

Additional field measurements are required to validate this interpretation. More before and after CPTs should be performed at different distances from the borehole, especially closer to the borehole wall. This would make it possible to determine where measurable CPT changes start to occur and to better validate the numerical stress redistribution.

Laboratory testing should also be performed on sand from the project location. This would allow calibration of the SANISAND parameters, including the void ratio limits, critical state parameters and stiffness parameters. A site-calibrated model would reduce the uncertainty in the numerical influence distance.

Further research should also focus on the foundation pile influence zone. This research used the Koppejan method which has an equivalent diameter range of $0.7D_{eq}$ to $4D_{eq}$. In this research the mean was chosen, however, further research should investigate whether this range alters with pile geometry, pile type, loading conditions and soil state, including void ratio, relative density and stress state. Further numerical and field research is therefore required to determine whether the D_{eq} contribution can be refined for different foundation and soil conditions.

Finally, future field tests should consider direct strain measurements around the borehole. Optical fibre monitoring could be used to measure small strains during drilling and unloading. This would provide more direct evidence of the deformation field than CPT measurements alone and would improve validation of the numerical model.

7.6. Closing statement

This research shows that the minimum distance between an ATES borehole and a foundation pile should not be based only on borehole diameter. The borehole influence zone is localised, while the foundation pile influence zone depends on pile geometry. A combined approach using a practical minimum distance, a borehole influence factor and a pile influence zone provides a more rational basis for assessing borehole placement near existing pile foundations.

Bibliography

Addenbrooke, T. I., Potts, D. M., & Purnell, A. S. (2000). Displacement flexibility number for multi-propped retaining wall design. *Journal of Geotechnical and Geoenvironmental Engineering*, *126*(8), 718–726. https://doi.org/10.1061/(ASCE)1090-0241(2000)126:8(718)

Ahmadi, M., & Golestani Dariani, A. (2017). Cone penetration test in sand: A numerical-analytical approach. *Computers and Geotechnics*, *90*, 176–189. https://doi.org/https://doi.org/10.1016/j.compgeo.2017.06.010

Baldi, G., Belotti, R., Ghionna, N., Jamiolkowski, M., & Pasqualini, E. (1986). Interpretation of CPT and CPTU; 2nd part: Drained penetration of sands. *Fourth International Geotechnical Seminar*, 143–156.

Been, K., & Jefferies, M. G. (1985). A state parameter for sands. *Géotechnique*, *35*(2), 99–112. https://doi.org/10.1680/geot.1985.35.2.99

Bezuijen, A., & Van der Schrier, J. (1994). The influence of a bored tunnel on pile foundations. In C. F. Leung, F. H. Lee, & T. S. Tan (Eds.), *Proceedings of the international conference centrifuge 94* (pp. 681–686). A.A. Balkema.

Bjerrum, L. (1963). Allowable settlement of structures. *Proceedings of the European Conference on Soil Mechanics and Foundation Engineering*, *2*, 135–137.

Bogaards, J. (2025). *Second opinion eis 10 sikb protocol 2101_v2.0* (Prepared for SIKB). Royal HaskoningDHV. Delft, The Netherlands.

Burland, J. B., & Wroth, C. P. (1974). Settlement of buildings and associated damage [State of the Art Review]. *Proceedings of the Conference on Settlement of Structures*, 611–654.

Chen, L. T., Poulos, H. G., & Loganathan, N. (1999). Pile responses caused by tunneling. *Journal of Geotechnical and Geoenvironmental Engineering*, *125*(3), 207–215. https://doi.org/10.1061/(ASCE)1090-0241(1999)125:3(207)

Chong, S.-H., & Santamarina, J. C. (2016). Sands subjected to repetitive vertical loading under zero lateral strain: Accumulation models, terminal densities, and settlement. *Canadian Geotechnical Journal*, *53*(12), 2039–2046. https://doi.org/10.1139/cgj-2016-0032

Conrad Stanen B.V. (2024). COMBI 300 GT | Bodemenergie [Accessed: 2024-05-22]. https://www.conrad-stanen.nl/nl/producten/bodemenergie/combi-300-gt

CROW. (2022, January). Dwarscontractiecoëffiënt, ν [Geraadpleegd op 24 mei 2026]. https://kennisbank.crow.nl/public/gastgebruiker/GEO/Construeren_met_grond/Dwarscontractieco%C3%ABffici%C3%ABnt%2C_%CF%85/114239

Dafalias, Y. F., & Manzari, M. T. (2004). Simple plasticity sand model accounting for fabric change effects. *Journal of Engineering Mechanics*, *130*(6), 622–634. https://doi.org/10.1061/(ASCE)0733-9399(2004)130:6(622)

European Commission. (2026). European Climate Law [Accessed: 2026-06-15].

Firoozi, A. A., Firoozi, A. A., & Baghini, M. (2016). A review of clayey soils. *Asian Journal of Applied Sciences*, *4*, 2321–893.

Fjær, E., Holt, R., Horsrud, P., Raaen, A., & Risnes, R. (2008). Chapter 4 stresses around boreholes. borehole failure criteria. In E. Fjær, R. Holt, P. Horsrud, A. Raaen, & R. Risnes (Eds.), *Petroleum related rock mechanics 2nd edition* (pp. 135–174, Vol. 53). Elsevier. https://doi.org/https://doi.org/10.1016/S0376-7361(07)53004-9

Gaba, A. R., Simpson, B., et al. (2003). *Embedded retaining walls – guidance for economic design*. CIRIA.

Gao, Z., Kong, L., Chen, C., Wang, F., & Shang, Z. (2024). Small-strain stiffness properties of fissured clay with different fissure orientations. *Journal of Materials in Civil Engineering*, *36*(12), 04024401. https://doi.org/10.1061/JMCEE7.MTENG-17702

Gavin, K. (2025). Axial design of displacement piles in sand [Unpublished internal presentation; [CIEM2000, Base: Geotechnical engineering (2024/2025 Q2)]].

Gavin, K., Kovacevic, M. S., & Igoe, D. (2021). A review of cpt based axial pile design in the netherlands. *Underground Space*, *6*(1), 85–99. https://doi.org/https://doi.org/10.1016/j.undsp.2019.09.004

Gemeente Delft. (2025). *Resultaten monitoring 2024 grondwateronttrekking delft* (tech. rep.) (Accessed: May 2026). Gemeente Delft. https://www.delft.nl/sites/default/files/2025-08/resultaten-monitoring-2024-grondwateronttrekking-delft.pdf

Geoengineer.org. (n.d.-a). *Numerical modelling: The linear elastic model*. International Information Center for Geotechnical Engineers. Retrieved May 4, 2026, from https://www.geoengineer.org/education/numerical-constitutive-modeling/numerical-modelling-the-linear-elastic-model

Geoengineer.org. (n.d.-b). *Numerical modelling: The mohr-coulomb model*. International Information Center for Geotechnical Engineers. Retrieved May 4, 2026, from https://www.geoengineer.org/education/numerical-constitutive-modeling/numerical-modelling-the-mohr-coulomb-model

Grubben, T., Koulidis, A., van der Schans, M., Bloemendal, M., Hartog, N., Muraro, S., & Vardon, P. (2025). Investigating the stability of boreholes in sand [Under review. HAL Id: hal-05343997]. *3rd International Conference on Energy Geotechnics 2025*. https://hal.science/hal-05343997v1

Hashemi, S., Melkoumian, N., & Taheri, A. (2015). A borehole stability study by newly designed laboratory tests on thick-walled hollow cylinders. *Journal of Rock Mechanics and Geotechnical Engineering*, *7*. https://doi.org/10.1016/j.jrmge.2015.06.005

Houlsby, G. T., & Hitchman, R. (1988). Calibration chamber tests of a cone penetrometer in sand. *Géotechnique*, *38*(1), 39–44. https://doi.org/10.1680/geot.1988.38.1.39

Hughes, J. M. O., & Robertson, P. K. (1985). Full displacement pressuremeter testing in sand. *Canadian Geotechnical Journal*, *22*(3), 298–307. https://doi.org/10.1139/t85-041

International Organization for Standardization. (2017). Geotechnical investigation and testing — Identification and classification of soil — Part 1: Identification and description [Online standard sample preview]. https://cdn.standards.iteh.ai/samples/66345/eff3465a1c7246b9b6a723e9122a8770/ISO-14688-1-2017.pdf

Jaeger, J. C., Cook, N. G., & Zimmerman, R. (2009). *Fundamentals of rock mechanics* (4th). John Wiley & Sons.

Janbu, N. Soil compressibility as determined by oedometer and triaxial tests. In: In *Proceedings of the european conference on soil mechanics and foundation engineering*. *1*. 1963, 19–25.

Kaalberg, F., Teunissen, E., Tol, F., & Bosch, J. (2006). Dutch research on the impact of shield tunnelling on pile foundations. *16*. https://doi.org/10.1201/NOE0415391245.ch13

Korff, M. (2009). *Deformations and damage to buildings adjacent to deep excavations in soft soils: Literature survey f531* (tech. rep. No. 1001307-004-GEO-0002) (In cooperation with Centrum Ondergronds Bouwen (COB) and University of Cambridge). Deltares. Delft, Netherlands. https://publications.deltares.nl/1001307_004.pdf

Koulidis, A., Grubben, T. M., van Der Schans, M. L., Bloemendal, M., & Vardon, P. J. (2025). The impact of bridging additives on wellbore strengthening in shallow unconsolidated formations. *Groundwater*, *63*(2), 231–247.

Lehane, B. M., & Bittar, E. J. (2022). New cpt methods for evaluation of the axial capacity of driven piles. *Journal of Geotechnical and Geoenvironmental Engineering*, *148*(9). https://doi.org/10.1061/(asce)gt.1943-5606.0002847

Lehane, B. M., Jardine, R. J., Bond, A. J., & Frank, R. (1993). Mechanisms of shaft friction in sand from instrumented pile tests. *Journal of Geotechnical Engineering*, *119*(1), 19–35. https://doi.org/10.1061/(asce)0733-9410(1993)119:1(19)

Lehane, B. M. (2020). CPT-BASED DESIGN OF FOUNDATIONS. *Australian Geomechanics Journal*, *54*(4), 23–45.

Lengkeek, A. (2024). Cpt based classification with focus on organic soils [18-21 June 2024]. *Proceedings of the 7th International Conference on Geotechnical and Geophysical Site Characterization*.

Li, X. S., & Dafalias, Y. F. (2000). Dilatancy for cohesionless soils. *Géotechnique*, *50*(4), 449–460. https://doi.org/10.1680/geot.2000.50.4.449

Li, X. S., & Wang, Y. (1998). Linear representation of steady-state line for sand. *Journal of Geotechnical and Geoenvironmental Engineering*, *124*(12), 1215–1217. https://doi.org/10.1061/(ASCE)1090-0241(1998)124:12(1215)

Liu, H.-Y., Abell, J. A., Diambra, A., & Pisanò, F. (2019). Modelling the cyclic ratcheting of sands through memory-enhanced bounding surface plasticity. *Géotechnique*, *69*(9), 783–800. https://doi.org/10.1680/jgeot.17.p.262

Lunne, T., Eidsmoen, T., Gillespie, D., & Howland, J. D. (1986). Laboratory and field evaluation on cone penetrometers. *Proceedings of the ASCE Specialty Conference In Situ '86: Use of In Situ Tests in Geotechnical Engineering*, 714–729.

Manzari, M. T., & Dafalias, Y. F. (1997). A critical state two-surface plasticity model for sands. *Géotechnique*, *47*(2), 255–272. https://doi.org/10.1680/geot.1997.47.2.255

Marchetti, S. (2015). Some 2015 updates to the TC16 DMT report of 2001. *Proceedings of the 3rd International Conference on the Flat Dilatometer (DMT'15)*, 43–65.

Mayne, P. W. (2014). Interpretation of geotechnical parameters from seismic piezocone tests [Keynote Lecture KN2]. In P. K. Robertson & K. I. Cabal (Eds.), *Proceedings, 3rd international symposium on cone penetration testing (cpt'14, las vegas)* (pp. 47–73). http://www.cpt14.com

Misstear, B., Banks, D., & Clark, L. (2017). *Water wells and boreholes* (2nd). John Wiley & Sons.

Mroueh, H., & Shahrour, I. (2002). Three-dimensional finite element analysis of the interaction between tunnelling and pile foundations. *International Journal for Numerical and Analytical Methods in Geomechanics*, *26*(3), 217–230. https://doi.org/10.1002/nag.194

NEN. (2016). *Nen 9997-1: Geotechnical design of structures - part 1: General rules* (tech. rep.) (See Table 2.b). Netherlands Standardization Institute. Delft, The Netherlands.

Netzel, H., & Kaalberg, F. J. (2001). Monitoring of the North–South Metro line in Amsterdam. In M. S. Jardine & R. J. Standing (Eds.), *Response of buildings to excavation-induced ground movements: Proceedings of the international conference held at imperial college, london, uk* (pp. 243–255). Thomas Telford.

PatSnap. (2025). *What are the top geothermal drilling methods?* [Blog post]. PatSnap Eureka. Retrieved February 25, 2025, from https://eureka.patsnap.com/article/what-are-the-top-geothermal-drilling-methods

Peck, R. B. (1963). Deep excavations and tunneling in soft ground [State of the Art Volume]. *Proceedings of the 7th International Conference on Soil Mechanics and Foundation Engineering*, 225–290.

Polshin, D. E., & Tokar, R. A. (1957). Maximum allowable non-uniform settlement of structures. *Proceedings of the 4th International Conference on Soil Mechanics and Foundation Engineering*, *1*, 402–405.

Rankin, W. J. (1988). Ground movements resulting from urban tunnelling: Predictions and effects. In F. G. Bell, M. G. Culshaw, J. C. Cripps, & M. A. Lovell (Eds.), *Engineering geology special publication no. 5: Engineering geology of underground movements* (pp. 79–92). Geological Society. https://doi.org/10.1144/GSL.ENG.1988.005.01.06

Reyes, A., Taiebat, M., & Dafalias, Y. (2025). Modification of sanisand-msf model for simulation of undrained cyclic shearing under nonzero mean shear stress. *Journal of Geotechnical and Geoenvironmental Engineering*, *151*. https://doi.org/10.1061/JGGEFK.GTENG-12658

Risnes, R., Bratli, R. K., & Horsrud, P. (1982). Sand stresses around a wellbore. *Society of Petroleum Engineers Journal*, *22*(06), 883–898. https://doi.org/10.2118/9650-PA

Robertson, P. K. (2010a). Estimating soil unit weight from CPT. *Canadian Geotechnical Journal*, *47*(12), 1354–1363.

Robertson, P. K. (2016). Estimating K_0 in sandy soils using the cpt [Gregg Drilling & Testing, Inc., Signal Hill, CA, USA]. In B. M. Lehane, H. E. Acosta-Martínez, & R. B. Kelly (Eds.), *Geotechnical and geophysical site characterisation 5* (pp. 795–800). Australian Geomechanics Society.

Robertson, P. K., & Cabal, K. (2023). *Cone penetration testing guide to geotechnical engineering practice* (7th) [Available at ResearchGate]. Gregg Drilling LLC. https://www.researchgate.net/publication/370682668_CONE_PENETRATION_TESTING_GUIDE_TO

Robertson, P. K. (2009). Interpretation of cone penetration tests — a unified approach. *Canadian Geotechnical Journal*, *46*(11), 1337–1355. https://doi.org/10.1139/T09-065

Robertson, P. K., & Cabal, K. (2024). *Guide to cone penetration testing* (7th, Technical Manual). Gregg Drilling LLC. Signal Hill, CA. https://www.cpt-robertson.com/PublicationsPDF/CPT-Guide-7th-2024.pdf

Robertson, P. K. J. (2010b). Soil behaviour type from the cpt: An update. https://api.semanticscholar.org/CorpusID:15373054

Roylance, D. (2001). *Transformation of stresses and strains* (tech. rep.) (Course module for 3.11 Mechanics of Materials). Massachusetts Institute of Technology, Department of Materials Science and Engineering. Cambridge, MA. https://web.mit.edu/course/3/3.11/www/modules/trans.pdf

Sapkota, A. (2023). Chi-square test: Formula, uses, table, examples, uses [Accessed: June 13, 2026].

Seequent. (2024). *Plaxis 3d material models manual*. Seequent (A Bentley Systems Company). Delft, Netherlands. https://files.seequent.com/PLAXIS/Manuals/PLAXIS_3D/English/PLAXIS_3D_3_Material%20Models%20Manual.pdf

Skempton, A. W., & MacDonald, D. H. (1956). The allowable settlements of buildings. *Proceedings of the Institution of Civil Engineers*, *5*(6), 727–768. https://doi.org/10.1680/ipeds.1956.12202

Stichting Infrastructuur Kwaliteitsborging Bodembeheer (SIKB). (2021). *Beoordelingsrichtlijn mechanisch boren (brl sikb 2100), versie 4.1, 2 november 2021* [Version 4.1, 2 November 2021; available as PDF from SIKB]. SIKB. https://www.sikb.nl/doc/BRL2100/BRL_SIKB_2100_v4_1_20211102.pdf

Ter Linde, J. (1999). *Zakkingen van belendingen ten gevolge van het vervaardigen van diepwanden (Building settlements due to diaphragm wall installation)* [MSc Thesis]. Delft University of Technology.

Terzaghi, K., Peck, R. B., & Mesri, G. (1996). *Soil mechanics in engineering practice* (3rd ed.). John Wiley & Sons.

Timmermans Arribas, A. J. (n.d.). Borehole and cpt locations [Accessed: 2026-07-12]. https://www.google.com/maps/d/edit?mid=16SP7TC29iIosMrOv_ReXsFUeCuKHRt8&ll=52.48979567910877%2C6.0404654894999865&z=13

TNO – Geological Survey of the Netherlands. (2025). BRO REGIS II v2.2.3 [Visited on 2026-05-26]. https://www.dinoloket.nl/en/subsurface-models/map

TU Delft. (2026). Push-it: Accelerating the implementation of Sustainable Heat Storage [Accessed: 2026-06-15].

UNITRACC. (n.d.). Unconsolidated soil (lockergestein) [Accessed: 2026-03-04].

U.S. Navy. (1982). *Soil mechanics, design manual 7.01* (Design Manual). Naval Facilities Engineering Command (NAVFAC). Alexandria, VA.

van der Schans, M. L., van Loo, W., van Duijvenbode, M., de Ruiter, J., & Gunnink, J. L. (2022). Field testing of a novel drilling technique to expand well diameters at depth in unconsolidated formations. *Groundwater*, *60*(4), 539–550. https://doi.org/10.1111/gwat.13203

Witteveen+Bos. (2026). *Terraplus: Geotechnical data management and visualization platform* [Web application for soil survey data processing and CPT visualization. Accessed: 2026-06-16]. https://terraplus.app

Xometry. (2023). *Elastic limit: Definition, formula, and examples*. Xometry, Inc. Retrieved May 4, 2026, from https://www.xometry.com/resources/materials/elastic-limit/

Xu, C. (2012). Effect of grain bonding on the stability of a borehole drilled through low cemented formations [Accessed: 2025-02-25]. https://www.academia.edu/50429594/Effect_of_grain_bonding_on_the_stability_of_a_borehole_drilled_through_low_cemented_formations

Zainorabidin, A., & Wijeyesekera, D. C. (2008). Geotechnical characteristics of peat. *Proceedings of the International Conference on Construction and Building Technology (ICCBT)*, 271–282. https://resolver.tudelft.nl/uuid:63a9495f-1ddf-440e-a31e-49a3cf0d85c2

A

Soil classification

Classification	Description	SPT $(N_1)_{60}$ value[a]	D_r Relative Density[b]
Very loose	Easy to penetrated with a 12-mm diameter rod pushed by hand	< 4	0 - 15
Loose	Difficult to penetrate with a 12-mm diameter rod pushed by hand	4 - 10	15 - 35
Medium dense	Easy to penetrate 300 mm with a 12-mm diameter rod driven with a 2.3-kg (5-lb) hammer	10 - 17	35 - 65
Dense	Difficult to penetrate 300 mm with a 12-mm diameter rod driven with a 2.3-kg (5-lb) hammer	17 - 32	65 - 85
Very dense	Penetrated only about 150 mm with a 12-mm diameter rod driven with a 2.3-kg (5-lb) hammer	> 32	85 - 100

[a] These values are for sandy soils. If some fine gravel is present, use two-thirds of the field value. If significant quantities of coarse gravel are present, do not use this table.
[b] If CPT data is available, use Equation 4.25 to compute D_r

Figure A.1: United states navy Navy soil classification (U.S. Navy, 1982)

B

Soil distribution Delft

B.1. Soil profile

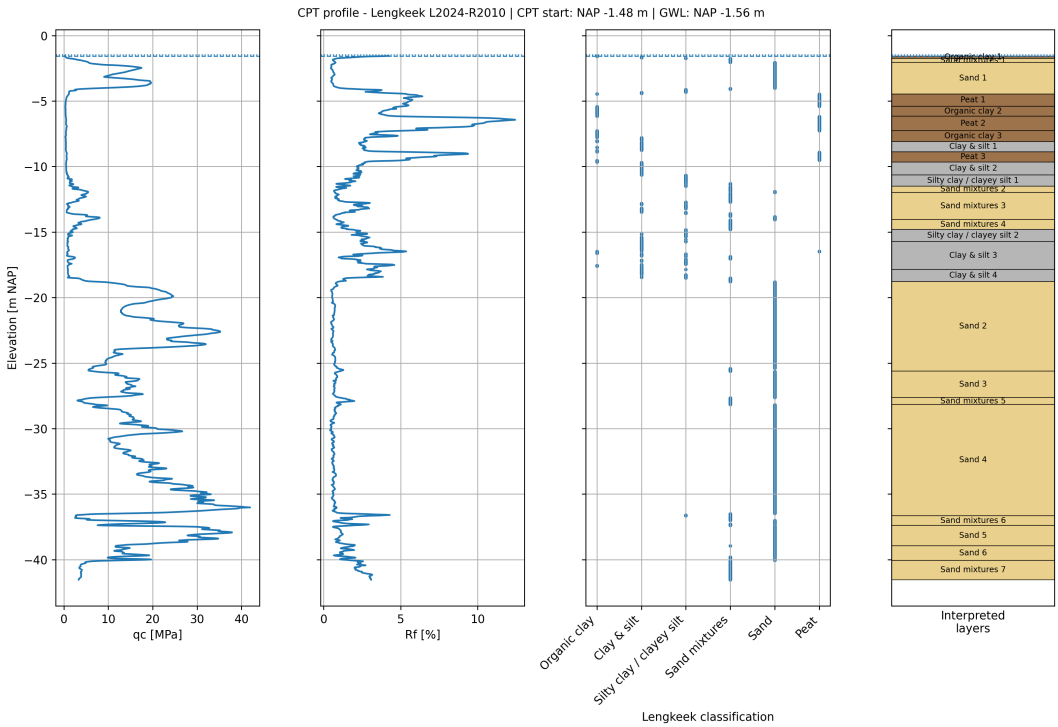

Figure B.1: Soil profile for CPT1-2.

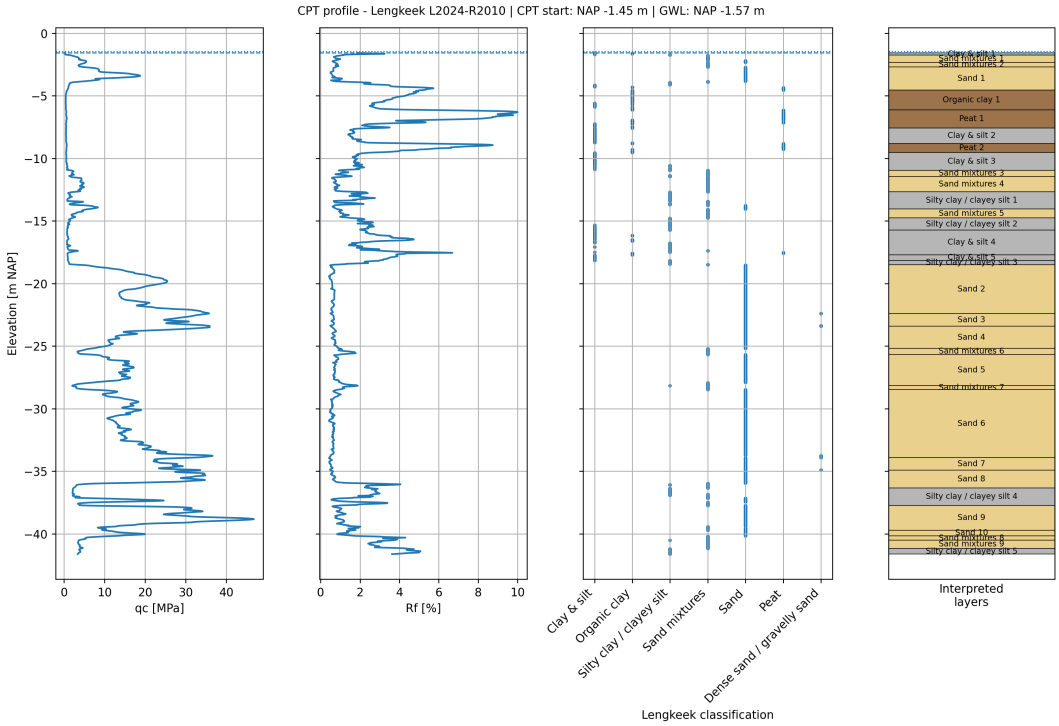

Figure B.2: Soil profile for CPT1-4.

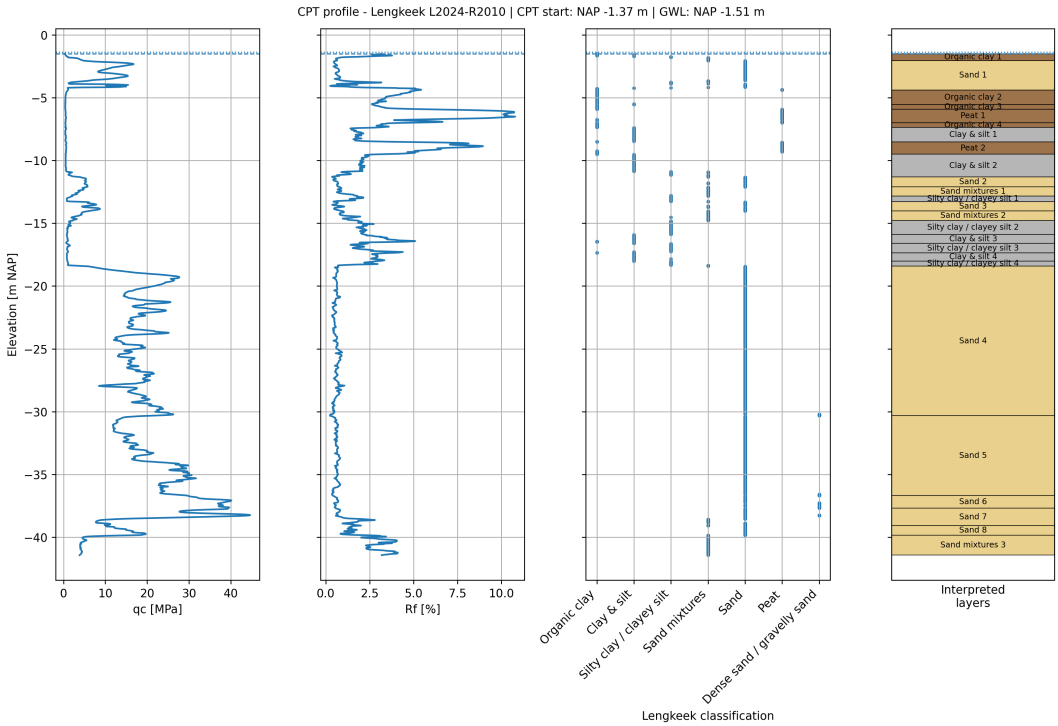

Figure B.3: Soil profile for CPT2-2.

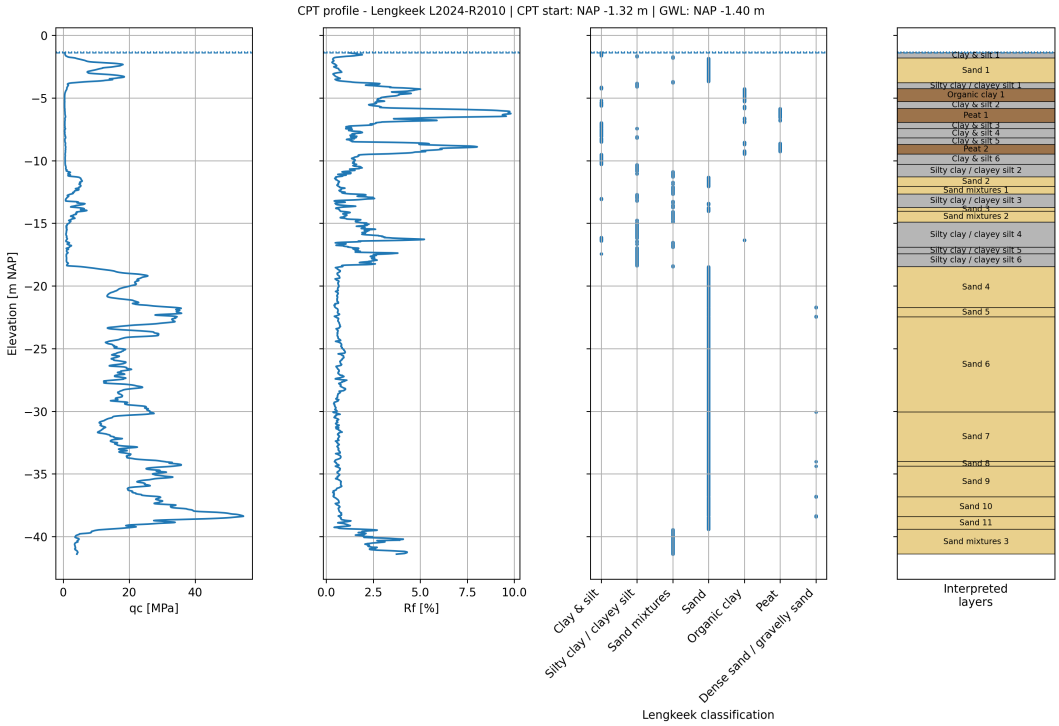

Figure B.4: Soil profile for CPT2-4.

B.2. Cone resistance delta

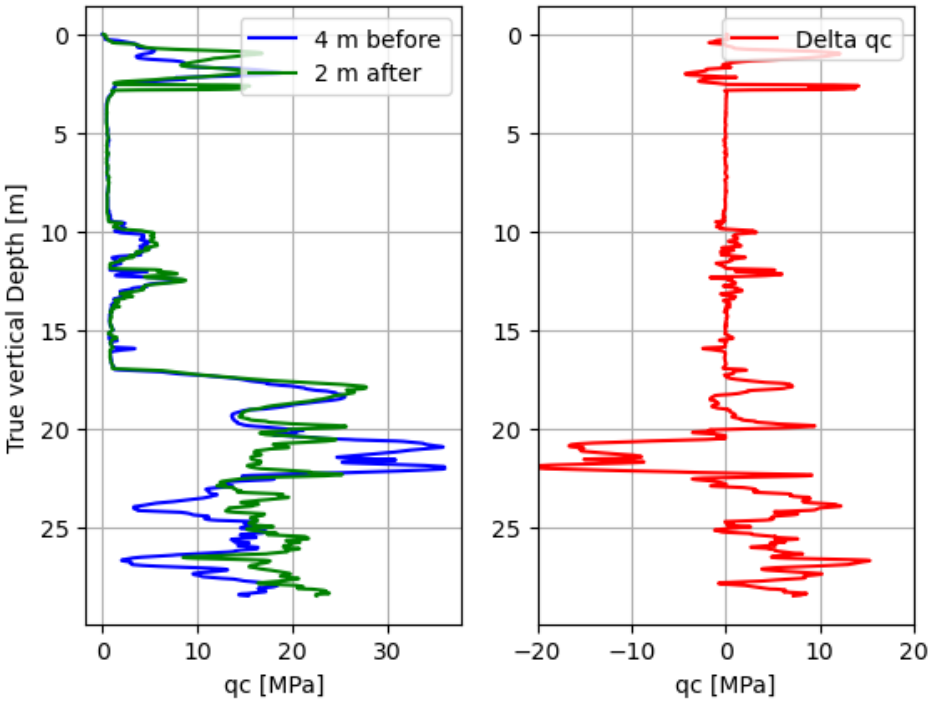

Figure B.5: Δq_c between 4 m before and 2 m after drilling.

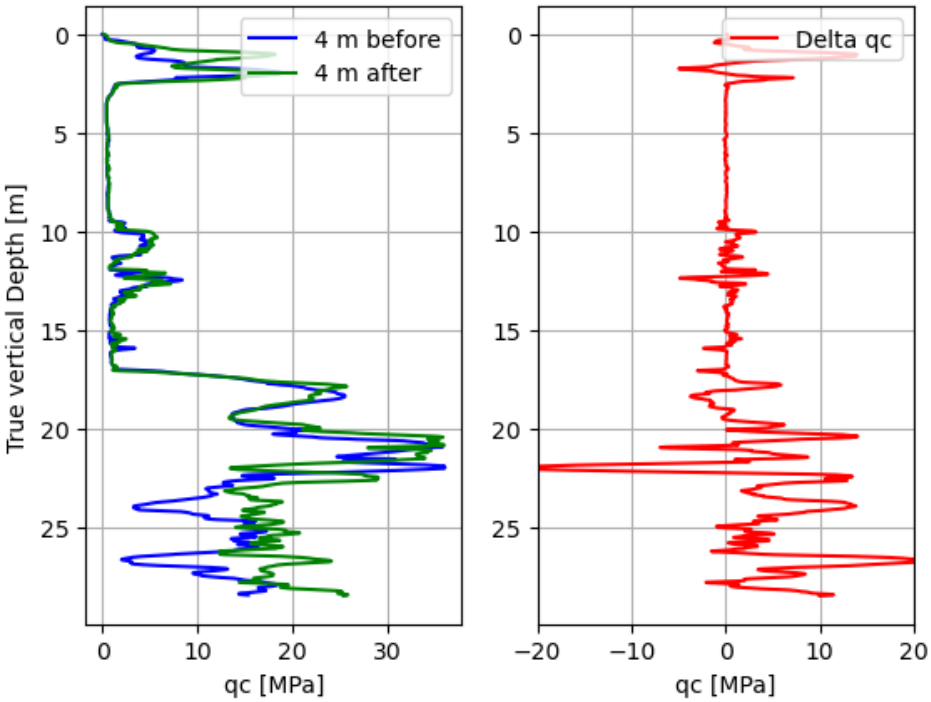

Figure B.6: Δq_c between 4 m before and 4 m after drilling.

B.3. Sleeve friction delta

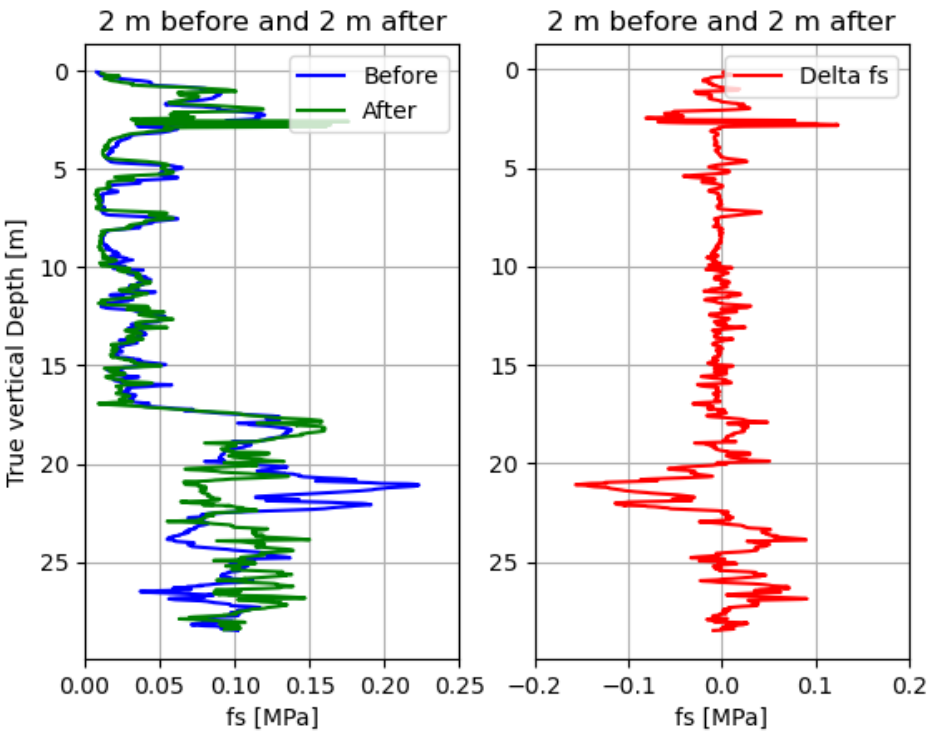

Figure B.7: Δfs between 2 m before and 2 m after drilling.

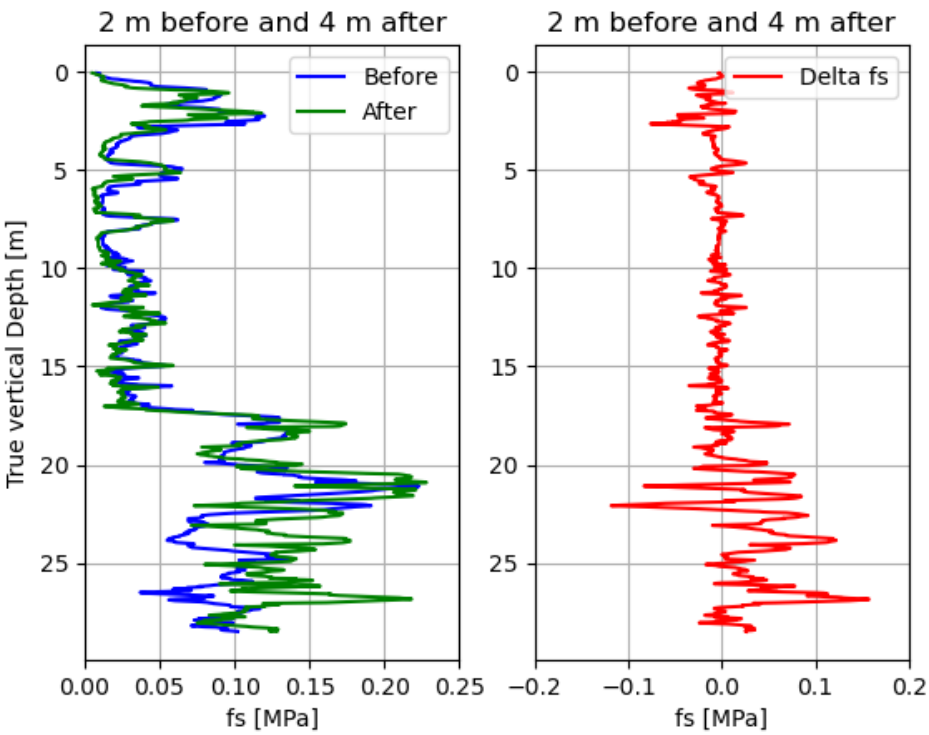

Figure B.8: Δfs between 2 m before and 4 m after drilling.

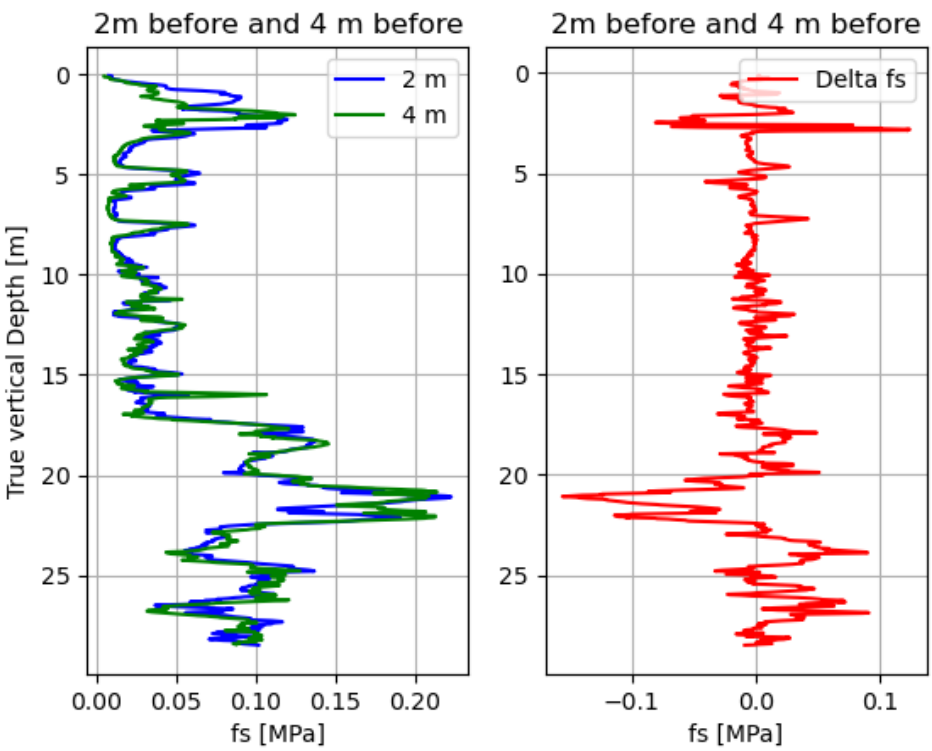

Figure B.9: Δfs between 2 m and 4 m before drilling

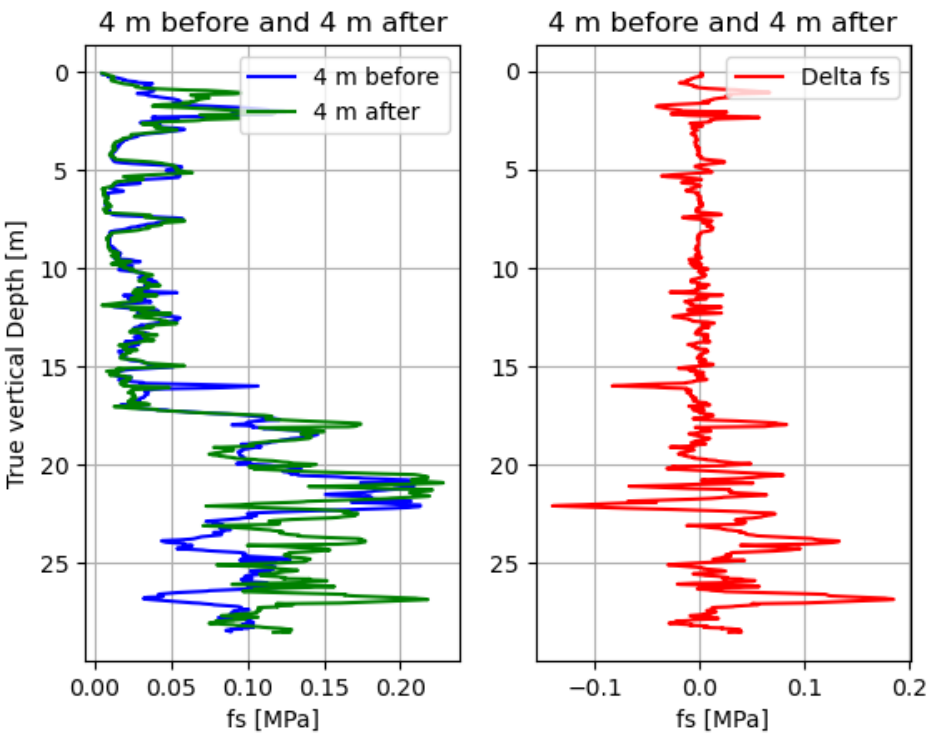

Figure B.10: Δfs between 4 m before and 4 m after drilling

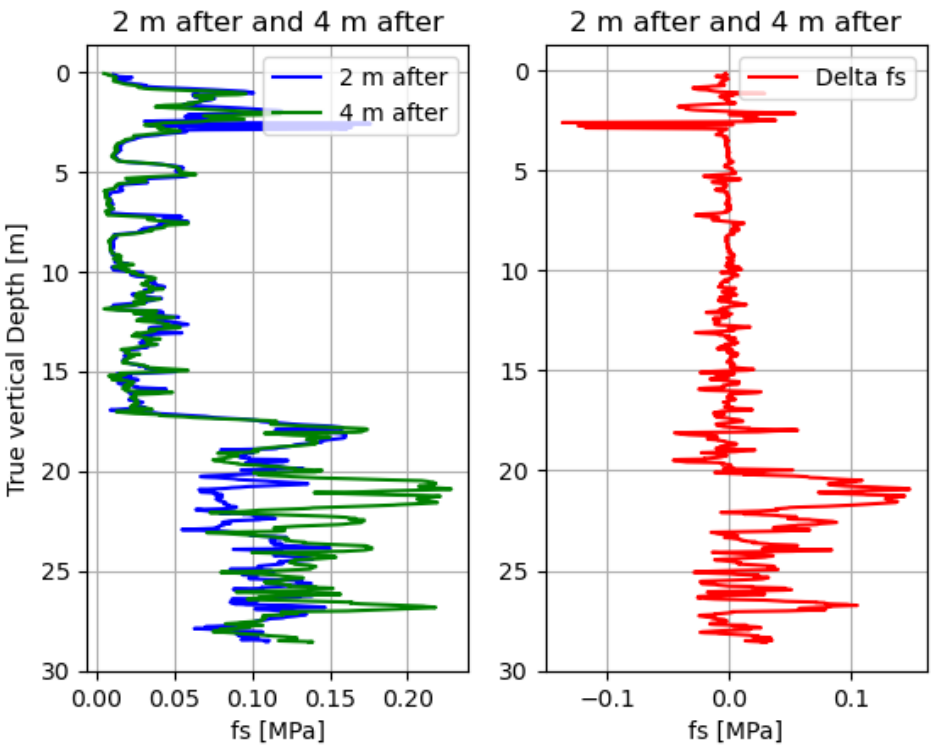

Figure B.11: Δfs between 2 m after and 4 m after drilling

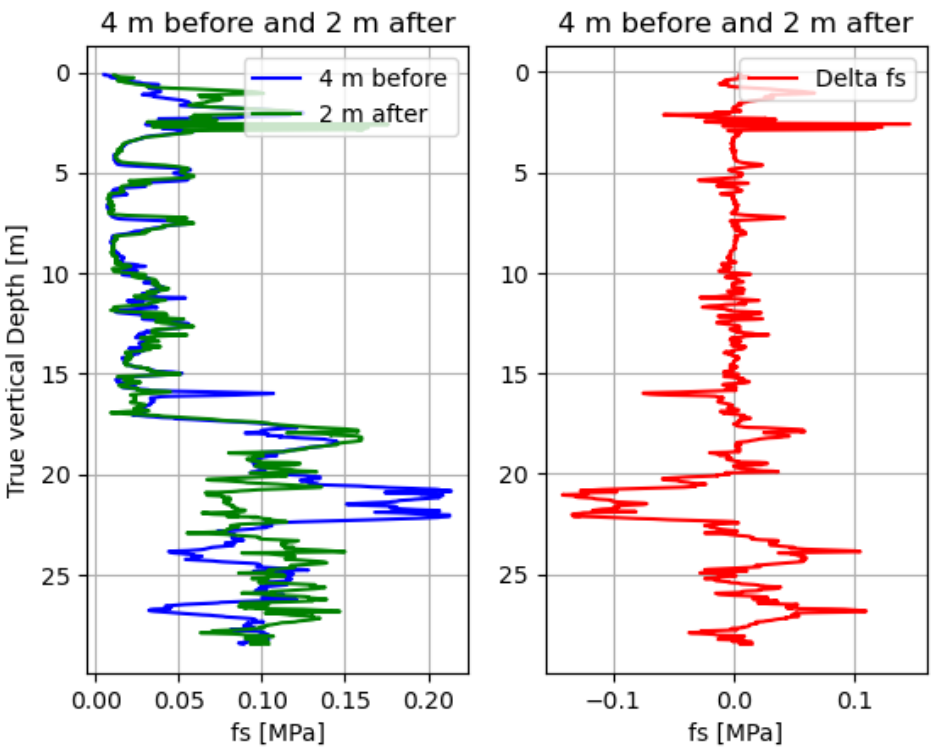

Figure B.12: Δfs between 4 m before and 2 m after drilling

B.4. Boxplots friction ratio in foundation pile sand layer

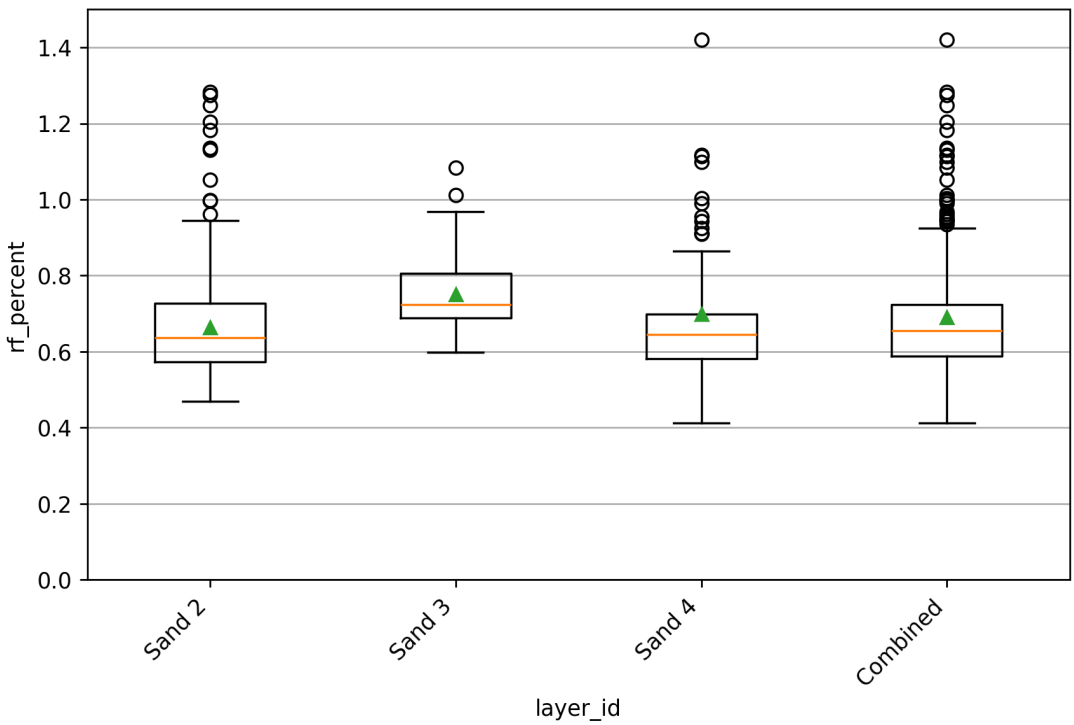

Figure B.13: Friction ratio for CPT1-2.

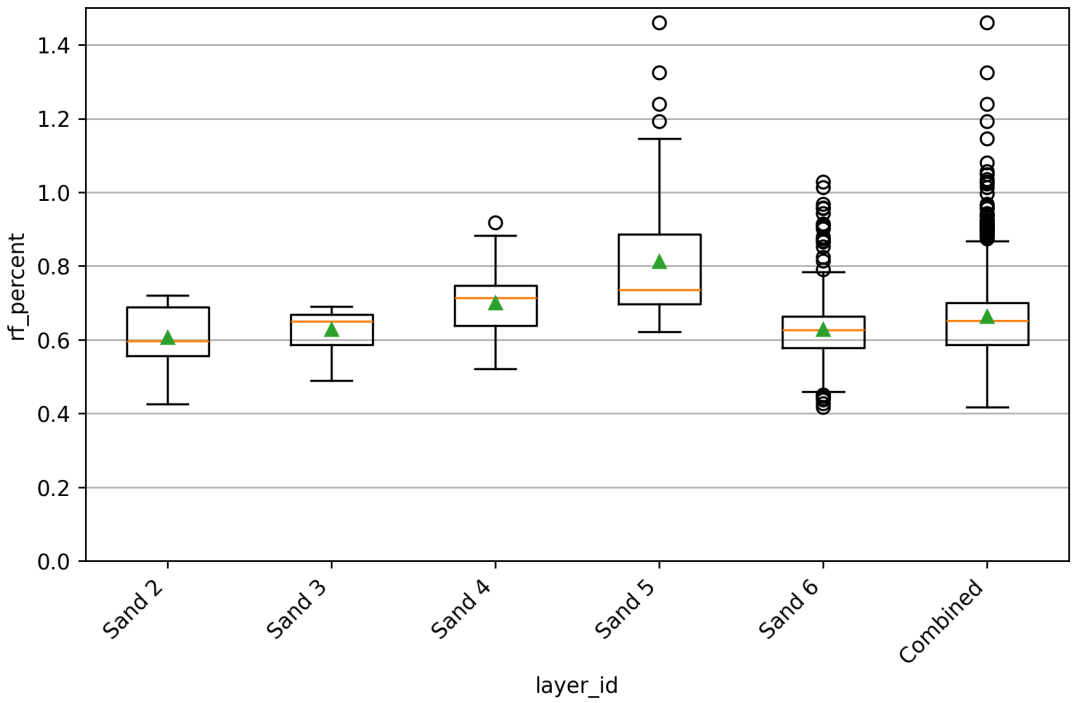

Figure B.14: Friction ratio for CPT1-4.

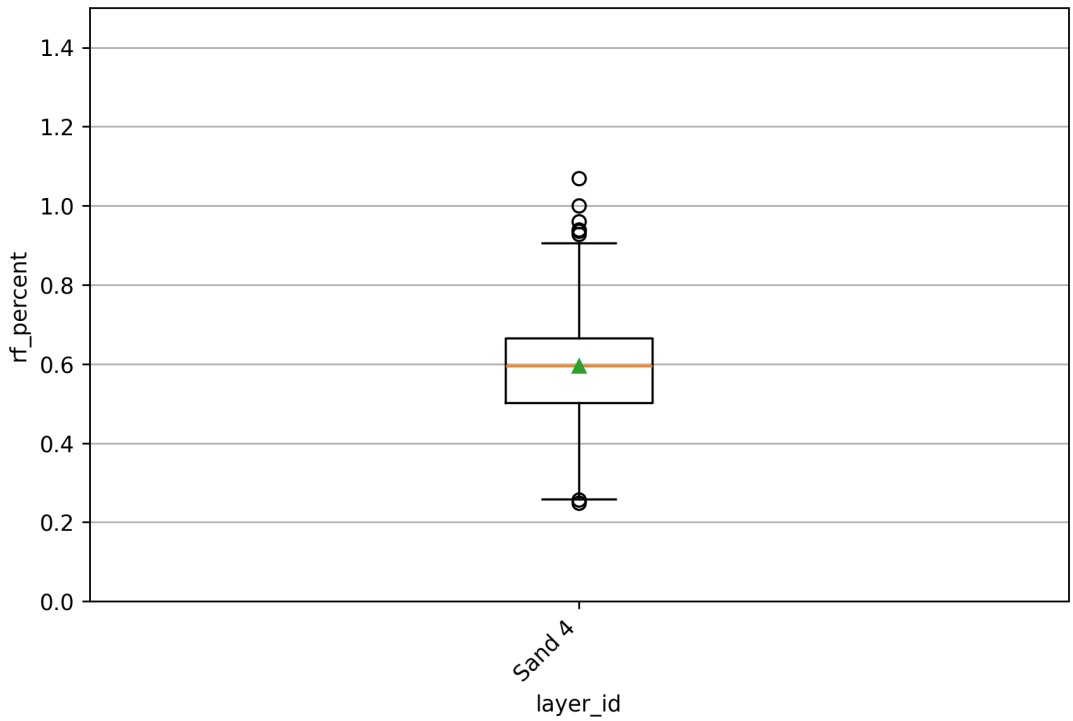

Figure B.15: Friction ratio for CPT2-2.

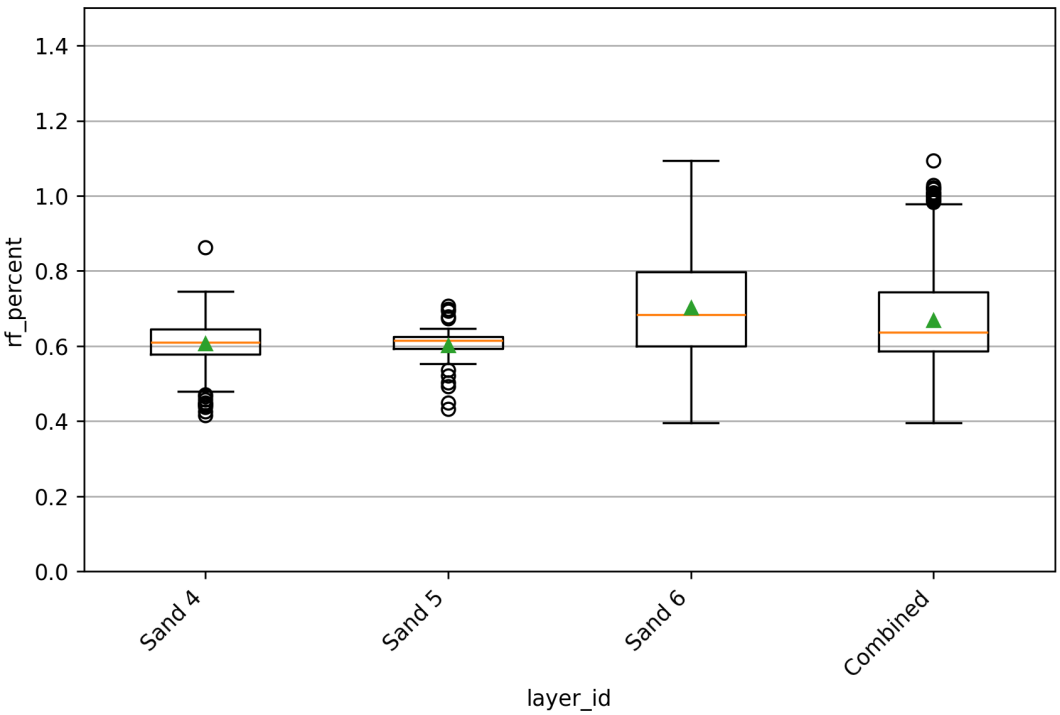

Figure B.16: Friction ratio for CPT2-4.

B.5. Robertson charts foundation pile sand layer around -18.5 m NAP

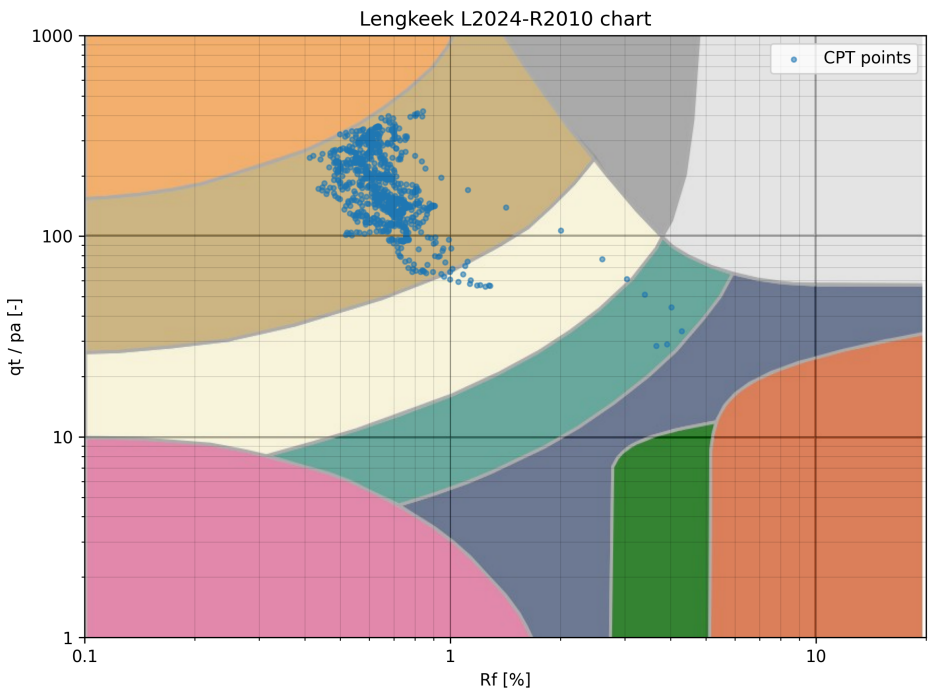

Figure B.17: Robertson soil behaviour type chart for CPT1-2 at foundation pile sand layer depth around -18.5 m NAP.

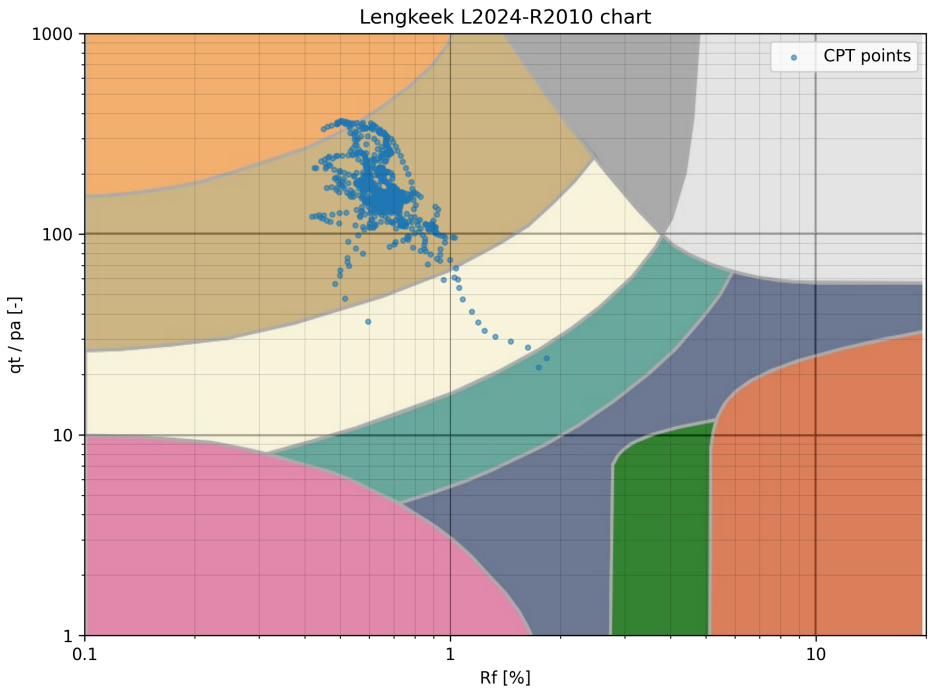

Figure B.18: Robertson soil behaviour type chart for CPT1-4 at foundation pile sand layer depth around -18.5 m NAP.

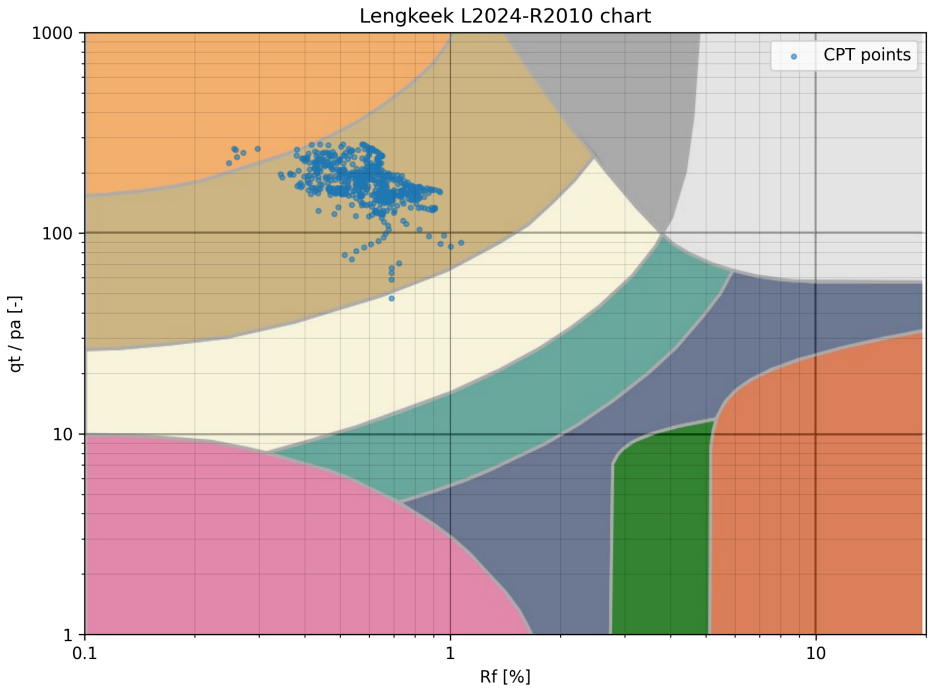

Figure B.19: Robertson soil behaviour type chart for CPT2-2 at foundation pile sand layer depth around -18.5 m NAP.

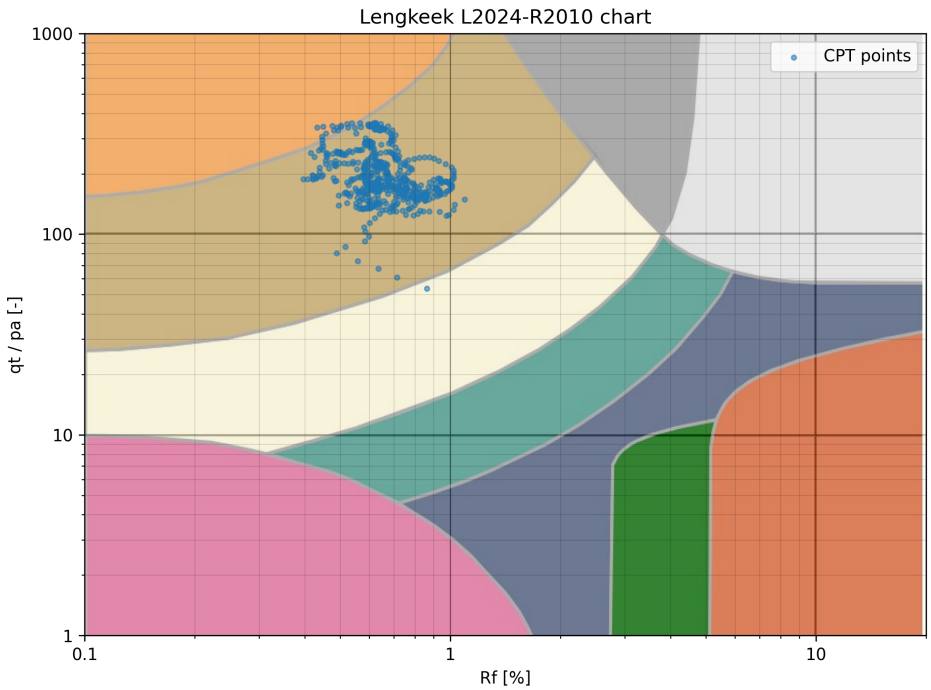

Figure B.20: Robertson soil behaviour type chart for CPT2-4 at foundation pile sand layer depth around -18.5 m NAP.

B.6. Confidence ellipse Robertson charts for other layers

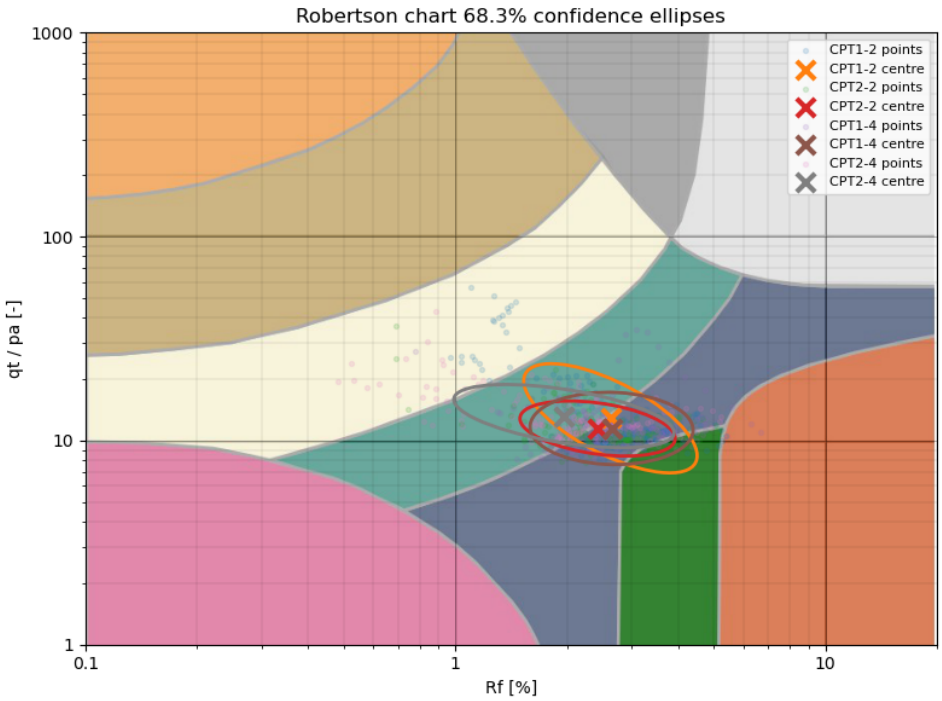

Figure B.21: Robertson chart with 68.3% confidence ellipse for silt and clay layers from -15 m NAP to -18.5 m NAP.

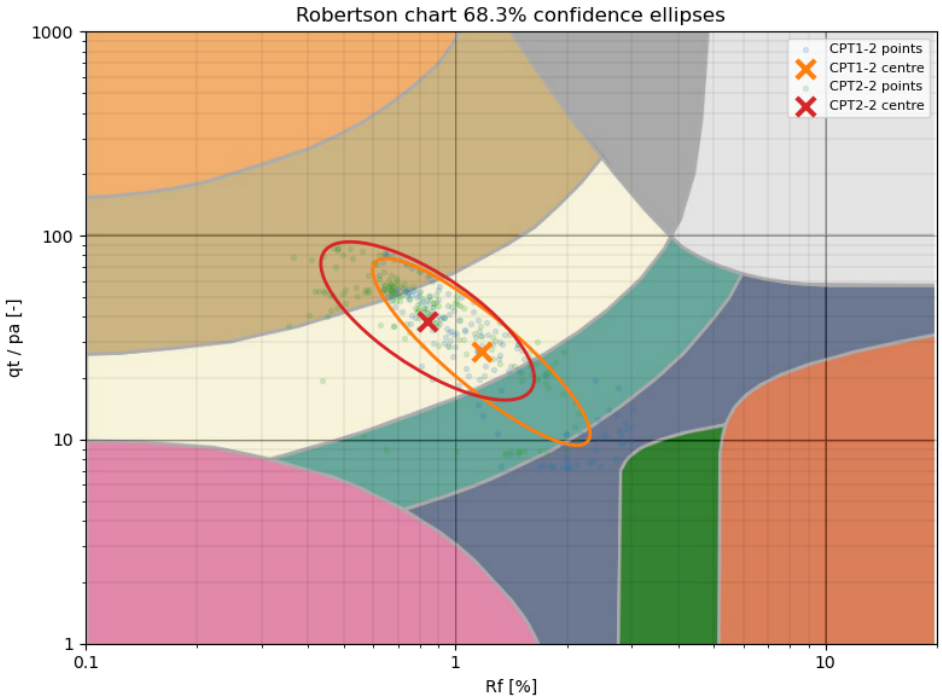

Figure B.22: Robertson chart with 68.3% confidence ellipse for sand mixtures, sand and silty clay layers from -11.5 m NAP to -15.5 m NAP.

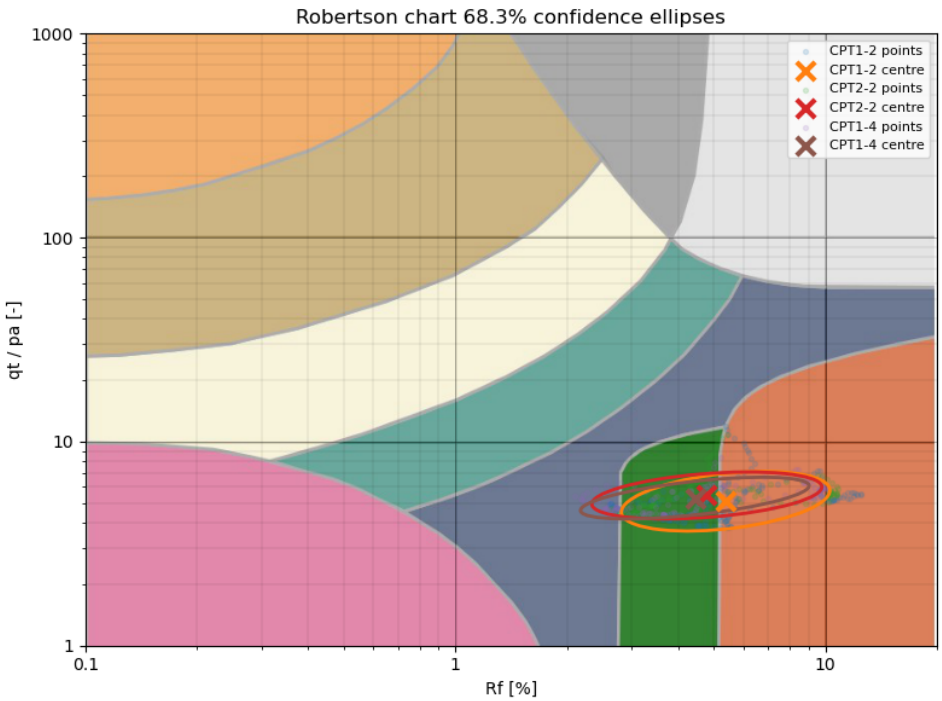

Figure B.23: Robertson chart with 68.3% confidence ellipse for organic layers from -4.5 m NAP to -8.0 m NAP.

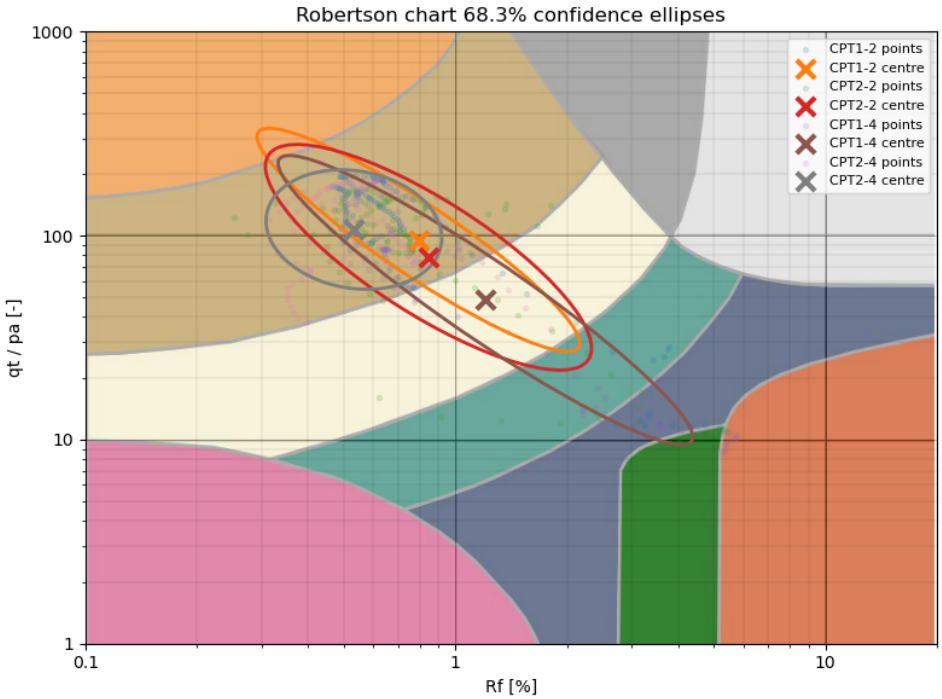

Figure B.24: Robertson chart with 68.3% confidence ellipse for the sand layer from -2.0 m NAP to -4.5 m NAP.

B.7. Soil parameters per layer

Table B.1: Soil layer parameters for CPT1-2.

Layer	Top [m NAP]	Bottom [m NAP]	γ_{sat} [kN/m^3]	E' [kPa]	ν' [-]	c' [kPa]	ϕ' [°]	ψ [°]
Organic clay 1	-1.56	-1.74	15.1	1350	0.350	0.5	15	0
Silty sand 1	-1.74	-2.04	20.5	22500	0.250	0	27.5	0
Sand 1	-2.04	-4.46	19.7	35930	0.250	0	31.7	1.7
Peat 1	-4.46	-5.40	12.5	750	0.350	3.75	15	0
Organic clay 2	-5.40	-6.16	14.7	1160	0.350	0.5	15	0
Peat 2	-6.16	-7.26	12.5	750	0.350	3.75	15	0
Organic clay 3	-7.26	-8.10	15.1	1340	0.350	0.5	15	0
Clay & silt 1	-8.10	-8.88	15.0	1500	0.350	0	22.5	0
Peat 3	-8.88	-9.66	12.5	750	0.350	3.75	15	0
Clay & silt 2	-9.66	-10.64	15.0	1500	0.350	0	22.5	0
Silty clay 1	-10.64	-11.50	19.3	2350	0.350	0.35	29.2	0
Silty sand 2	-11.50	-14.80	20.5	22500	0.250	0	27.5	0
Silty clay 2	-14.80	-15.74	19.3	2270	0.350	0.27	29.1	0
Clay & silt 3	-15.74	-17.86	16.4	2200	0.350	2.34	22.5	0
Clay & silt 4	-17.86	-18.78	19.0	4730	0.350	8.46	23.5	0
Sand 2	-18.78	-30.00	20.5	57921	0.250	0	33.77	3.88

Table B.2: Soil layer parameters for CPT1-4.

Layer	Top [m NAP]	Bottom [m NAP]	γ_{sat} [kN/m^3]	E' [kPa]	ν' [-]	c' [kPa]	ϕ' [°]	ψ [°]
Clay & silt 1	-1.57	-1.75	15.0	1500	0.350	0	22.5	0
Silty sand 1	-1.75	-2.71	20.5	22500	0.250	0	27.5	0
Sand 1	-2.71	-4.55	19.3	22750	0.250	0	30.6	0.6
Organic clay 1	-4.55	-6.13	15.3	1420	0.350	0.5	15	0
Peat 1	-6.13	-7.57	12.5	750	0.350	3.75	15	0
Clay & silt 2	-7.57	-8.81	15.0	1500	0.350	0	22.5	0
Peat 2	-8.81	-9.53	12.5	750	0.350	3.75	15	0
Clay & silt 3	-9.53	-10.95	15.0	1500	0.350	0	22.5	0
Silty sand 2	-10.95	-12.67	20.5	22500	0.250	0	27.5	0
Silty clay 1	-12.67	-14.05	21.4	5770	0.350	2.98	31.2	0
Silty sand 3	-14.05	-14.77	20.5	22500	0.250	0	27.5	0
Silty clay 2	-14.77	-15.73	19.1	2140	0.350	0.14	28.9	0
Clay & silt 4	-15.73	-17.71	16.3	2130	0.350	2.1	22.5	0
Clay & silt 5	-17.71	-18.15	15.8	1910	0.350	1.38	22.5	0
Silty clay 3	-18.15	-18.51	19.3	2260	0.350	0.26	29.1	0
Sand 2	-18.51	-30.00	20.38	54904	0.250	0	33.38	3.55

Table B.3: Soil layer parameters for CPT2-2.

Layer	Top [m NAP]	Bottom [m NAP]	γ_{sat} [kN/m^3]	E' [kPa]	ν' [-]	c' [kPa]	ϕ' [°]	ψ [°]
Organic clay 1	-1.51	-2.05	15.5	1500	0.350	0.5	15	0
Sand 1	-2.05	-4.39	19.5	29660	0.250	0	31.2	1.2
Organic clay 2	-4.39	-5.55	15.5	1500	0.350	0.5	15	0
Organic clay 3	-5.55	-5.91	14.8	1240	0.350	0.5	15	0
Peat 1	-5.91	-6.99	12.5	750	0.350	3.75	15	0
Organic clay 4	-6.99	-7.37	15.3	1440	0.350	0.5	15	0
Clay & silt 1	-7.37	-8.53	15.0	1500	0.350	0	22.5	0
Peat 2	-8.53	-9.51	12.5	750	0.350	3.75	15	0
Clay & silt 2	-9.51	-11.31	15.3	1670	0.350	0.56	22.5	0
Sand 2	-11.31	-12.11	19.0	15630	0.250	0	30.1	0.1
Silty sand 1	-12.11	-12.83	20.5	22500	0.250	0	27.5	0
Silty clay 1	-12.83	-13.29	19.2	2160	0.350	0.16	28.9	0
Sand 3	-13.29	-14.01	19.2	20150	0.250	0	30.4	0.4
Silty sand 2	-14.01	-14.79	20.5	22500	0.250	0	27.5	0
Silty clay 2	-14.79	-15.89	19.2	2180	0.350	0.18	29	0
Clay & silt 3	-15.89	-16.61	15.7	1830	0.350	1.09	22.5	0
Silty clay 3	-16.61	-17.35	19.0	2040	0.350	0.04	28.8	0
Clay & silt 4	-17.35	-18.01	15.5	1750	0.350	0.84	22.5	0
Silty clay 4	-18.01	-18.41	19.2	2230	0.350	0.23	29	0
Sand 4	-18.41	-30.00	20.5	59950	0.250	0	34.1	4.1

Table B.4: Soil layer parameters for CPT2-4.

Layer	Top [m NAP]	Bottom [m NAP]	γ_{sat} [kN/m^3]	E' [kPa]	ν' [-]	c' [kPa]	ϕ' [°]	ψ [°]
Clay & silt 1	-1.40	-1.82	16.3	2150	0.350	2.16	22.5	0
Sand 1	-1.82	-3.80	19.7	35080	0.250	0	31.7	1.7
Silty clay 1	-3.80	-4.26	19.4	2440	0.350	0.44	29.3	0
Organic clay 1	-4.26	-5.30	15.5	1500	0.350	0.5	15	0
Clay & silt 2	-5.30	-5.84	15.0	1500	0.350	0	22.5	0
Peat 1	-5.84	-6.96	12.5	750	0.350	3.75	15	0
Clay & silt 3	-6.96	-8.72	15.0	1500	0.350	0	22.5	0
Peat 2	-8.72	-9.48	12.5	750	0.350	3.75	15	0
Clay & silt 4	-9.48	-10.30	15.0	1500	0.350	0	22.5	0
Silty clay 2	-10.30	-11.30	19.3	2280	0.350	0.28	29.1	0
Sand 2	-11.30	-12.06	19.0	15700	0.250	0	30.1	0.1
Silty sand 1	-12.06	-12.68	20.5	22500	0.250	0	27.5	0
Silty clay 3	-12.68	-13.74	21.0	4940	0.350	2.39	30.8	0
Sand 3	-13.74	-14.04	19.1	17740	0.250	0	30.2	0.2
Silty sand 2	-14.04	-14.90	20.5	22500	0.250	0	27.5	0
Silty clay 4	-14.90	-16.92	19.2	2250	0.350	0.25	29.1	0
Silty clay 5	-16.92	-17.44	19.3	2260	0.350	0.26	29.1	0
Silty clay 6	-17.44	-18.46	19.2	2190	0.350	0.19	29	0
Sand 4	-18.46	-30.00	20.72	67744	0.250	0	34.88	4.88

B.8. SANISAND parameters Ottawa sand

Table B.5: SANISAND parameters used in the numerical model (Chong & Santamarina, 2016).

Parameter	PLAXIS input	Value	Description
G_0	User 1	90	Elastic shear modulus coefficient
ν	User 2	0.05	Elasticity parameter
M	User 3	1.28	Critical state parameter
c	User 4	0.80	Critical state parameter
λ_c	User 5	0.012	Critical state parameter
e_0	User 6	0.898	Critical state void ratio parameter
ξ	User 7	0.7	Critical state line parameter
m	User 8	0.01	Yield surface parameter
h_0	User 9	5.25	Plastic modulus parameter
c_h	User 10	1.01	Plastic modulus parameter
n^b	User 11	1.2	Plastic modulus parameter
A_0	User 12	0.4	Dilatancy parameter
n^d	User 13	1.35	Dilatancy parameter
μ_0	User 14	44	Memory surface parameter
ζ	User 15	0.005	Memory surface parameter
β	User 16	1	Memory surface parameter
e_{ini}	User 17	0.6855	Initial void ratio
e_{max}	User 18	0.86	Maximum void ratio
e_{min}	User 19	0.55	Minimum void ratio

C

Numerical model results

C.1. Linear results

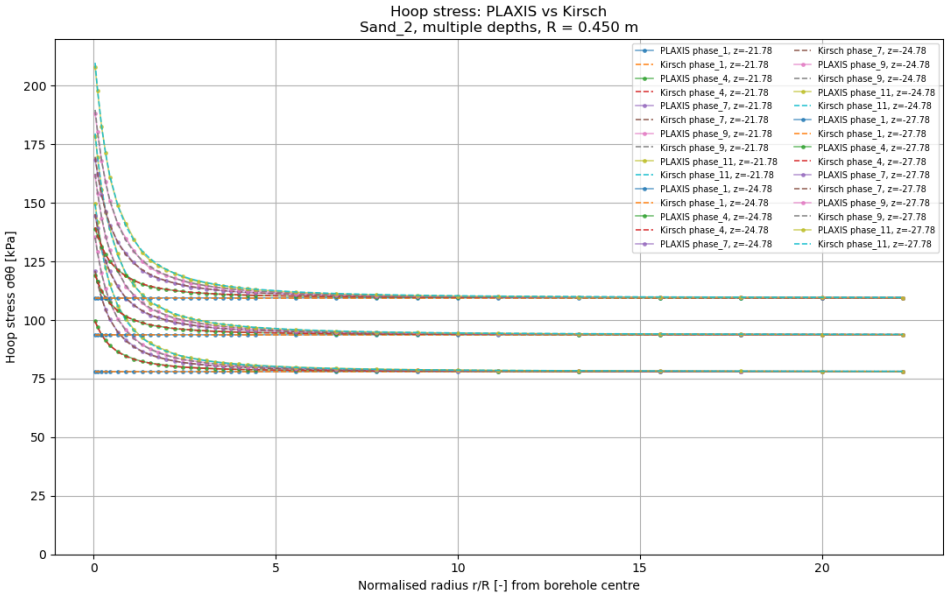

(a) Hoop stress at different depths compared to the Kirsch solution.

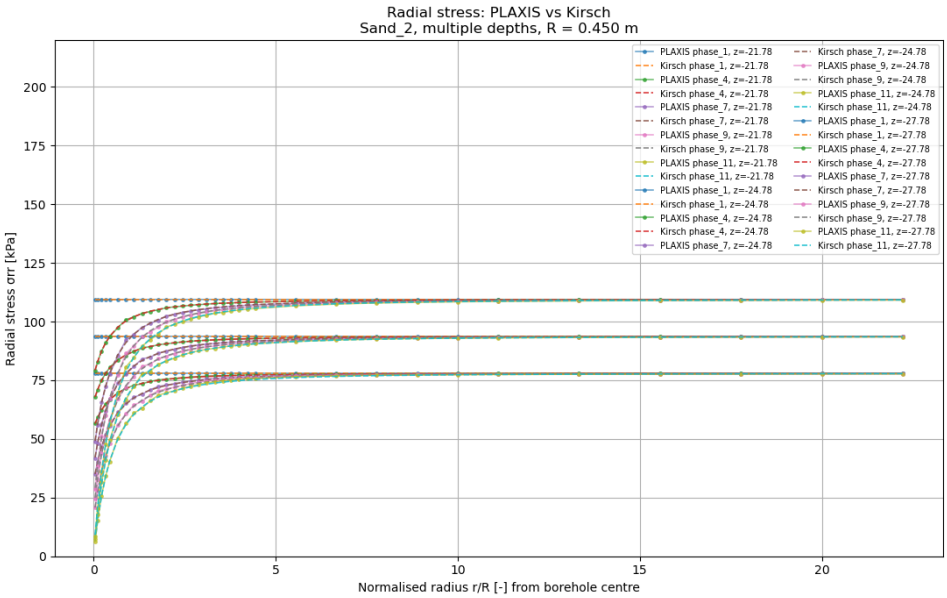

(b) Radial stress at different depths compared to the Kirsch solution.

Figure C.1: Hoop and radial stress at different depths compared to the Kirsch solution.

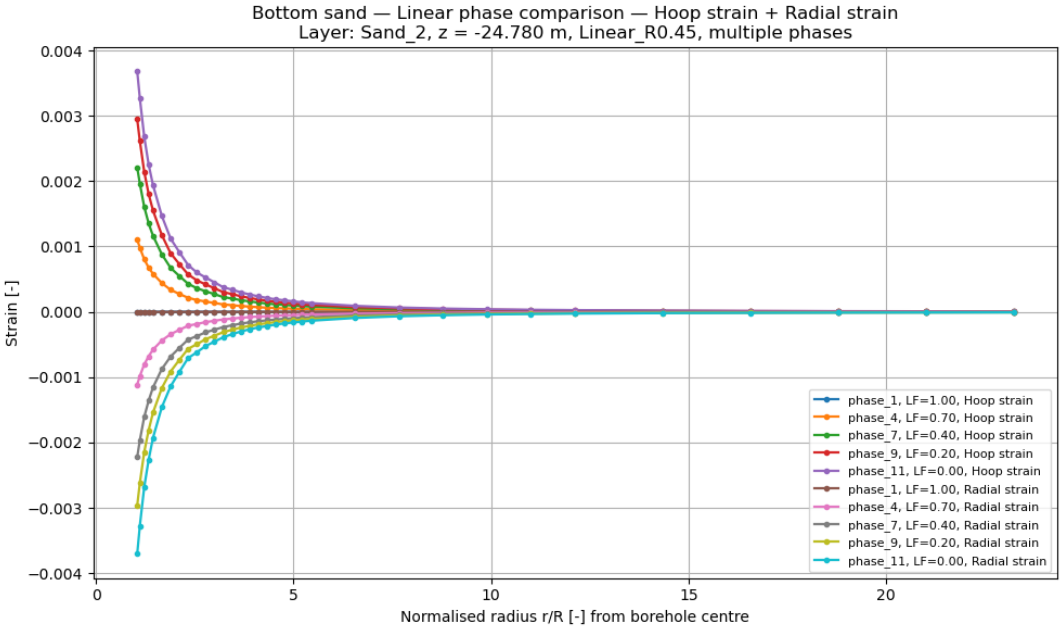

Figure C.2: Hoop and radial strain at phase 11 across different depths.

C.2. Mohr-Coulomb

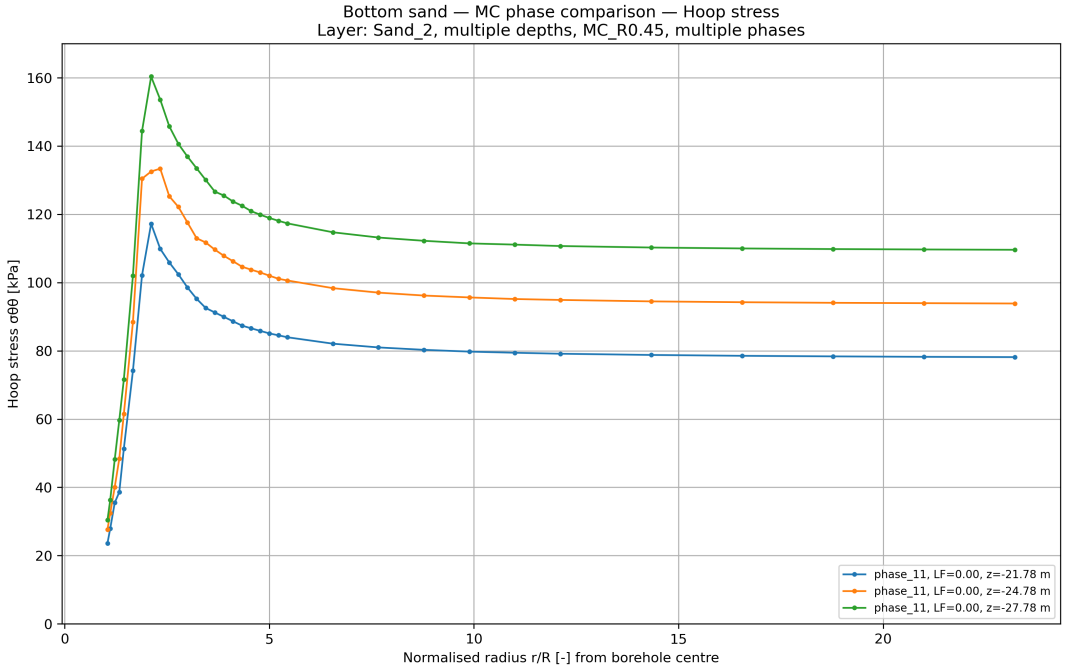

(a) Hoop stress at phase 11 across different depths.

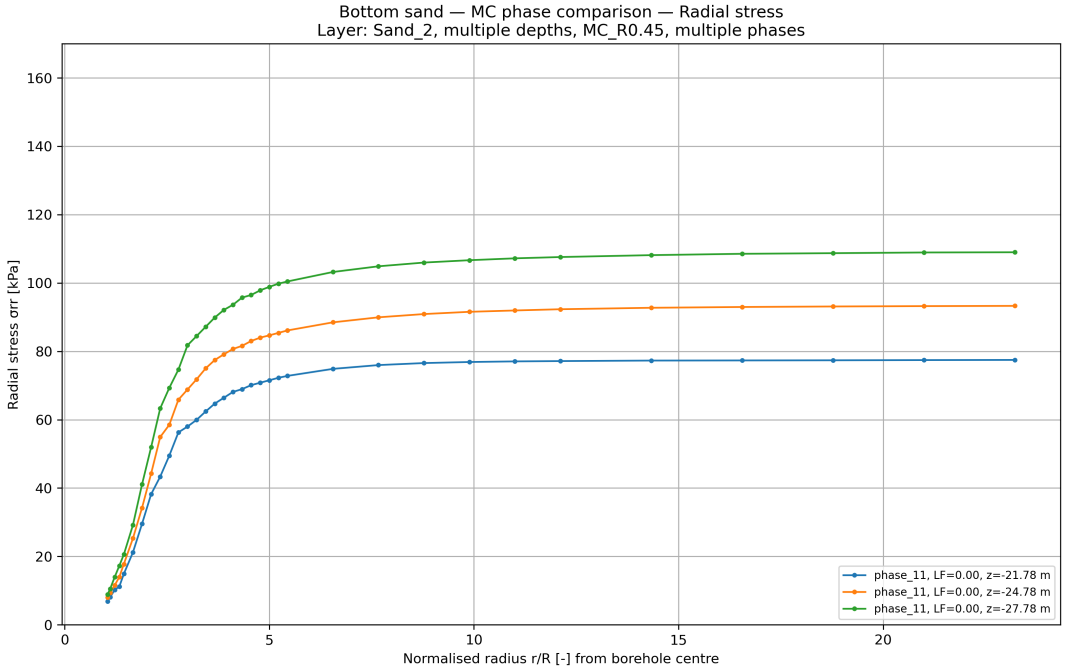

(b) Radial stress at phase 11 across different depths.

Figure C.3: Hoop and radial stress at phase 11 across different depths for Mohr-Coulomb model.

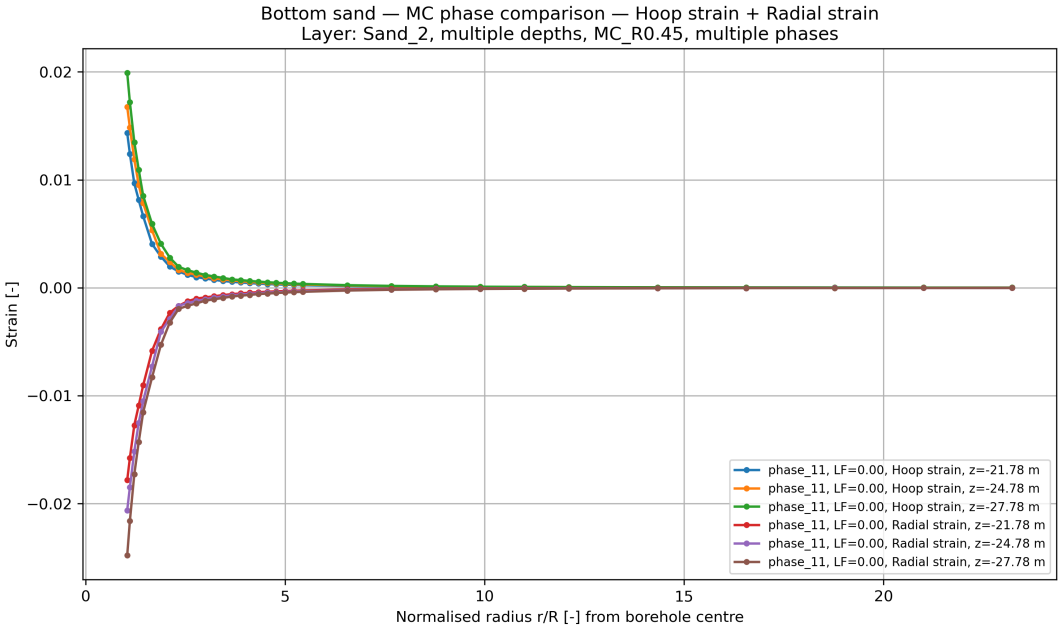

Figure C.4: Hoop and radial strain at phase 11 across different depths for Mohr-Coulomb model.

C.3. SANISAND

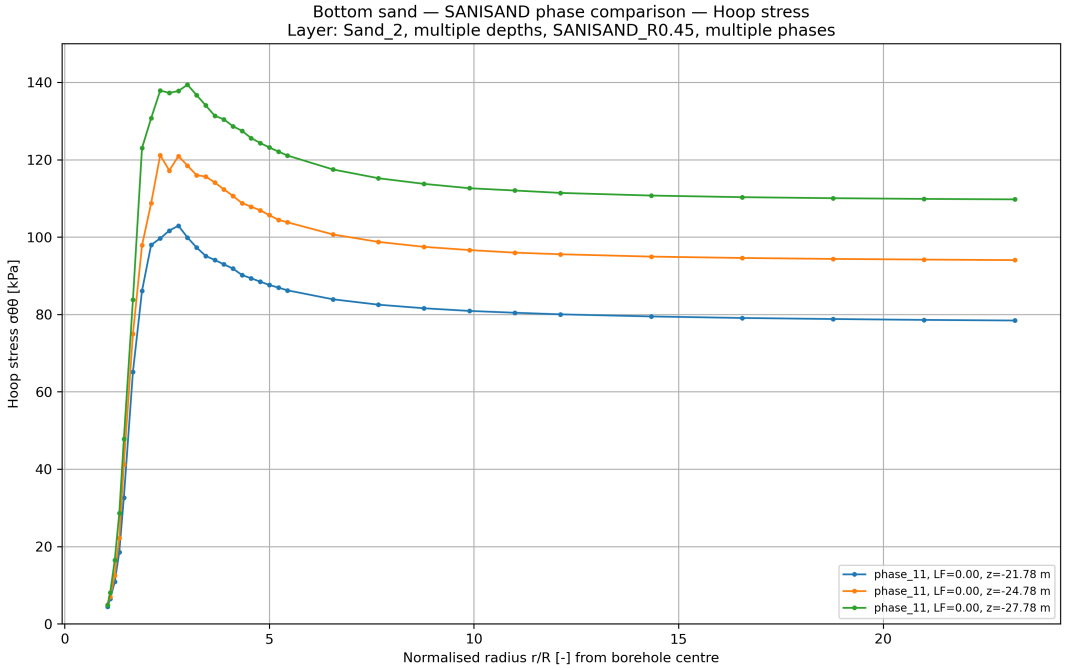

(a) Hoop stress at phase 11 across different depths.

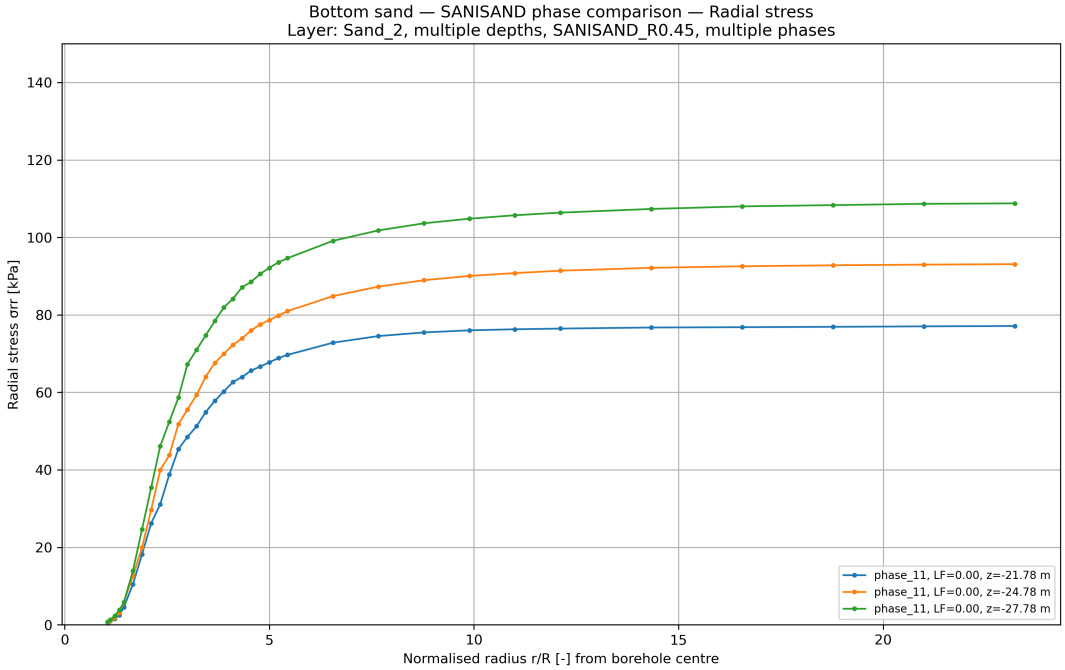

(b) Radial stress at phase 11 across different depths.

Figure C.5: Hoop and radial stress at phase 11 across different depths for SANISAND model.

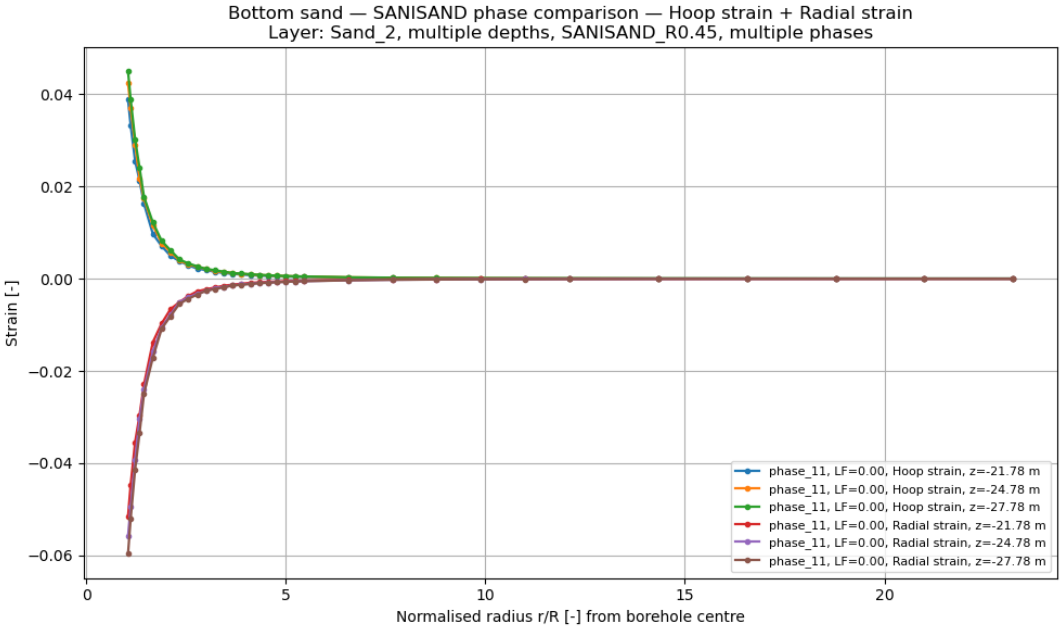

Figure C.6: Hoop and radial strain at phase 11 across different depths for SANISAND model.

C.4. Comparing models

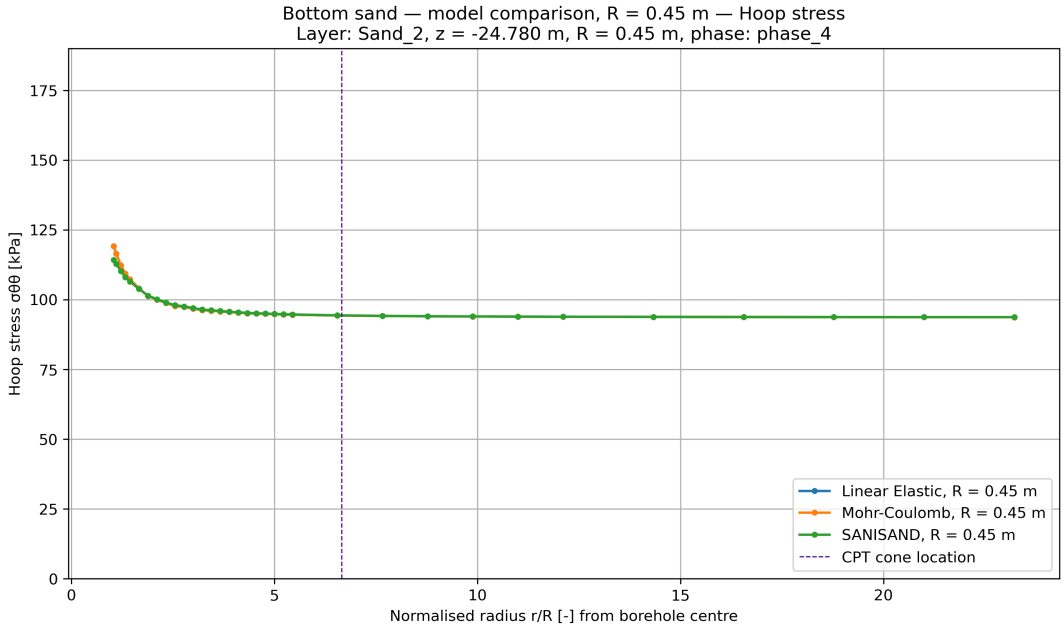

(a) Hoop stress at phase 4.

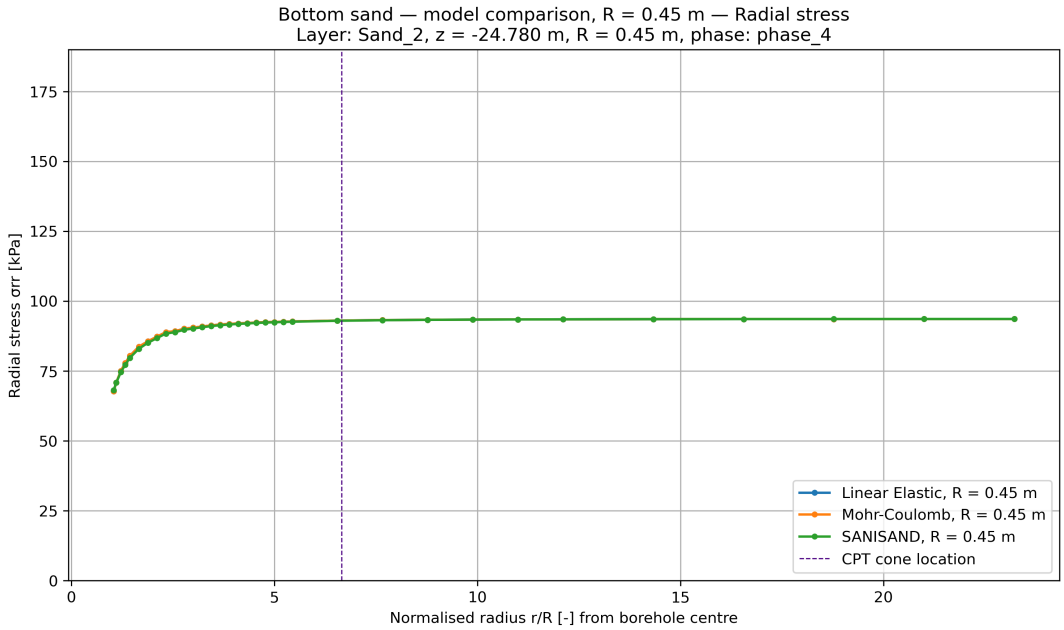

(b) Radial stress at phase 4.

Figure C.7: Comparison of hoop and radial stress at -24.78 m NAP for phase 4 for all constitutive models.

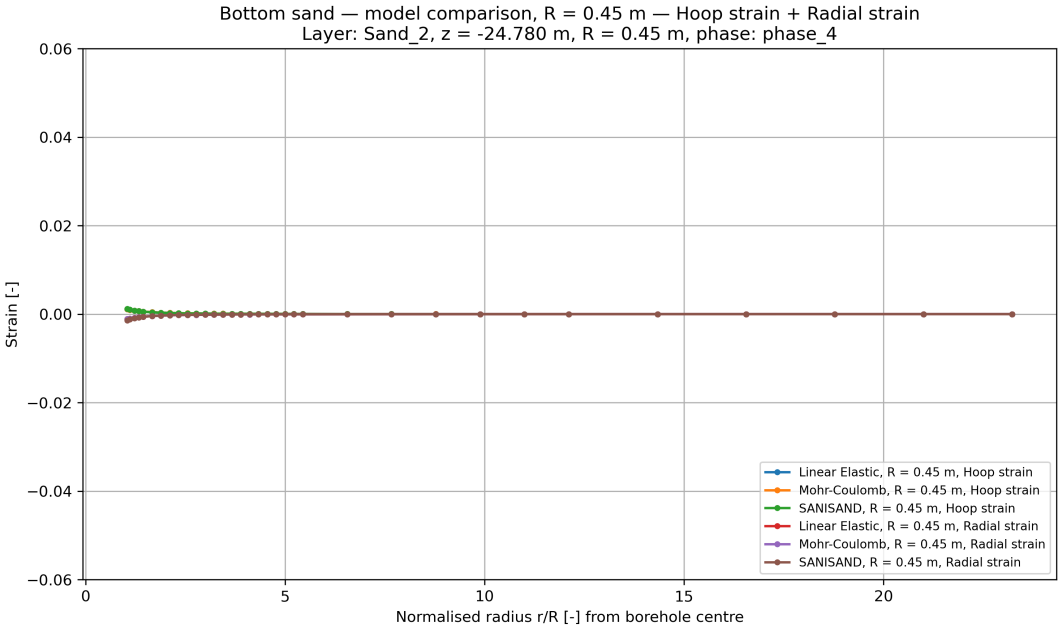

Figure C.8: Comparison of hoop and radial strain at -24.78 m NAP for phase 4 for all constitutive models.

C.5. Vertical stress

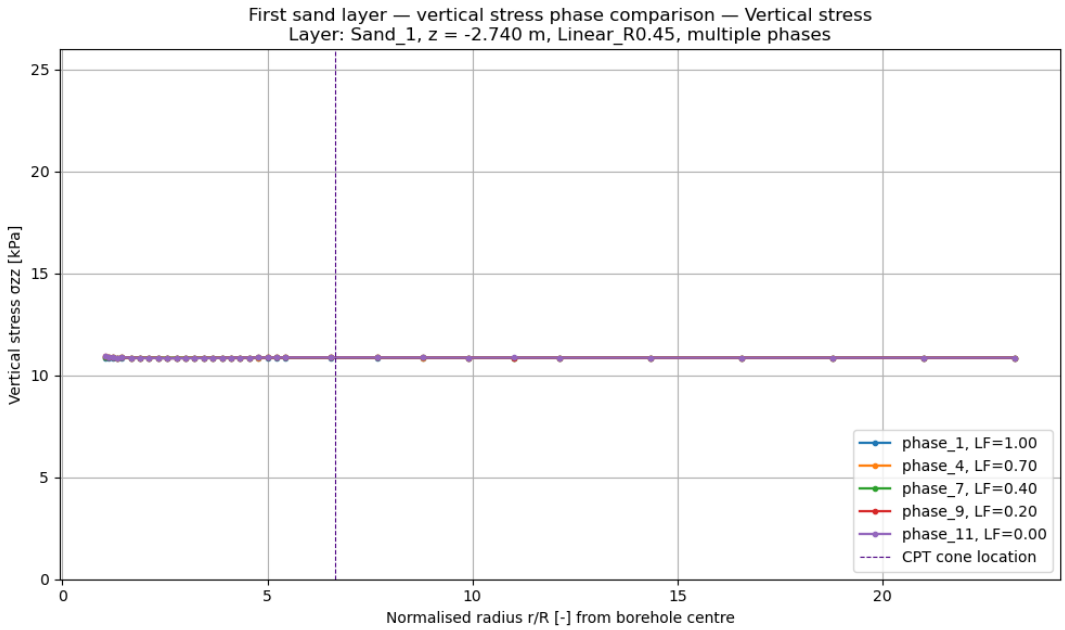

(a) Linear-elastic vertical stress development at -2.74 m NAP for different phases.

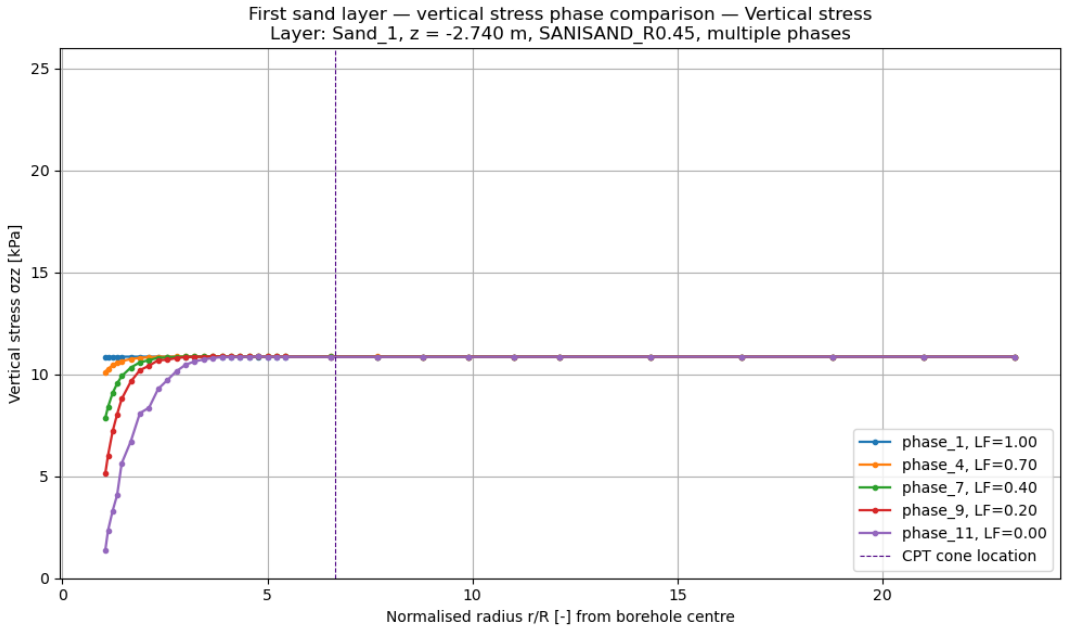

(b) SANISAND vertical stress development at -2.74 m NAP for different phases.

Figure C.9: Vertical stress development from constitutive models Linear-Elastic and SANISAND at a depth of -2.74 m NAP. The vertical line indicates the CPT location at that depth.

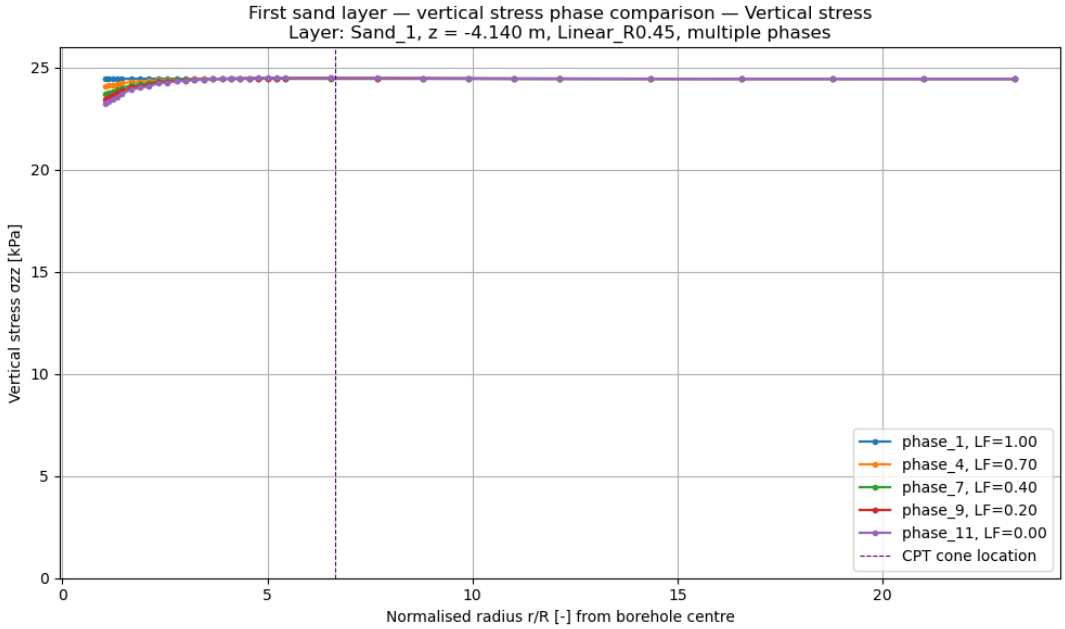

(a) Linear-elastic vertical stress development at -4.14 m NAP for different phases.

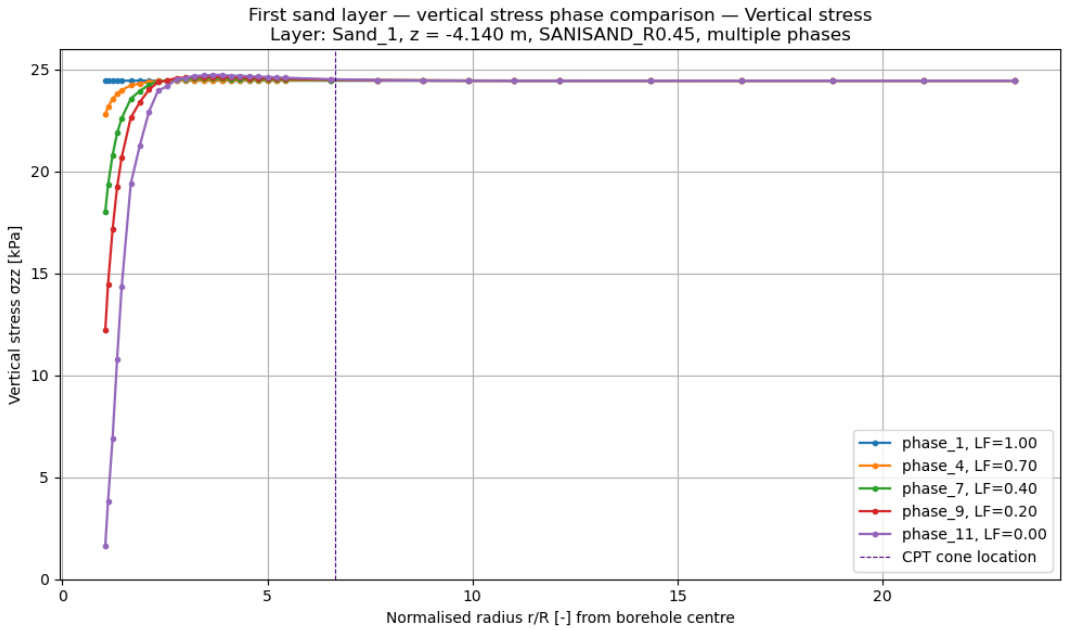

(b) SANISAND vertical stress development at -4.14 m NAP for different phases.

Figure C.10: Vertical stress development from constitutive models Linear-Elastic and SANISAND at a depth of -2.74 m NAP. The vertical line indicates the CPT location at that depth.

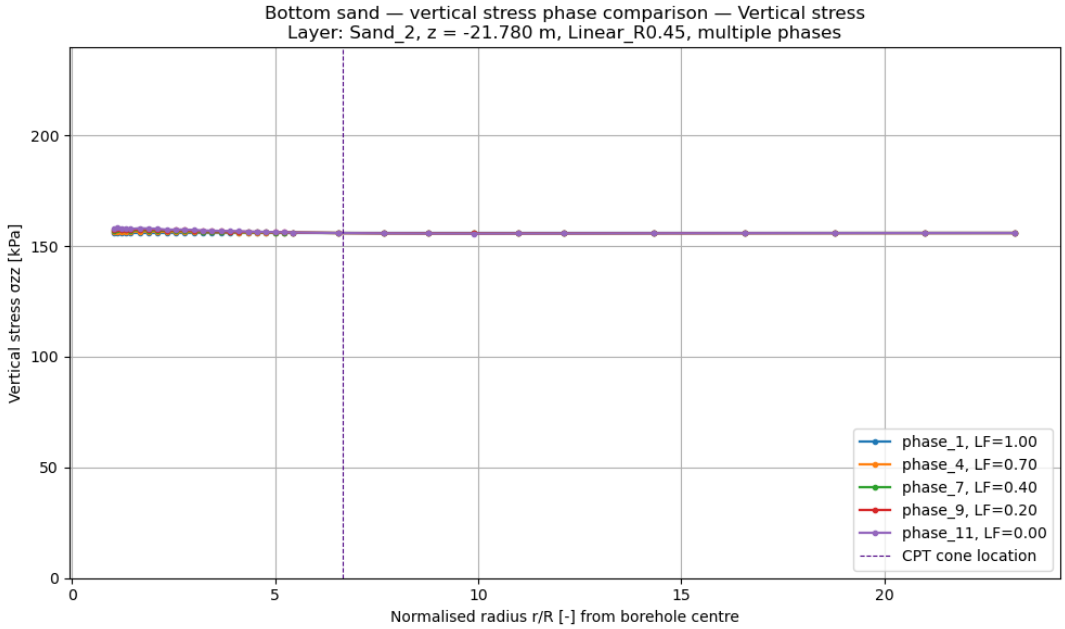

(a) Linear-elastic vertical stress development at -21.78 m NAP for different phases.

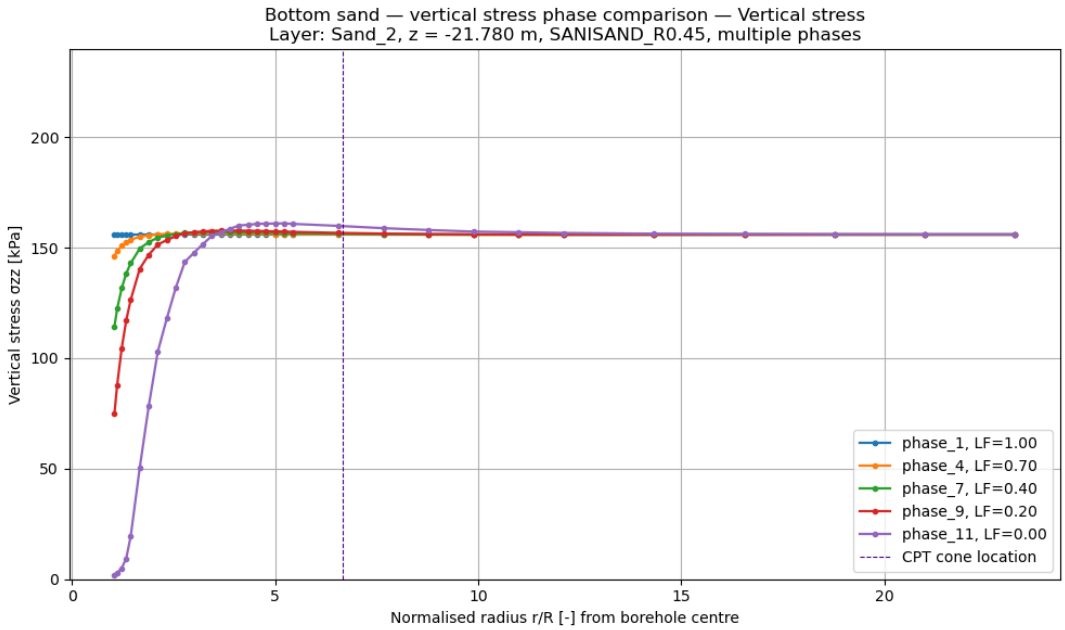

(b) SANISAND vertical stress development at -21.78 m NAP for different phases.

Figure C.11: Vertical stress development from constitutive models Linear-Elastic and SANISAND at a depth of -21.78 m NAP. The vertical line indicates the CPT location at that depth.

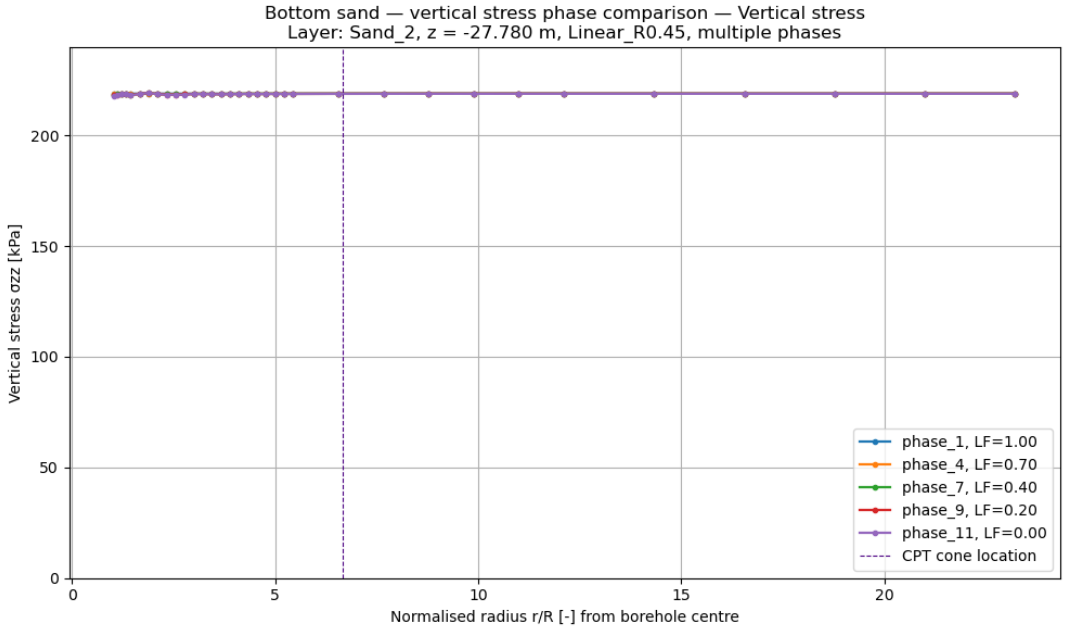

(a) Linear-elastic vertical stress development at -27.78 m NAP for different phases.

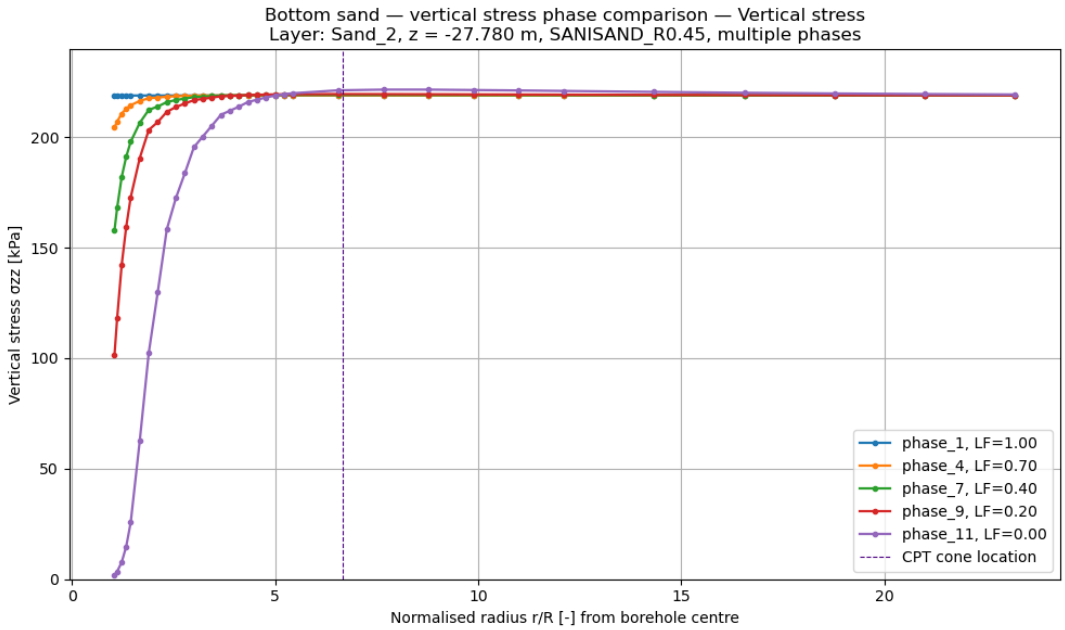

(b) SANISAND vertical stress development at -27.78 m NAP for different phases.

Figure C.12: Vertical stress development from constitutive models Linear-Elastic and SANISAND at a depth of -27.78 m NAP. The vertical line indicates the CPT location at that depth.

C.6. Vertical stress under different initial void ratio

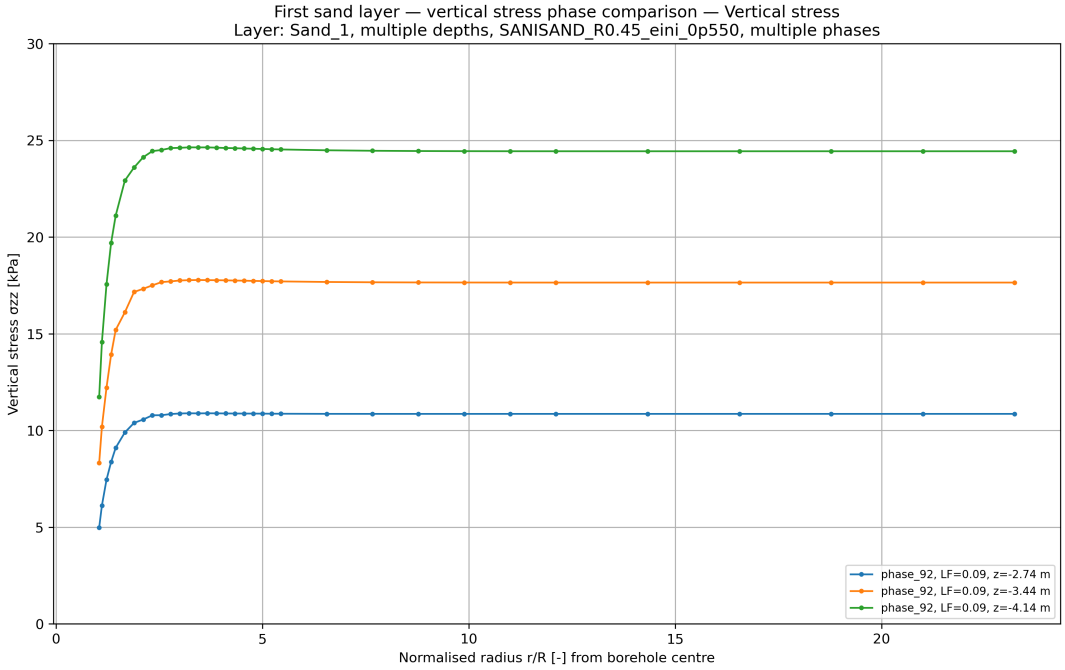

(a) SANISAND vertical stress in the first sand layer at different depths for initial void ratio 0.55.

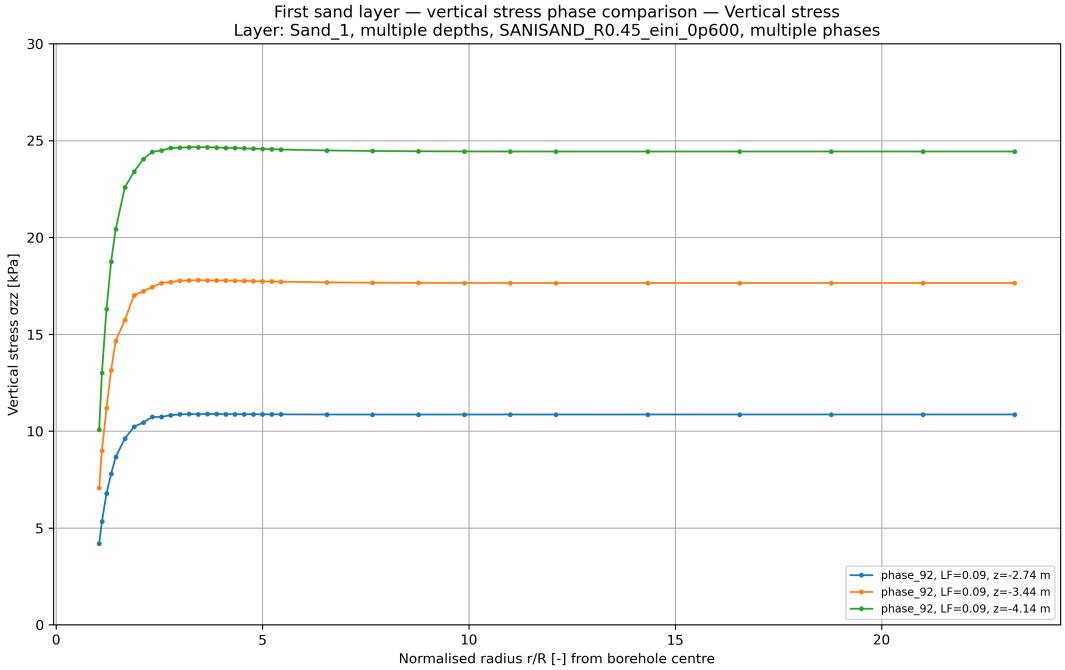

(b) SANISAND vertical stress in the first sand layer at different depths for initial void ratio 0.60.

Figure C.13: SANISAND vertical stress in the first sand layer at different depths for initial void ratios 0.55 and 0.60.

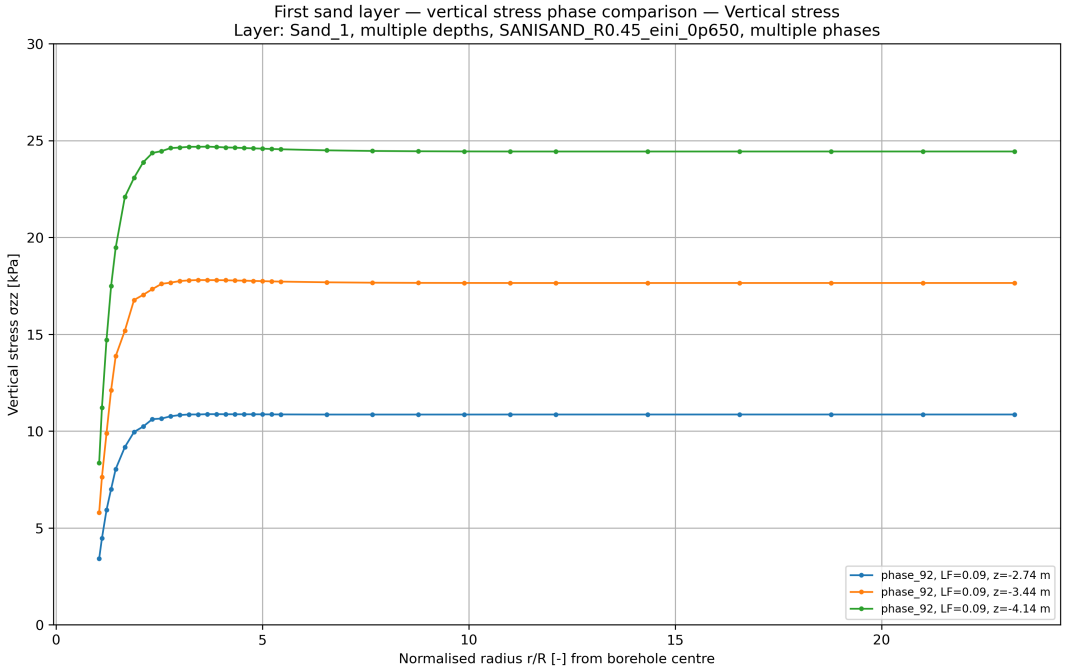

(a) SANISAND vertical stress in the first sand layer at different depths for initial void ratio 0.65.

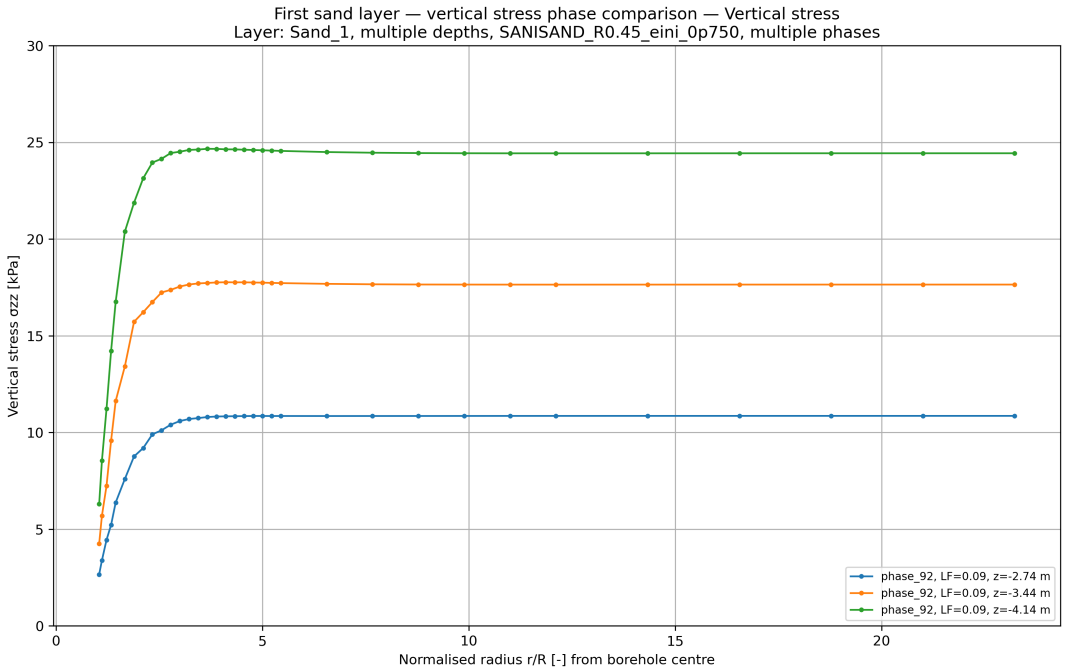

(b) SANISAND vertical stress in the first sand layer at different depths for initial void ratio 0.75.

Figure C.14: SANISAND vertical stress in the first sand layer at different depths for initial void ratios 0.65 and 0.75.

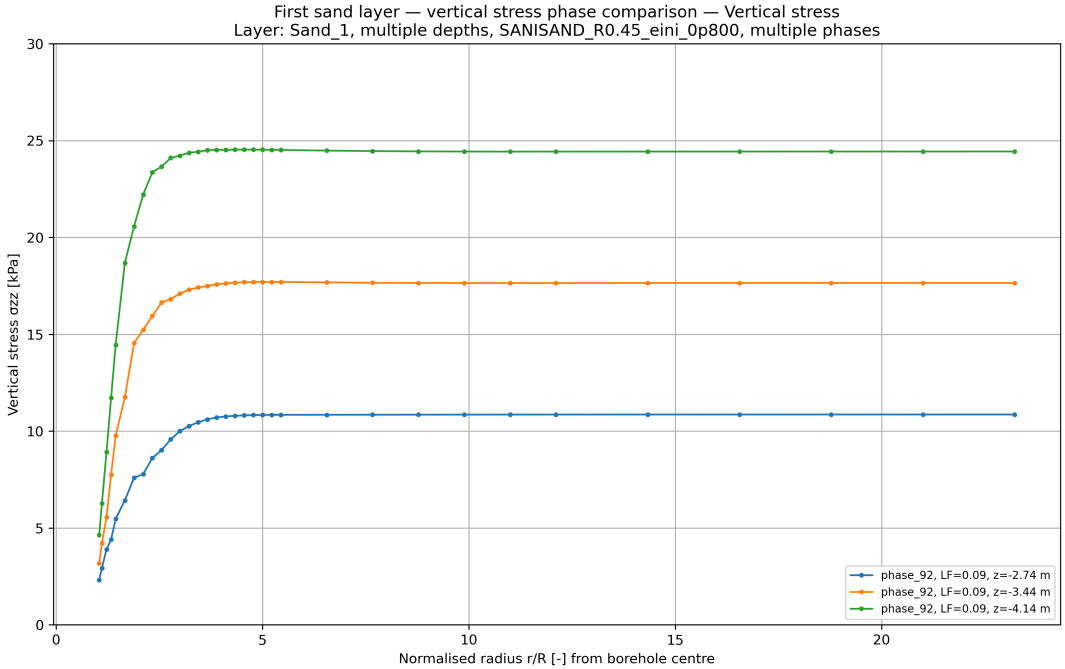

(a) SANISAND vertical stress in the first sand layer at different depths for initial void ratio 0.80.

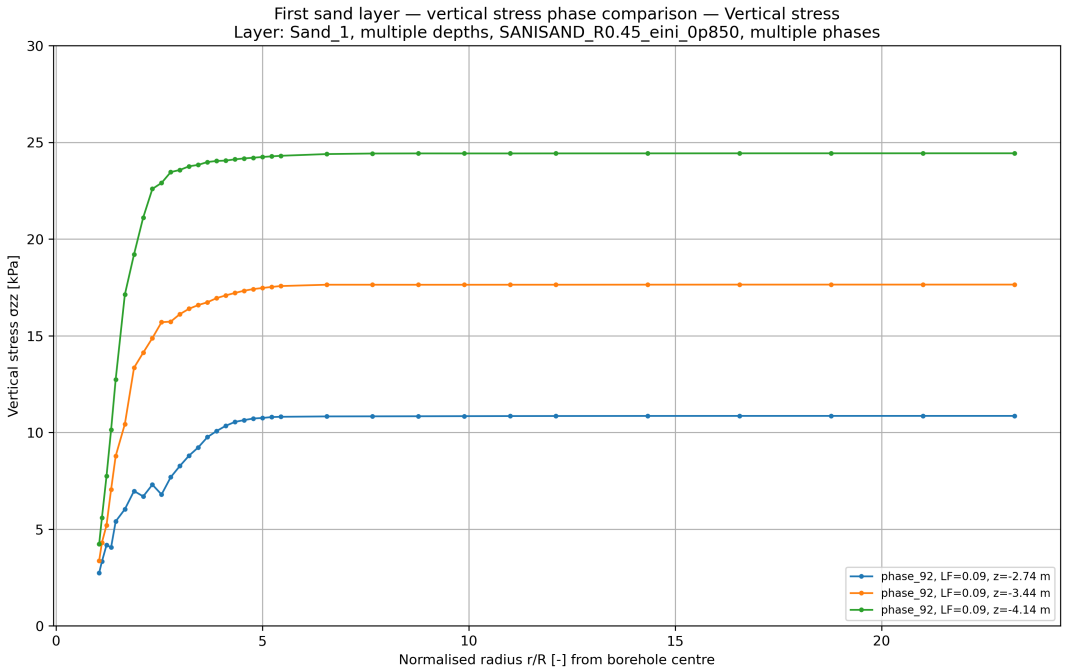

(b) SANISAND vertical stress in the first sand layer at different depths for initial void ratio 0.85.

Figure C.15: SANISAND vertical stress in the first sand layer at different depths for initial void ratios 0.80 and 0.85.

C.7. Hoop and radial stress and strain under different initial void ratio

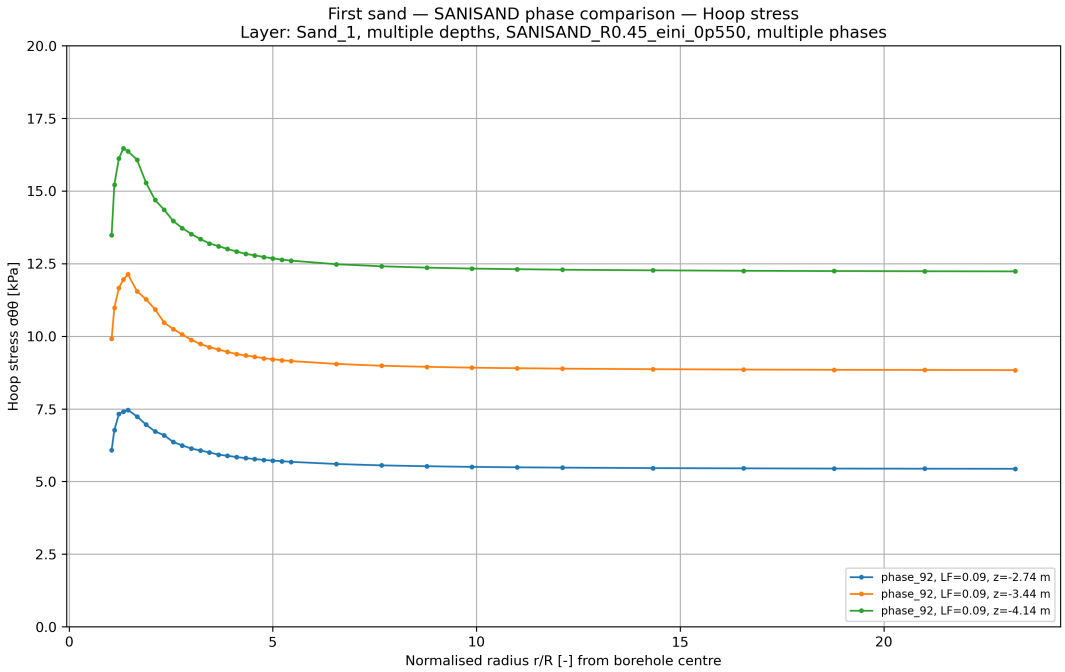

(a) SANISAND hoop stress in first sand layer at different depths for initial void ratio 0.55.

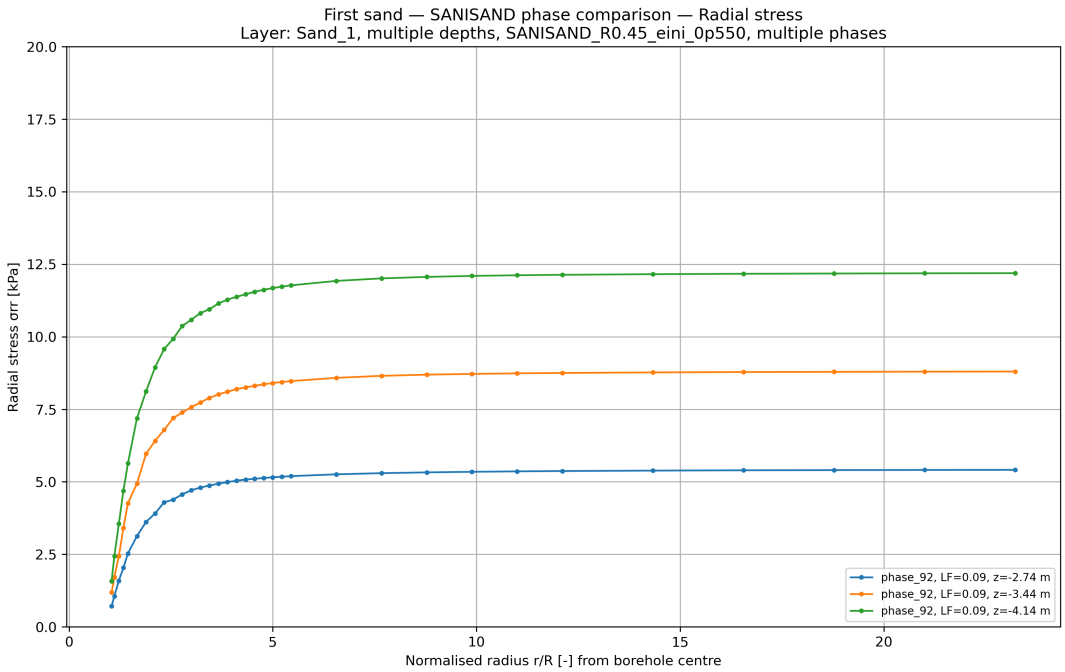

(b) SANISAND radial stress in first sand layer at different depths for initial void ratio 0.55.

Figure C.16: SANISAND hoop and radial stress at different depths for initial void ratio 0.55.

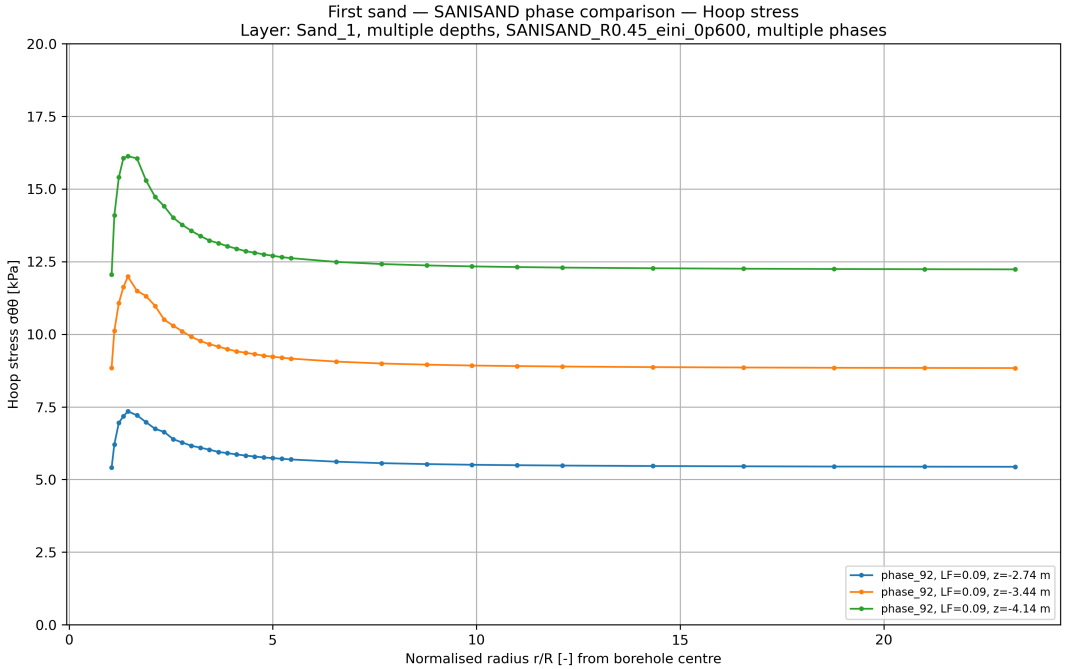

(a) SANISAND hoop stress in first sand layer at different depths for initial void ratio 0.6.

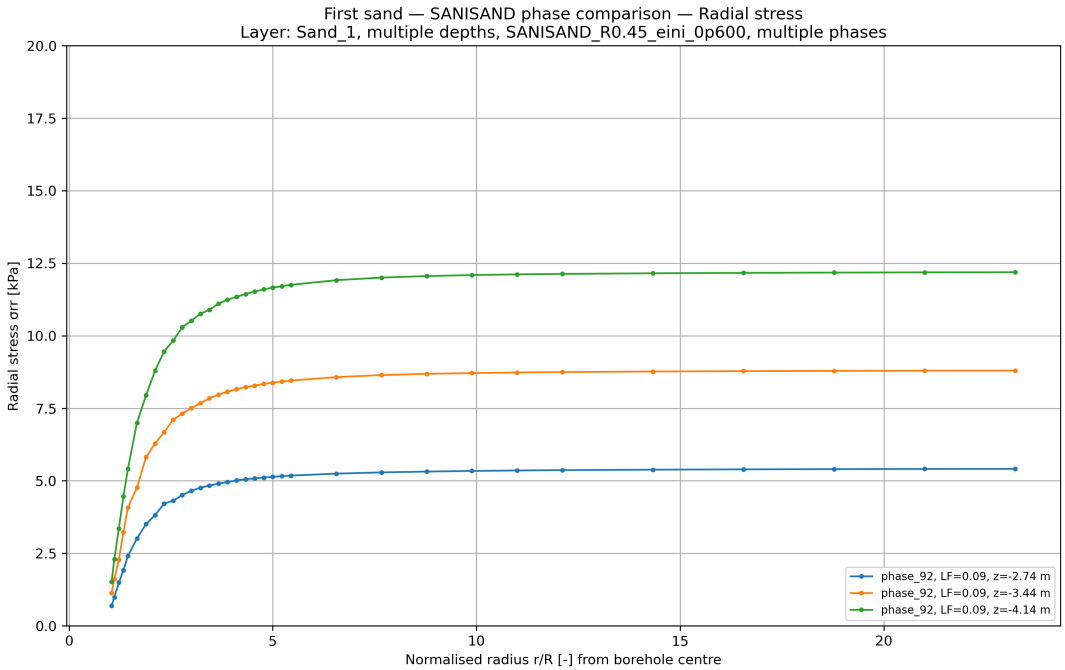

(b) SANISAND radial stress in first sand layer at different depths for initial void ratio 0.6.

Figure C.17: SANISAND hoop and radial stress at different depths for initial void ratio 0.6.

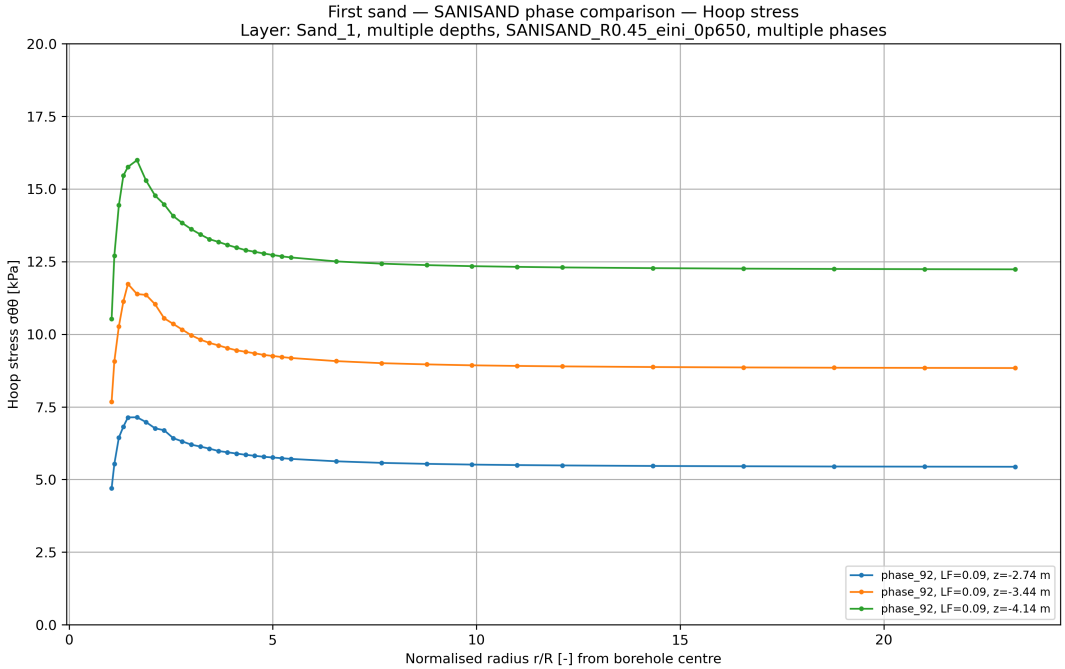

(a) SANISAND hoop stress in first sand layer at different depths for initial void ratio 0.65.

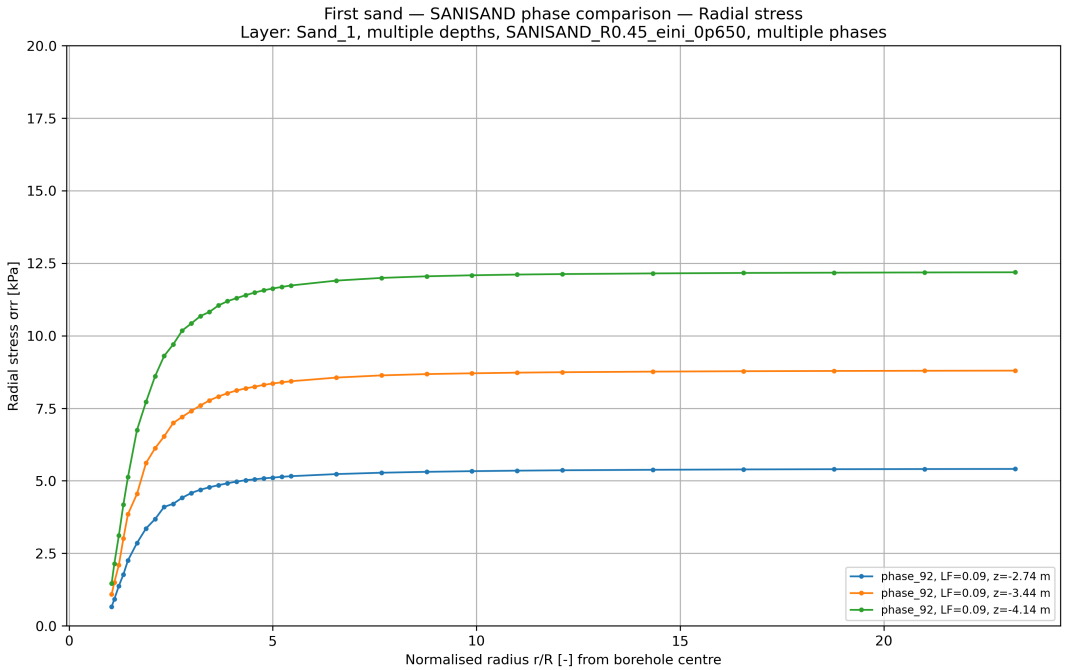

(b) SANISAND radial stress in first sand layer at different depths for initial void ratio 0.65.

Figure C.18: SANISAND hoop and radial stress at different depths for initial void ratio 0.65.

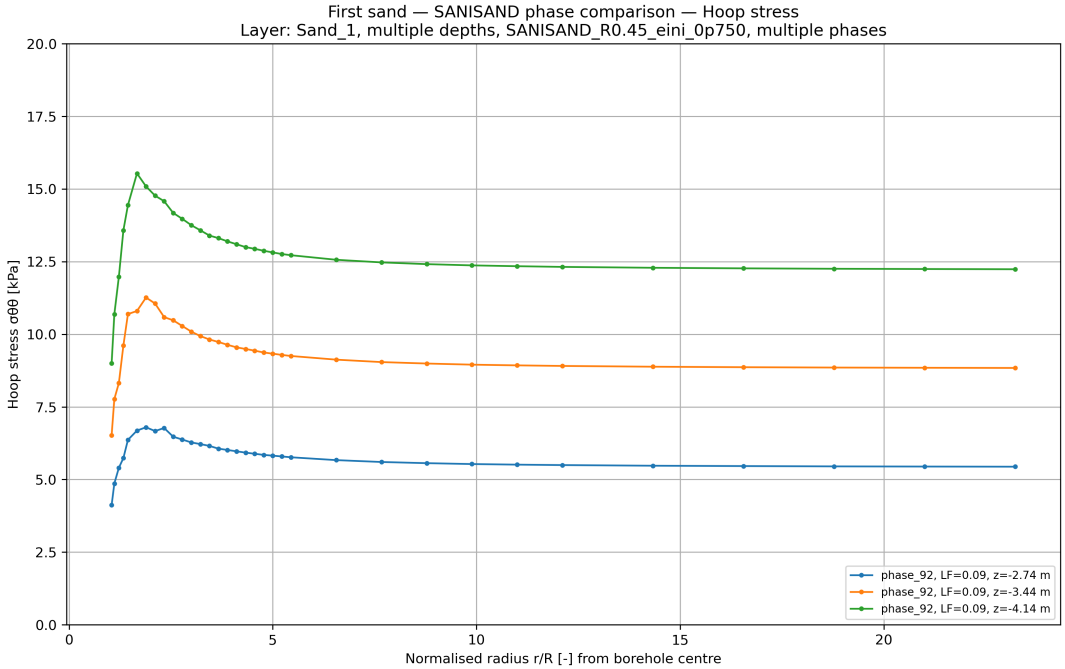

(a) SANISAND hoop stress in first sand layer at different depths for initial void ratio 0.75.

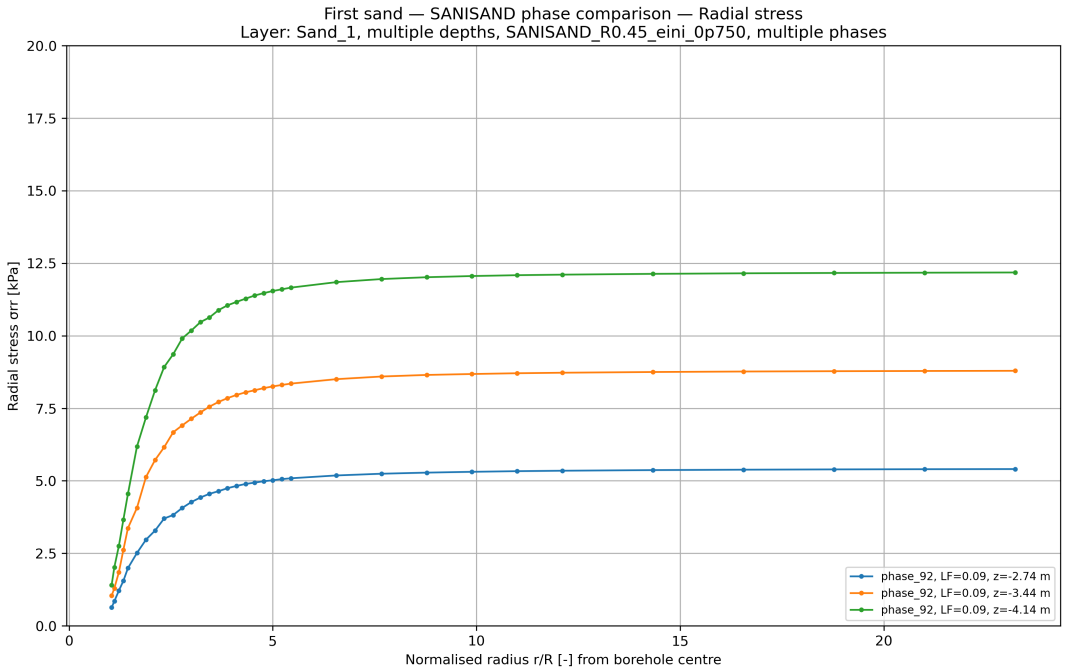

(b) SANISAND radial stress in first sand layer at different depths for initial void ratio 0.75.

Figure C.19: SANISAND hoop and radial stress at different depths for initial void ratio 0.75.

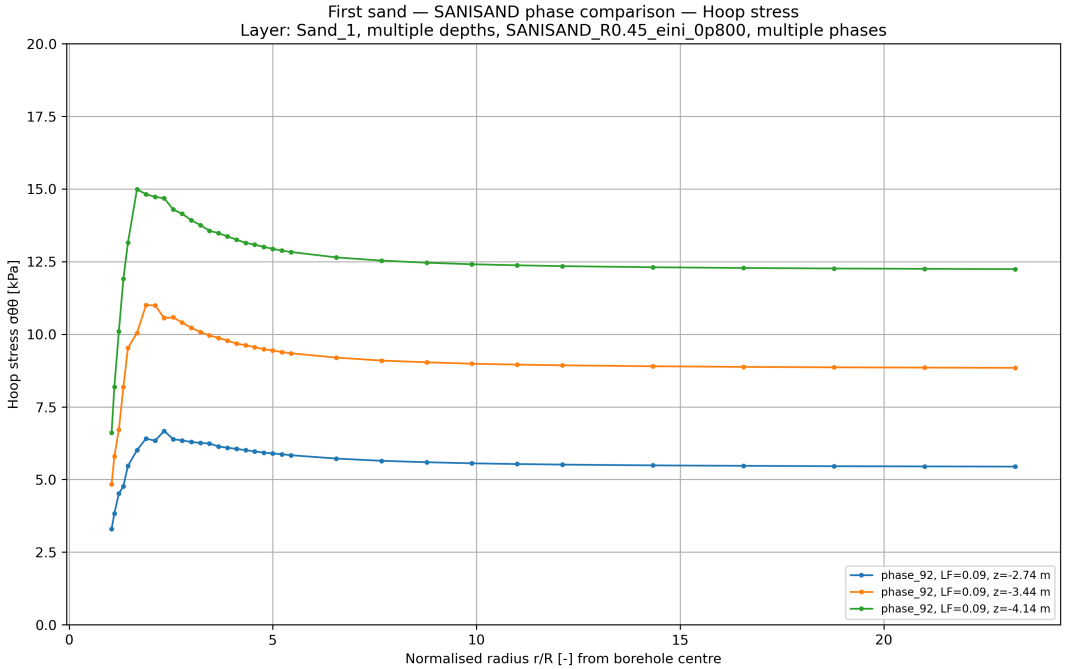

(a) SANISAND hoop stress in first sand layer at different depths for initial void ratio 0.8.

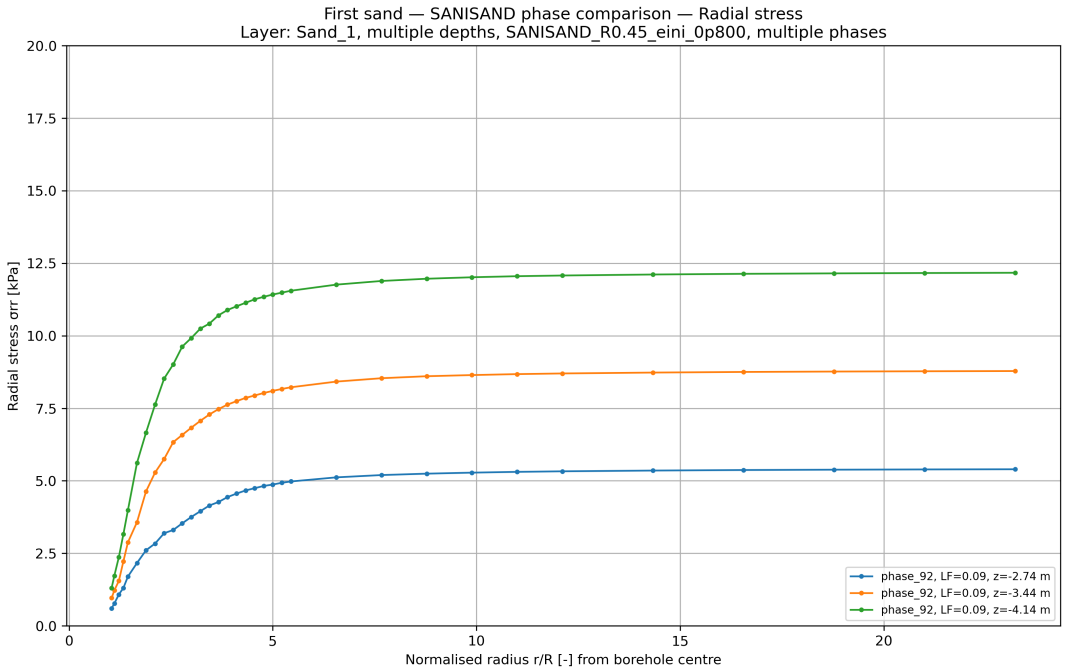

(b) SANISAND radial stress in first sand layer at different depths for initial void ratio 0.8.

Figure C.20: SANISAND hoop and radial stress at different depths for initial void ratio 0.8.

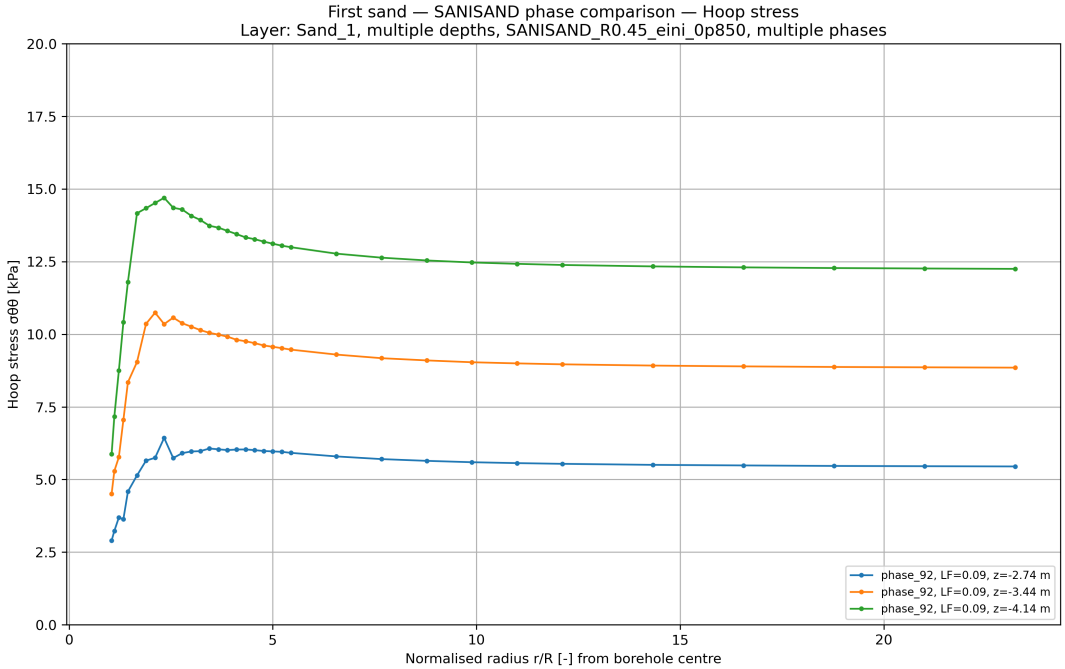

(a) SANISAND hoop stress in first sand layer at different depths for initial void ratio 0.85.

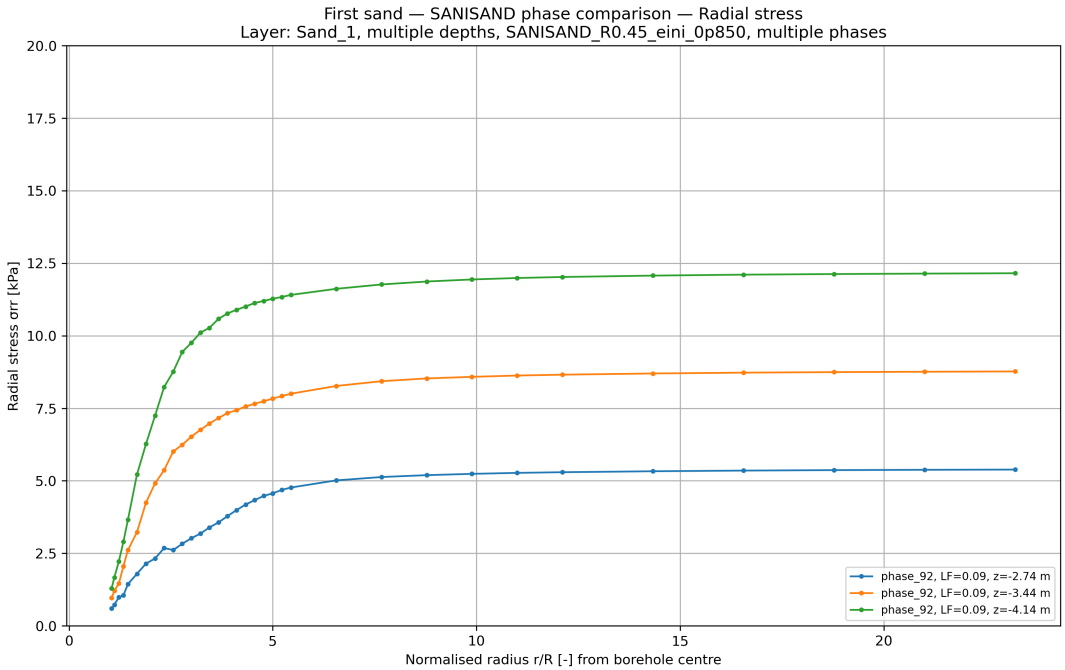

(b) SANISAND radial stress in first sand layer at different depths for initial void ratio 0.85.

Figure C.21: SANISAND hoop and radial stress at different depths for initial void ratio 0.85.

D

Github repository

https://github.com/AJGoest/CPT_Analysis.git

E

Soil distribution Wezep & Zwolle

E.1. Soil profile

E.1.1. Wezep

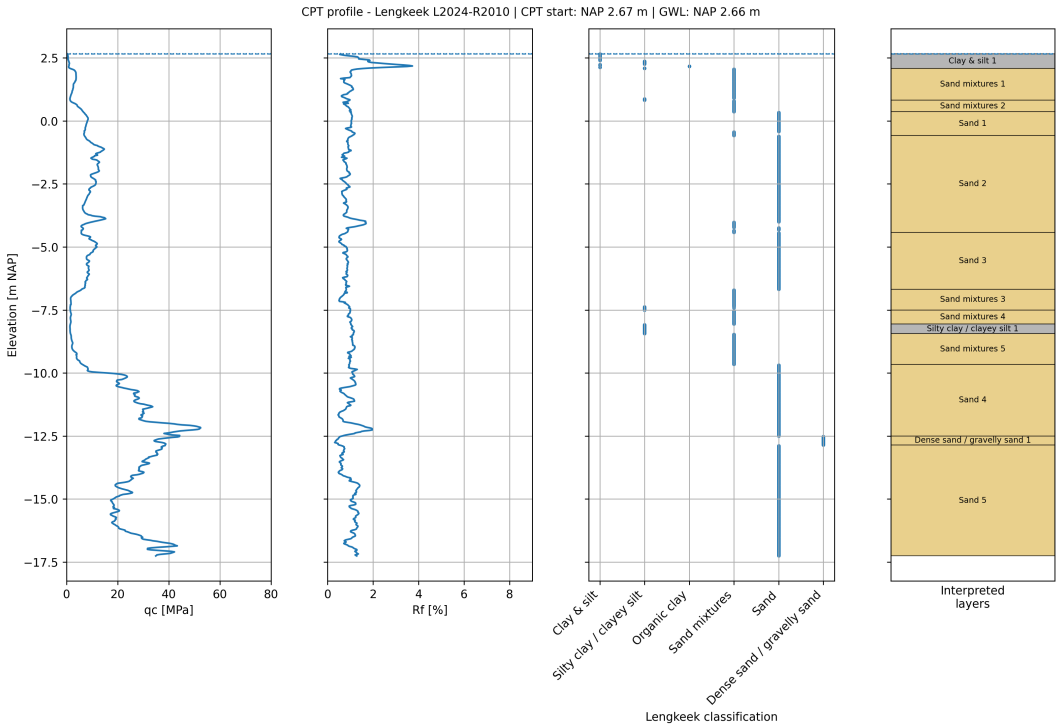

Figure E.1: After drilling soil profile for CPT S11 borehole 9.

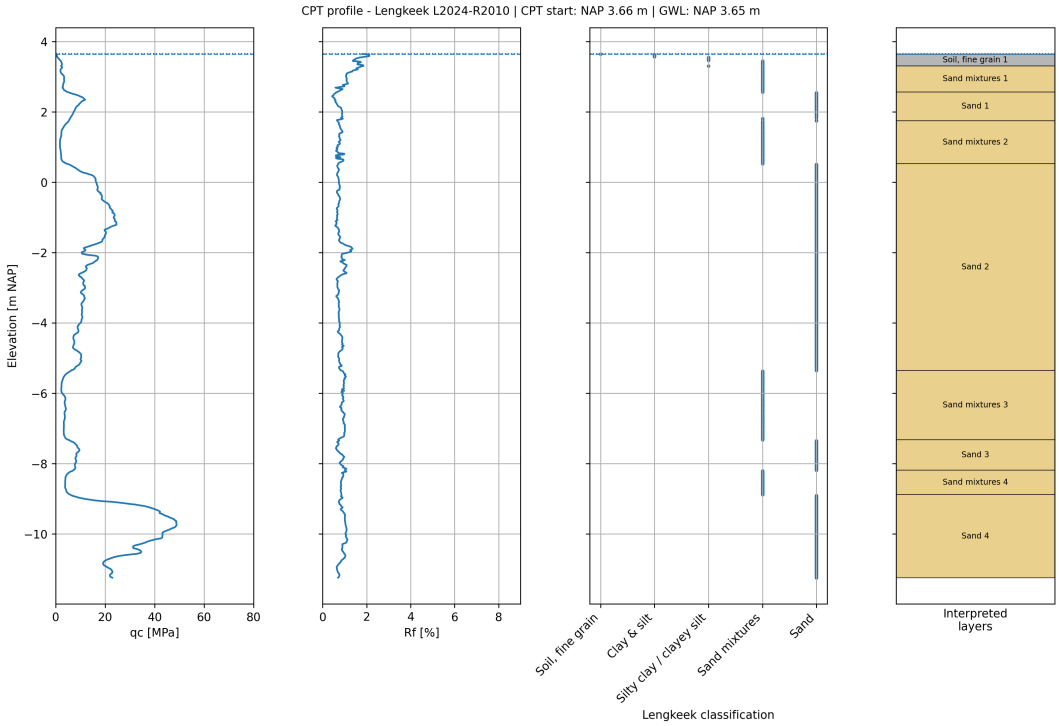

Figure E.2: Before drilling soil profile for CPT S6 borehole 10.

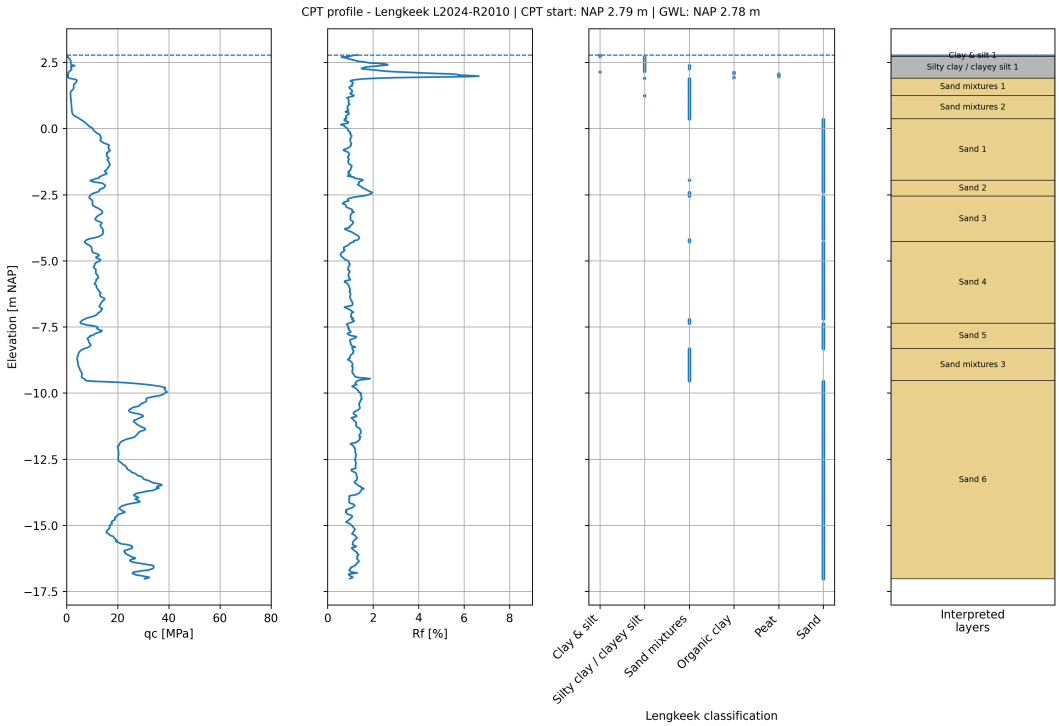

Figure E.3: After drilling soil profile for CPT S13 borehole 10.

E.1.2. Zwolle
Borehole 26

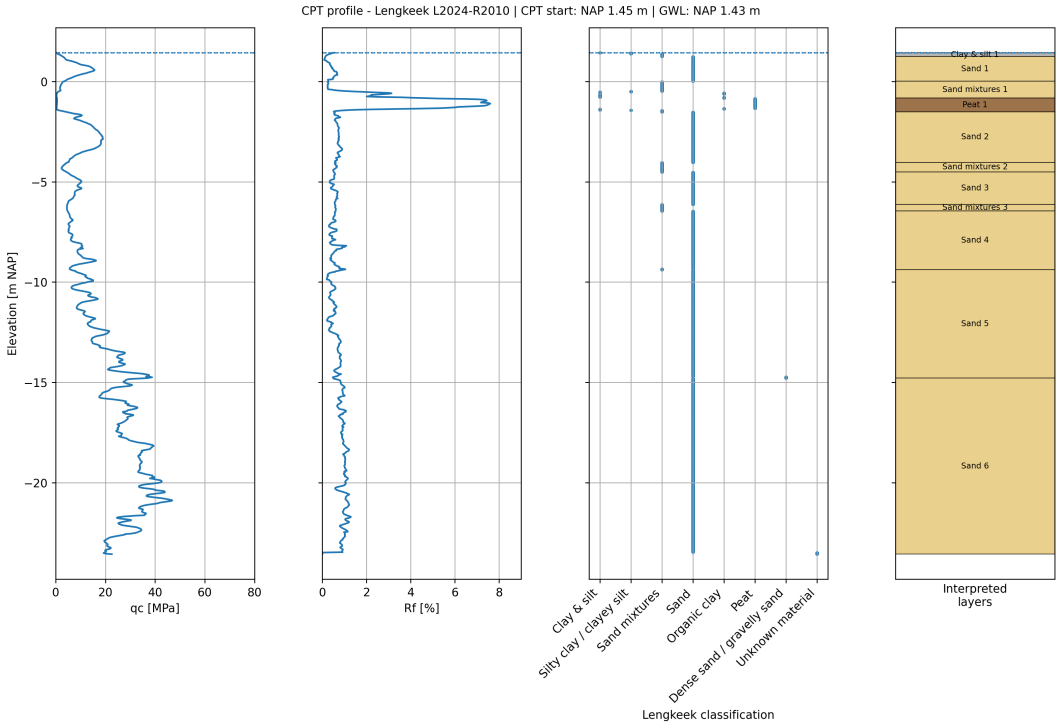

Figure E.4: Before drilling soil profile for CPT 2 borehole 26.

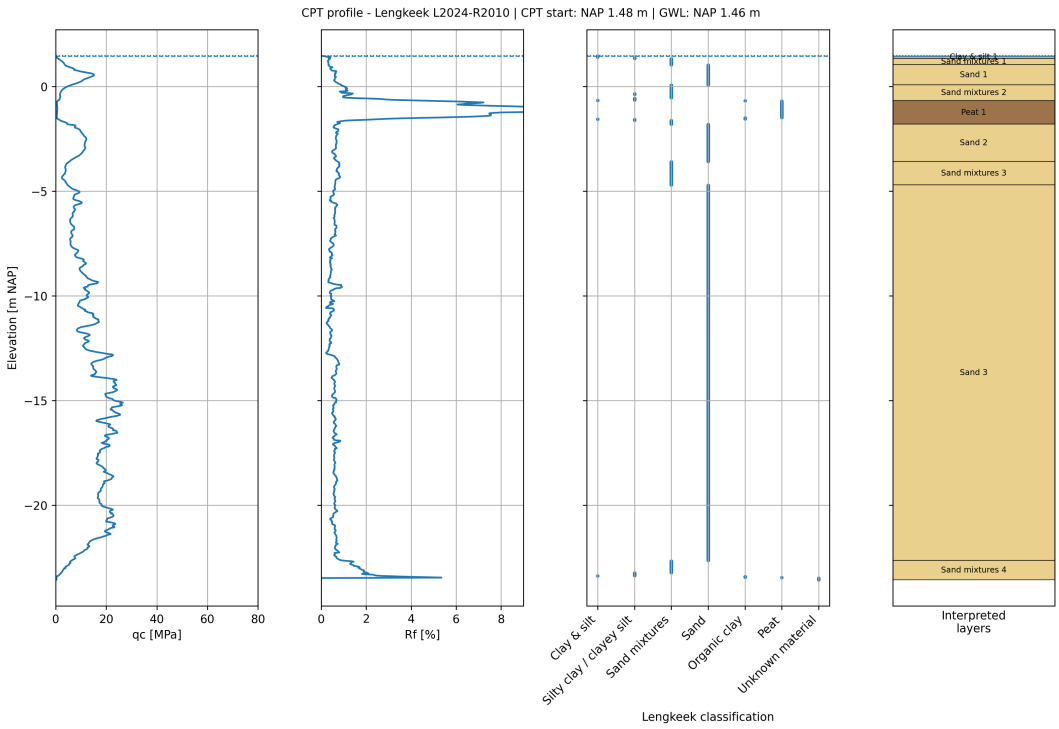

Figure E.5: After drilling soil profile for CPT 8 borehole 26.

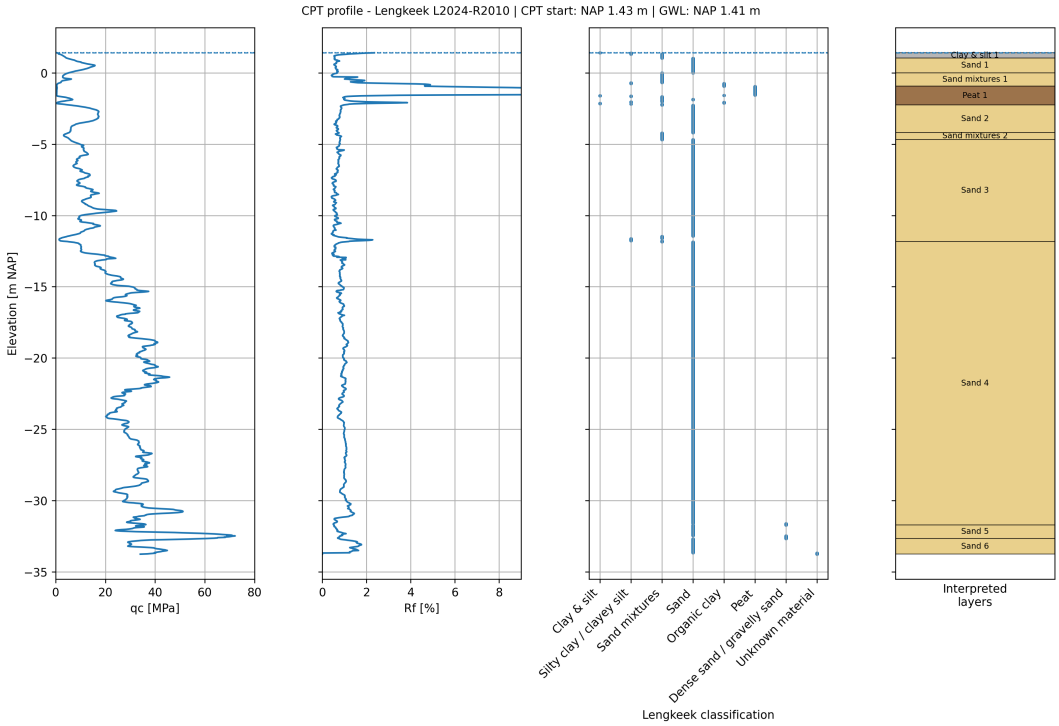

Figure E.6: After drilling soil profile for CPT 16 borehole 26.

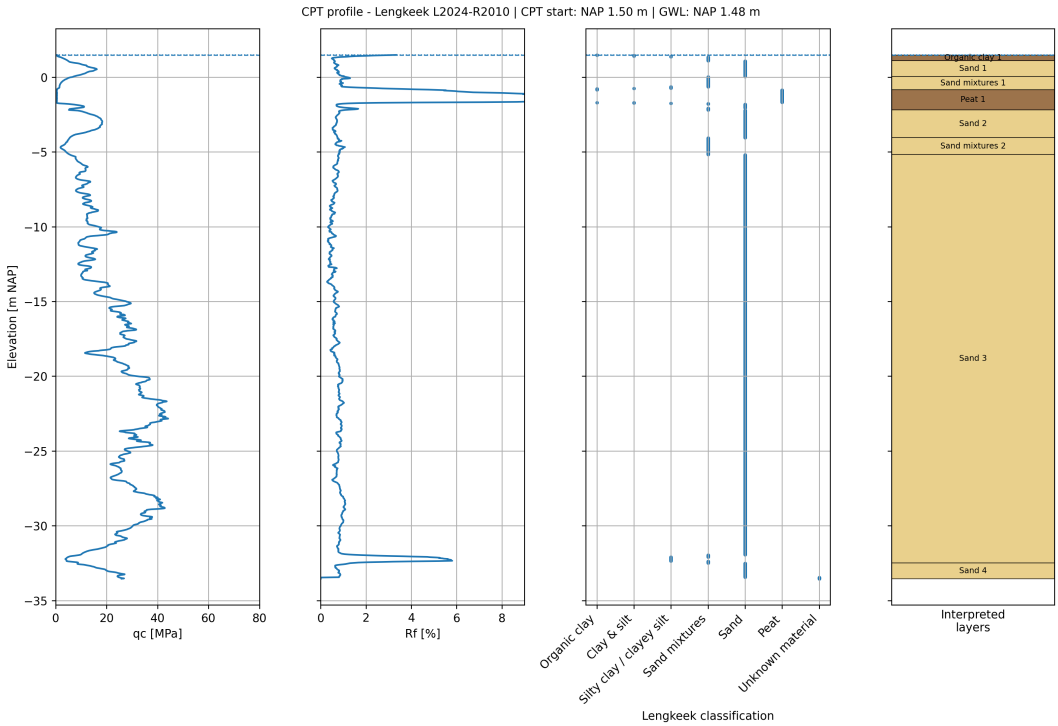

Figure E.7: After drilling soil profile for CPT 206 borehole 26.

Borehole 52

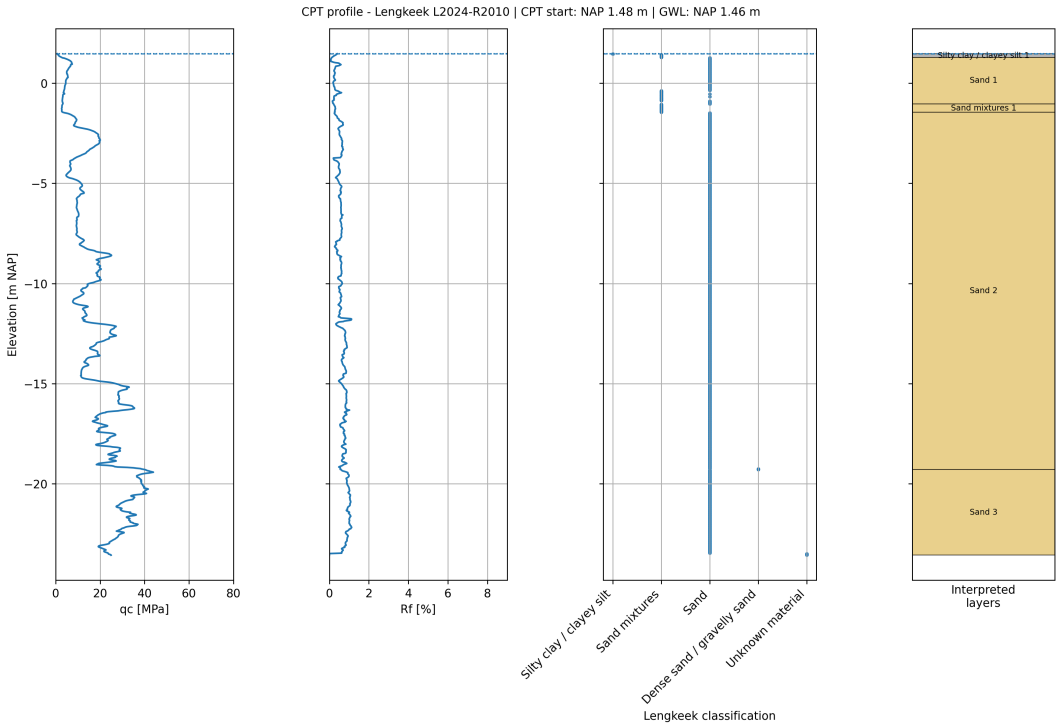

Figure E.8: Before drilling soil profile for CPT 3 borehole 52.

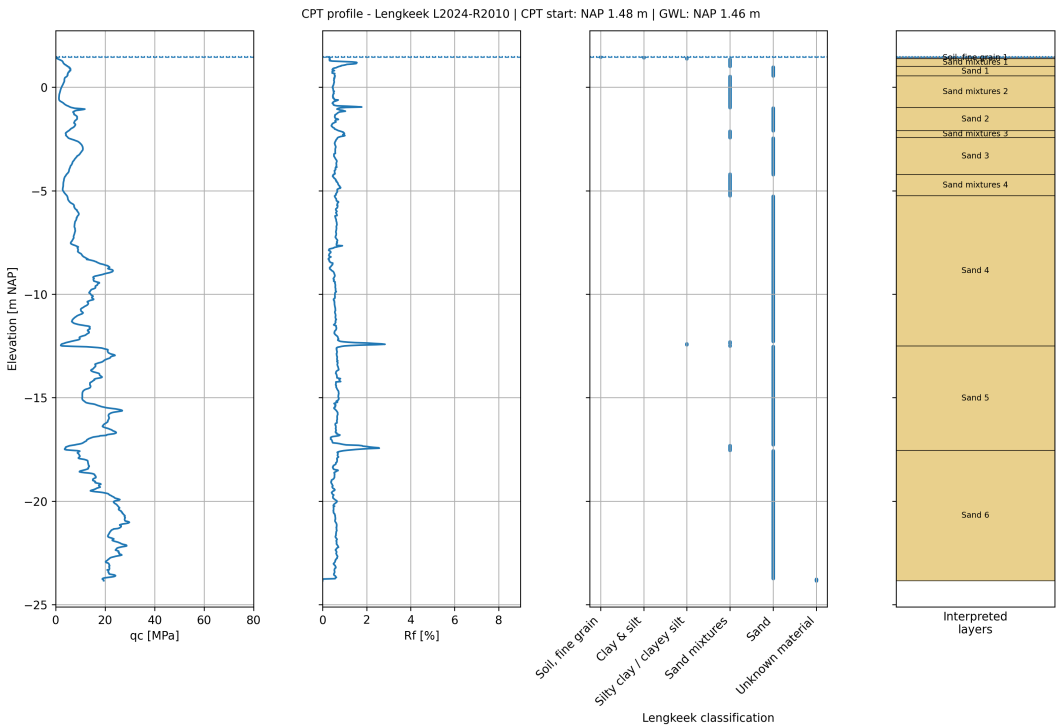

Figure E.9: After drilling soil profile for CPT 10 borehole 52.

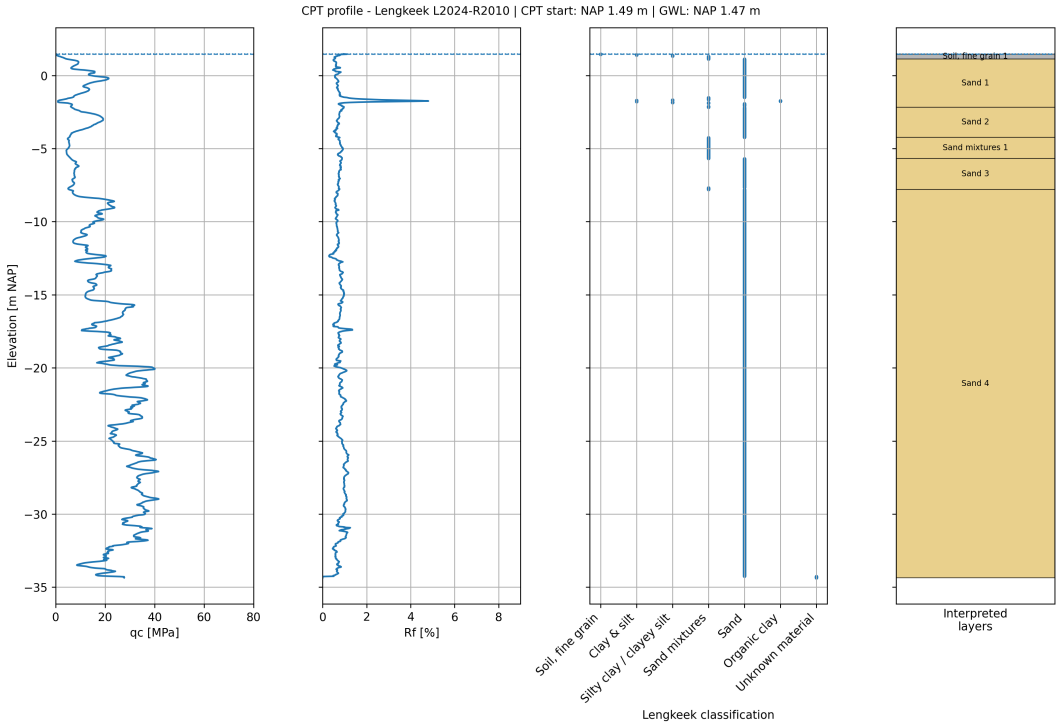

Figure E.10: After drilling soil profile for CPT 18 borehole 52.

Borehole 55

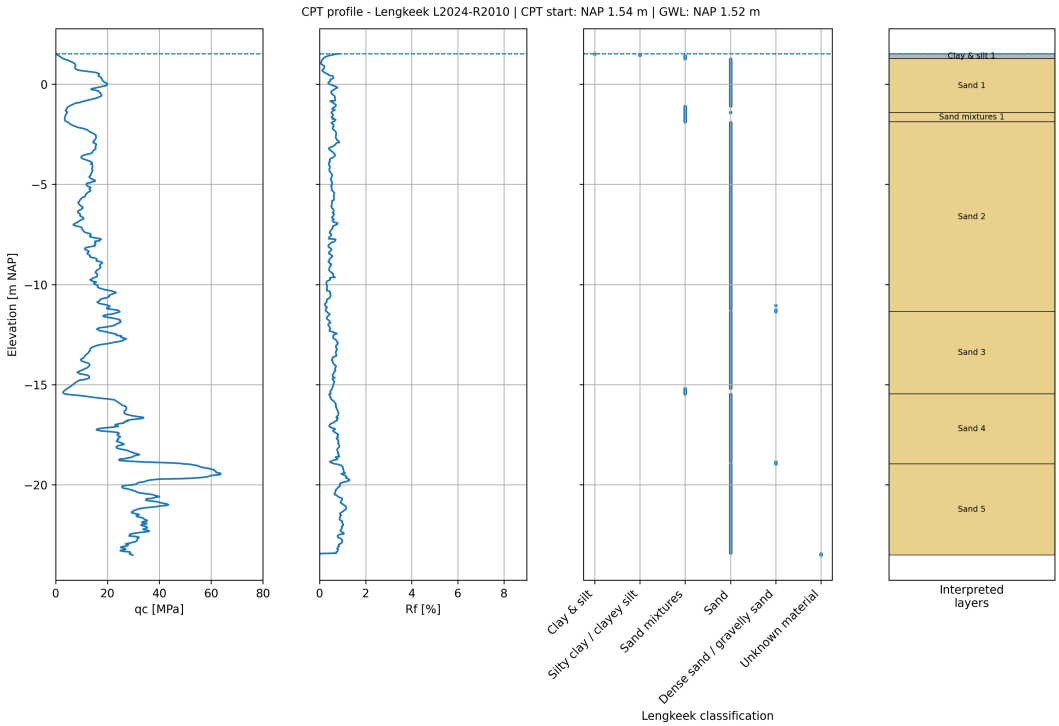

Figure E.11: Before drilling soil profile for CPT 4 borehole 55.

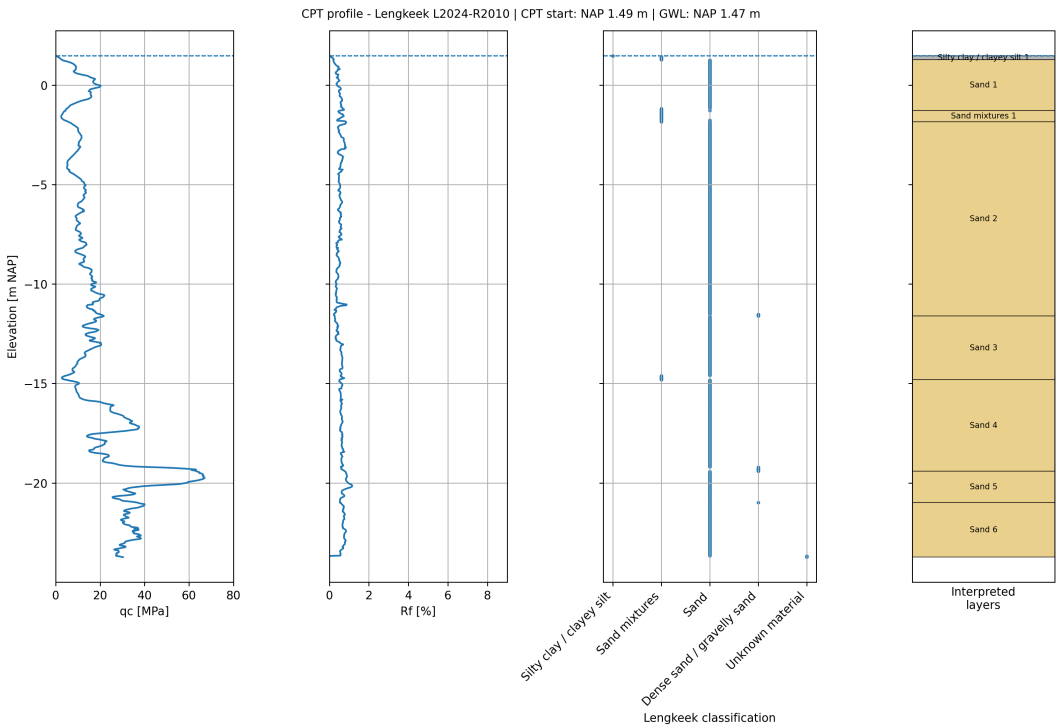

Figure E.12: After drilling soil profile for CPT 12 borehole 55.

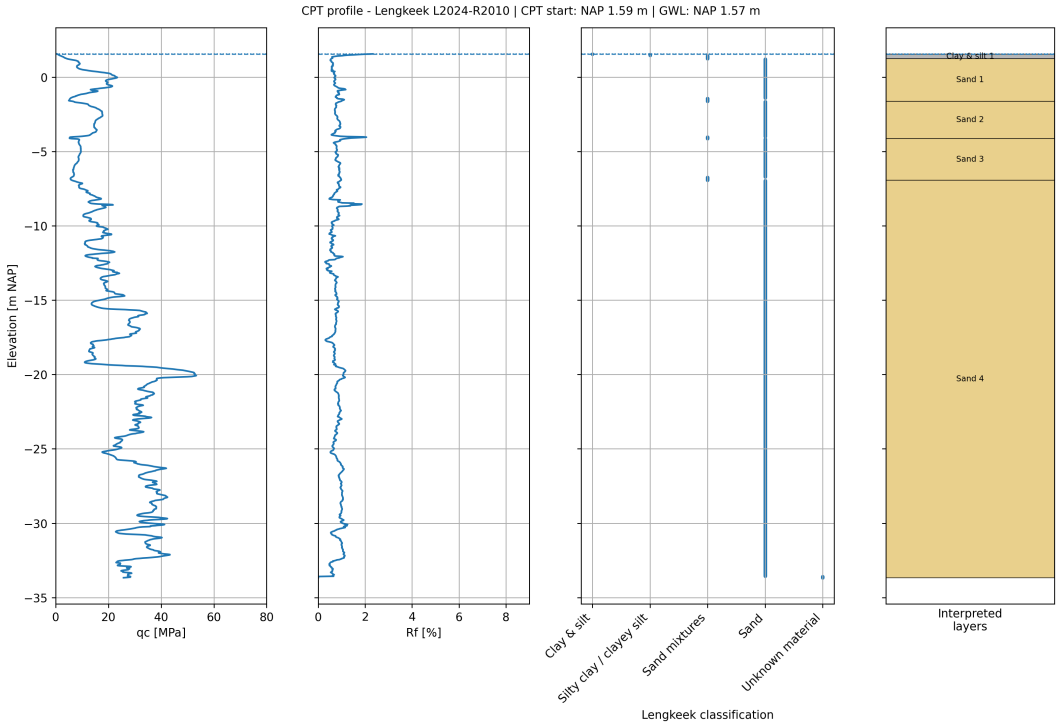

Figure E.13: After drilling soil profile for CPT 20 borehole 55.